Ultrafast Investigations of Materials using Angle-Resolved Photoemission Spectroscopy with High Harmonic Generation

by

Adra Victoria Carr

B.S., University of Arizona, 2007

M.S., University of Colorado Boulder, 2011

A thesis submitted to the

Faculty of the Graduate School of the

University of Colorado in partial fulfillment

of the requirements for the degree of

Doctor of Philosophy

Department of Physics

2015

This thesis entitled:
Ultrafast Investigations of Materials using Angle-Resolved Photoemission Spectroscopy with High Harmonic Generation
written by Adra Victoria Carr
has been approved for the Department of Physics

Margaret M. Murnane

Prof. Henry C. Kapteyn

Date

The final copy of this thesis has been examined by the signatories, and we find that both the content and the form meet acceptable presentation standards of scholarly work in the above mentioned discipline.

Carr, Adra Victoria (Ph.D., Physics)

Ultrafast Investigations of Materials using Angle-Resolved Photoemission Spectroscopy with High Harmonic Generation

Thesis directed by Prof. Margaret M. Murnane

Knowing the electronic states of materials and how electrons behave in time is essential to understanding a wide range of physical processes, from surface catalysis and photochemistry to practical electrical behavior of devices. Combining Angle-Resolved Photoemission Spectroscopy (ARPES) with short wavelength high-harmonics to drive the photoemission process, allows for the direct probing of a wide range of electronic states and momenta within a material. Furthermore, in a pump-probe approach, electron dynamics can be probed by mapping the response of a system at specific instances after an excitation. I present results from three studies utilizing time-resolved ARPES, spanning the conventional" approach of mapping electron/hole dynamics of a material after an excitation - to more exotic experimental schemes that probe fundamental electronic properties via interferometric attosecond electron spectroscopy and band-bending at semiconductor interfaces. In addition to providing information on the fundamental behavior of charge carriers and electronic states in condensed matter, such studies illustrate the versatility of the high harmonic time-resolved ARPES technique, and demonstrate the potential of this technique to be extended with new experimental high-resolution and circular-polarization capabilities.

Dedication

For Jing.

Acknowledgements

This work is the result of the teaching, mentoring, collaboration, patience, and drive of many great people. I especially thank my advisors, Margaret and Henry, for awarding me incredible opportunities, academically and professionally, and having unwavering patience in the construction of a new experiment. I am also grateful to have traveled and collaborated with some of the best mentors and minds in the surface science community: Martin Aeschlimann (TU Kaiserslautern) and Michael Bauer (TU Kiel), Dan Dessau (CU Boulder), and Mark Keller (NIST). Thank you to my mentors at IBM, especially Richard Haight, who has been a pioneer in this field from its beginning and whose perspectives on science and life have been invaluable.

I have had the pleasure of working with two incredibly talented post-docs during my tenure. Stefan Mathias, who implemented the initial apparatus that ours currently resembles, has been a great personal and professional mentor. This experiment would not be possible without his expertise and courage to tear everything down and start anew. Piotr Matyba has been a great contribution in offering fresh perspectives and ideas for experiments. He has had tremendous patience and diligence in seeing the experiment finally produce results and it could not have been done without him. Thank you to the PES team: Cong Chen and Zhensheng Tao. The experiment is in excellent hands with their direction and there is assuredly more great science to come.

Jing, this should have been your work. Im sad others wont get to experience late nights in lab laughing about horrible mistranslations in Chinese. Ethan, Ive been trying to incorporate your fantastical view of the world and love for adventure. Thank you for giving me the best motivational speech still ringing in my head: “Go team!” I miss you both tremendously.

I gratefully acknowledge support from the JILA staff, especially the instrument shop staff: Hans Green, Blaine Horner, Todd Asnicar, Kim Hagen, Tracy Keep, Dave Alchenberger, and Kels Detra. The realization of the constant redesigns to this experiment would not have been possible without their fined tuned expertise. To the JILA computing team, especially JR Raith who should be given a cape for his superhero ability to always have the right replacement part at 8pm or know exactly which commands to execute when the Windows machines decide to rebel.

To the Kaiserslautern crew: especially Steffen Eich, Sebastian Emmerich, Jurij Urbancic, Andy Ruffing, and Martin Wiesenmayer. Thank you for making the late night runs *way* more fun than they should be and education on all things definitively "German". Thank you to the past (esp. Luis Miaja-Avila, Daisy Raymondson, Sterling Backus) and present KM group members.

To Eric, Kevin, Steve, Carrie, Travis, Joe, Jrr, Dan H., Alejandra, Andrew, Dan W., Katie and Phoenix who are the best support to my sanity. To my roommate here for 6 years, Tara Drake, who amazingly shares my love of all things ridiculous and is always able to help with late night existential crises. You are the best person to laugh with about science not making any sense. Thank you to Craig Hogle, for much needed dance interludes, coffee breaks, stories, and introduction to horrible, horrible songs that should not be listened to by anyone.

To my Dad- who taught me that everything is a "project", nothing is ever a "black box", and not to fear taking things apart (while having a few choice swears reserved in case things go wrong). To my Mom- who instilled curiosity and constant reminders that the world is a really, really big place to explore. To my big brother, Jake- who is the beautiful dichotomy of being the constant voice of pragmatism while having airplane/drag racing/boar hunting hobbies that make me scared just how relative the term "pragmatism" can be. You are a great support and thanks for reminding me that its ok to have fun occasionally.

Finally, Yance. I 100% would have been unable to do this without you. 9 years and always willing to talk science, horrible tv shows (even if you spoil the ending to them all), philosophy, games, and life. After 2 states, 5 houses, innumerable cross country flights, and the inevitable 4 ER visits (Im really sorry Im such a clutz), thank you for being the best copilot on this adventure.

Contents

Chapter

Tables

Table

Figures

Figure

Chapter 1

Introduction

One of the key motivations in the field of Material Science has been in determining precisely how a material's underlying structure- meaning geometric and, by extension, electronic- dictates its macroscopic properties and behavior. For example, a material's electrical conductivity is largely determined by its electronic structure, with metals and semiconductors having larger conductivity than insulators due to the increased mobility of their charge carriers. The chemical reactivity of a surface is dictated by the electronegativity and dangling bonds of the atoms or molecules terminating it. A material's electronic structure- whether probed at a surface, interface, or within the bulk- encapsulates these characteristics and can inform on these macroscopic properties.

Of particular interest is the local electronic structure at surfaces and interfaces. Surfaces serve as the primary stage for processes like adsorption, desorption, diffusion, and surface-assisted chemical reactions (ie surface catalysis and surface photochemistry). This is evident in everyday applications like the Platinum-mediated redox reaction used in modern automobile catalytic converters, reducing CO pollution. Electronic structure and carrier transport through interfaces is also vital to the function and operating characteristics of electronic and opto-electronic devices, from transistors to photovoltaics. Considerable effort has therefore been made at being able to probe this local electronic structure. Understandably, one of the most direct methods in which to do this is to probe the energy states of the electrons directly, "mapping" the energy levels (E) and, in well-defined crystalline structures, crystalline momentum (k) at the surface of the material through a method like photoemission spectroscopy. In photoemission, the energy of detected electrons can

be related back to the energy state from which it came, allowing the direct "imaging" of electronic band structure in materials.

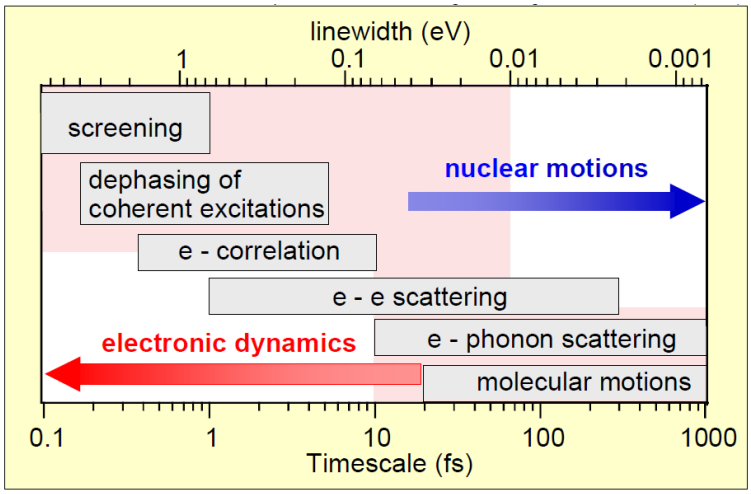

Figure 1.1: Timescales for dynamical processes determined via direct time-resolved measurements or line-width analysis. Dynamical screening of the incident external laser field occurs on the shortest timescales, followed by dephasing of coherent excitations (seen in metals). The original nonthermal distribution of electrons/holes relaxes quickly to a Fermi-Dirac distribution via electron-electron (hole-hole) scattering, followed by slow electron-phonon scattering and resulting in heating of the overall lattice. From presentation by M. Wolf, originally adapted with permission from [1].

The majority of the examples given above deal with reactions and processes at surfaces. Interest in understanding *processes* necessarily means understanding of the process as it evolves *in time*. In particular, the excitation and relaxation dynamics of the carriers in a material are important for understanding properties like ablation in optical material processing [2], magneto-optical recording [3], photochemical reactions [4], superconductivity, anomalous skin effect [5], etc. The timescales in which these dynamics occur tend to depend on the fundamental scattering and interaction of electrons, phonons, and spins of the particular system. In mapping out the response of a system to an external perturbation, like an optical laser pulse, different physical processes are dominant on varying timescales- picoseconds for electron-phonon mediated diffusion, ten to hundreds of femtoseconds for electron interactions, and even down to the attosecond realm for core hole relaxation and electron screening [1, 6]. Experiments have been able to determine these

dominant timescales through either direct time-resolved studies, sequentially probing a system at snapshots in time after an initial excitation, or indirectly through linewidth measurements of spectral features, where the Energy-time bandwidth limit ($\Delta E \Delta t \sim 4.14$ in eV and fs for Gaussian pulses [1]) sets an upper limit on the timescale of a process. A general illustration of these timescales, with electronic-dominated processes characterized by short timescales and heavy nuclear motions by longer timescales, is shown in Figure 1.1. Due to inhomogeneous broadening mechanisms in spectroscopic lineshapes being difficult to fully account for [7], direct time-domain studies are preferable. The timescales of these mechanisms are even seen to dictate reaction pathways of some surface-mediated chemical reactions. One notable example is the case of CO coadsorbed with O on a Ru(111) surface, where an initial 100 fs IR pulse can excite a hot electron population, overcoming the chemical activation barrier to form CO_2 and subsequently desorbing from the surface. At longer timescales, electron-phonon scattering yields a thermally excited CO population that, with insufficient energy to overcome the activation barrier for CO_2 formation, simply desorbs as CO [8]. The ability for electron-mediated vs phonon-mediated processes to dictate macroscopic properties like *which products result from a chemical reaction* underscores the need to understand the timescales in which they occur.

In order to study these dynamics, a probe is needed that acts on similar or faster timescales than the processes we want to capture. This is akin to using a fast shutter speed on a camera when capturing fast moving objects. Traditional radiation sources for photoemission spectroscopy have been continuous-illumination plasma discharge lamps or 10-100 ps pulse-length synchrotron facilities- neither is well suited for capturing the fastest dynamics that we're interested in (c.f. Fig 1.1). Short pulse lasers capable of readily producing pulselengths of 10s of femtoseconds have become increasingly available, with a number of companies now selling off-the-shelf products. With nonlinear techniques and tricks in its generation, groups have even demonstrated isolated attosecond pulses down to 67 as [9], with 140 as pulses used in time resolved spectroscopies [10]. Nonlinear conversion techniques of these short-pulse lasers can be used to produce laser-driven high harmonics from the vacuum UV to soft x-ray region [11, 12]. More commonly generated in the 10-100

eV range due to higher flux, these high harmonics provide a suitable photon source to be used in photoemission studies, enabling a wider range of momentum and energy to be probed while maintaining short pulses fit for time-resolved studies [13, 14]. First demonstrated in carrier dynamics studies in semiconductors like GaAs(110) [15], this EUV laser-based technique has since been successfully used to study dynamics including femtosecond surface chemistry processes [16], metal-insulator phase transitions [17], and transient charge screening in semiconductors [18]. Other work in time resolved photoemission studies has recently focused on the generation of tunable ∼6 eV sources to improve the lower energy resolution that often is a consequence of the necessarily broad bandwidth needed for the high harmonic generation process [19, 20]. As such, current efforts to improve energy resolution of higher energy harmonics (21 eV) using blue-driven harmonics [14] will be briefly discussed in this work. It should be noted that successful work has also been done at the newly-available Free Electron Laser (FEL) facilities [21], where EUV emission is produced via electrons accelerated to relativistic speeds using linear accelerators. These facilities have only recently been implemented in time resolved experiments [22, 23] and show promise for future solid state studies.

With the field of time-resolved photoemission spectroscopy still being highly explored, these "traditional" time-resolved techniques have been recently extended to different geometries and applications. Most notably, with the demonstration of attosecond pulse trains and isolated attosecond pulses using high harmonic generation schemes, attosecond spectroscopy has emerged as a ripe new field of interest for dynamical investigations of materials. This holds promise for in-depth studies of the fastest electron dynamics including inner shell relaxation dynamics, electron screening, and electron-electron processes [24]. Initially applied to atomic systems and only recently extended to solids, a common trait seen in these investigations has been the observation of phase delays when comparing spectra of different electronic states within the atom or solid. Modeling of these phase delays and interpretation of why they arise has proved challenging, with classical and quantum mechanical models trading-off being able to reproduce experimental observations, with little agreement and constant debate underway.

While the carrier dynamics on the femtosecond and attosecond timescales are important to study, the hot-carrier population generated as a consequence of our laser-based time-resolved technique can itself be used to measure band-bending in semiconductor systems. In traditional "photovoltage" techniques [25, 26, 27], a moderate electron-hole population partially screens the original dipole that is the cause of band bending at the semiconductor interface. The absolute band bending, therefore, needs to be determined via extrapolating the screening effect over time. With the large electron-hole population and high photon energy probes utilized in our experimental approach, this screening effect can be pushed to saturation [28, 29], canceling out the dipole all together and allowing the band bending to be directly probed. This technique can serve as a powerful probe for measuring minor changes to this dipole, namely changes in the total number of detrimental charge defects present that can effect the overall properties of the material when used in devices [30, 31].

In the following work, an array of studies are performed with high harmonic time-resolved photoemission spectroscopy that incorporate these conventional and alternative techniques. The specific technical implementations range from the "traditional" ultrafast mapping of carrier dynamics to more recent extensions of this technique to the field of attosecond spectroscopy and band-flattening measurements at semiconductor interfaces. While the well studied Cu(111) surface is used in our attosecond spectroscopy measurements to make fundamental investigations of attosecond delays of valence states, the later two materials investigated- graphene and InGaAs multilayer stacks- are of interest in the realm of "post-silicon" electronics. These materials are strong candidates hoping to replace the increasingly-failing silicon in devices such as diodes, transistors, and photovoltaics. In studies on graphene, carrier dynamics and controllable modifications of its electronic structure via surface adsorbates are probed. Lastly, deposition and thermal annealing studies on InGaAs multilayer stacks are used to determine the evolution of defects and trapped charge through observing changes to the overall band bending at the semiconductor interface.

1.1 Organization of thesis

In Chapter 2, the relevant theoretical background will be presented on the techniques common to *all* experiments presented within the work- namely photoemission spectroscopy, high harmonic generation and the advantages that come with pairing them together. Chapter 3 outlines the experimental apparatus in its current form, describing the laser system, spectroscopic detector, and sample preparation/ characterization tools. Modifications to this layout are noted in each respective experimental chapter. Chapter 4 discusses interferometric attosecond spectroscopy, where the interferometric attosecond spectroscopy technique utilizing multiple harmonics is extended to surfaces for the first time. By comparing the resulting interferometric signals of two unique valence states in Cu(111), the nature of the observed phase delay is discussed in the context of current theoretical models. Chapters 5-6 then probe two technologically relevant materials in detail- graphene (Gr) and InGaAs multilayer stacks. In Chapter 5, carrier dynamics studies are performed on Gr/SiC(0001). Alkali intercalation studies on Gr/Ni(111) are also presented. In Chapter 6, InGaAs/high-k/metal gate stacks are probed with the band flattening photovoltage technique. Relevant theoretical details pertaining to each material and experiment will be presented in each respective experimental chapter (Chapters 4-6). Future work including the recent realization of circular harmonics and overall conclusions will be discussed in Chapter 7.

These results represent the culmination of a complete redesign of the previously existing experiment, with past experimental capabilities being extended to include angularly-resolved electron detection, a state-of-the-art sample manipulator, and an updated laser system for use with new High Harmonic Generation (HHG) schemes. Further details of this redesign are left for discussion in Chapter 3. The interfacial band-flattening measurements in Chapter 6 were performed using a similar experimental apparatus during a research internship in the High-κ/metal gate Division at IBM Yorktown Heights.

Chapter 2

General Theoretical Background

While the specific techniques vary in the experiments presented within this work, several methods are common to all experiments. Primarily, all experiments utilize photoemission spectroscopy (PES) or angle resolved photoemission spectroscopy (ARPES) initiated with femtosecond high-harmonic pulses, allowing the electronic states of a material to be probed directly. In a time-resolved approach, these techniques can be implemented to study unfilled electronic states or macroscopic phase changes in a material by electron excitation- "pumping" electrons into unfilled bands or nonequilibrium states and subsequently "probing" them via photoemission.

The following sections outline the necessary theoretical background for these common techniques that are employed in the experimental studies to follow. After providing the theoretical description for PES (Section 2.1) and high harmonic generation (Sec 2.2), the specific advantages of pairing HHG with PES are highlighted in Section 2.3.

2.1 Photoemission Spectroscopy

Photoemission spectroscopy has long been one of the most direct methods for studying electronic energy levels in solid state systems. First observed by Hertz in 1887 and explained by Einstein in 1905 (see [32] and references therein), the photoelectric effect occurs when a photon is incident on a medium, giving the possibility of emitting an electron. An electron can be emitted with kinetic energy according to:

$$E_K = h\nu - \phi_m - E_B \tag{2.1}$$

where ν is the incident photon frequency, ϕ_m is the work function of the material, and E_B is the initial binding energy of the electron. Detecting the resultant electron's kinetic energy, E_K, and presumably knowing the incident photon frequency and work function of the solid, the original binding energy of the electron can be determined (as shown in Fig 2.1a). It follows that higher photon energies ($h\nu$), like those employed here with the use of high harmonics, give access to a wider range of electron binding energies. This provides a more "complete" picture of the state of the electrons in the material at given snapshots in time.

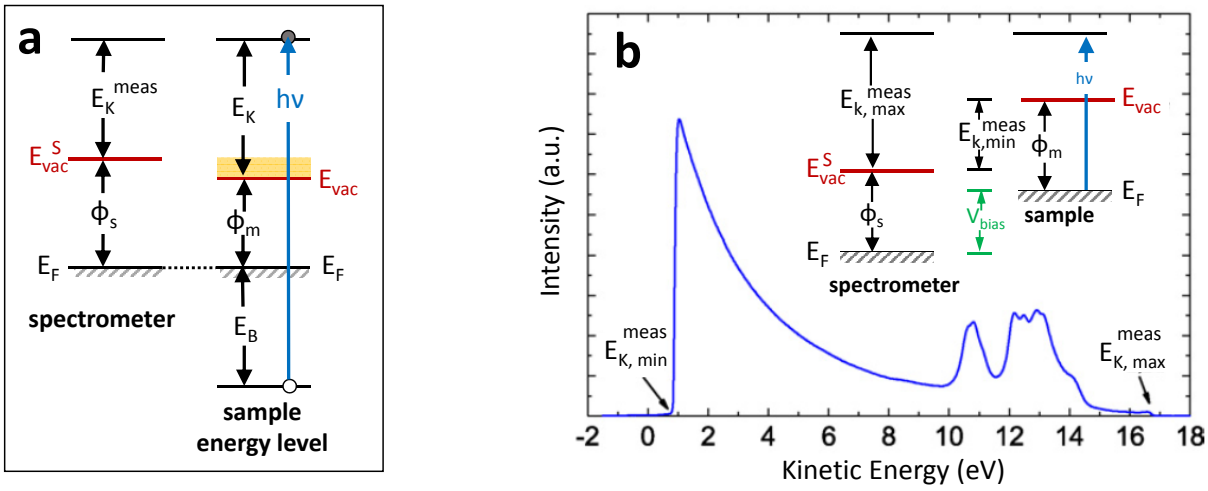

Figure 2.1: (a) General energy level diagram for the photoemission process of a photon with energy $h\nu$ ejecting an electron from Binding Energy E_B to a kinetic energy E_K. With the sample in electrical contact with the spectrometer, their Fermi levels (E_F) also equilibrate. This gives a final *measured* kinetic energy E_K^{meas}. Electrons falling in the orange E_K range are not detected by the spectrometer with $\phi_s > \phi_m$ (b) Photoemission spectrum of Gold using He I radiation (21.22 eV) with a -10V applied bias (Kinetic Energy scale already bias corrected). The corresponding energy level bias is shown inset. Adapted with permission from [33].

In practice, the actual *measured* Kinetic Energy of the electron (E_K^{meas}) must have the work function of the spectrometer taken into account. With the sample and spectrometer in good electrical contact, the Fermi levels necessarily equilibrate with each other to give different respective vacuum levels (E_{vac}) due to intrinsic differences in work function (ϕ_s and ϕ_m for the spectrometer and material, respectively). This is shown in red in Fig 2.1a. The resultant "contact potential" difference can be expressed as the difference in work function with $\Delta\phi = (\phi_m - \phi_s)$. The measured

kinetic energy can then be written as:

$$E_K^{meas} = h\nu - E_B - \phi_m + \Delta\phi \tag{2.2}$$

$$= h\nu - E_B - \phi_m + (\phi_m - \phi_s) \tag{2.3}$$

$$= h\nu - E_B - \phi_s \tag{2.4}$$

E_K^{meas} is seen to only depend on the work function of the spectrometer, ϕ_s. In the collected photoelectron spectra, this has the consequence of the measured binding energies (with respect to the Fermi level), not being dependent on changes to the sample work function due to effects like surface contamination [33, 34]. The spectrometer work function can then be easily determined through analyzing the photoelectron spectrum of a material with states occupied up to E_F (typically metals, commonly Gold as shown in Fig 2.1b), determining the corresponding kinetic energy of E_F ($E_{k,max}^{meas}$), and solving for ϕ_s in Eq 2.4.

Sample work function measurements, can prove useful in diagnosing changes to surface composition, such as the surface adsorbate coverage measurements presented in Chapter 5 or evaluating compositional changes with high-temperature thermal treatments in Chapter 6. Therefore, a method for determining the sample work function is also desirable. With the typical $\phi_s > \phi_m$, the lower cut off of the spectrum ($E_{k,min}^{meas}$) is dictated by ϕ_s. Shown in the orange region in Fig 2.1(a), the lowest energy electrons that would otherwise demarcate the ϕ_m edge have enough kinetic energy to escape the sample, but are essentially repelled from the detector due to the local vacuum level difference. Applying a bias (V_{bias}) then allows these lower-edge electrons to be measured by the spectrometer. Shown in Fig 2.1 (b), with the corresponding energy level diagram shown inset, the sample work function can be determined by looking at the full range in kinetic energies of the photoemission spectrum:

$$\phi_m = h\nu - (E_{K,max}^{meas} - E_{K,min}^{meas}) \tag{2.5}$$

Sample work function measurements for the studies in Chap 5-6 were collected in this manner [33].

2.1.1 Angle Resolved Photoemission

With the addition of angular detection of photoelectrons, *Angle Resolved* Photoemission spectroscopy is one of the most direct ways of studying electronic *dispersion*, or "band structure", in solids. During the photoemission process, the energy and momentum of the electron need to be conserved (where the contribution of the photon's momentum is negligibly small). Shown schematically in Fig 2.2 (left), momentum is conserved in the in-plane direction ($k_{||}$, with a k_x and k_y component) due to translational symmetry. The angle of emission of the electron from the surface (θ) can be related to this momentum according to:

$$p_{||} = \hbar k_{||} \tag{2.6}$$

$$= \sqrt{2mE_K} sin(\theta) \tag{2.7}$$

$$k_{||} = \sqrt{\frac{2m}{\hbar^2} E_K} sin(\theta) \tag{2.8}$$

where m is the electron mass. Therefore, simultaneous detection of both the electron's kinetic energy and emitted angle allows one to create a two-dimensional energy vs. momentum "map" in momentum space, commonly referred to as k-space [35]. This gives information on the dispersion ($E(k)$) of the filled electronic bands in the material and is directly measurable with modern ARPES detectors. An example of a collected spectra of Graphene/SiC is shown in Fig 2.2 (right) with bright regions indicating electron occupation, as a function of binding energy ($E_K - E_F$). Due to the requirement that only a well ordered real-space structure gives a well-defined k-space structure, samples probed via angle-resolved photoemission necessarily need to be well ordered and low in defects.

The out-of-plane momentum ($k_\perp$) is more difficult to determine due the presence of the surface potential, V_0, breaking translational symmetry. With V_0 known or assumed, this can be calculated as:

$$k_\perp = \sqrt{\frac{2m}{\hbar^2}(E_K + V_0)} cos(\theta) \tag{2.9}$$

One approach typically used in mapping out the dispersion of electronic states in $k_\perp$ is by

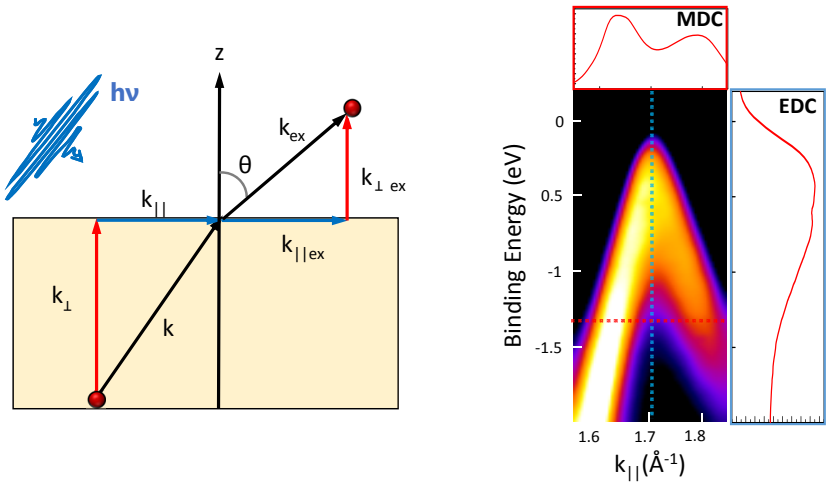

Figure 2.2: (left) General illustration for photoemission from surfaces upon illumination of photon with energy $h\nu$, with $k_\perp$ and $k_{||}$ components identified for the photoelectron within the solid (k) and upon photoemission into the vacuum (k_{ex}. (right) typical ARPES spectra, shown for Graphene/Si(0001), with denoted energy distribution curve (EDC) and momentum distribution curve (MDC) extracted along the blue and red lines, respectively.

varying the photon energy, but these types of measurements will not be employed in the studies presented here. For the case of 2D materials, like graphene, $k_\perp$ is zero and can be ignored in dispersion considerations. As will be shown in Chapter 4, surface states are special electronic states that also are only described by a $k_{||}$ component, due to their wavefunction decaying exponentially into the bulk.

One advantage of the ARPES technique is that it allows direct measurement of the single particle spectral function of the solid, containing information on many-body interactions. In high resolution studies, these quantities can be directly extracted from spectral linewidth measurements, properly accounting for experimental broadenings [35]. In the studies presented here, the lineshape of the collected spectral features is not analyzed in depth due to the dramatic energy broadening due to the high harmonics. Our spectral linewidth is dictated by the temporally short pulses required in the HHG process ($\Delta E \Delta t > \hbar$), necessitating a broad spectral bandwidth, as well as non-ideal phase matching in the harmonic generation.

Typical ARPES distributions are usually represented in two ways:

- Energy Distribution Curves (EDCs): fixed (k_x, k_y) as a function of energy
- Momentum Distribution Curves (MDCs): fixed E_B as a function of either k_x or k_y

Representative MDC and EDC curves are shown in Fig 2.2 (right), with the horizontal MDC lineout shown in red and vertical EDC lineout shown in blue. The majority of distributions discussed in this thesis will be looking at EDCs at a fixed value of $k_{||}$ or integrated over a small range of $k_{||}$. While the bulk of the experimental results presented are collected using an angle-resolved photoelectron detector, resulting in spectra similar to Fig 2.2 (right), the InGaAs experiments in Chapter 6 are performed using a Time-of-flight detector. In this geometry, an electrostatic lens collects electrons emitted over an angular acceptance range of $\pm 20^\circ$ from the surface normal. This gives an EDC integrated over this entire angular acceptance and loses any dispersion information that one might gain with angular detection.

2.1.2 Photoemission: Three step model vs one step model

The photoemission process can intuitively be described by the so-called "three-step model" [36], where the process is artificially broken into three distinct steps that can be individually modeled to produce the observed photoemission spectral intensity. A schematic illustration of this model is shown in Figure 2.3 (left).

Isolating each event that happens to the electron, these three steps can be represented as:

(1) **optical excitation of the electron within the bulk** The probability of a transition between an initial state's wavefunction and final state within the bulk, as calculated via Fermi's Golden rule.

(2) **travel of the excited electron to the surface** Electrons propagating towards the surface are able to scatter with electrons, plasmons, or phonons. This gives rise to a low energy secondary electron background, to be discussed further in Sec 2.3.3.

(3) **escape of the photoelectron into vacuum** Electrons are able to be transmitted through the surface and can be considered free.

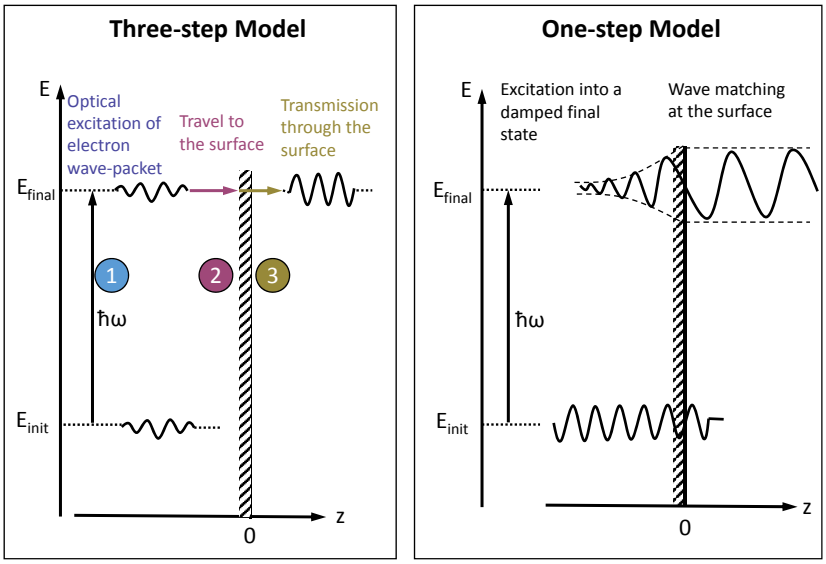

Figure 2.3: Illustration of three step (left) versus one-step (right) model of photoemission. The *three step* model is denoted by three separate processes of (1) initial optical excitation (2) electron travel to the surface (3) transmission through the surface into vacuum, with the z axis denoting depth into the bulk material. The *one step* model directly calculates the transition element of a initial wavefunction into a final state that incorporates damping and transmission through the surface. Adapted with permission from [36].

The total detected electron yield, or photocurrent I, is then proportional to the product of the (1) probability for initial excitation (2) probability for transmission through the bulk to the surface without scattering (3) the transmission probability through the surface.

Focusing on the initial electron excitation, this photocurrent I can be represented generally as:

$$I \propto \frac{2\pi}{\hbar}|\langle\Psi_f|\overrightarrow{H_{int}}|\Psi_i\rangle|^2\delta(E_f - E_i - \hbar\omega) \tag{2.10}$$

where the initial (Ψ_i) and final (Ψ_f) state wavefunctions are characterized by the eigenvalues E_i and E_f, respectively. H_{int} is the interaction Hamiltonian for the electron/photon coupling (ie. the dipole operator) and the delta function serves to conserve energy from the initial to final states when using a photon of energy $\hbar\omega$. In the three step model, the transition matrix elements calculated in "Step 1" are between initial and final Bloch states within the crystal. The other Step 2-3 terms "modify" this matrix element to take into account scattering and the transmission through the

surface.

A more accurate *"one-step model"* [37] is to directly calculate the transition matrices from an initial state to a *damped* final photoemitted state, shown in Fig 2.3 (right). In this manner, it is able to incorporate the entirety of these three steps into a single Fermi's Golden Rule transition matrix with a more accurate choice of final states, already taking into account these scattering and surface effects. The initial Bloch wavefunction is coupled to a damped final state wavefunction via the dipole operator, where the damping of the final state incorporates the scattering probability for the electron. This matrix element is, unsurprisingly, inherently difficult to evaluate and requires a number of simplifications. Theoretical approaches trying to directly evaluate these transition matrix elements are important for the attosecond measurements presented in Chapter 4, where the observed phase delays can be related to the phase of the transition matrix element.

2.2 High Harmonic Generation

Development of EUV/Soft XRay laser sources with high spatial and temporal coherence is greatly desired for solid state studies due to greater accessibility to momentum and energy states and specific advantages offered when using the photoemission technique. However, such sources have proved difficult to realize due to the tendency for most materials to be highly absorbing at shorter wavelength than 200 nm. This makes production via traditional nonlinear crystals not feasible and greatly limits the choice of material if used as a laser gain medium. In general, the pump power required to produce a given output wavelength roughly scales as λ^{-5}. This would mean an output wavelength in the X-Ray region of 1 nm would already require Terawatt pump power, making practical experimental implementation difficult [13].

Since its first observation in 1987 [38], High Harmonic Generation (HHG) has been one of the most viable candidates for a versatile, compact source of EUV to Soft X-Ray light. In this process, coherent visible light is nonlinearly upconverted to EUV and Soft X Ray wavelengths, generating a comb of harmonics that ideally spans the entire spectrum between the fundamental and the EUV/ X-Ray region. Due to the magnitude of the perturbation needed to the generating

medium's Coulombic potential, this phenomena was only made possible on table-top scale with the advent of ultrafast (sub-picosecond), high intensity (10^{15} to 10^{18} W/cm^2) laser sources [38, 39]. Recent experimental work in improved generation regimes with long driving wavelengths (> 1 μm) have been seen to generate wavelengths up to the keV regime [12].

Multiple sources exist for the generation of EUV-X-Ray light. Laser-driven high harmonic generation is attractive for several reasons compared to other available sources like synchrotrons, femtosecond slicing electron bunches, EUV lasers, and FELs. Several reviews overviewing the benefits of femtosecond x-ray sources from synchrotrons, FELs, and tabletop sources are available [40, 41] and only a brief comparison will be outlined here. EUV lasers that use a highly excited gain medium generate a high photon flux, but are limited in wavelength to the lasing transition of the generating medium. On the other hand, synchrotrons and FELs generate high intensity pulses that are *tunable* in wavelength, making then flexible in experimental applications. However, due to the physically large layouts of the apparatuses, control over the exact timing of the generated laser pulses is difficult, introducing a temporal "jitter" that makes them unsuited for studies requiring high temporal resolution. High Harmonic generation fits into this EUV/ X Ray source toolbox by having its characteristics being dependent on the driving laser source. Used with a femtosecond laser source like the Titanium-doped Sapphire (Ti:Saph) oscillator/amplifier system employed here, the characteristic energy and temporal resolution offered are well suited for time-resolved photoemission studies. The ability to pick from a range of generated harmonic wavelengths also allows for a wider range of material applications. This combination of high spatial and temporal coherence with favorable energy and temporal resolution on a continuously accessible tabletop source has become an attractive technique increasingly used in high resolution photoemission static and dynamical studies.

2.2.1 Semi-Classical Model

While a quantum mechanical description is needed to obtain an accurate model of high harmonic generation [42], approximations can be made that allow for an intuitive semi-classical,

quasi-static "three step model". This model was first proposed by Kulander and Corkum in 1993 [43, 44]. Initially, a femtosecond laser pulse is focused into the medium (a gas, in the present case, but clusters [45], molecules [46], and solids [47] have also been used) and, through ionization of the individual atoms, creates a copropagating beam of the high harmonic and fundamental beams. Multilayer optics, spectral gratings, and filters, can then be used to isolate specific wavelengths of the generated harmonics for experimental use.

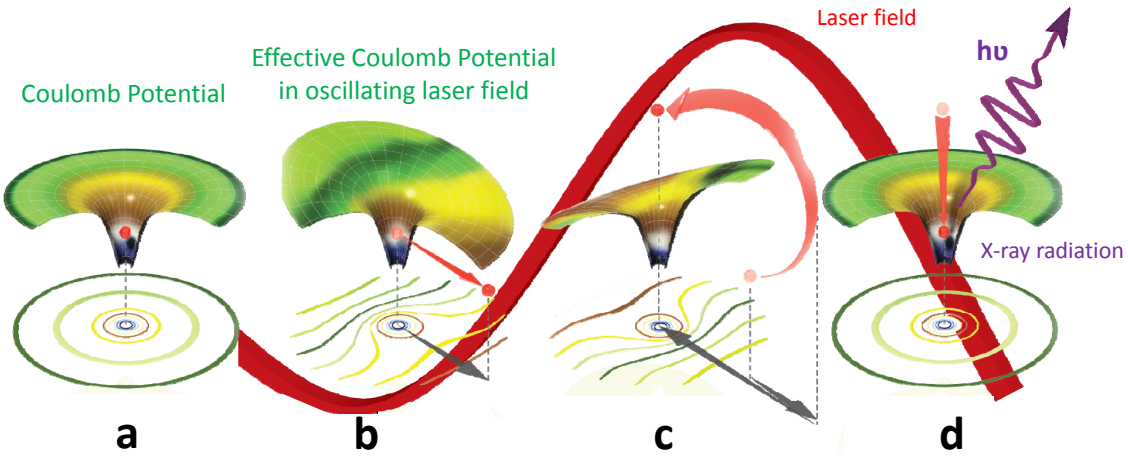

Figure 2.4: Three Step model of High Harmonic Generation where the grounded state (a) is initially perturbed by the driving laser field to ionize the atom (b), accelerates and returns the electron in the field back to the parent atom (c), resulting in the recombination and relaxation of the electron to the ground state (d). This emits a photon that can span up to EUV/soft X-Ray wavelengths. Adapted with permission from [48].

Upon focusing the laser pulse into the gas medium, the three steps of Kulander and Corkums theory (a conceptual illustration of which is found in Fig 2.4) can be modeled as:

- **ionization** of an electron from the atom by an intense laser field
- **motion in the field after ionization:** acceleration of the free electron in the laser field, followed by return to the ion upon the laser E-field switching direction.
- **recombination** of the free electron with the parent ion, emitting a photon with energy dependent on the ionization potential of the parent atom and the classical kinetic energy gained by its acceleration in the field.

With each step having an associated probability of occurrence, the total probability of occurrence per atom can be calculated to predict the output intensity of each harmonic order. The details of each of these processes will be discussed individually in the following sections.

2.2.1.1 Ionization

A Coulomb potential can be used to model the initial, unperturbed atomic potential. Depending on the strength of an external electric field from the laser pulse, this potential can be weakly to strongly distorted, resulting in three possible ionization regimes of the valence electron: multiphoton ionization, tunnel ionization, and "barrier suppression" ionization [43, 40]. A schematic illustration of these regimes is shown in Fig 2.5. The factor that is commonly used to determine which of these processes is dominant is the *Keldysh parameter* which relates the incident laser frequency to the tunneling frequency:

$$\gamma = \frac{\omega_{laser}}{\omega_{tunnel}} = \sqrt{\frac{I_p}{2U_p}} \tag{2.11}$$

where I_p is the ionization potential of the atom and U_p is the pondermotive potential (the "classical" kinetic energy gained by the electron accelerating in the laser electric field). The pondermotive potential is defined as $U_p = \frac{e^2 E_0^2}{4m\omega^2}$ or directly in terms of the laser intensity (W/cm^2) and driving wavelength (in μm):

$$U_p \approx 9.33 * 10^{-14} I \lambda^2 \tag{2.12}$$

If the laser intensity is small ($\gamma >> 1$), with little perturbation to the initial coulomb potential, than multiphoton ionization is dominant (Fig 2.5a). As such, the resultant ionization can be treated with perturbation theory. Since the electron does not have enough time to tunnel through the potential barrier during each laser cycle, it is able to "bounce" back and forth within the potential as the electric field oscillates until enough photons are absorbed to ionize.

If $\gamma < 1$ than the Coulomb potential is severely distorted by the electric field and the electron can undergo tunnel ionization through the suppressed effective potential barrier, shown with the dotted line in Fig 2.5b. The rate at which it ionizes has been described by Ammosov, Delone, and

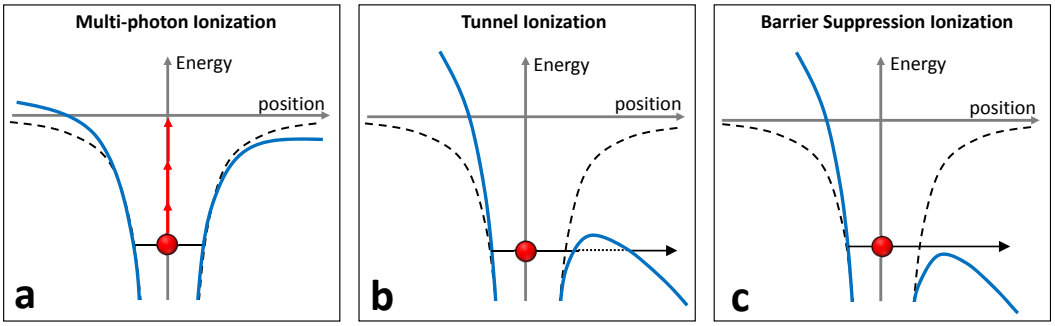

Figure 2.5: The three possible ionization potential schemes: a) multiphoton ionization b) tunnel ionization c) barrier suppression ionization. The dashed curve represents the unperturbed Coulomb potential with the blue curve being the effective potential when including the driving laser field. The horizontal and vertical gray axes represent the position and binding energy, respectively. Adapted with permission from [40]

Krainov [49]. For the case of Argon ($I_p = 15.76eV$) illuminated with a 800 nm pulse, this regime is dominant for $I_p > 10^{14}$ W/cm^2. With laser intensities in the range $10^{14} - 10^{16}$ W/cm^2, this ionization process is dominant in most high harmonic generation schemes. Finally, for $\gamma << 1$, the population of electrons in the ground state can be easily ionized since the effective potential is suppressed below the ionization barrier (Fig 2.5c). This is barrier-suppression ionization.

2.2.1.2 Acceleration

Once ionized, the laser field intensity is much greater than the Coulomb potential and the electron can be modeled as free to evolve in the field. Since the electron effectively has a continuum of states available to it, it can be modeled classically instead of strictly quantum mechanically. The electric field then has the form:

$$E(t) = E_0 cos(\omega t)\hat{e}_x + \alpha E_0 sin(\omega t)\hat{e}_y \tag{2.13}$$

where α represents the polarization of the fundamental light (0 for linear and ± 1 for circularly), E_0 is the amplitude of the electric field, ω is the field frequency, and $\hat{e}$ is the unit vector denoted in the x and y directions. Since the electron needs to eventually recombine with its parent ion, this can only happen with $\alpha = 0$, requiring our incident light to be linearly polarized when using one

driving field. The recent realization of circular harmonics [50], as explained further in Chapter 7, can be achieved through the use of multiple driving fields. The equations of motion for the electron can be obtained through solving $ma = e\mathbf{E}$ as:

$$v_x(t) = \frac{eE_0}{\omega m} sin(\omega t) + v_{0x} \tag{2.14}$$

$$x(t) = -\frac{eE_0}{\omega^2 m} cos(\omega t) + v_{0x} t + x_0 \tag{2.15}$$

$$v_y(t) = -\frac{\alpha e E_0}{\omega m} cos(\omega t) + v_{0y} \tag{2.16}$$

$$y(t) = -\frac{\alpha e E_0}{\omega^2 m} sin(\omega t) + v_{0y} t + y_0 \tag{2.17}$$

This assumes that the electron is at rest and at the origin once it tunnels through the potential barrier since the displacement position after tunneling is small compared to its maximum deviation position from the atom (Å vs nm). Only electrons released within a specific range of driving laser phases (ϕ) will allow the electron to actually return to the parent atom. Plotting a range of electron trajectories depending on the tunneling phase (shown in Figure 2.6a), one can see this only occurs between $0 - 90$ degrees.

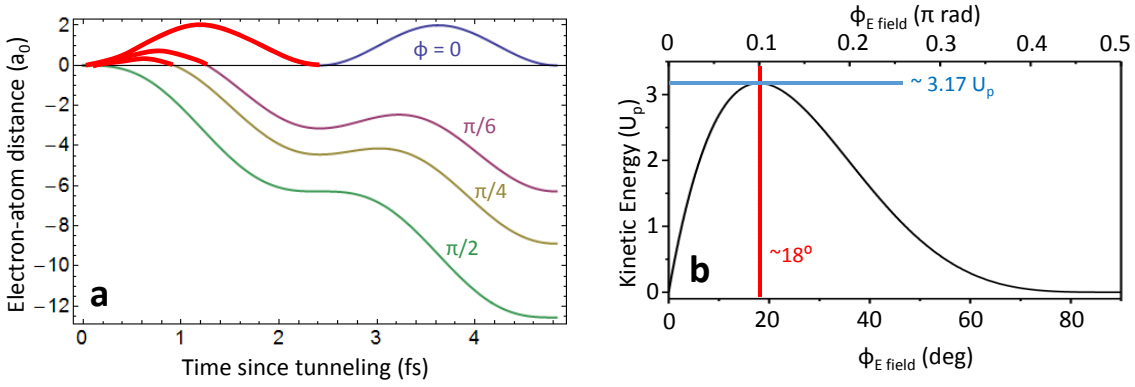

Figure 2.6: (a) plot of electron trajectory obtained from derived equations of motion (Eq 2.16). This trajectory is only "closed", returning to the ion (highlighted in red), when the electrons tunnels out between phases corresponding to $0 - \pi/2$ rad of the driving laser phase. (b) the kinetic energy gain versus the laser phase when the electron tunnels out of the potential. Adapted with permission from [40]

The resultant final kinetic energy of the electron accelerating in the field depends on the phase of the driving laser field at the time it tunnels out of the potential. Plotting the total kinetic

energy gain as a function of the driving electric field phase to find its maximum, this occurs at $\sim 18^\circ$ and $\sim 3.17U_p$, as seen in Figure 2.6 b. If the electron evolves longer than this in the driving field, it can either return 180° out of phase or after an even number of optical cycles, which has an extremely low probability of occurrence.

2.2.1.3 Recombination

After gaining kinetic energy from accelerating in the laser field, the electron has a certain probability to recombine with the parent ion and emit a photon equal to the energy having gained in the field. For an accurate model, other scattering processes need to be considered such as elastic scattering and collisional ionization. The total emission probability can be calculated via the dipole operator, taking into account the associated phase. The maximum emitted photon energy can be calculated via conservation of energy, where the amount of extra energy the electron has is dependent on the ionization potential of the atom and the maximum energy that it is able to gain from its evolution in the field:

$$h\nu_{max} = I_p + 3.17U_p \tag{2.18}$$

This serves as a maximum "cutoff" photon energy to our possible generated high harmonics [44].

2.2.2 HHG Characteristics

Without knowing anything of what the resultant spectrum looks like, some general observations can be made of what aspects of the process most drastically influence the overall harmonic emission output. From looking at Eqs 2.18 and 2.12, the higest generated wavelength is dependent on the laser peak intensity. Therefore, shorter laser pulses with higher peak intensity allow for shorter cutoff wavelengths since the electron is allowed to "survive" for longer in the field (to higher field strength) before ionizing. This allows it to gain more kinetic energy from the pondermotive force. Another dependent factor is the ionization potential of the atom. Higher ionization potentials lead to higher cutoff frequencies. The influence of these two factors on the highest cutoff photon energy can be seen when looking at atoms like Neon and Helium, with $I_p = 21.6eV$ and

$24.6eV$ respectively. With a 25 fs driving laser pulse width centered at 800nm and $6 \times 10^{15}\mathrm{W/cm}^2$ intensity, the highest harmonics possibly generated are the 163^{rd} and 333^{rd} (4.9nm and 2.4 nm respectively). By comparison, with a longer 100 fs pulse width assuming the same peak intensity, the cutoffs drop to the 119^{th} and 237^{th} harmonics for Neon and Helium, respectively [51].

Looking at the periodicity of the driving laser field, the HHG process also takes place every *half* cycle of the driving field, producing a series of attosecond bursts. Therefore, only *odd* harmonics are generated due to the odd symmetry of the generating process. To generate even harmonics, a medium without inversion symmetry would be required, making the harmonic emission always add constructively no matter if the photon is generated from the field oscillating one way or the other. This does not exist for a gas. Introduction of a second pulse with a different fundamental wavelength could generate the even pulses via filling in the gaps of the harmonic spectrum.

With the three step model as a general guide to the high harmonics generation process, the resultant spectrum is seen to have three primary characteristics:

- An initial strong peak close to the fundamental wavelength
- A long plateau region with relatively equal intensity
- A sharp cutoff at high photon energies

In the time domain, HHG occurs every half cycle of the laser field in short attosecond bursts. The initial strong peaks in the emission are where the generated intensity can be modeled by perturbation theory. Relativity uniform intensity of the harmonics on the plateau are due to the efficiency in ionization being "nonperturbative" and relatively independent of generated harmonic order [43, 40]. In reality, these intermediate orders are not discretized. Since there are many electron trajectories that contribute the each harmonic order, each contribution to the order has a discrete frequency phase shift depending on when the emission of the HHG photon occurs. This leads to an interference effect that somewhat "smears" out the orders. The sharp cut off is then dictated by the limit in energy that an electron is able to gain from accelerating in the electric field after ionization.

The decrease in signal intensity at high energies is due to the fact that only few electrons contribute to such high generated energies since these electrons would be ionized near the peak of the fundamental field. Also, due to this smaller number of electrons contributing to these orders, the interference effects are not as drastic and the orders are more discretized. The overall conversion efficiency of the entire process is typically on the order of $10^{-5} - 10^{-7}$ depending on the driving wavelength [52, 12].

2.2.3 Phase Matching in a Capillary Waveguide

Up until now, certain assumptions have been made about the characteristics of the high harmonic light generated in the gas, the main assumption being that the light generated from an atom in one portion of the gas is exactly in phase with the light generated a certain distance later. If this is not the case, then the harmonic light does not add coherently and the output intensity is greatly reduced. If we are able to forcibly phase match our harmonic light, this corresponds to a 10^2 to 10^3 factor increase in output intensity compared to the non-phase matched case, allowing for greater experimental applications [53]. The characteristic length in which the phase of the harmonically generated light "slips" from the phase of the fundamental phase by π is called the *coherence length* and can vary from the mm scale for low ($< 150eV$) photon energy to micrometer scale for high ($> 200eV$) photon energy. Maximizing this coherence length allows for greater interaction length in which the harmonics are able to constructively interfere.

Several factors contribute to the spatial "phase mismatch" that needs to be corrected for so that the output light is intense enough for practical applications. First, the gas in which the harmonic light is generated is a nonlinear medium. As the light propagates, it inherently picks up a phase lag such that:

$$E_q \propto \int_0^L E_f^n d(z) e^{-i\Delta k z} dz \tag{2.19}$$

propagating through a medium with length L where E_q is the electric field of the q^{th} harmonic, n is the order of the nonlinear process, $d(z)$ is the nonlinear coefficient, Δk is the phase mismatch ($\Delta k = qk_f - k_q$) between the fundamental laser field wavevector, k_f, and the harmonic field k_q.

Thus, with a $\Delta k = 0$, then the E_q is maximized, corresponding to a maximum in output intensity. To see how much this effects the final intensity, this expression can be integrated assuming E_f^n and $d(z)$ are independent of propagation direction. This gives:

$$E_q \propto L^2 sinc^2(\frac{\Delta kL}{2}) \tag{2.20}$$

With no phase mismatch, the output harmonic signal grows as L^2, serving as a strong motivation to try to make the mismatch zero. If Δk is nonzero then it oscillates over the propagation distance with the fields slipping in and out of constructive interference.

Seeing how strongly the phase mismatch effects the output intensity, several phase matching approaches have been tried attempting to minimize Δk. Expressing this mismatch more precisely, three district components contribute to the overall phase difference:

$$\Delta k_{total} = \Delta k_{disp} + \Delta k_{plasma} + \Delta k_{geom} \tag{2.21}$$

where Δk_{disp} is the dispersion due to propagation in the neutral gas medium, Δk_{plasma} is the plasma dispersion from the plasma created from the unrecombined free carriers in the generating medium, and Δk_{geom} is the geometrical dispersion when confined. One of the most successful approaches at minimizing Δk_{total} has been by using a gas-filled capillary waveguide. In this configuration, the total Δk expression can be written accounting for the inherent waveguide dispersion as:

$$\Delta k_{total} = [n(\omega_f) - n(m\omega_f)]\frac{\omega_f}{c} + \frac{\omega_p^2(1-m^2)}{2mc\omega_f} + \frac{u_n l^2 c(1-m^2)}{2ma^2\omega_f} \tag{2.22}$$

where ω_f is the fundamental laser frequency, $n(\omega)$ is the frequency dependent index of refraction of the medium, m is the mth harmonic order, ω_p is the plasma frequency, a is the inner radius of the capillary and $u_n l$ is the lth zero of the Bessel function $J_{n-l}(u_{nl}) = 0$ [40]. In general, the positive dispersion of the index of refraction term k_{disp} can be made to cancel the negative dispersions of the plasma (Δk_{plasma}) and waveguide (Δk_{geom}). A final phase-matched harmonic signal can then most easily be achieved by tuning the gas pressure within the capillary to adjust the density of the neutral medium.

2.3 Advantages of pairing High Harmonics with Photoemission

Specific advantages are present in utilizing short wavelength high harmonics as the photon source for the photoelectron process. In addition to simply being able to access a larger Binding Energy range for the electrons within material, allowing more electronic states to be probed, several secondary features allow for either greater characterization of the electronic states or better discrimination of the photoelectron signal compared to utilizing longer wavelengths. Each of the experiments presented in Chapters 4-6 exploit at least one of these advantages, to be discussed further in each respective chapter.

2.3.1 Accessible Momentum Range

Following Eq 2.8, the corresponding emission angle for a given momentum ($k_{||}$) can be plotted dependent on the kinetic energy of the electron, as shown in Fig 2.7 (b). An important consequence of this is seen when denoting the typical Brillouin zone size ($\sim$ 1.5-1.6 Å^{-1} for most materials, 1.7 Å^{-1} for graphene), shown in blue. For lower electron kinetic energies like 6 eV (red), this means that electrons at higher momenta (towards the edge of the Brillioun Zone) will be emitted more parallel to the sample surface. This makes photoelectron detection and the physical geometry of the incident photon source more difficult, due to the more grazing spot on the sample being spread over a large sample area. At higher kinetic energy, shown for 21 eV (blue) and 42 eV (black), this emission angle approaches closer to the surface normal.

Ultimately, this has the effect of "viewing" a larger momentum window for a fixed collected emission angle range. As is the case with the ARPES detector employed in the presented experiments, where the lens system of the detector selects out a fixed θ range (max. $\pm 15°$), this larger window can be easily seen when comparing lower (6 eV) and higher (21 eV) incident photon energy, shown in Fig 2.7a. For an acceptance angle of $\pm 7°$, the range of accessible momenta increases from $\pm 0.09 \mathring{A}^{-1}$ to $\pm 0.25 \mathring{A}^{-1}$ when going from 6 eV to 21 eV photon energy, respectively. This is beneficial when probing transient energy dispersions, like the time resolved photoemission stud-

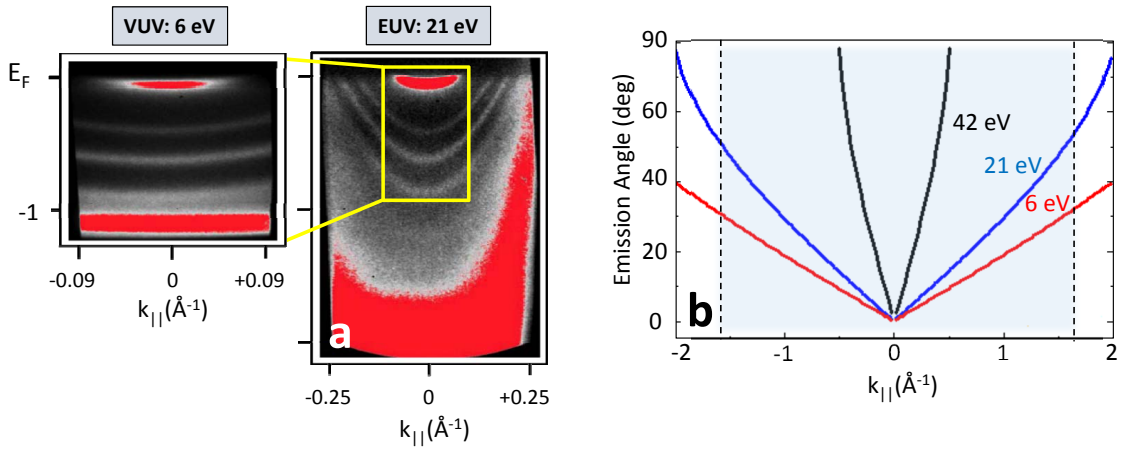

Figure 2.7: (a) ARPES Spectra using 21 eV vs 6 eV, showing the larger access to momentum and energy ranges, adapted with permission from [13]. (b) Emission angle of electrons versus $k_{||}$, shown for a range of initial photon energies. Typical Brillouin Zone size of $\sim 1.6\mathring{A}^{-1}$ is denoted in blue.

ies presented here, since a larger energy *and* momentum range can be probed compared to lower photon energy photoelectron spectroscopies [13].

2.3.2 Surface Sensitivity

The surface sensitivity of any experimental electron spectroscopy is inherently dictated by the escape depth of the electrons. Even though electrons may be excited over a large spatial extent into the material (as is the case with long wavelength excitation pulses), only electrons nominally within the inelastic mean free path length (λ) from the surface will emerge with their energy and momenta unperturbed. This is defined according to the probability of the electron traveling in the solid a distance, t, without scattering as $P(t) = e^{-t/\lambda}$. This distance is governed by electron-electron interactions, with electron-phonon interactions contributing only at very low energy and are traditionally neglected. In most materials, the electron-electron distance is approximately equivalent, meaning their mean free path length behaves similarly as a function of the electron's Kinetic Energy, roughly independent of atomic mass. This "universal curve" is shown in Fig 2.8, with experimentally measured inelastic mean free paths shown in black [54]. The general λ vs E

relationship has been empirically determined to be, for elemental materials:

$$\lambda(E) = \frac{538}{E^2} + 0.41\sqrt{aE} \tag{2.23}$$

where E is the kinetic energy of the electron (in eV) and a is the monolayer thickness (in nm) [54]. This gives two dominant regions where, at lower energies, λ increases due to electrons having insufficient energy to initiate excitations like plasmons. This makes the probability of inelastic scattering progressively less likely. At higher energies, the decreased interaction times again decrease the probability for scattering having the effect of increasing λ.

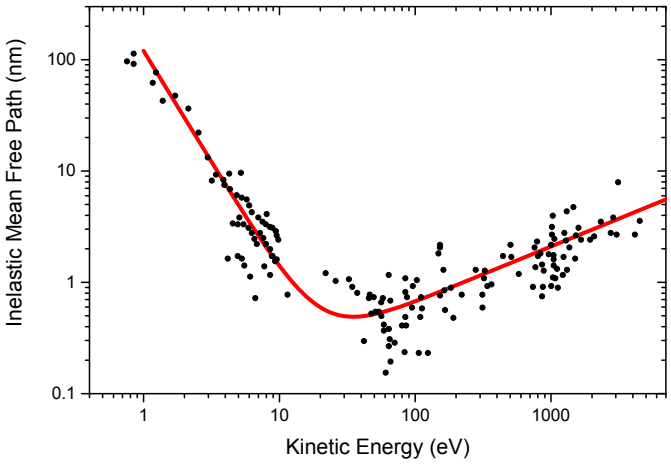

Figure 2.8: "Universal curve" of electron mean free path as a function of energy (red) plotted according to Eq 2.23 with experimental data from [54]

The minimum in this universal curve corresponds nicely with the 10 - 100 eV energy range typically employed in our ARPES experiments. In general, the fraction of electrons detected originating within the first mean free path (as calculated via $P_{total}(d < \lambda) = \int_0^{\lambda} P(t)\,dt$) is 0.63. Virtually all sampled electrons then come from within the first 3λ. In the 10-100 eV range, this corresponds to electrons originating within the first 10 Å. High harmonics therefore act as an extremely surface sensitive probe of electronic structure and dynamics. This serves as an advantage when probing local modifications to surface electronic structure due to additions like adsorbates, as will be seen in the alkali adsorption studies on graphene presented in Chapter 5.

By the same token, one consequence of this surface sensitivity is the possibility for a dominant contribution to the photoemission spectra from surface contamination or scattering due to surface roughness. This necessitates using well-ordered, atomically clean surfaces that require preparation *in-situ* in the Ultra High Vacuum environment.

2.3.3 Background Separation

Inherent to any photoemission process is a low-energy secondary electron background. In photoemitting a given material's density of states, shown in gray in Fig 2.9 (left), a low energy background is formed (brown) from photoexcited electrons scattering inelastically within the crystal prior to escaping the surface. For the IR pump and EUV/VUV probe used here, each source contributes to this background. In the directly photoemitted electrons using EUV/VUV photons (right, top), a large secondary electron background can be seen below ∼6 eV. This background is directly dependent on the surface/ crystal quality, with increased defects and impurities increasing the number of scattering centers for the photoexcited electrons and yielding a higher number of secondary electrons. With only IR light incident, the photon energy being below the work function of the material means that absorption of multiple photons is necessary to photoemit an electron from the surface. In the case shown in Fig 2.9 (right, bottom), this *Above Threshold Photoemission* (ATP) has a significant contribution up to 20 eV kinetic energy when initiated with 1.5 eV IR light. Shown for the typical intensities employed in the experiments here, these intensities ($\sim 10^{11}$ W/cm^2) are necessary to create the large hot electron populations studied in Chapter 5 and a sufficient dressing field for the interferometric measurements in Chapter 4. This ATP background is lessened, but still present up to $\sim$ 7 eV, when using longer dressing wavelength light (0.95 eV at 10^{10} W/cm^2) due to the increased number of photons necessary to photoemit electrons from the surface.

Combined, these effects are seen to produce a dominant low-energy background that can bury the spectroscopic features one is interested in probing. On surfaces compared to atomic photoemission, increased ATP is seen from local field enhancement and distortion effects around

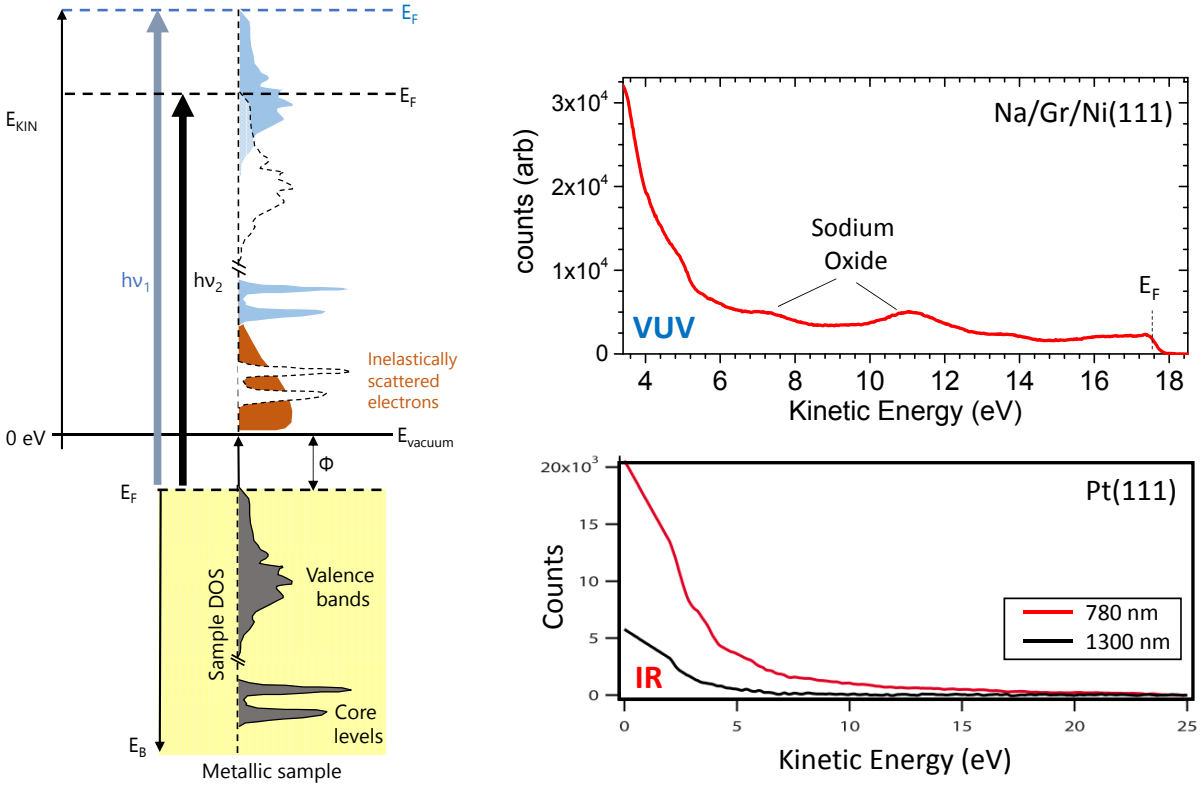

Figure 2.9: (left) Photoemission spectra with inelastically scattered background using higher (blue) and lower (black) photon energies. (right top) EDC of Na/Gr/Ni(111) system using 21 eV photon energy, showing primary spectral features from sodium oxides and inelastically scattered electron background at lower energies (right bottom) multiphoton emission background using IR photon energies of 1.59 eV (780 nm) and 0.95 eV (1300 nm) adapted with permission from [55].

surface defects and differences in topography [56]. Due to the high sensitivity of this background to both surface and bulk defects, these features can be reduced with proper sample preparation, namely well-ordered crystals with atomically clean surfaces. It is therefore necessary to use photon energies higher than this low-energy background ($\gtrsim 10eV$) so that the directly photoemitted spectra can be well separated from this "parasitic" background [13]. Illustrated in Fig 2.9 (left), spectroscopic features lost in the low-energy background using lower photon energies (dashed black line) can be separated using higher energy incident photons (blue), allowing these spectroscopic features to be better resolved.

Chapter 3

Experimental Apparatus and Techniques

The pump-probe technique has been a powerful tool for studying material dynamics by allowing one to precisely map the response of a system at specific instances after an initial excitation. In our case, this is accomplished through producing EUV and IR pulses that can be delayed with respect to each other. Over this thesis, the Ultra High Vacuum, laser, and detection systems have either been greatly improved or replaced entirely. The Graphene and interferometric attosecond spectroscopy studies in Chapters 4-5 were carried out using the setup described below (slight modifications are found in the respective chapters). InGaAs studies were performed using a similar technique, but with modifications outlined in Chapter 6.

3.1 Ti:Sapphire Oscillator & Amplifier

As discussed in Section 2.2, intensities required for efficient HHG are typically in the $> 10^{13}$ W/cm^2 region. One method in which to achieve these intensities is with a short pulse laser in the femtosecond regime. Traditional Ti:Sapphire oscillator systems, with their > 200 nm bandwidth, can output pulses as short as 5 fs [57]. However, assuming a focal spot of 100 μm that is typical of our capillary generation scheme, this would only produce an intensity of $2.6 * 10^{10}$ W/cm^2-insufficient for HHG. As such, amplification of these ultrashort pulses is necessary. The method we choose to accomplish this is Chirped Pulse Amplification (CPA) [58]. A schematic layout of this is shown in Figure 3.1. In this method, the initial pulse is stretched in time, or "chirped", to reduce peak power and allow for amplification without damaging optical components. The pulse can then

be recompressed to give an amplified short pulse.

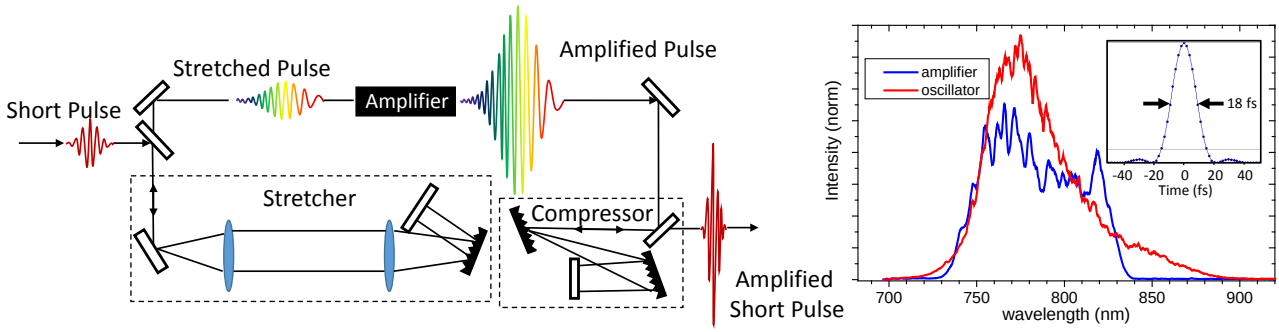

Figure 3.1: (left) Chirped Pulse Amplifier layout, adapted with permission from [58]. (right) representative oscillator spectrum (red) and resultant spectrum after chirped pulse amplification (blue). Inset shows the transform-limited pulse length of 18 fs from the amplifier bandwidth.

In our CPA scheme, pulses are input from a Ti:Sapphire oscillator operating at ∼80 MHz with 6 nJ, ∼10 fs pulses. These pulses are stretched in time via two grating reflections (shown folded in Fig 3.1) to roughly 150 ps. A Pockels cell (KMLabs) then selects the repetition rate of the amplified pulses (between 3 - 6kHz) to yield a higher energy/pulse of the output pulses. Each pulse is then amplified in a Ti:Sapphire crystal pumped via a Nd:YAG 532nm pump laser operating in sync with the Pockels cell timing, with the ability to fine tune its delay. The Ti:Sapphire crystal is cryocooled (Cryomech PT90) to take advantage of the greater thermal conductivity of the sapphire at low temperature [59] and minimize thermal distortions of the beam. Pulses are amplified by multiple passes through the crystal until gain saturation is reached. They are then recompressed via a set of negative dispersion compensating gratings to account for the initial stretching of the pulse and extra propagation through the crystal and optics. A representative spectrum for the initial oscillator and resultant amplifier spectrum is shown in Fig 3.1. While, the bandwidth from the amplifier is transform-limited down to ∼15 fs (shown in inset), pulse lengths are typically limited to 23-25 fs due to higher order dispersion.

Many modifications have been made to the laser system during this thesis, resulting in a higher power, higher repetition rate output. This was done for several reasons. Previous output

powers were, at maximum, 2 mJ /pulse at 2 kHz with 25 fs pulses. High output powers (ie. high energy/pulse) are desirable for efficient HHG of higher energy photons in gases like Helium (> 80 eV). In our pump/probe layout, it also provides sufficient power per branch for EUV generation as well as low conversion efficiency processes like optical parametric amplification (OPA) for longer pump wavelengths [55].

While maintaining a high energy per pulse, a higher repetition rate was also advantageous. In addition to obviously generating a higher volume of detected events in real time, this offers some advantages specific to our photoemission process. Specifically, maintaining the same number of photoelectron events per second, less photoelectrons per pulse is preferred to give increased energy resolution in the resultant spectra. This advantage can be understood when more closely analyzing the nature of the photoemitted electron bunch from the surface. The number of photoelectrons emitted from the surface is proportional to the number of incident EUV photons per pulse. Upon being emitted from the surface with the ultrashort pulse, this results in a closely packed volume of electrons that can Coulomb interact when in sufficiently high numbers. This Coulomb interaction has been seen to give energy shifts, distortions in lineshape, and broadening of spectral features due to the modifications to the electron's kinetic energy on the way to the detector[60, 61]. An analytical model of these space charge effects taking into account electron-electron Coulomb interactions, neglecting effects like induced image charges at the surface, can be used to calculate the energy broadening, ΔE, in a disk of photoemitted electrons of a radius, r_0. This is calculated according to:

$$\Delta E = [\frac{2e}{\pi\epsilon_0}(\frac{2}{3\pi} + \frac{1}{6})]^{1/2}\sqrt{E_i}(\frac{N}{r_0})^{1/2} \tag{3.1}$$

where E_i is the initial kinetic energy of the emitted electrons, N is the number of electrons in the packet, e is the elementary charge, and ϵ_0 is the vacuum permittivity [62]. This model, with $\Delta E \propto N^{1/2}$, has been seen to agree with experimental data of electrons emitted via femtosecond pulses quite well [60, 61]. It should be noted that this dependence is observed to be closer to a linear relationship with N for picosecond pulses [63, 64] due to the larger lateral extent of the emitted

electron packet. Energy broadening for our experimentally relevant kinetic energies are plotted in Fig 3.2.

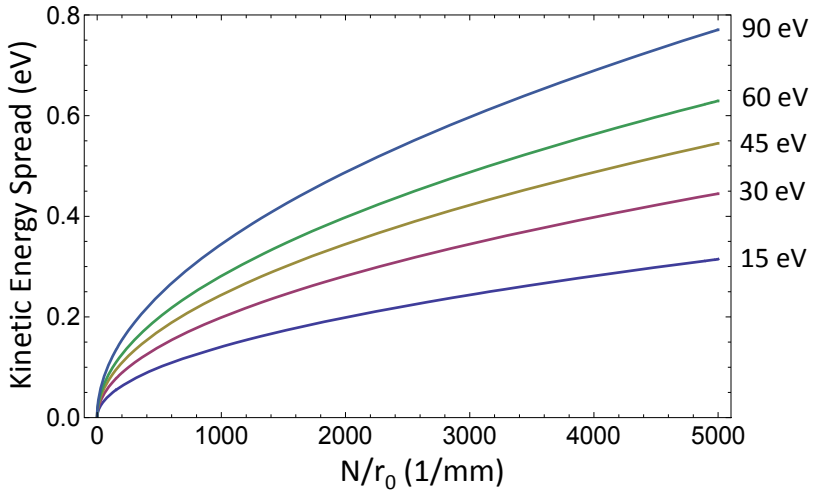

Figure 3.2: Calculation for kinetic energy broadening exclusively taking into account electron-electron coulomb interactions, modeled after [61, 62].

This space charge effect results in a worsening of the overall energy resolution For the higher EUV photons. It also increases with photoelectron number, effectively capping the usable photons/pulse from the HHG process for photoemission studies. This necessitates a lowering of the number of electrons per pulse, making a higher repetition rate, low photon per pulse scheme desirable.

repetition rate (kHz)	output energy/pulse (mJ/pulse)	pump energy/pulse (mJ/pulse)
2 (prev)	2	19.5
4	2.3	18.6
5	1.8	16.1
6	1.6	13.2

Table 3.1: Present output energy/pulse and required pump power for Ti:Sapphire amplifier before (prev) and after upgrades.

In line with this, a pump laser (Lee Laser LDP-200MQG-HP) was installed that provided

operational ranges to between 4-6 kHz. The corresponding amplifier output energies are found in Table 3.1. To handle the higher average power, a dielectric compressor roof mirror and copper backed compressor gratings were also installed to minimize distortions due to thermal loading of the optics. Continuous operation of the system (compared to initially turning the system on daily) was seen to be necessary to reach a thermal equilibrium in output power, spectrum, and beam pointing. The beam pointing was still observed to drift over the day due to $\pm 2^{\circ}$ temperature fluctuations within the lab, effecting efficient coupling and possibly damaging the EUV generation capillary. Homewritten, 4-axis beam pointing stabilization software was used to compensate for this residual thermal drift. More details in its implementation can be found in Ref [65].

3.2 Beamline

The amplifier output repetition rate and energy/pulse was chosen specific to each experiment. This was due to the different intensity demands in EUV generation for the desired probe wavelengths, with higher generated photon energies requiring higher energy/pulse of the driving light. The output of the amplifier was initially split via a beam splitter with 5-10 % of the beam energy into a IR pump line and the remainder used for HHG. A general schematic of the current setup is shown in Figure 3.3, with each component explained in detail in the following sections.

3.2.1 EUV Beamline

After the beamsplitter, the beam was focused into a 150μm- 250μm inner diameter (ID) gas filled capillary using an AR-coated lens whose focal length was chosen to gave a waist size of $\sim$ 60 % of the capillary's ID. This gave optimal single-mode (EH_{11}) couping into the waveguide and was between 75- 150 cm. Depending on the generated harmonic wavelength, the largest ID capillary was used that still yielded sufficient IR intensity for harmonic generation. This both maximized the harmonic output and minimized the impact of overionization of the gas medium due to driving IR intensities being too high. At too high of laser driving intensities, nonlinear effects on the final harmonic output can be seen such as self-phase modulation [66], self-compression of the laser pulse

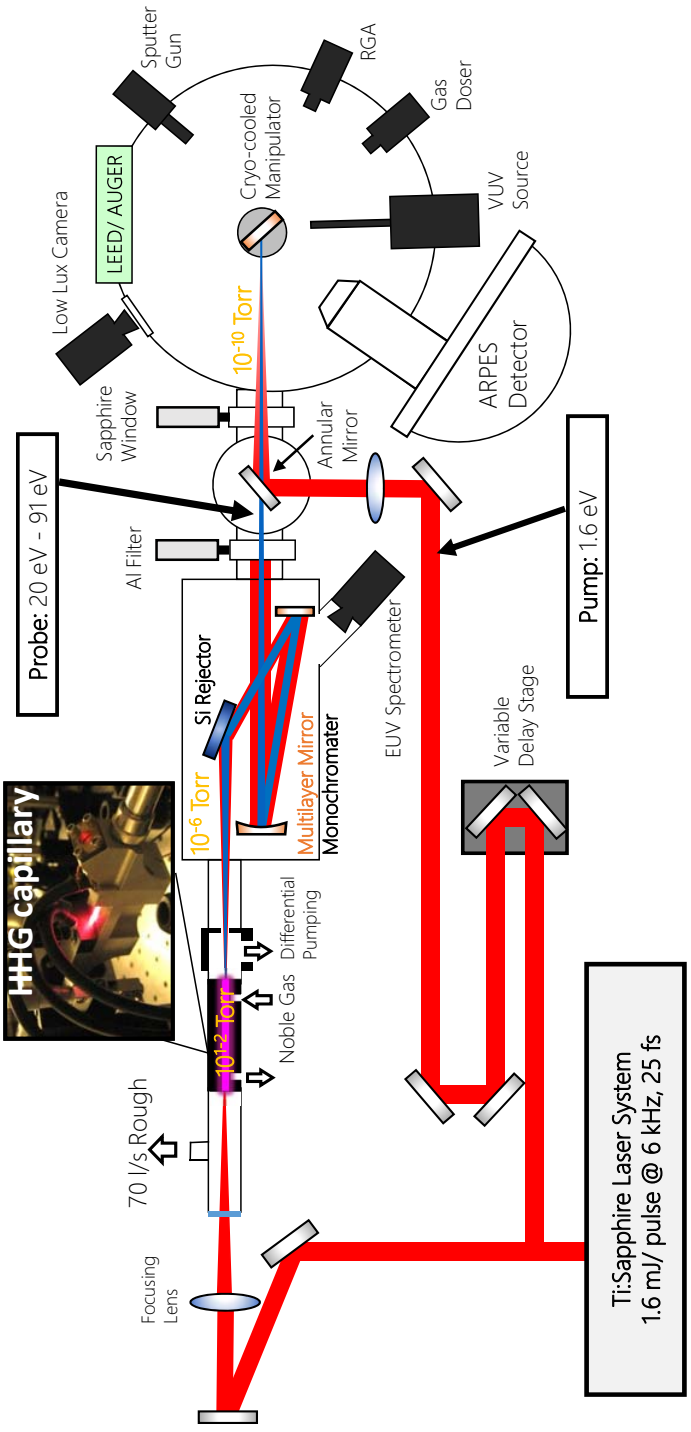

Figure 3.3: Simplified current experimental Layout for EUV/IR photoemission studies. Monochromator with spectral selection is shown.

during propagation [67], or spectral blue shifting [68]. The specifics of the generating parameters for the range of harmonic wavelengths used in experiments discussed here are presented below.

3.2.1.1 High Harmonic Generation Schemes

Core level states of a material are accessible by using higher photon energies. However, the added complication of variation in photoemission cross section of spectral features as a function of photon wavelength mean that simply choosing the highest or brightest photon energy may be ill suited for a specific material. For example, the surface state of Cu(111), studied in detail in Chapter 4, has multiple peaks in its relative intensity compared to neighboring states when incident photon energy is scanned- occurring at photon energies of 6 eV [69] and 70 eV [70] and nearly vanishing at "mid-range" energies ∼30 eV. With the additional desire to perform experiments requiring resonant excitation, tunability of the high harmonic source over a large photon energy range is preferred in order to offer the highest experimental capability possible.

Laser-driven harmonics have traditionally required a trade-off between energy resolution, temporal resolution, and overall photon flux. The time-bandwidth limit necessarily dictates a trade-off between pulse length and bandwidth of the harmonics, as modeled by:

$$\Delta E \Delta t = \alpha * 4.141 \tag{3.2}$$

where E is the energy bandwidth in eV, t is the pulse length in fs, and α either 0.44 or 0.32 for Gaussian or Sech^2 pulses, respectively. For a 10 fs Gaussian harmonic pulse, the energy resolution of the photoemitted electrons is already larger than 180 meV. In general, therefore, higher harmonic photon energies are characterized by an increasingly broader energy bandwidth and lower photon flux. This introduces another trade off of energy resolution for access to a greater range of electron binding energies. This trend can be seen in the generation parameters for 4 common harmonics used throughout this thesis (and in experimental attempts not included in this work), namely 22, 42, 65, and 90 eV. Characteristic generation parameters for these wavelengths such as gas medium, typical optimal gas pressure, energy bandwidth, estimated photon flux, and corresponding spectral

filter are included in Table 3.2.

Photon Energy (eV)	Generation Gas	Pressure (Torr)	Harmonic Bandwidth (meV)	Est. Flux (photons/harm/s)	Filter Material
22 (2ω)	Kr/ Ne	15-20	$150^{\diamondsuit}$	$10^{11} - 10^{12}$	Al
42	Ar	40-60	$350^{\flat}$	$9 * 10^{10}$*	Al
65	Ne	700-800	$450^{\triangle}$	$9 * 10^{9}$	Al
91	He	> 900	850	$5 * 10^{9}$	Zr

Table 3.2: Common harmonics with generation parameters, measured bandwidth for each harmonic, and estimated flux. Bandwidth values presented here are experimentally measured and have been independently verified as $\diamondsuit$ [14], $\flat$ [17], and $\triangle$ [71]. Flux estimates *at the capillary output* are done using a EUV calibrated photodiode for measurement of (*) and correcting for the loss due to Al foil filters. Other values are estimated from ARPES spectral intensities and collection times on reference samples of Cu(111) and $TiSe_2$.

References to additional verification of presented experimental energy bandwidths are indicated in the table. The noted flux measurements are based on an absolute measurement using a calibrated EUV photodiode for 42 eV (noted with a *), accounting for the loss of Al foils used to filter out residual IR light. This gave the flux of photons/harmonic/sec (using a 3-4 kHz laser rep rate) *at the output of the capillary*, meaning before any lossy optical elements. Other flux values are estimated from ARPES spectra under identical exposure times on reference samples of Cu(111) and $TiSe_2$. Note that, due to unaccounted differences in photoemission cross section, these are rough estimates and are only meant to serve an approximate guide.

Of particular interest has been the recent development of using 2ω (390 nm) pulses to drive the high harmonic process, yielding high energy resolution, high photon flux pulses at 22 eV. This photon energy is high enough to still access the entire Brillouin zone of most materials and has only recently been implemented in time-resolved electron studies [14, 72]. Due to the high interest in using this wavelengths in future, higher energy resolution photoemission studies, this configuration will be discussed in further detail in the next section.

3.2.1.2 2ω driven Harmonics

Driving the high harmonic process with 2ω fundamental light has recently demonstrated narrow (< 150 meV), short (< 25 fs) EUV pulses with high photon flux ($\sim 10^{12}$ photons/harmonic/s). Producing a relatively isolated 7^{th} harmonic around 22.3 eV in the HHG process, this intrinsically quasi-monochromatic light has a high potential for future photoemission studies. Notable qualities of its generation and experimental configuration will be reviewed here. For a more in-depth discussion, the reader is referred to Ref [14].

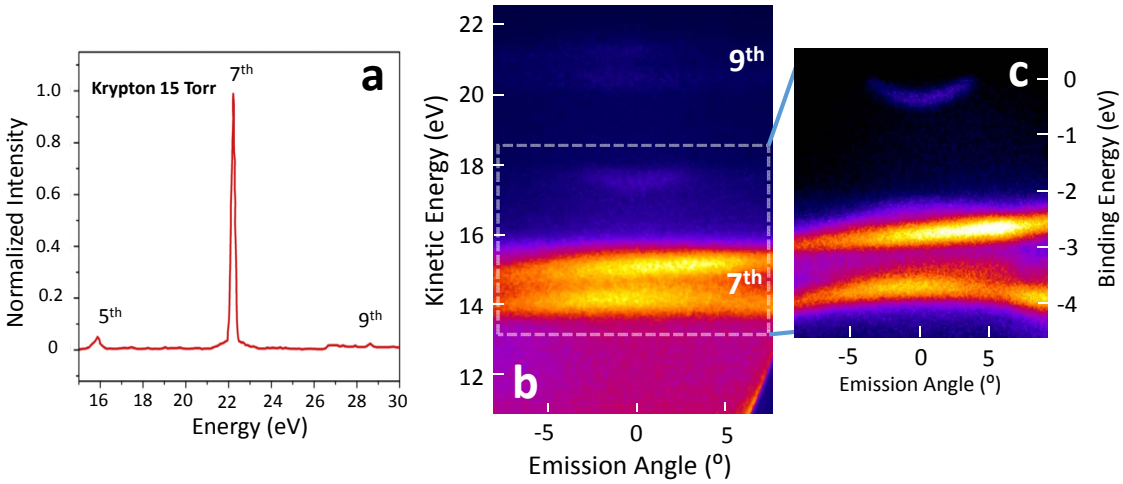

Figure 3.4: (a) Harmonic spectrum of 2ω driven harmonics showing nearly monochromatic 7th harmonic generation using Krypton at 15 Torr. Adapted with permission from [14]. (b) ARPES Spectra on Cu(111) showing dominant 7th harmonic and weak 9th harmonic with non-overlapping electronic features in 6 eV collection "window" (c) Enlarged 7th harmonic spectra showing narrow harmonic bandwidth and well-resolved surface state feature around E_F.

Several factors contribute to the higher resultant photon flux of the 22 eV harmonic. In the conventional configuration, monochromating elements are needed after harmonic generation in order to isolate one wavelength for use in photoemission studies. These elements, usually multilayer mirrors or gratings as explained in Section 3.2.1.3, have low throughput efficiency and can temporally chirp (stretch) the resultant pulse. With the 2ω driven harmonics, the dominant 7th harmonic output gives near-monochromatic output (shown in Fig 3.4 a-b), allowing for the removal of these lossy optical elements. Instead, only a focusing toroidal mirror at grazing incidence is

used to focus the harmonics onto the sample. Furthermore, in generating harmonics using 3.2 eV driving light, resultant harmonics are produced with a spacing between harmonics of 6.4 eV. This means that, when used in photoemission studies, replica spectra are produced every 6.4 eV Kinetic Energy (shown in 3.4 b). This gives a 6.4 eV "window" in which to clearly capture the relevant spectral features of the material without being overlapped with the adjacent harmonic. This is sufficient for including the dominant valence structure of most materials.

Another advantage of the shorter wavelength driving laser is in the quantum efficiency of the HHG process. A shorter driving wavelength means less spreading of the quantum electron wavepacket upon ionization from the parent atom. This results in a higher recombination probability and an increase in the overall single-atom photon yield. Since single-atom HHG efficiency scales with driving wavelength at $\lambda^{-5} - \lambda^{-9}$, a doubling of the fundamental driving frequency results in roughly two orders of magnitude increase in single-atom yield [48, 43, 12]. Due to the electron spending less time in the continuum, this has the additional bonus of the electron motion, and therefore harmonic bandwidth and central frequency, being less sensitive to the local plasma conditions in the gas medium. The use of moderate intensities in the harmonic generation also avoids the possible nonlinearities in the generating medium mentioned previously. This results in a high yield, more stable harmonic source.

Understanding as to why the harmonic output results in such narrow energy bandwidth can be seen when looking at the specifics of the harmonic generation. 2ω light is initially generated using a 200 μm thick β barium borate (BBO) crystal in order to convert an incident beam of 1.8 mJ/pulse at 780nm into 390 nm centered light at 0.3 mJ/pulse (note: the spectra shown in Fig 3.5 (right) used a 1.1 mJ/pulse 780nm beam with similar resultant power) and subsequently focused into the gas medium. These pulses are *not* recompressed after these optical elements and are estimated to be 35-40 fs long with $\sim$200 fs^2 positive chirp). Due to the longer pulse length of the generating light, while still maintaining sufficient intensities for HHG, the resultant energy bandwidth is therefore narrower. This has been measured to yield 20 ± 16 fs harmonic pulses [14] that are still sufficiently short for use in time-resolved studies. In photoemission studies, this

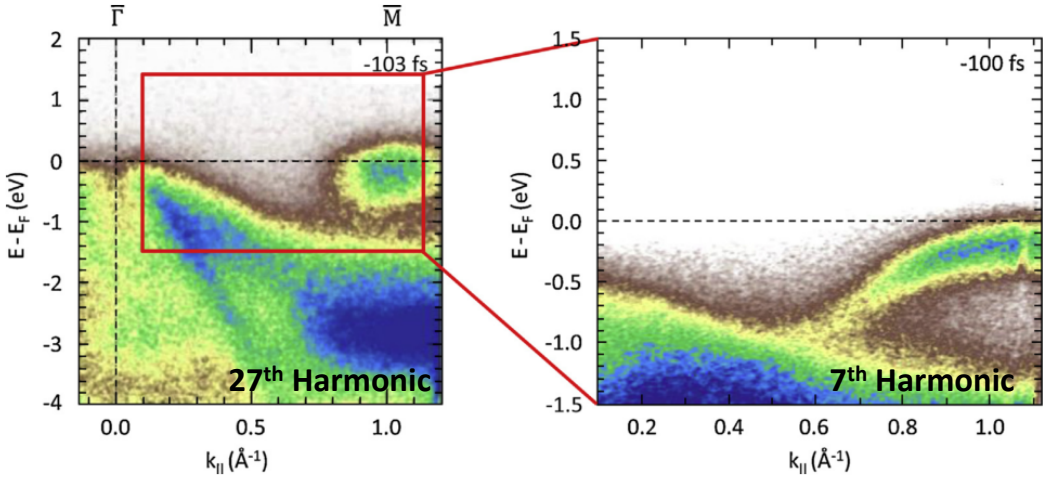

Figure 3.5: ARPES Spectra of metal dichalcogenide $TiSe_2$ collected using 42 eV (27^{th} harmonic, left [17]) and 21 eV (7^{th} harmonic, right), with energy resolution $\sim$ 400 meV and <150 meV respectively. Adapted with permission from [14].

results in a dramatic improvement in energy resolution compared to high photon flux wavelengths previously used like 42 eV. Shown in Fig 3.5 for the case of $TiSe_2$, the distinction of certain spectral features like the downward dispersing Ti 3d band is dramatically enhanced with the use of 22 eV harmonics. With the extension to even shorter wavelength driving lasers, this technique can be extended to even higher efficiency, narrower bandwidth harmonics [12]. Similar implementations to generate 60 eV harmonics in Neon have yielded high flux, narrow (230 meV) harmonics as well [73], showing promise for high resolution studies with access to an even larger range of electron Binding Energies.

3.2.1.3 Monochromator and Toroidal Geometry

Depending on the specific experiment, one of two configurations was used to focus the generated high harmonics onto the sample - one spectrally selecting a single harmonic from the HHG comb and one with no spectral selection and only a focusing element. Due to the low conversion efficiency of the high harmonic process, a high intensity of IR light copropagates with the generated EUV beam until a foil spectral filter. With the push to higher repetition rates in our studies came

the unwanted consequence of a higher average power of IR light incident on the foil. At sufficiently high intensities, this caused the fragile 200 nm foil to heat, distort, and subsequently break. A solution to this was the inclusion of a "rejector" mirror at grazing incidence after the fiber that served to reflect the EUV and absorb the majority of the IR. This rejector was either a bare superpolished Silicon Substrate (Gooch and Housego GO-S100-1) or a 200 nm ZrO_2 -coated Silicon substrate. The ZrO_2 coating was primarily used for better reflectivity of higher order harmonics (> 60 eV). The reflectivity comparing these ZrO_2 vs bare Si is shown in Fig 3.6a for 10 degree grazing incidence.

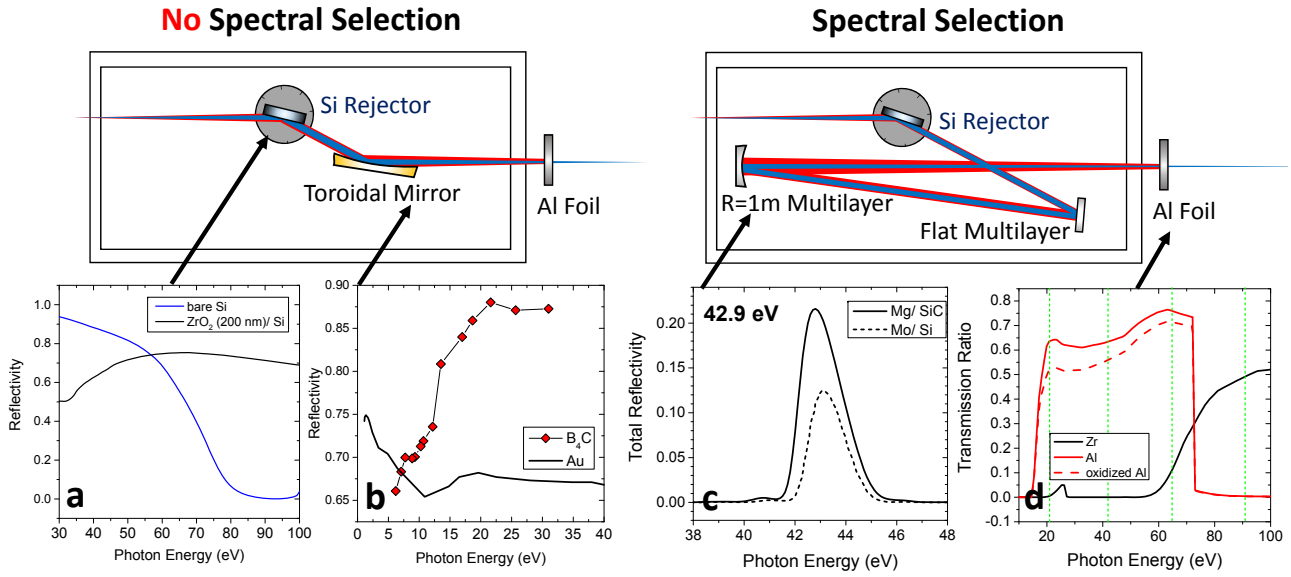

Figure 3.6: Mirror Chamber for Spectral and Non-spectral selection layouts. Reflectivity and transmission characterizations for each setup are shown bottom. (a) Reflectivity curves for bare and ZrO_2 coated rejector mirrors, calculated using CXRO database (b) Reflectivity curves for Gold (Au) and Boron Carbide (B_4C) coated toroidal mirrors. B_4C curve from [74] and *Au* from [75]. (c) Representative reflectivity curve for 42.9 eV multilayer mirrors, showing difference in reflectivity with choice of multilayer material (Mo/Si vs. Mg/SiC). Both experimental data sets collected on the ALS (d) Foil spectral filter that is common to both configurations. Transmission curves are shown for Al (lower energy wavelengths), oxidized Al, and Zr (higher energy wavelengths), with commonly used harmonic wavelengths denoted with green lines. Calculated using CXRO database.

In the case with no spectral selection, as was the case for the attosecond studies presented in Chapter 4, the EUV beam copropagating with the remainder of the IR light was focused using

a toroidal mirror at grazing incidence (ARW Optical #TM1-50X25-OPT1, R_1 = 350 cm; R_2 = 20 cm) of 12 degrees. After initially trying a gold coating, a 100 nm thick Boron Carbide (B_4C) coating was investigated due to its higher reflectivity, as seen in Fig 3.6 b reported for reflectivity at wavelengths of ∼30 eV and 10 degree grazing incidence. This yielded a higher flux and had the added advantage of being more robust than the 500nm thick Au coating, which easily damaged.

In the case with spectral selection, as was the case for the time-resolved graphene studies in Chapter 5, multilayer mirrors were used to isolate the desired harmonic. Previous to this thesis, only multilayer mirrors using Molybdenum and Silicon as multilayer components had been used in any experiments within the KM Group. In the time since the last set of multilayer mirror had been fabricated with collaborators at Lawrence Berkeley National Lab, several new coatings became available that offered higher reflectivity than their Mo/Si counterparts. As an example, for 42.9 eV, Mg paired with SiC offered as peak reflectivity of 45 %, giving a total throughput of 24 % after the pair of mirrors (one flat, one R=1 m). This is in comparison to Mo/Si where the total throughput was only 12 %, as shown in Fig 3.6 c. In total, Mg/SiC coatings were well served for lower photon energies < 45 eV, Al/Zr in "mid-range" energies from 45-65 eV, and Mo/Si for $65-95$ eV. Further details of the design of these multilayers with current coatings is left for Appendix A.1. Note that, for the studies presented in Chapter 6, a toroidal grating was used for spectral selection instead of multilayer mirrors.

After both configurations, a 200-300 nm thick foil (Lebow Company) was used to filter the residual IR light and transmit the EUV beam. Zirconium was used for 90 eV harmonics, with Al reserved for all lower energies due to transmission efficiency, as seen in Fig 3.6d. Secondarily, these also served as a pressure differential between the 10^{-6} mirror chamber and 10^{-10} main chamber. While these foils were stored in a vacuum desiccator when not in use, they did develop oxidation overtime due to periodic venting of the mirror chamber. This gave a notably lower transmission efficiency.

3.2.2 IR Beamline

The 5-10 % of the initial amplifier output was used as the pump/ dressing light for experiments discussed here. The beam was then propagated using silver mirrors to minimize extra dispersion that would increase pulse length. A computer interfaced delay stage (Aerotech ANT130-1110-L-25DU-MP) was used to control the relative pump/ probe delay with a resolution of 200 as. The beam was then focused using a R=3m concave silver mirror and entered into a high vacuum "recombination chamber", for copropogating the IR and EUV light. A silver 45° angled annular mirror with a 1 mm hole through the center is used to reflect the outer 60 % of the IR light onto the sample, while letting the EUV light propagate through the center hole. In this configuration, the IR and EUV beams are collinear with $< 0.1°$ between them, as verified through their optical interference pattern projected onto a screen after propagation through the UHV chamber.

3.2.3 IR Pump Temporal Compression

Temporal compression of IR pulses has been previously done with Ti:Sapphire pulses from 30 fs down to < 5 fs [76]. This was primarily done with the aim of subsequently generating isolated attoseconds bursts through high harmonic generation. However, in modern IR pump- EUV probe schemes, the temporal resolution of the studied electron dynamics is limited due to the convolution of the temporal width of the IR pulse with the EUV temporal pulse width. For the realm of surface science, it is then already advantageous to temporally compress the IR pump pulse, therefore increasing the overall temporal resolution of the studied dynamics. One implementation of this, investigated during this thesis, is "self-phase modulation" (SPM), where the 30 fs pulse from the Ti:Sapphire amplifier is compressed to achieve a < 10 fs pulse length. As the ultrashort pulse propagates through a medium with an intensity dependent refractive index, a frequency shift is induced in the spectral components in the pulse. For a positive nonlinear index gas according to: $n(I) = n_0 + n_2 * I$, where I is the laser intensity, n_0 is the linear refractive index, and n_2 is the nonlinear refractive index (2nd order), this results in a broadening of the overall initial spectrum.

This greatly decreases the achievable driving pulse length according to the time-bandwidth limit. The resultant positive dispersion of the pulse can then be compensated for with negative dispersion compensating mirrors (chirped mirrors).

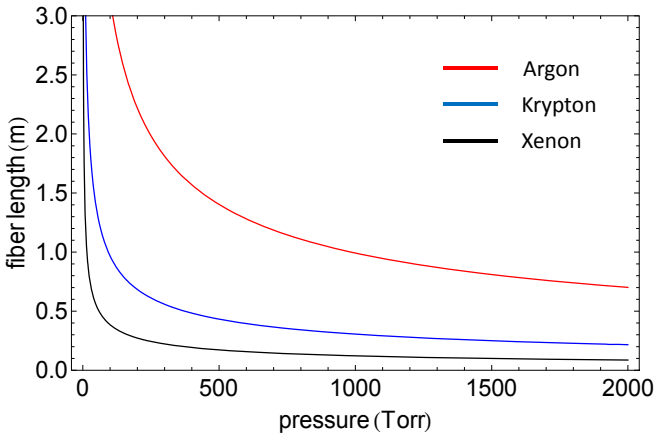

Figure 3.7: Calculation for optimal SPM length for a given pressure, calculated after [76]

In practice, this was achieved through focusing a 25 fs, 0.6 mJ/pulse into a hollow-core gas-filled capillary. Fiber lengths of 20 cm and 1 m were investigated to determine the effects on overall spectral broadening and throughput. Xenon, Krypton, and Argon gases were investigated to determine the optimal gas for maximum spectral broadening and recompression. Estimates of the optimal pressure for given fiber lengths were initially calculated according to literature [76] using:

$$L_{optimal} \approx (6 L_{NL} L_D)^{1/2} \tag{3.3}$$

where L_{NL} is the nonlinear length calculated according to $1/\gamma P_0$ where P_0 is the peak power of the pulse and γ is the nonlinear coefficient. γ can be calculated according to $n_2 * w_0 / c A_{eff}$ where w_0 is the frequency of the driving laser, c is the speed of light, and A_{eff} is the area of the mode coupled into the fiber. The dispersion length, L_D, can be calculated according to T_0^2/β_2 where T_0 is the FWHM pulse length of the driving laser and β_2 is the group velocity dispersion of the gas filled fiber. Results of this calculation for a 200 μm waveguide are shown in Figure 3.7 using values of

n_2 and β from literature [77, 78]. This gave rough estimates for expected optimal pressure ranges for the 20 cm and 1 m fibers investigated.

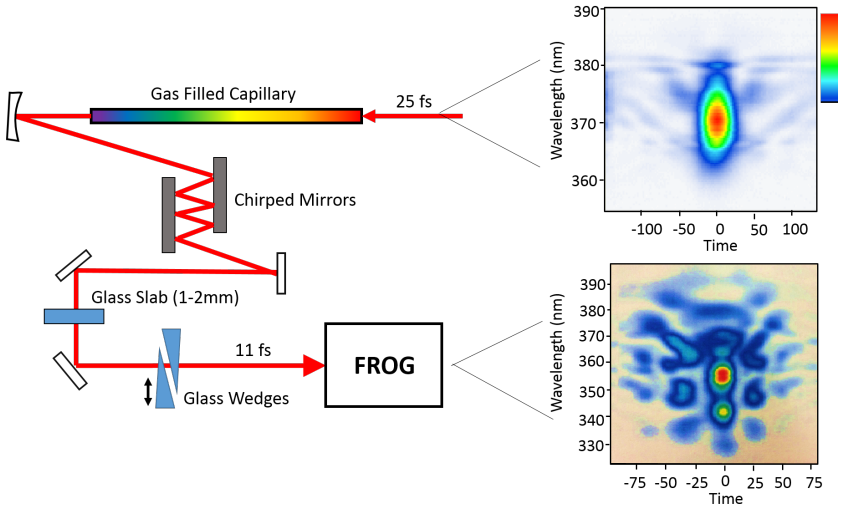

Figure 3.8: SPM layout and pulse recompression using chirped mirrors and glass. FROG traces pre-SPM (25 fs) and post-compression (12 fs) are shown to the right using Krypon at 880 Torr.

The apparatus, shown in Figure 3.8, consisted of a 20 cm or 1 m, 400 μm ID gas-filled capillary settled in a v-groove with horizontal and vertical translation stages mounted on the front and back for alignment. To minimize defocusing of the input pulse due to the dominant higher-order effects within the gas [79], gas was input at the exit of the capillary and evacuated at the entrance, setting up a pressure gradient from 0 Torr to the nominally read value [80]. The output was then recollimated and sent to a set of chirped mirrors for negative dispersion compensation (Layertec, $-40fs^2$ per reflection). Due to the set negative dispersion per reflection from the chirped mirrors, finer adjustment to the dispersion compensation was done by over-compensating the dispersion with the chirped mirrors (for a net negative dispersion), and adding glass to yield little to no second order dispersion. Glass wedges were also inserted, mounted on horizontal translation stages for fine tuning of this dispersion compensation. Pulse lengths were then verified using Frequency Resolved Optical Gating (FROG) with an appropriately thin BBO (thickness = 100 μ m) to phase match the full bandwidth of the pulse. FROG traces yielding reconstructed pulse widths of 25 fs

and 12 fs for the initial and final pulses, respectively, are shown Fig 3.8 (right).

Systematic spectral comparisons were made for optimal generation in Argon, Krypton, and Xenon and with fiber length, as shown in Figure 3.9. Xenon gave the largest spectral broadening with its highest nonlinear index, as expected, followed by Krypton and Argon. However, due to limited availability of Xenon, Krypton was investigated in comparing the effect of fiber length on spectral broadening. For the same pressure of Krypton, the 1 m fiber was seen to have a smaller spectral broadening compared to the shorter fiber, probably due to reabsorption in the gas. It should be noted that, for 800 Torr, 20 cm is closer to the ideal generation length, as calculated via Eq. 3.3. Lower pressure for the 1 m was seen to give much smaller spectral broadening. Using a 25 fs incident pulse, the spectra shown for 20 cm in Krypton at 800 Torr yielded a FROG reconstructed pulse width of 11 fs, with a theoretical transform limit of 5 fs. This difference between theoretical and experimental pulse lengths is expected since we are primarily compensating for second order dispersion, neglecting higher order terms due to optics and nonlinearities in the generation process.

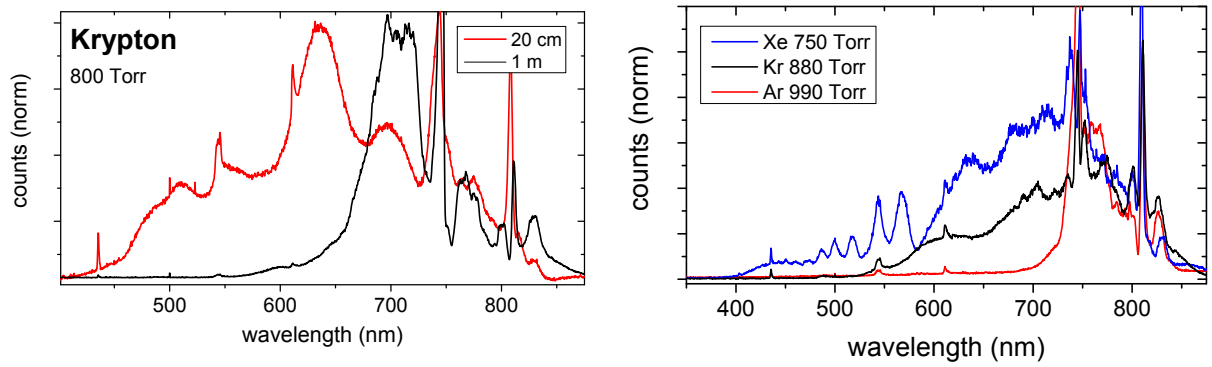

Figure 3.9: SPM spectra comparing (left) Krypton spectra at 800 Torr varying capillary length from 20 cm to 1 m (right) spectra with 1m capillary for optimal generation in Xenon, Krypton, and Argon.

3.3 UHV Chamber

Upon beginning this thesis work, the initial version (V1.0) of the double μ metal shielded ultra-high-vacuum (UHV) chamber was pumped by a 500 l/s Turbo molecular pump (Balzers TMU-

520-SG) and a 270 l/s ion pump (Varian VacIon Plus). The μ metal shielding was used to prevent residual magnetic fields from penetrating into the chamber and altering the electron trajectory into the analyzer. The current chamber (V2.0), is fabricated directly from μ metal and pumped by the 270 l/s ion pump and a 700 l/s magnetically-levitated turbo pump (Pfieffer Hi Pac 700 M) to reduce vibrations. In addition to being able to accommodate the angle-resolved detector, the dramatically increased number of vacuum ports in the new chamber design gave more versatility in experimental design and positioning new components. Base pressures were $2 * 10^{-10}$ Torr and maximally $8 * 10^{-10}$ Torr during pump/probe measurements due to small pinholes in the pressure differential Al filter.

3.3.1 Sample Preparation Tools

Several tools are available in the UHV chamber to aid in preparation of atomically ordered and clean surfaces for photoemission measurements. An Ar-ion sputter gun (LK Technologies NGI3000-SE) was used to remove the top monolayers of atoms in metal samples (primarily Cu(111) in the studies presented here) via collisionally ejecting surface atoms through bombardment with energetic Ar ions. Reconstructing the surface ordering was then achieved through thermal annealing.

A gas doser with a precision leak valve was used for creating a locally concentrated source for surface deposition. This was used in deposition of oxygen, noble gases, as well as the ethylene gas for use in *in situ* graphene growth. The locally high pressure environment near the sample during dosing enabled having a lower overall chamber pressure, minimizing pump-down time back to the 10^{-10} Torr background and residual chamber contamination.

An alkali metal doser (SAES Getter source) equipped with 2 filaments was mounted on a long-travel linear shift attached to the main chamber through a pneumatic value and differentially pumped through a 80 l/s turbo pump (Pfeiffer HiCube 80 Eco). This enabled adjustable and close positioning of the alkali filaments to the sample during dosing. It also allowed for changing of the filaments without the need for breaking main chamber vacuum by withdrawing the filaments and closing the pneumatic valve. The filament attachment could then be independently baked

and reopened to the main chamber with minimal contamination. Filaments were well outgassed after insertion through slowly ramping an applied current (using a GWInstek GPP-1810HP) from 0-5A while monitoring outgassed compounds using the Residual Gas Analyzer (RGA, as discussed below). During dosing, possible contaminants were also monitored using the RGA.

3.3.2 Sample Characterization Tools

Extensive characterization of the sample surface was done prior to all EUV measurements to ensure a well defined and understood surface before adding in the experimental difficulties of EUV generation and pump/probe photoemission. A Low Energy Electron Diffraction (LEED) spectrometer (OCI BDL800IR) was used to determine crystal orientations via imaging the diffraction of low energy electrons from the sample surface onto a phosphor screen. This served to determine sample orientation as well as the atomic ordering of the surface and was routinely used to diagnose the degree of surface contamination on metallic samples and surface quality of graphene samples. In the case of rotated crystalline overlayers, arcs in the diffraction pattern were observed, as was the case on multilayer C-terminated Graphene/SiC. Poor crystalline quality was seen to give blurred diffraction spots.

The implementation of a incoherent source of EUV light was also crucial for efficient surface characterization. Due to the typically broad bandwidth and lower flux of EUV harmonics, a high-intensity, narrow bandwidth EUV source was preferred to give high-resolution, quick characterization of prepared surfaces. These characterizations were indispensable in providing feedback during the "learning phases" of determining the proper surface cleaning and sample dosing procedures, without the additional difficulty of optimizing the EUV generation setup. A duo plasmatron discharge lamp [81] (Spec UVS 300) was used for this purpose. Electrons are initially generated via a tungsten filament in an ambient 10^{-4} Torr He environment and accelerated towards a positivity biased "funnel shaped" aperture. A strongly bottlenecked magnetic field confines electrons generated from electron/gas collisions into a narrow region between this cathode and anode. The resultant EUV emission from the plasma is then leaked through the aperture and, in our case,

focused to a ~ 1 mm spot after a metal capillary. Ratios between the two dominant emission lines could be tuned to give either primarily He I (21.2 eV) or He II (40.8 eV) radiation with a flux of 10^{16} photons/sr·s.

Lastly, a Residual Gas Analyzer (RGA, Leybold Inficon Transpector 2) was used to monitor the partial pressure of gaseous species in the chamber. This mass spectrometer was used to primarily detect atmospheric and hydrocarbon contaminants in the system upon alkali and gaseous dosing. Using the RGA, Temperature Programmable Desorption (TPD) studies could also be performed by ramping the sample temperature at a fixed rate and observing the desorbed species from the sample surface. This could then be used to inform on the nature of the chemical bonding of the adsorbed species on the surface.

3.4 ARPES Detector

The most beneficial upgrade to the system implemented during this thesis has been the installation of an angle-resolved electron detector (Specs Phoibos 100). Previous experiments were carried out using a time-of-flight detector with a narrow photoemitted electron acceptance angle, as described in [82]. This collected an energy density curve (EDC) for effectively one photoemitted electron angle relative to the surface. In order to obtain similar spectral information to angle-resolved detectors, multiple EDCs needed to be collected for different photoemitted angles (via rotating the sample angle relative to the detector) and the spectra subsequently "stitched" together to form a full band map as a function of θ. This time-consuming scheme is not feasible for time-resolved measurements where long integration times would mean full scans would require days of integration stability. Hemispherical angle-resolved detectors, therefore, have become the dominant design for obtaining high energy and angular resolution spectra of photoemitted electrons. The detector is composed of primary three sections: An electrostatic lens system for collecting and separating electrons by their photoemitted angle, a hemispherical analyzer for separating electrons based on their kinetic energy, and a detector for electron multiplication and actually imaging the 2D electron distribution. The following sections will individually discuss the implementation of

each component.

3.4.1 Lens System

Photoemitted electrons from the sample diverge at their original respective angles from the surface (θ as defined in Figure 2.2a) until they reach the entrance aperture of the analyzer lens system. Once inside, a series of plates held at varying potentials create an electrostatic lens system to focus the electrons onto the entrance plane of the hemispherical analyzer, as schematically shown in Figure 3.10. These potentials also dictate the angular acceptance of electrons that are able to propagate to the entrance plane without hitting the detector walls. Measurements presented here are primarily collected using either $\pm 6^{\circ}$ (Low Angular Dispersion, LAD) or $\pm 15^{\circ}$ (Wide Angle Mode, WAM) collection angles. Additionally, the lens system serves to modify the electron's initial kinetic energy (E_{kin}) to a user-defined Pass Energy (E_p), as defined in Section 3.4.2. The electrons then pass through a narrow slit (0.5-1 mm) to confine the studied angular information along one direction in $k_{||}$.

3.4.2 Hemispherical Analyzer

The inner and outer walls of the hemispherical analyzer are held at potentials V_{in} and V_{out}, respectively. Electrons initially enter the analyzer through the entrance slit centered along: $R_0 = \frac{R_{in}+R_{out}}{2}$, where R_{in} and R_{out} are the inner and outer hemisphere radii. The schematic representation of electron trajectories at varying kinetic energies within the hemisphere, with varying θ as being into and out of the page, is shown in Fig 3.11 a. Electrons with the nominally defined pass energy (E_p) propagate along R_0 until the exit plane, with the trajectory shown in red. Within a certain kinetic energy window, electrons with a lower E_{kin} are deflected toward the inner radius and higher E_{kin} toward to outer radius. Electrons outside the defined energy window are deflected towards the walls of the detector and do not propagate through to be detected. This scheme has the effect of dispersing the kinetic energy of the electrons along the axis perpendicular to electron emission angle. The complementary trajectories for electron emission angle, θ, are shown in Fig

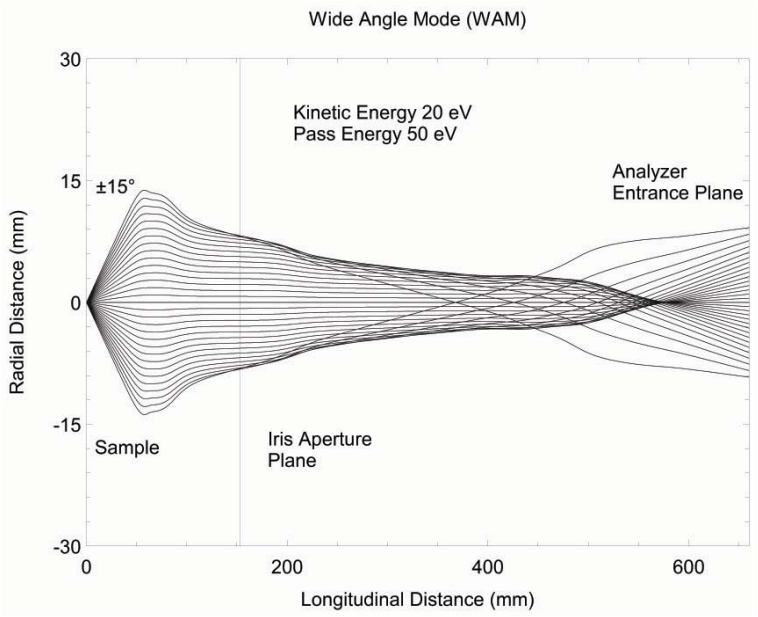

Figure 3.10: Electron trajectories in the electrostatic lens system for wide angular acceptance ($\pm 15°$) of electrons from the sample into the beginning of the hemispherical analyzer, from Ref [83]. Calculated for a $E_{kin} = 20$ eV and $E_p = 50$ eV.

3.11 b. The exit slit used in measurements is usually a large aperture than the one shown, allowing a large window of the dispersed electrons along E_{kin} to pass through. It is shown as a narrow slit here to clarify trajectories at one value of E_{kin}.

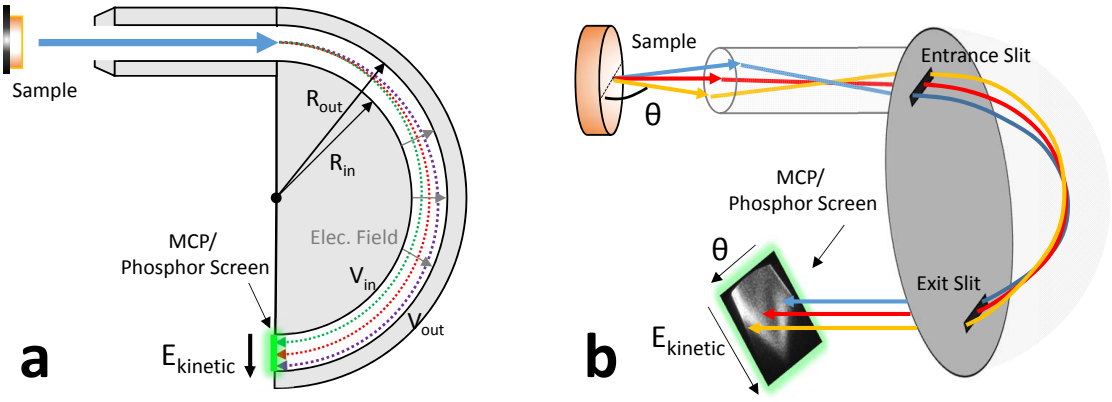

Figure 3.11: schematic for ARPES analyzer highlighting (a) electron trajectories for varying Kinetic Energy at a fixed θ (b) electron trajectories for varying θ at a fixed Kinetic Energy, adapted after [84]

3.4.3 Electron Detection

The 2D electron pattern, being dispersed according to θ in one direction and E_{kin} in the other, is then amplified via a set of multichannel plates (MCP). The secondary electron cascade, usually a multiplication of 10^7 per incident electron, can then detected after the MCP by a phosphor screen, registering each electron-cascade packet as a glowing point on the screen. A charge-couple-device (CCD) camera is then used to image the phosphor screen. Analysis software is then used to assign energy and angle values to the 1376 x 1040 channels. It should be noted that, due to aberrations in the lens system, significant "warping" occurs for the lower kinetic energy region of the recorded spectra. The degree of this spectral warping as a function of angle and energy can be calculated and is corrected for in presented spectra. Additionally, the photoemission angle is converted to $k_{||}$, according to Equation 2.8.

3.5 Custom Cryogenic Cooling Manipulator and Sample Holder

One of the largest engineering and design endeavors during this thesis was the optimization of a sample holder design that had:

(1) high temperature capabilities, for metal sample surface preparation and *in-situ* graphene growth

(2) low temperature capabilities, for surface-adsorbate systems (metal/CO, metal/alkali, metal/noble gas) and low temperature phase-change materials (e.g. metal di-chalcogenides)

The initial sample holder design (V1.0) had been used to primarily investigate single-crystal metal surfaces. Mounted on a 4-axis manipulator (horizontal and vertical translation with rotation about the vertical axis), the sample was permanently mounted in the proper orientation. Heating was controlled through directly flowing a high current ($> 10A$) through the crystal, with cooling achieved through contacted copper feedthrough connections coupled to an external liquid nitrogen reservoir. Temperature performance data for this and subsequent designs can be found in Table 3.3.

	V1	**V1.5**	**V2**	**V2.5**
sample mounting	fixed	transferable	transferable	transferable
cooling capabilities	LN_2	LN_2	LN_2 & LHe	LN_2 & LHe
heating method	direct current-resistive	exposed filament-radiative	housed filament-conductive	exposed filament-radiative
Lowest temp (K)	80	105	40	50
Highest temp (K)	1300	675*	995	1250

Table 3.3: Heating and cooling design performance for V1-2.5 sample holder. *V1.5 was primarily designed for low temperature samples that only required minimal heating. As such, high temperature limits were not investigated.

The primary disadvantage of this design was the fixed sample, making us unable to study varied sample types or perform in-situ sample cleaves without venting and baking of the entirety of the UHV system. The next iteration (V1.5), shown in Fig 3.12, had a separable sample plate, with the ability to change samples through the use of a magnetically coupled transfer arm and a small load-lock chamber that enabled exchange of samples into the chamber without breaking vacuum. Designed for use with low temperature phase-charge materials in mind, the sample plate was cooled through a copper braid connected to the external liquid nitrogen reservoir, achieving a low temperature of 105 K. High temperatures for this design were only required for moderate sample heating, achieved through an exposed tungsten filament behind the sample plate, to remove gradual surface contamination. As such, high temperature limits were not determined.

The V2.0 manipulator design was specifically designed for the V2.0 μ metal chamber, for use with high temperature graphene growth and lower temperature surface adsorbate studies. Therefore, this required a much more dramatic change in dimensions. It was initially a packaged custom company-designed sample holder (VG Scienta CRYOAX4), cryogenic cold-finger, and larger vertical travel range (50cm) manipulator. This also had a transferable sample plate with a mounting screw. Especially important for achieving low temperatures, tightly fastening the angled sample plate with the screw to its mating surface allowed for a better thermal interface and better coupling to the LN_2/ LHe reservoir. However, underperformance in high temperature specifications

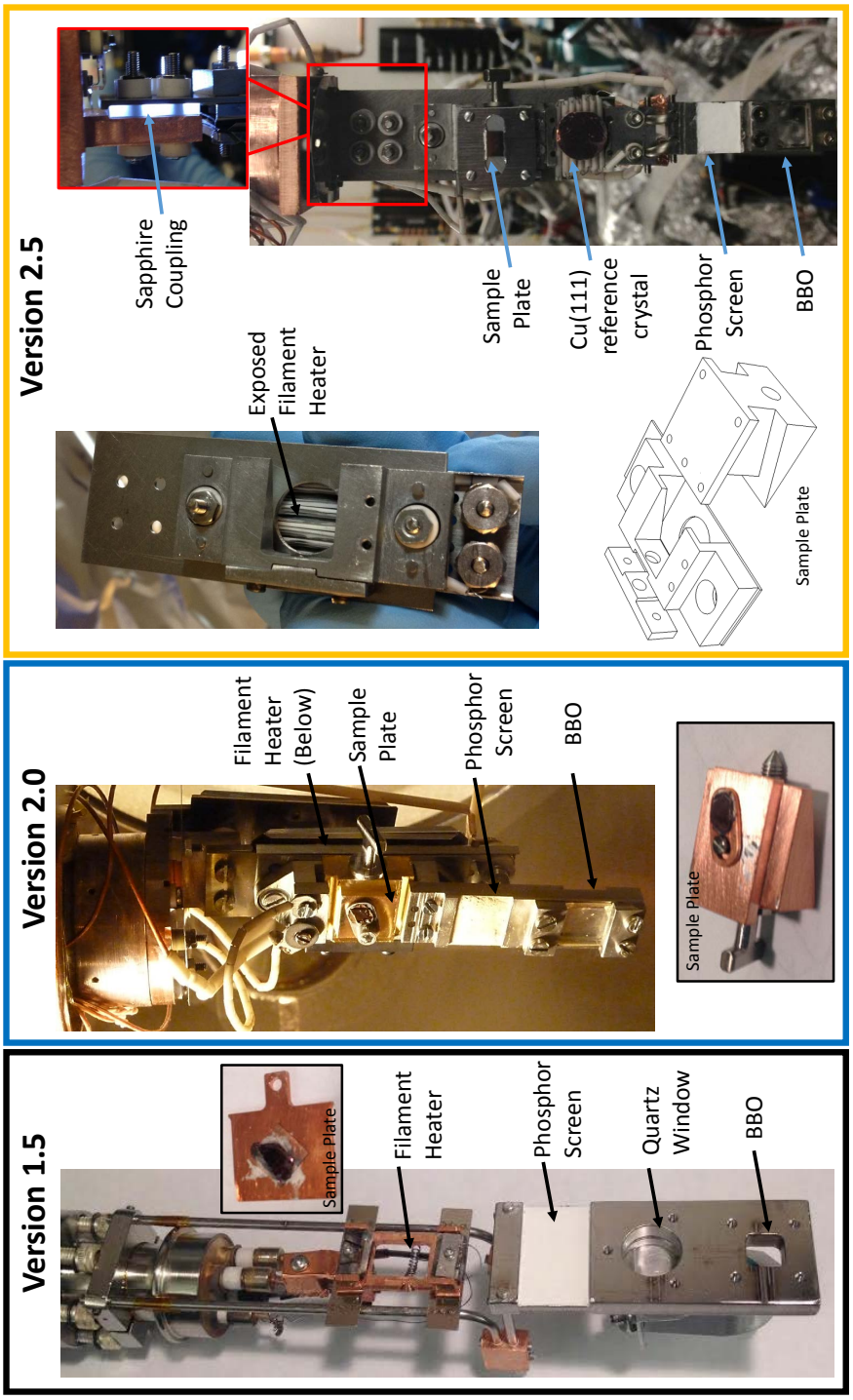

Figure 3.12: Sample holder design iterations after V1.0 fixed mounted sample with direct heating design (not shown).

(initially 995 K) and lacking of robust components and materials (brittle, work-hardened fasteners upon annealing, degrading ceramics, and outgassing of non-high temperature materials) required several redesigns.

The current sample holder, V2.5, has several heating improvements over the V2.0 design. The primary improvement was the use of a tungsten filament (1600K) heater, encased in alumina rods, with holes in the alumina to expose the bare filament towards the sample (see Fig 3.12). With the addition of a hole in the encasing plate, this allowed for direct radiative heating of the sample plate and was able to achieve a maximum temperature of 1250K. Heating set points was precisely controlled using homewritten proportional- integral- derivative (PID) controlled software interfaced with a digital DC power supply (Agilent E3634A). Similar to the V2.0 design, the cold finger was connected to the sample holder via a sapphire coupling plate (shown in Fig 3.12, right). Due to the $>$ 10 x thermal conductivity of sapphire at low temperatures (50 K) compared to high temperatures ($> 300K$) [59], this acted as a "one-way heat valve." This allowed excellent conductivity for cryogenic cooling from the cold finger to the sample mount, but poorly conducted the localized high temperatures of the sample mount back to the cold finger. In addition to decreasing LHe consumption from having an extra heat load, this gave more efficient cooling of the sample upon heating and cooling cycles since the cold finger could serve as a better, more isolated cold reservoir.

Due to the lack of rotation about either horizontal axes, accurate alignment for samples along the correct crystalline axes, and therefore the correct cut in k-space, was a concern. This was accomplished by either initially determining crystalline orientation through *ex-situ* Laue diffraction or *in-situ* LEED measurements. Once the orientation was determined, the sample mounting angle could be readjusted by either remounting the sample with silver paste (Ted Pella, Leitsilber 200 Silver Paint: V1.5) or adjusting the angle of a secondary sample plate via a screw attachment (V2 & V2.5), as seen in Fig 3.12, center.

Common to these designs was the addition of multiple diagnostic tools located directly below the studied sample. A Cu(111) sample with secondary heater was permanently mounted to serve

as an *in-situ* diagnostic for possible issues with the analyzer due to its well established surface preparation procedure and a well-defined band structure. After seeing any abnormalities in the photoemission spectrum of the current studied sample, having the Cu(111) spectrum as a reference allowed us to determine if possible issues were with the detector/systematic or with the sample itself. A phosphor screen (P1 phosphor) was also deposited for imaging the EUV spot to aid in fine tuning spatial overlap of the IR pump and EUV probe (as discussed in the next section). A 0.5 mm thick β-barium borate (BBO) crystal was mounted underneath this to find rough temporal overlap between the pump and probe beams.

3.6 Finding spatial and temporal overlap

An efficient and reproducible procedure is needed in order to routinely find temporal and spatial overlap of the EUV and IR pulses for the studies presented. This consists of primarily two routines whereby gross adjustment is made using optical methods and fine tuning of this adjustment accomplished through photoemission spectroscopy.

Not being able to see the EUV beam via conventional visible imaging cameras, secondary methods are used for finding good spatial overlap of the two spots. In the EUV beam line, the Al foil is removed and a sapphire window inserted after the red recombination chamber (to maintain pressure differential between the mirror chamber and main chamber). Inserting the window after the recombination chamber ensures equal additional dispersion due to the sapphire on both the IR and EUV beams. Neutral density (ND) filters are then inserted into both beams to reduce the intensity of the spots on the sample for better overlap of their central modes. A low lux camera (Mintron 12V2), mounted outside a chamber viewport, is used to image the spot in the sample plane. The residual IR of the EUV beam and IR pump beam are then overlapped on the sample. Care is taken that the pump beam, when spatially overlapped, is still well centered on the annular mirror in the recombination chamber otherwise mode distortions become evident. The ND filters are then removed and the sample is vertically translated so the beams are incident on a 0.5 mm thick BBO crystal mounted directly underneath it, on the same plane as the sample (as shown

in Fig 3.12). Rough temporal overlap, or "time-zero", is then found through scanning the pump delay stage position and looking for the cross-correlation signal between the IR pump and IR probe pulses. This rough temporal overlap procedure only needs to be done initially. With no major realignments to the system, temporal overlap remains within roughly 100 fs for weeks and can be re-found with the multiphoton process outlined below.

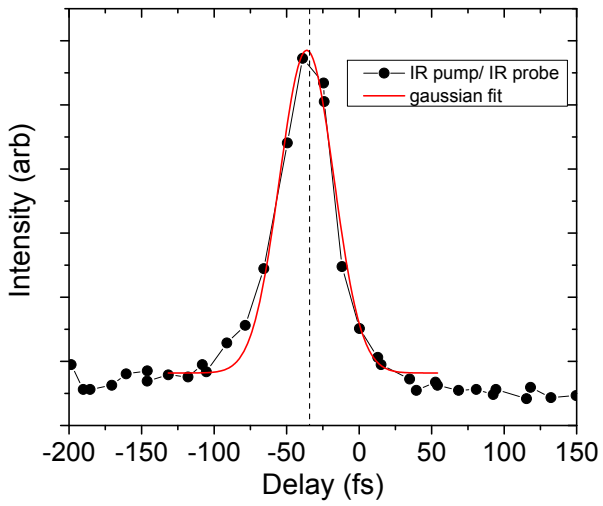

Figure 3.13: Cross correlation for IR pump- IR probe multiphoton ionization showing the integrated intensity of photoemitted electrons around 10 eV as a function of IR pump delay.

Fine tuning of the BBO temporal overlap is done through looking at the cross correlation of the IR pump/ IR probe multiphoton photoemission. Integrated intensities of photoemitted electrons around $E_{kin} = 10eV$ can be plotted as a function of the IR pump delay time. A representative example of this is shown in Fig 3.13, with the maximum in the multiphoton emission seen to be shifted by roughly 30 fs from the initial estimate obtained from optical methods. The cross correlated FWHM of 44 fs (extracted from the red line fit) corresponds to IR pump/ IR probe pulse durations of 31 fs, assuming identical Gaussian intensity profiles. This is in good agreement with FROG characterizations of the pulse when measured after the slightly dispersive lenses and vacuum windows present in both arms. In collinear geometry, optical interference fringes can also be observed on the sample. Lastly, to verify the spatial overlap of the smaller spot-sized EUV beam

with the IR pulse, the Al filter is reinserted and sapphire window removed. The manipulator is then raised to have the beams incident on a phosphor screen mounted directly below the sample. With the IR pump intensity greatly reduced, the EUV spot can be seen on the phosphor screen and small adjustments made to overlap the peak intensities. The sample is then lowered to its original measurement position.

3.7 Future Improvements

While the current manipulator redesign has been successful in giving a larger available sample temperature range, there is one hindrance that many other ARPES systems already incorporate; That is the addition of rotation about the surface normal, or "ϕ" rotation as defined in red in Figure 3.14 (left), and rotation on the axis parallel to the surface, η, shown in green. The current 4 axis manipulator only has capabilities of "θ" rotation. This limits the easily accessible range of the Fermi surface. As an example, with a horizontally oriented spectrometer slit, as shown in yellow in Fig 3.14 (left), this has the effect of selecting one momentum direction (equivalently, a range of angles along one direction from the cone of electron emission), either k_x or k_y, to give a cut in k-space represented inset. Rotation along the θ direction then confines one along the horizontal k-space direction (blue arrow, inset), leaving the rest of the Fermi surface unavailable for study without the help of external rotation or remounting of the sample. With the addition of ϕ and η rotations, this allows the relative rotation of the Fermi map with respect to the slit (red/green arrows, inset) and a larger region of k-space to be easily detected. An example of the resultant band structure mapping that is capable with these rotations is shown in Fig 3.14 (right) for Bi_2Se_3. With both ϕ and θ rotation, energy dispersions in both k_x and k_y are able to be mapped in order to reconstruct the full 3 dimensional band structure of Energy vs. $k_{||}$. Another redesign of the sample holder is currently underway to incorporate these ϕ and η rotations while still maintaining low temperature capabilities.

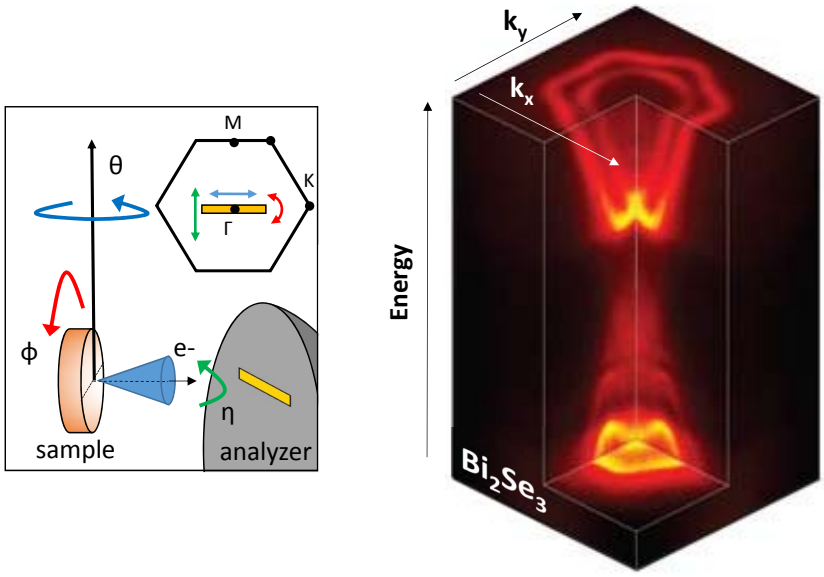

Figure 3.14: (left) angle definitions relative to sample surface. The equivalent "cut" in k-space of the oriented analyzer slit, shown in yellow, is shown inset for a hexagonal Brillioun zone. Equivalent rotations for this cut upon θ (blue), ϕ (red), and η (green) are also shown. (right) Band structure map of Bi_2Se_3 with θ and ϕ rotation available for analyzer. Fermi map adapted with permission from [85].

Chapter 4

Two-Photon Photoelectron Interferometry on Cu(111)

With the realization of isolated attosecond pulses, electron dynamics measurements have been pushed from the femtosecond to the attosecond regime. Recent experiments in time-resolved attosecond spectroscopy have been extended to the realm of condensed matter systems, with the hope of mapping ultrafast dynamical electronic processes akin to studies done on atomic systems [24, 86, 87, 88]. However, benchmark studies on W(110)[89] and Mg(0001)[90] (and most recently on Mg adlayers on W(110)[91]) employing attosecond "streaking", where the photoemitted electron packet traces the electric field modulation of a coincident laser pulse, have faced with the problem of interpreting the cryptic temporal delays seen in these streaking spectra between different energy states. Similarly seen in atomic systems like Ne [92] and in numerous atomic [93, 94, 95] and molecular [96] systems using Attosecond Pulse Trains (APT), the quantitative interpretation of these delays in solid state systems is still a matter of debate.

The extension of these attosecond techniques from atomic systems to surfaces is not a trivial one. Fundamental questions about the nature of photoionization from atoms versus surfaces arise that need to be considered experimentally and theoretically. For instance, the attosecond streaking technique utilizes an IR field to modulate the energy of the electron in a transition between two free states. With the presence of a surface, screening effects and standing waves of the incident E-field can possibly distort or destroy the controlled energy modulation of the electron wavepacket [1] . Of particular interest is the delocalization of electronic states in solids. In condensed matter

[1] This has been addressed on surface streaking experiments by operating at Brewster's Angle to minimize this effect [89]

systems, 10^8 more atoms are probed than their atomic counterparts. Closely spaced with overlapping valence states, this forms a non-localized band that is difficult to model classically as a localized electron "escaping" into the vacuum [97]. Surprisingly, however, of the limited attosecond spectroscopy experiments that have been performed on surfaces, classical ballistic-transport models of a localized electron traveling to the surface have worked remarkably well in reproducing observed delays between energy bands for *both* localized core and delocalized valence bands.

We seek to elucidate this issue through directly probing phase delays of *two* conduction bands of unique symmetry in Cu(111). We explore the nature of this photoemission by combining attosecond electron interferometry utilizing attosecond pulse trains [98, 99] with angle-resolved photoemission. This allows us to access the phase imprinted on electrons during photoemission from delocalized states in different conduction bands. Our data unambiguously show that photoemission from the conduction band cannot be ascribed to excitation followed by semiclassical transport of the electrons to the surface. Instead, we attribute differences due to the quantum phase of the photoemission process that is state-dependent, notably distinguishing them from a labeled transport "time". These results highlight the quantum wave-like aspects of photoemission of electrons originating in conduction bands.

In the following Chapter, the general theoretical background of attosecond spectroscopy techniques (namely attosecond streaking and the interferometric laser-assisted technique employed in studies here) are described in Section 4.1. The experimental technique and configuration for the valence band study on Cu(111) is described in Sec 4.2 and 4.3. Experimental observations are then presented in Sec 4.4, followed by a discussion in the context of previous atomic and surface studies (Sec 4.5), with conclusions discussed in Sec 4.6.

4.1 Theoretical Background

Three unique experimental schemes can be delineated in utilizing EUV attosecond pulses for surface spectroscopy. These approaches employ either a single EUV harmonic (Sec 4.1.1) or multiple harmonics (Sec 4.1.2) with a coincident IR field. While most approaches were initially

implemented for the characterization of harmonic spectral envelopes or the attosecond bursts within each harmonic, they have since been applied to atomic, molecular, and condensed matter systems to determine properties and dynamics of the electron systems themselves. The following sections outline the differences between these experimental approaches and current theories of the observed phase delays between electronic features. This will serve as a platform in which to interpret our experimental results for the valence states of Cu(111).

4.1.1 Single EUV Harmonic

Two regions of behavior are seen to exist when utilizing a single harmonic of the HHG comb depending on the length of the EUV pulse (t_{EUV}) compared to the period of the IR pulse (τ_{IR}). Generating the high harmonics with a fundamental IR field of frequency ω_0, attosecond harmonic bursts are produced every half cycle of the driving field. Depending on whether a single isolated attosecond burst is produced or a train of them, the resultant photoemitted wave packet interacts differently with the coincident IR field. These two regions are analyzed separately in the following sections.

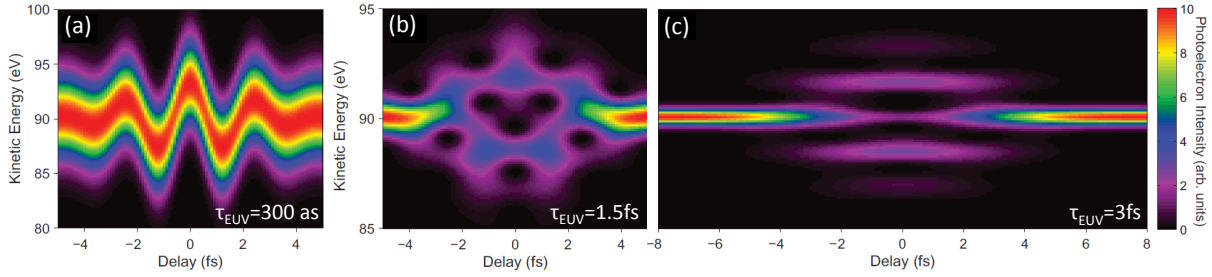

Figure 4.1: Attosecond "streaking" photoelectron distribution depending on EUV pulse length with IR field modulation. Calculated for central wavelength of $\lambda = 750nm$, IR intensity of $2 * 10^{11}$ W/cm^2 and a 5 fs IR pulse compared to a τ_{EUV} of (a) 300 as (b) 1.5 fs (c) 3 fs. Adapted from [100].

4.1.1.1 "Isolated" Pulse ($t_{EUV} < \tau_{IR}/2$)

In the case when the EUV pulse length is less than a half cycle of the driving field, the EUV pulse consists of only a single, isolated attosecond burst. Several different experimental approaches exist for the actual generation of these isolated pulses including high-frequency filtering [101] and various gating schemes of the photoionization [102] and optical [103] configuration. Once the photoemitted wavepacket is liberated from the atom or surface, the temporal evolution of these electrons can be reasonably understood by a semi-classical picture (for a full quantum description, see Ref [104]). For photoionization from an atom (for simplicity), an electron's initial momentum can described by: $p_i = \sqrt{2m_e(\hbar\omega_{EUV} - E_B)}$, with m_e being the mass of the electron, ω_{EUV} is the frequency of the incident EUV light, and E_B is the initial binding energy (note, this would include the work function for the case of solids). With the coincident IR field, the electron is accelerated like a classical particle in the electric field $E_{IR}(t)$ polarized in the z direction. The change in momentum for an electron emitted at time τ can be then calculated by the integrating the classical equation of motion for the electron:

$$m_e\ddot{z} = -qE_{IR}(t) = -qE_0(t)cos(\omega_{IR}t + \phi_{CE}) \tag{4.1}$$

$$m_e\dot{z} = \Delta p_z(\tau) = -q\int_{\tau}^{\infty} E_0(t)cos(\omega_{IR}t + \phi_{CE})\,dt \tag{4.2}$$

where ϕ_{CE} is the carrier-envelope phase of the IR light and $E_0(t)$ follows the intensity of the Gaussian wavepacket. Under the adiabatic approximation where, $dE_0/dt \ll E_0\omega_{IR}$ (ie. slowly varying) the momentum can be further evaluated to:

$$\Delta p_z(\tau) = \frac{eE_0(\tau)}{\omega_{IR}} sin(\omega_{IR}\tau + \phi_{CE}) \tag{4.3}$$

$$= \sqrt{4U_p(\tau)m_e}\, sin(\omega_{IR}\tau + \phi_{CE}) \tag{4.4}$$

Where $U_p(\tau)$ is the pondermotive potential. Given an angle (θ) between the incident laser polarization and z-component of momentum p_z, the final momentum (p_f) and final kinetic energy

of the electron can be calculated.

$$\begin{aligned} p_f^2 =& p_i^2 + 2p_f\Delta p_z cos\theta - \Delta p_z^2 \\ \Rightarrow E_{kin,f} =& \frac{p_f^2}{2m_e} = E_{kin,i} + 2U_p(\tau)cos2\theta sin^2(\omega_{IR}\tau + \phi_{CE} \\ &+ \sqrt{8U_p(\tau)E_{kin,i}}cos\theta sin(\omega_{IR}\tau + \phi_{CE}) \end{aligned}$$

Assuming an experimental configuration where the laser polarization is aligned with the z-component ($\theta = 0°$), this simplifies to a kinetic energy modulation of:

$$\Delta E_{kin}(\tau) \approx \sqrt{8U_p(\tau)E_{kin,i}}sin\theta sin(\omega_{IR}\tau + \phi_{CE}) \tag{4.5}$$

in the case where $E_{kin,i} = \hbar\omega_{EUV} - E_B \gg U_p$ (U_p usually $\sim$ 50 meV for the IR intensities used in experiments compared to 50-100 eV for $\hbar\omega_{EUV}$). This results in a kinetic energy modulation following the IR field modulation.

This gives the spectrogram shown in Figure 4.1(a) centered around 90 eV, where the photoemitted electron packet is modulated with the IR field and is commonly referred to as attosecond *streaking*. Initially applied to atomic systems, all currently published work in attosecond spectroscopy on solids have used this approach.

4.1.1.2 "Non-isolated" Pulse- ($t_{EUV} > \tau_{IR}/2$)

When the EUV pulse envelope becomes comparable or longer than a half cycle of the fundamental IR field, "sidebands" emerge that can be thought of as the subsequent adsorption or emission of IR photons after direct photoemission. Shown in Figure 4.1(c), this results in a direct photoemission peak (shown at 90 eV) flanked by sidebands of $\pm\omega_0$ spacing when the IR and EUV fields are temporally overlapped. Scanning the relative IR/EUV delay, this results in a convolution of the IR and EUV envelopes, allowing the pulse length of the EUV wave packet to be measured assuming an independently verified IR pulse length [105]. For comparison, the "transition region" assuming an intermediate EUV pulse length of $\tau_{EUV} = 1.5fs$ is shown in Figure 4.1(b).

While not able to give attosecond temporal resolution due to the pulse length being necessarily longer than a half IR cycle, spectroscopies in this regime have still been able to probe ultrashort electron dynamics (as long as the dynamics as longer than the EUV pulse length). This approach has been particularly well-suited to study inner-shell auger relaxation processes in gas phase, clocking the time to fill the M-shell vacancy hole of the MNN Auger transition in Krypton [24], and of the N-shell vacancy hole of the NOO Auger transition of surface-adsorbed Xe on Pt(111) [106, 107].

4.1.2 Multiple Harmonics- RABITT

An increasingly common technique using *multiple* harmonics has become the two-photon photoelectron interferometry technique of RABITT (for Reconstruction of Attosecond Beating by Interference of Two-photon Transitions) [98, 108, 99, 109]. Originally used to measure the spectral phase of the harmonics and characterize the attosecond pulse trains [98], it has since been applied to atomic and molecular systems to measure phase delays associated with the photoionized electrons to give information on the systems themselves [95, 110].

In general, a comb of odd-order EUV harmonics photoionizes electrons from their initial ground states ($|g>$) to produce a series of energetically equally-spaced photoemission peaks. In the presence of an incident IR field, the energy of these EUV emitted electrons (whose state we will deem as an intermediate state, $|i>$, in this two-photon process) is modulated by either the absorption ($+\omega_0$) or emission ($-\omega_0$) of an IR photon. This yields a series of sideband peaks, denoted final state $|f>$, of even harmonic order, illustrated in Fig 4.2(b). Scanning the delay of the IR pulse with respect to the harmonic comb, τ_{IR}, the intensity of these sidebands peaks is seen to modulate with a frequency of $2\omega_0$, as described in depth in Section 4.1.2.1. An exemplary photoelectron spectrum as a function of IR/EUV delay in Ar gas [112] showing this temporal modulation is seen in Fig 4.2(a).

This technique has several advantages over the attosecond streaking approach. First, the generation of isolated attosecond pulses requires a considerable amount more of experimental effort, usually requiring nonlinear pulse compression techniques and a carrier-envelope phase-stabilized

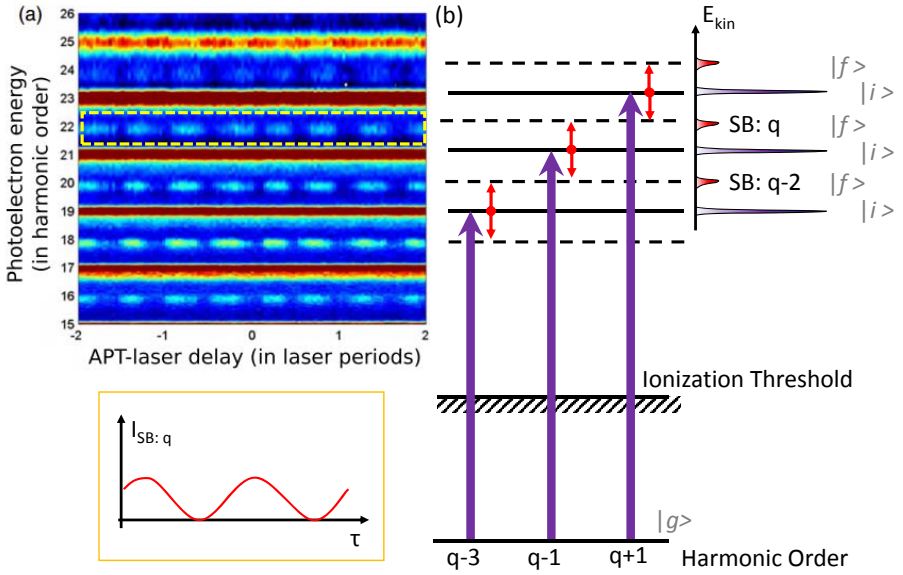

Figure 4.2: General Description of RABITT method showing (a) the photoelectron spectrum as a function of IR/EUV delay. Taking the temporal lineout of the sideband features giving an oscillating intensity in delay time, illustrated for the (q) sideband shown below. (b) The corresponding energy diagram for the harmonic comb emitting from the ground state ($|g>$), to the intermediate primary photoionization state (purple peaks, $|i>$), to the final sideband states (red peaks, $|f>$). Initially adapted with permission from [111, 112].

laser source [113, 101]. Second, the use of multiple harmonics gives a narrower resultant energy bandwidth, allowing for higher resolution studies of narrowly-spaced energy bands. Sub 1 fs isolated pulses used in streaking experiments necessarily give an energy bandwidth of 1 eV, making high resolved studies not possible. Lastly, the IR intensity required for the IR dressing process is lower than is necessary for streaking, reducing possible nonlinear effects [111]. Reduction of this IR intensity is especially helpful on surfaces where the resultant large ATI background can both distort and wash out the photoelectron spectral features (see Section 2.3.3).

4.1.2.1 RABITT Theoretical Description

The modulation of this sideband signal and, specifically, the relative delay of the modulation between different spectral features will be the focus of the study presented here. As such, the specifics of this modulation and the relative "physical" contributions to this phase delay are consid-

ered in more detail. For a full theoretical description, the reader is referred to Refs [109, 114, 115]. Described using second-order perturbation theory, the total intensity for a given sideband of order q is dependent on the two contributing "energy pathways" in the two-photon process that result in the same sideband energy, namely the photon *absorption* pathway ($A_{abs}(t)$) according to $\omega_{q-1}+\omega_0$ and the photon *emission* pathway ($A_{em}(t)$) according to $\omega_{q+1}-\omega_0$. Specifically:

$$S(q,\tau) \propto \left| \int_{+\infty}^{+\infty} (A_{abs}(t) + A_{em}(t))\, dt \right|^2 \tag{4.6}$$

where

$$A_{abs}(t) = \sum_i \frac{\langle f|\overrightarrow{e}\,\overrightarrow{r}|i\rangle\langle i|\overrightarrow{e}\,\overrightarrow{r}|g\rangle}{\epsilon_i-\epsilon_g-(q-1)\omega_0} E_{IR}(t-\tau)E_{EUV}(q-1,t)\, e^{iI_p t} \tag{4.7}$$

$$A_{em}(t) = \sum_i \frac{\langle f|\overrightarrow{e}\,\overrightarrow{r}|i\rangle\langle i|\overrightarrow{e}\,\overrightarrow{r}|g\rangle}{\epsilon_i-\epsilon_g-(q+1)\omega_0} E^*_{IR}(t-\tau)E_{EUV}(q+1,t)\, e^{iI_p t} \tag{4.8}$$

with I_p being the ionization potential, $\overrightarrow{e}$ is the common polarization between the EUV and IR field, τ is the relative delay between the IR and EUV fields, and ϵ_i and ϵ_g are the corresponding energies of the $|i>$ and $|g>$ states, respectively. E_{IR} and E_{EUV} are the complex representations of the IR and EUV fields given in by:

$$E_{EUV}(q,t) = \tilde{E}_q e^{-iq\omega_0 t-\phi_q} \tag{4.9}$$

$$E_{IR}(q,t) = \tilde{E} e^{-i\omega_0 t} \tag{4.10}$$

With $\tilde{E}_q$ and $\tilde{E}$ being the amplitude of the harmonics and IR fields, respectively and ϕ_q being the relative phase of the qth harmonic. The complicated summation term over intermediate states in Eqs 4.7 and 4.8 only contributes at energies corresponding to the two quantum pathways that lead to the final state energy, namely $\epsilon_i = \epsilon_q + (q \pm 1)\omega_0$. For simplicity, these summation terms can be written in complex form:

$$A^{q-1}_{abs} e^{i\phi^{q-1}_{abs}} = \sum_i \frac{\langle f|\overrightarrow{e}\,\overrightarrow{r}|i\rangle\langle i|\overrightarrow{e}\,\overrightarrow{r}|g\rangle}{\epsilon_i-\epsilon_g-(q-1)\omega_0} \tag{4.11}$$

$$A^{q-1}_{em} e^{i\phi^{q+1}_{abs}} = \sum_i \frac{\langle f|\overrightarrow{e}\,\overrightarrow{r}|i\rangle\langle i|\overrightarrow{e}\,\overrightarrow{r}|g\rangle}{\epsilon_i-\epsilon_g-(q+1)\omega_0} \tag{4.12}$$

Making the assumption that there is little variation in intensity between the $(q-1)$ and $(q+1)$ harmonics ($\tilde{E}_{q-1} = \tilde{E}_{q+1}$), we can substitute Eq 4.11 and 4.12 into Eq 4.7 and 4.8 to obtain a

reduced expression for Eq 4.6:

$$S(q,\tau) \propto M \left| \int_{+\infty}^{+\infty} (\tilde{E}_{IR}\tilde{E}_q e^{iq\omega_0 t + iI_p t})\ dt \right|^2 \tag{4.13}$$

where

$$M = \left| A_{abs}^{q-1} e^{i\phi_{abs}^{q-1}} exp(i\phi_{abs}^{q-1} - i\phi_{q-1} + i\omega_0 t) + A_{em}^{q-1} e^{i\phi_{abs}^{q+1}} e^{i\phi_{abs}^{q+1}} exp(i\phi_{abs}^{q+1} - i\phi_{q+1} + i\omega_0 t) \right|^2 \tag{4.14}$$

With the introduction of terms $S_0 = \left|A_{abs}^{q-1}\right|^2 + \left|A_{em}^{q+1}\right|^2$ and $S_1 = 2\sqrt{A_{abs}^{q-1} A_{em}^{q+1}}$, Eq 4.13 simplifies to an easier to interpret expression:

$$S(q,\tau) \propto S_0 + S_1 cos(\Delta\phi_q^{at} + \Delta\phi_q + 2\omega_0\tau) \tag{4.15}$$

Where $\Delta\phi_q^{at} = \phi_{em}^{q+1} - \phi_{abs}^{q-1}$ is deemed the "atomic" phase difference, to be discussed further, and $\Delta\phi_q = \phi_{q+1} - \phi_{q-1}$ is the phase difference between consecutive harmonics.

This demonstrates that the sideband amplitude should oscillate with $2\omega_0$ as a function of temporal delay. It should be noted that a simple optical interference of the IR pulses would result in a 1ω interference, as seen in Appendix A.2. With measurement of the harmonic phase difference being the original motivation for the RABITT technique [98], initial estimates for contribution of the *atomic* phase difference were small and therefore ignored. However, recent gas and molecular phase experiments have found phase shifts where a non-negligible contribution can be attributed to this atomic phase. Due to its importance in interpreting our results in the present study, more detail on this atomic phase and this class of experiments will be given in the following section.

4.1.2.2 RABITT Studies on Atomic & Molecular Systems

Studies applying this interferometric RABITT technique to atomic and molecular systems have noticed delays in the observed interferogram between different energy states. By recording the photoelectron interferograms of different energy states simultaneously with, for example, a wide energy-acceptance time-of-flight detector, the group delay term in Eq 4.15 is identical and all observed changes between states can be attributed to the atomic delay, ϕ_q^{at}. Studies on Argon using RABITT revealed a delay of up to 110 as between the 3p and 3s states [95]. Subsequent

studies on Helium [93] and molecular Nitrogen [96] then observed large phase differences when their intermediate ($|i>$) direct photoionization state was resonant with a direct transition, theoretically ramping through a π phase shift over the resonance.

With the ability to measure this atomic phase contribution directly, its helpful to understanding the observed phase delays by determining what physical effects this term can be attributed to. In the theoretical description given in Section 4.1.2.1, any hint as to what actually contributes to the total ϕ_q^{at} was hidden due to not assuming any specific form for the wavefunctions of the states themselves (we only assumed an amplitude and phase for the absorption and emission pathways in Eq 4.11 and 4.12). Theory has since been done expanding the $|g>$,$|i>$, and $|f>$ wavefunctions into partial waves and analyzing the radial part of the two-photon transition matrix element. While the details of the derivation can be found elsewhere [95, 111], its worth analyzing the resultant "recast" form of the transition matrix elements seen in Eq 4.7 and 4.8. For the *absorption* case in momentum space, this gives:

$$A_{abs}(k) \propto \underbrace{e^{i\eta_l(k_a)}}_{\text{I}} \times \underbrace{\left(\frac{i}{k_a - k}\right)^{iz} \frac{(2k)^{i/k}}{(2k_a)^{i/k_a}} \Gamma(2+iz)}_{\text{II}} \tag{4.16}$$

where $z = 1/k_a - 1/k$, k_a is the momentum associated with the photon absorption pathway, η_l is the scattering phase of the final state, and $\Gamma(k)$ is the complex gamma function. Analyzing each piece: (I) describes the scattering phase of the intermediate state while the phase of (II) is associated with the laser-driven transition from the intermediate to final continuum states ("continuum-continuum") in the presence of the long range Coulomb potential, ϕ_a^{cc}. Taking into account the absorption and emission pathways then, this gives a total expression for the atomic phase being comprised of:

$$\tau_{at} = \underbrace{\frac{\eta_l(k_e) - \eta_l(k_a)}{2\omega}}_{\tau_W} + \underbrace{\frac{\phi_e^{cc}(k) - \phi_a^{cc}(k)}{2\omega}}_{\tau_{CC}} \tag{4.17}$$

In summary then, the two resultant terms can be thought of as:

- τ_W: A Wigner delay of the single-photon photoionization or the delay of the photoelectron

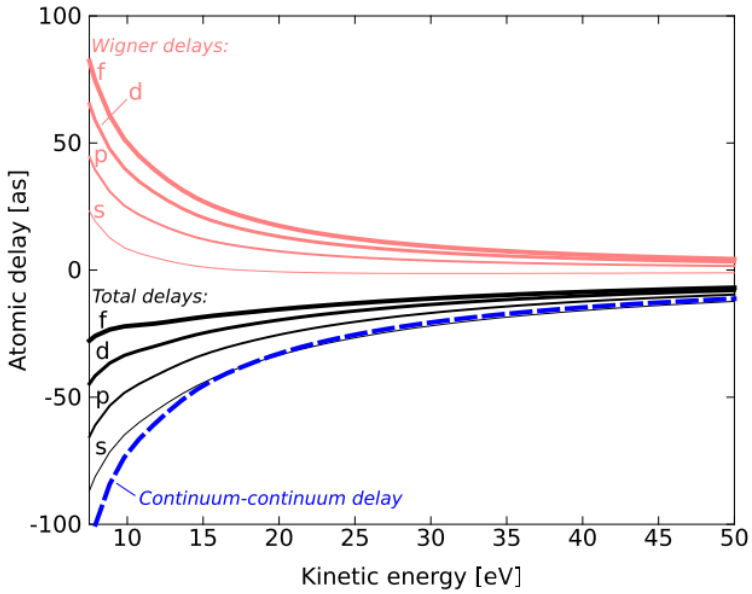

Figure 4.3: Wigner (red) and Continuum- Continuum (blue) delay contributions to total atomic delay (black curves), shown for s, p, d, & f states assuming Z=1 and $\hbar\omega_0$= 1.55 eV. Adapted with permission from [111]

wave packet as its being photoemitted from the atom.

- τ_{cc}: a measurement-induced continuum-continuum delay due to the electron being probed by the IR field in the presence of a Coulomb potential of charge Z.

Plotting these terms for different values of angular momenta (s, p, d, and f), the total atomic delay is shown in Fig 4.3 assuming Z=1. Such models have been able to reasonably reproduce experimentally measured delays for atomic systems and will be discussed in the context of our RABITT phase delays between sp and d states.

4.1.3 Previous Attosecond Studies on Surfaces

To date, only three attosecond spectroscopy experiments have been conducted on surfaces, all utilizing the attosecond streaking technique. With experimental results on Cu(111) to be discussed in the context of these results, the details and theoretical models of these systems are described in the following sections.

4.1.3.1 Experimental Studies

In a benchmark study on W(110) [89], Cavalieri et al. used attosecond streaking to observe a phase delay in the streaking spectrograms between the conduction band and the 4f core state. Generating 300 as isolated pulses via high harmonic generation in Neon using a 5fs, 750 nm centered laser-pulse, emitted photoelectrons up to 88 eV kinetic energy were detected using a time-of-flight spectrometer. Comparing to the streaking spectra of the conduction band, the spectrogram for the 4f electrons were shifted 110 ± 70 as. This delay was initially attributed to transport of the core electrons to the surface, due to the mean free path of the core electrons being 1Å longer.

A subsequent study on Mg(0001) [90] demonstrated little to no delay between the valence band spectrogram and the 2p state, within the experimental error of ± 20 as. Due to the final excited states within the crystal being well approximated by a free-electron parabola, free-particle velocities for both the valence and core electrons could be calculated. Taking into account the varying escape depths of the two states, the modeled ballistic propagation time was found to be identical between the states, yielding the negligible observed delay.

Most recently, this work has been extended to observed "controllable" attosecond delays between (1) the conduction band and Mg 2p state and (2) W 4f and Mg 2p state with the addition of Mg adlayers on W(110)[91]. With additional monolayers of Magnesium, the observed time delay in the underlying Tungsten and conduction band states was progressively increased. For the 4f core level delay, a transport model similar to that applied in Mg(0001) studies [90] yielded good experimental agreement. They additionally found that the IR dressing field was screened almost completely within the first atomic overlayer of Mg. Surprisingly, the delocalized conduction band delay was reproduced with the same classical transport model, after properly weighting the Mg and W contributions to the blurred, joint conduction band.

4.1.3.2 Theoretical Models

More closely analyzing the contributions to the RABITT atomic delay seen in Eq 4.16, the streaking delay in atomic systems can be described by the contribution of two factors: a "Wigner time delay" (τ_W) associated with the group delay of the photoelectrons and a "Coulomb-laser coupling" delay (τ_{CLC} that describes the IR field interaction with the ionic Coulomb potential. In total then, this streaking time delay is represented as:

$$\tau_{streaking} = \tau_W + \tau_{CLC} \tag{4.18}$$

and has been extensively modeled for atomic systems with various modifications to the core potential (CLC term) [116, 92] to explain the 21 $\pm$ 5 as time delay in Neon between the 2p and 2s electrons [92]. However, these models were only able to account for less than half of the observed delay, leaving the full theoretical description still actively explored. It should be noted that the τ_{CLC} term in Eq 4.18 and the τ_{CC} term described in Eq 4.16, while introduced in the separate contexts of attosecond streaking and RABITT, respectively, equivalently describe the two-photon IR/EUV interaction [117, 111].

Present models to explain the observed attosecond delays in solids have applied a wide range of approaches from quantum mechanical to classical, including: direct calculation of dipole matrix element phases while accounting for the degree of localization of the initial state wavefunctions [118], applying a jellium model [119] accounting for wavefunction localization [120, 121], and classical ballistic-like theories of electron transport to the surface. These classical models have taken into consideration the group velocities for the initial [122] and final [89] states. Somewhat surprisingly, the simple ballistic transport model has worked exceptionally well in describing the phase delay behavior of the localized core-levels. In W(110), the 110 as delay of the 4f state compared to the valence band (VB) electrons has shown reasonable quantitative agreement with such models [89, 122], along with the lack of delay (< 20 as) seen between the VB and 2p electrons in Mg(0001) [90]. The delocalized nature of the valence bands, however, has proved a challenge to agree on a well-suited description. Recent results for the VB phase delay in Mg/W(110) have been reproduced

with ballistic models [91] even though theories have suggested them to be ill-suited for describing delocalized states [121, 123]. This suggests a more intricate interpretation of these delays is required and the need for further experimental systems.

4.2 RABITT on Surfaces

Illustrated for the case of bulk (sp & d states, blue) and surface-state (green) electrons, once photoemitted using EUV light, electrons are modulated by the coincident IR field, illustrated in electron kinetic energy in Figure 4.4, left. This gives rise to "sideband features bracketing the original photoelectron energy at $\pm\omega$ corresponding to simultaneous absorption and emission of IR photons, taking place after the electron has reached a final state in the continuum [105, 124]. When using the comb of harmonics, the detected photoemission spectra feature a manifold of equidistant one-photon photoemission peaks (shown in black, for surface and valence states), with intensity modified by the incident HHG intensity and any changing photoemission cross-sections, and two-photon sideband peaks (red peaks) formed by contributions from neighboring harmonics. The magnitude and shape of these sidebands are modulated as the time delay between the HHG and laser beams is changed (illustrated top right for sp & d state sideband features), encoding temporal information about emission from the underlying initial electronic state [93, 95, 96]. If the HHG waveform consists of an isolated attosecond burst, then the energy of the photoelectrons are streaked, as in the experimental studies mentioned previously. These oscillations and, more specifically, the nature of observed phase delays ($\Delta\phi$) between sidebands corresponding to different electronic states be will be the central focus in the following discussions.

4.2.1 Surface States

Due to the termination of the solid by the surface, new electronic states are allowed that are not present in an ideal infinite solid. These states are localized around the surface and decay into vacuum. If its energy lies within the band gap, these states are discrete and the wave function decays exponentially into the bulk as well. Otherwise, they have a linewidth due to hybridization

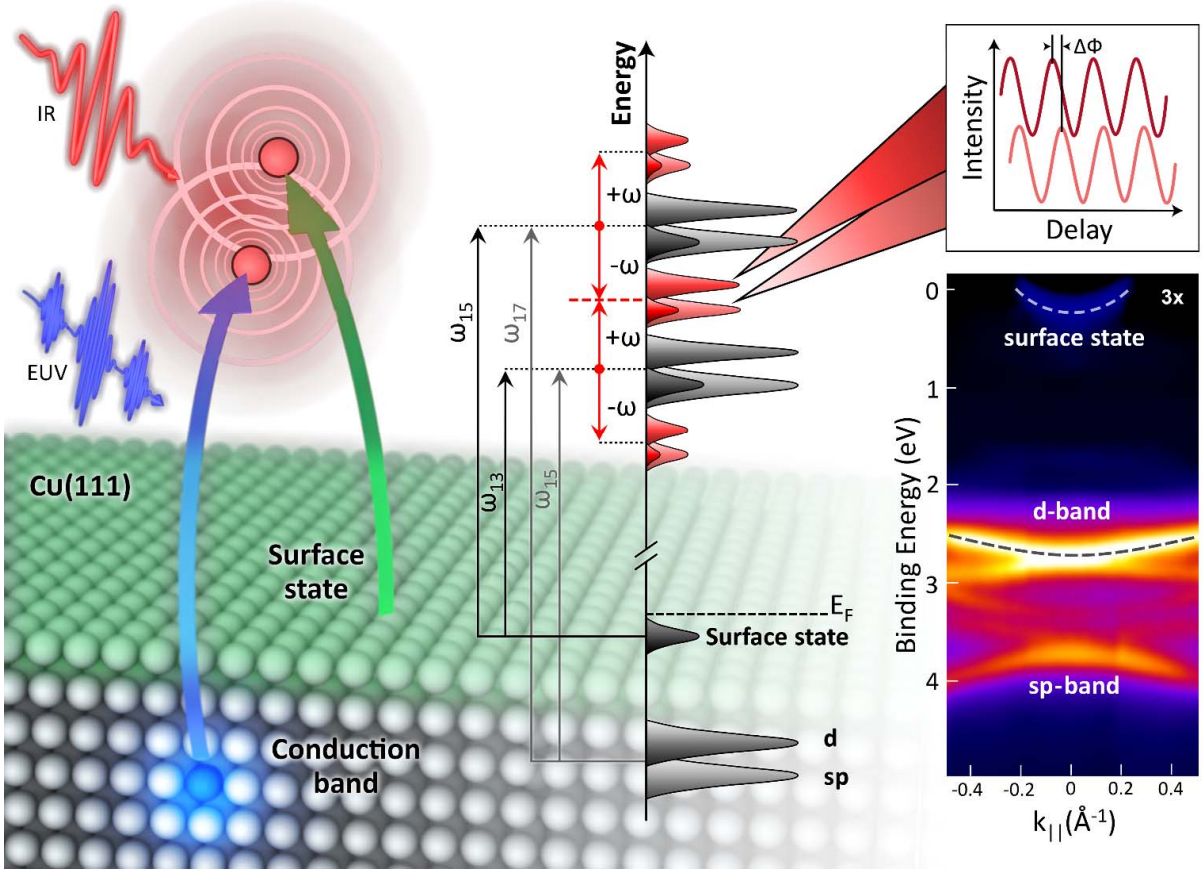

Figure 4.4: (left) Illustration of IR dressing of electrons emitted from Cu(111) surface from a conduction (blue) and surface (green) state after photoemission with a EUV pulse. (middle) Energy diagram denoting harmonic comb photoemission from sp & d and surface states of Cu(111) using harmonics $\omega_{13} - \omega_{17}$ (black states). The interfering two-photon transition "sidebands due to the IR field (red states) yield oscillating intensities with relative IR/EUV delay. Phase delays ($\Delta\phi$) are seen between different states, eg. shown top right for sp & d sidebands. The sideband collection denoted with (*) are comprised of (*d derived*) $(\omega_{19} - \omega)$ + $(\omega_{17}\omega)$ (*sp-derived*) $(\omega_{19} - \omega)$+$(\omega_{17} + \omega)$ and (*surface-state derived*) $(\omega_{17} - \omega)$+$(\omega_{15} + \omega)$. (bottom right) Experimental ARPES band structure of Cu(111).

with bulk bands and can propagate into the solid. These surface states are located within the topmost $\mathring{A}$ near the surface and have a notably near free electron dispersion. Looking at the momenta components, surface states are described only by $k_{||}$, with bulk states having both $k_{\perp}$ and $k_{||}$ allowed. For each value of $k_{||}$ an array of $k_{\perp}$ value extends into the bulk 3D Brillioun zone. In measuring the photoelectron spectra for bulk states, these $k_{\perp}$ values are projected onto

the measured $k_{||}$ value. Due to the sole $k_{||}$ component for the surface state, it should not disperse with $k_{\perp}$ as photon energy is varied.

4.2.2 Cu(111) Band structure

ARPES spectra were recorded along the $\overline{\Gamma M}$ line of the surface-projected Brillouin zone, shown in Fig 4.4 (right) using the He Iα line from a helium discharge source, and an acceptance cone of $\pm 6^{\circ}$ in a 2D electron analyzer in order to map the dispersion (energy, E vs momentum, $k_{||}$) of the valence states of Cu(111). Three distinct spectral features can be observed near the $k_{||}$=0 ($\overline{\Gamma}$) point. The d & sp bands appear at energies around 2.9 eV and 3.8 eV below the Fermi level, respectively, while the Shockley surface state appears near the Fermi level, in the surface projected band gap of Cu(111) at $\sim$0.4 eV [125, 69, 126, 127].

The two valence states have notably different symmetries, with the d band having Λ_3 symmetry while the sp band is comprised of two weaker states of Λ_1 and Λ_3 symmetry that mix near Γ and split at higher momenta. This is shown in the band diagram in Fig 4.5(left, top) with the experimental band structure for the full Brillouin zone shown bottom. The state of symmetry Λ_1 dominates the photoelectron signal around the lower momenta range investigated here, as evident in polarization measurements, where the sp band has a strong polarization dependence between s and p polarizations. The d state with dominant Λ_3 symmetry has little to no polarization dependence. The surface state also is seen to have higher emission for p-polarized light, indicative of a more Λ_1 symmetry (often described as a sp- derived surface state).

4.3 Experimental Configuration

To generate the high harmonic and infrared laser fields, we used a multipass Ti:Sapphire amplifier delivering 0.8 mJ pulses at a repetition rate of 5 kHz (pulse duration 25 fs and central wavelength 790 nm). The output of the amplifier was divided into two phase locked beams and actively stabilized. Approximately 90 % of the laser output was focused into a 250 μm inner-diameter waveguide filled with Kr gas at a pressure of 14 Torr, to generate a comb of five p-

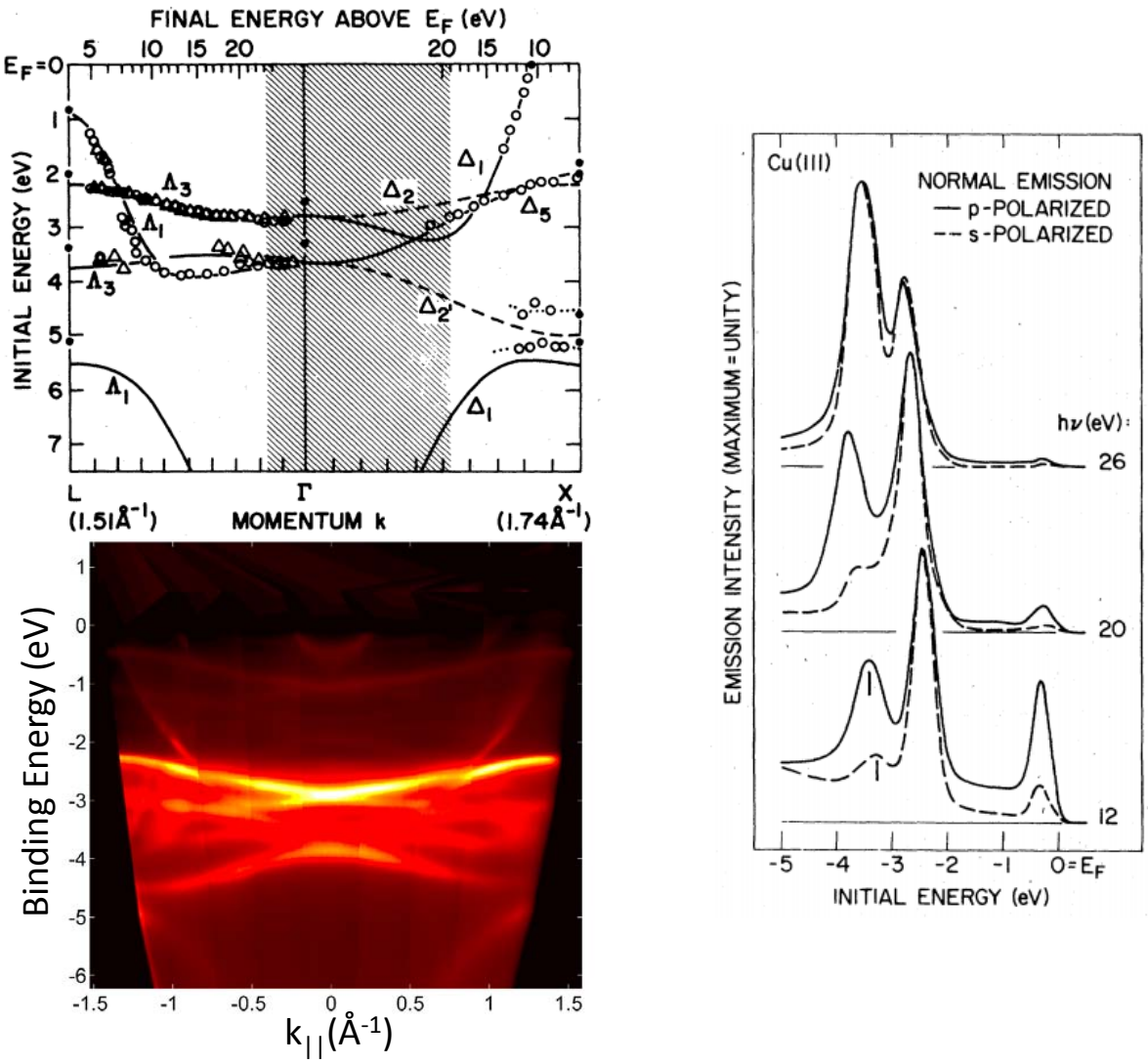

Figure 4.5: Representative electronic band structure for a crystal with bulk band structure ($k_\perp$) projected onto $k_{||}$, producing broadened bands (gray areas). Dotted lines represent allowed surface states within the band gaps. Band structure and polarization dependent curve adapted with permission from [69].

polarized high harmonics from the 13^{th} through the 21^{st} orders. A flat silicon rejector was then used to attenuate the fundamental laser field, and a gold coated toroidal mirror was subsequently used to focus the HHG beam onto the Cu sample. A 300 nm thick aluminum filter was used to block any residual fundamental light and compress the high harmonics in time. The transform limit of each individual pulse in the pulse train was ∼200 as, within an envelope of 8 fs. The combined

experimental energy resolution was < 180 meV.

The dressing infrared beam was adjustable in energy up to ~ 12 μJ/pulse. The HHG and infrared beams were recombined using an annular silver mirror. The harmonics passed through the central hole while 60% of the incident IR beam was reflected and focused at an angle of 45 degree to a spot size of 180 μm onto the sample. The pump-probe delay was controlled using a stepper motor calibrated with an external interferometer. Annular portions of the IR components of both beams were used in this interferometer for in-situ diagnostics of the time delay.

An atomically clean Cu(111) surface was prepared in a UHV chamber (base pressure $6 * 10^{-10}$ Torr) by cycles of sputtering at room temperature (using 0.5 keV argon ions at 60 degree incidence angle at the surface), followed by annealing at 820 K for 10 minutes. Only surfaces exhibiting sharp low-energy electron diffraction patterns and narrow Shockley surface state, as verified by PES, were used for our time-resolved experiments. Static photoelectron spectra were measured using the helium discharge source operating at 21 eV the hemispherical photoelectron analyzer (acceptance angle set to $\pm 6^{\circ}$ at all times). Time-resolved measurements were performed in the same chamber, with a voltage of 3 V applied to sample at all times. Spectra presented here have been energy-corrected for this applied bias.

4.4 Experimental Results

Figure 4.6 plots the photoelectron emitted via the harmonic comb at snapshots in time to highlight the appearance of IR generated sidebands. The spectra in Fig 2b is collected when the IR laser arrives 1000 fs before (defined as negative time) the HHG comb, so that no IR modulation is expected. Due to the harmonic spacing and spacing of the sp & surface state, at the point, the surface state peak from the $(2n-1)^{th}$ harmonic overlaps with the sp band from the $(2n+1)^{th}$ harmonic [Figs. 4.6(b) and (c)]. However, since the surface state exists only in a finite range of momenta around [indicated by the oval regions in Fig. 4.6(b), $0 \leq k_{||} \leq \pm 0.15 \mathring{A}^{-1}$], and we employ momentum-resolved detection, we can collect photoelectrons at higher momenta where the different states do not overlap. This allows for simultaneous study of sideband features for the sp,

d, and surface states extracted from energy and momenta ranges where these states are unique, after performing a proper background subtraction [128].

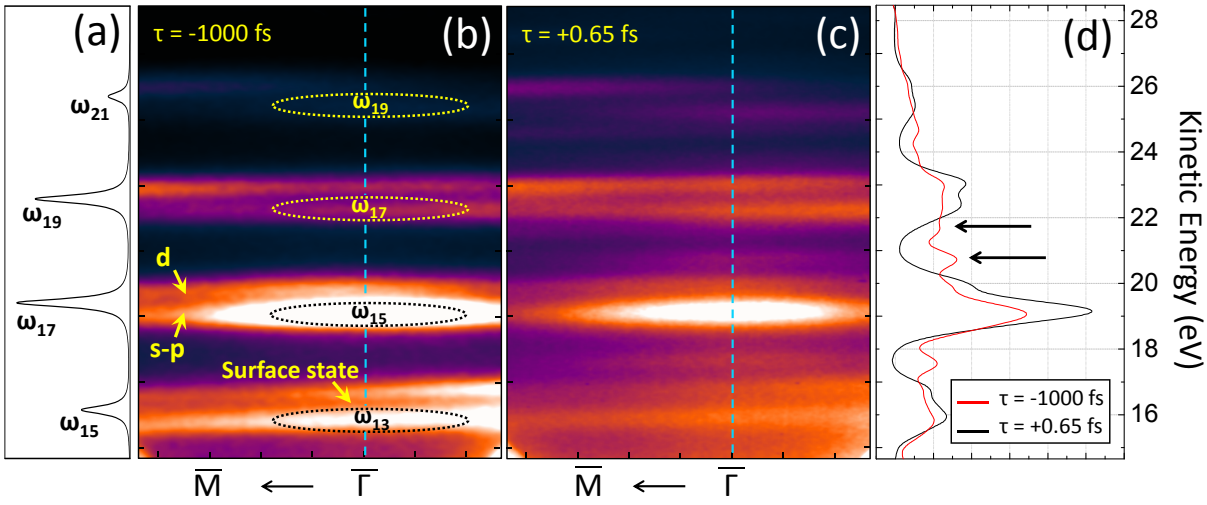

Figure 4.6: (a) HHG comb used for one-photon photoemission, with relative intensity shown horizontally (b) ARPES spectra when HHG and IR fields are not overlapped in time. Spectral features overlapped in energy can be separated using angle-resolved detection, since the surface state is localized near the Γ-point, while the s-p band extends to higher momenta. (c) Same as (b) with the IR and HHG fields temporally overlapped. (d) Angle-integrated energy distribution for IR-assisted and direct photoemission, from (b) and (c).

Figure 4.6c plots the photoelectron spectrum at the maximum sideband intensity, recorded near HHG-pump/ infrared-probe delays of $\tau = +0.35$ fs. Integrating over a large momenta range to more easily demonstrate their difference, the black curve in Fig. 4.6(d) shows the angle integrated spectrum of Fig. 4.6(b), while the red curve shows an angle integrated spectrum of Fig. 4.6(c). The increase in intensity at energies assigned to sidebands of the d and sp bands, and the surface state [as indicated with horizontal arrows, ←], causes a corresponding decrease in intensity in the one-photon peaks, consistent with previous measurements in gas phase and with theory [105, 124, 106, 55, 129, 130, 110] due to the conservation of total photoemitted electron number. This sideband intensity can be modulated periodically by adjusting the phase (time delay) of the IR laser field. Since a given electron can give rise to a sideband by absorbing one $\hbar\omega_{2m+1}$ photon and then emitting one infrared photon, or by absorbing a $\hbar\omega_{2m-1}$ photon and an infrared photon, the

sideband intensity is modulated as a result of the two-pathway interference phenomena outlined in Section 4.1.2.1, representing a coherent interaction of the emitted electron wavepacket with the infrared field. The frequency of this modulation is seen to occur at the second harmonic of the IR field, 2ω, as expected.

When the phase of the IR field is scanned with respect to the phase of the HHG field, the sideband oscillation encodes information about the emitted electronic states via contributions to the observed phase delay. The sidebands at energy $2m\omega_L\hbar$ (m=7,,10) oscillate as a function of the infrared phase as:

$$S_{2m\omega_L\hbar}(\tau) = \alpha + \beta cos(2\underbrace{\omega_L\tau}_{I} + \underbrace{\phi_{2m+1} - \phi_{2m-1}}_{II} + \underbrace{\phi^{em}_{2m+1} - \phi^{abs}_{2m-1}}_{III}) \tag{4.19}$$

In Eq 4.19, the phase term is comprised of a sum of three terms: first, the phase differences between the HHG and infrared fields, $\phi_{IR} - \phi_{Comb} = \omega_L\tau$; second, the intrinsic phase difference between two consecutive harmonics, $\phi_{2m+1} - \phi_{2m-1}$; and third, a difference in the photoemission phase $\phi^{em}_{2m+1} - \phi^{abs}_{2m-1}$ acquired by an electron during photoemission in the presence of the laser field along two equivalent excitation paths. By measuring this latter phase term for the sp and d bands and the surface state, we show that this phase is sensitive to the unique properties of the electronic states.

This phase was determined through extracting the dynamic oscillations corresponding to the sp, d, and surface state sidebands for each harmonic. Time-resolved ARPES spectra were collected at pump-probe delays from -3 fs to +3 fs near the maximum intensity of the IR laser field. Scanning the IR-HHG time delay is equivalent to scanning the phase of the IR field with respect to the phase of the high harmonic comb. By integrating the ARPES spectra over the proper momentum range and subtracting the single-HHG photon photoemission spectrum (which has no laser-assisted processes, a la Fig 4.6(b)), we obtain dynamic difference spectra that are plotted as a function of time delay to highlight the observed modulation. Figure 4.7a shows the surface state and d band dynamics, integrated over momenta around $k_{||} = 0$, while Fig. 4.7(b) shows the sp and d band dynamics, recorded at momenta where the surface state does not overlap with the sp band.

The resulting signal is negative where when spectral features are less intense than the reference spectra (primary photoemission peaks) and positive where features are more intense (sidebands).

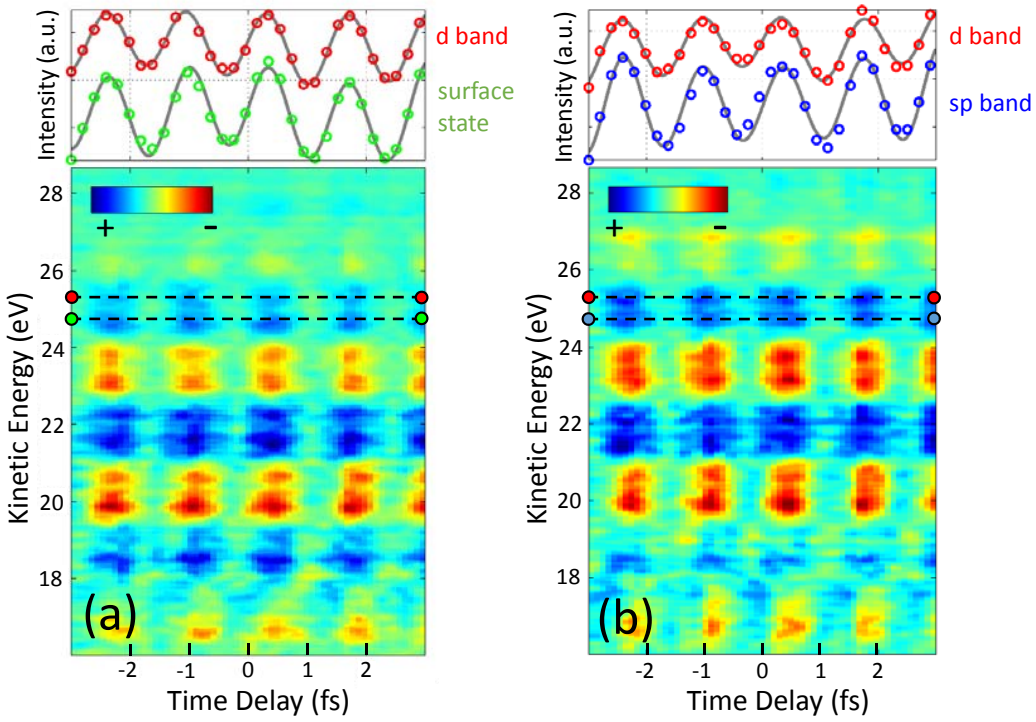

Figure 4.7: (a) The dynamics of the surface state (SS) and d band sidebands as a function of time delay and kinetic energy. In the color map used, blue indicates an increase in intensity of the sidebands while red indicates a decrease in intensity the one-photon peaks. Sp/ surface state sidebands are at kinetic energy: 17.5 eV, 20.7 eV, and 23.8 eV; with d band sidebands at 18.4 eV, 21.6 eV, and 24.7 eV. Periodic temporal modulation at a 2ω frequency is seen at energies indicated by horizontal dashed lines shown above (b) Similar map and extracted dynamics for the sp and d band sidebands, integrating over the higher momenta region.

As a general observation of the 2D map, the modulation as a function of time is seen to oscillate between a strong sideband signal and one which is nearly unperturbed. Plotted above Fig. 4.7(a) are lineouts taken along the horizontal dashed lines, showing the oscillations of the sideband photoemission intensity corresponding to the d band and surface state, with both occurring at frequency 2ω. We note that this indicates that a classical description of electrons exchanging photons with the infrared field is insufficient since the frequency of the sidebands modulation ($2\ \omega$) points to an interference phenomenon rather than absorption/emission of photons from the infrared

field (frequency of ω). Similar temporal lineouts are shown for the high momenta extracted region in Fig 4.7 (b) to give interferograms for the d band and sp band features.

The intensity modulation of sidebands from the sp, d, and surface states are similar to that shown above in Fig. 4.7(a) & (b) - but all show different phase offsets. Fourier analysis was used to extract the phases of all of the sidebands. For a more detailed discussion of the extraction technique, see Appendix A.4. For the surface state, the sum of the HHG and the photoemission phase terms increases monotonically with energy [as shown in Fig. 4.8a], consistent with previous measurements in gases [99, 110, 130]. This phase is indicative of the atto-chirp present on the HHG comb.

The two conduction band features are then compared in two ways: (1) Using the surface state interferogram as a benchmark (Fig 4.8 b) in order to use the localized surface emission from the surface state electrons as a "start time" to our classical electron transport clock, as proposed by Ref [119], and (2) comparing the d band emission benchmarked to the sp band (Fig 4.8 c). In Fig 4.8 b, while both exhibit an almost linear decrease as a function of increasing kinetic energy, the phase of the d sideband at the lowest kinetic energy is notably larger (0.88 $\pm$ 0.05) rad than the corresponding phase of the sp sideband (0.39 $\pm$ 0.05) rad. In addition, at highest kinetic energies, both the sp and d sidebands have negative phases, i.e. (-0.38 $\pm$ 0.12) rad and (-0.18 $\pm$ 0.12) rad, respectively.

4.5 Discussion

The linear behavior of the sp and d band photoemission phase seen in Fig. 4.8 might suggest that a classical transport mechanism of the conduction electrons to the surface, giving rise to a time/phase delay. Assuming an electron escape depth $\lambda_e = 6\mathring{A}$ for Cu(111), we estimate a transit time of 95 as for photoelectrons of the lowest kinetic energy shown in Fig. 4.8. The corresponding transport time for the highest kinetic energy electrons yields 85 as, for a total change in delay of $\sim$10 as over the kinetic energy range probed. The d-band phase delay is actually observed to change $\sim$250 as over the KE range. It should be noted that the difference in transport time between the

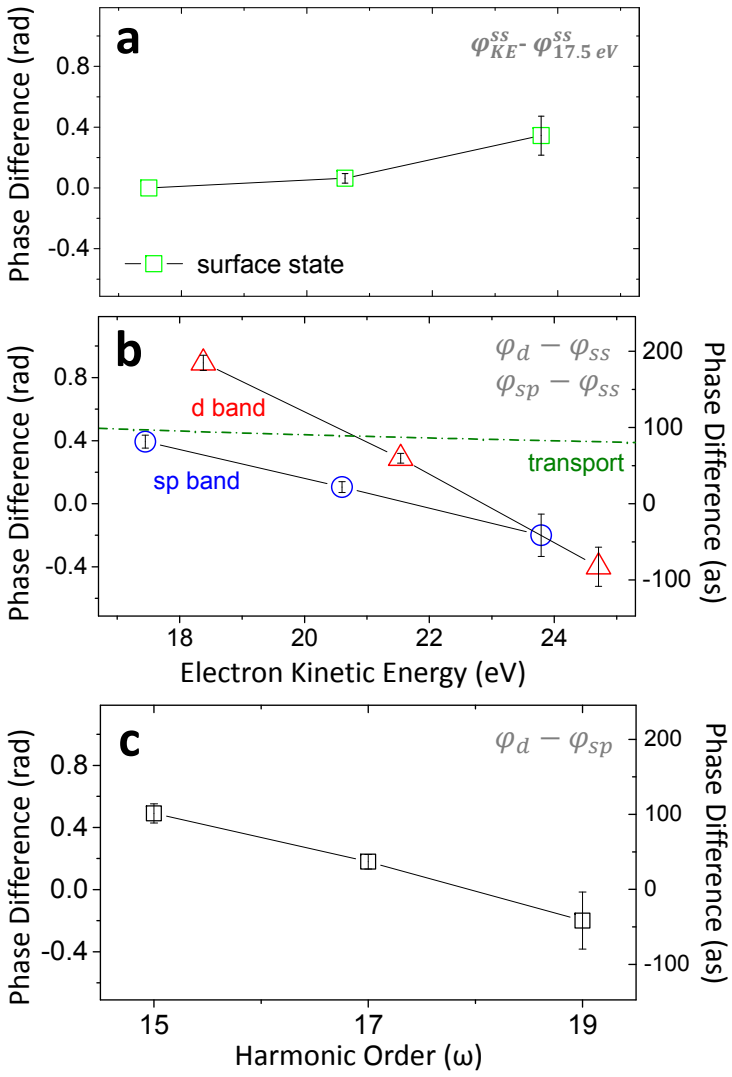

Figure 4.8: (a) High harmonic and atomic phases extracted from the periodic modulation of the surface state sidebands versus electron kinetic energy; the lowest energy point is set to zero for reference. (b) Atomic phase extracted from the sp band and the d band sidebands versus electron kinetic energy, after subtracting the corresponding surface state phase as a reference. Classical electron transport is also shown (green) (c) phase difference between d and sp states for each harmonic sideband.

d band and sp band electrons, having only 1 eV KE difference, gives a negligible 5 as difference.

In addition to the magnitude of the delay with this ballistic transport model changing insufficiently over the probed kinetic energy range, additional reasons add to why this model is incomplete in describing our results: First, the ballistic model was applied in the case of Mg(0001) under the

assumption that the final excited states within the crystal were free-electron like in their dispersion. This allowed the electron to be modeled as a freely propagating particle within the material. In the case of Cu(111), excited final states are not free-electron like, voiding the model's applicability. Secondly, no parameter within the transport model can account for differences between the sp and d states. Qualitatively, they are similarly delocalized and their small binding energy difference yields a minimal transport time delay (5 as).

A natural comparison for these results is to look at the case of delays observed using RABITT on atomic systems, where a classical transport model of electrons is inherently not applicable. As introduced in Section 4.1.2.2, models on atomic systems identified two contributions to the observed phase delay: a Wigner phase and continuum-continuum phase. While there is no obvious analogue of delocalized valence states for atomic systems, applying this atomic model in the case of s, p, and d electrons for Copper *atoms* demonstrates a diminishing phase difference between these states as a function of increasing kinetic energy (see Fig 4.3). To first order then, this reproduces the diminishing phase difference between the d and sp states in the case of the solid (Fig 4.8c). This demonstrates that, while screening and other solid state effects are not accounted for, the dominant factor governing these delays is akin to the atomic case and the due to the properties of the states themselves. We expect with full time dependent density functional calculations (TD-DFT) that properly simulate the crystalline potential and wavefunctions, this phase difference will be accounted for entirely.

One remaining question is then, how do we rectify the core level and valence states being adequately modeled by ballistic transport in these other experimental systems? Agreeing with the most extensive quantum mechanical theory that localization of the wavefunction needs to be taken into account, its not difficult to argue that the localized core level wavefunctions can be approximated as classically propagating particles. In the case of the valence state, why the transport model may still adequately hold can be seen in the details of the experimental approach in the Mg adlayers on W(110). Modeling of the IR field within the metal demonstrated near complete damping after the first atomic layer. This means that the effect of the streaking field was

negligible before the electrons had escaped into the vacuum. Therefore, the delocalized valence state was essentially confined in space to the first atomic layer. This *effective* localization of the state might then allows the transport model give reasonable experimental agreement. In our case of Copper, this does not hold, since the infrared skin depth is large compared to the electron escape depth ($\delta_{IR} \sim 100\mathring{A}$)[131, 132]. While the dominant contribution to the photoemission signal is from the surface (see Appendix A.3) the delocalized electrons are dressed within a larger extent of the solid.

4.6 Conclusions

We have used the interferometric attosecond technique of RABITT to study two unique valence states of Cu(111), observing a phase difference between them. We interpret this phase delay as being intrinsically linked to properties of the bands themselves, such as symmetry and dispersion, with the magnitude not fully explained in the context of a classical ballistic transport model. Finally, our measurements demonstrate the first example of applying this interferometric attosecond technique to surfaces, illuminating new possibilities to measuring coherent phenomena in materials without the need for isolated attosecond pulses. We expect these results to provide a wider context in which to interpret previous attosecond delays in condensed matter systems and to serve as a test case for more through Quantum Mechanical modeling of interferometric delays on surfaces.

Chapter 5

Graphene

With the still relatively recent experimental realization of Graphene [133], a single sheet of carbon atoms bonded in benzene-ring structures, a floodgate of studies have been released to fully characterize its behavior. Graphene is the building block for all other sp^2 carbon dimensionalities. Fullerenes can be formed by wrapping graphene into a zero dimensional bucky ball, nanotubes formed by rolling graphene into a 1D cylinder, and graphite form by stacking sheets into a 3D structure. Of particular interest was the discovery of its relativistic ($\sim 10^6 m/s$) massless Dirac fermions [134], a consequence of its linear energy band dispersion near the edge of its Brillouin zone ($\overline{K}$ point). This can be used as a condensed matter analogue to study quantum electrodynamics effects like the anomalous quantum hall effect and quantum conductance [134] due to electron transport being governed by Dirac's (relativistic) equation rather than Schroedinger's equation. More applied interest in graphene has come from the device world, where its high electron mobility [135], ability to continuously tune its carrier concentration via an electric field has [133, 134], and variable band gap dependent on external doping and coupling with substrates [136] show promise for use in electronics and logic-gate applications.

Graphene is of high interest for its potential to be used in electronic (field effect transistors, pn diodes, optical sensors, terahertz oscillators) and even spintronic [137] devices. This is due to high carrier mobility even at room temperature ($> 20,000\ cm^2 V^{-1} s^{-1}$ [138]) and its relative insensitivity of this mobility on carrier concentration and temperature. Many of these properties are the result of the unique linear dispersion of its electronic band structure, giving graphene's charge carriers

effectively zero mass, relativistic behavior. The potential tunability of its electronic structure from controllable factors like Electric field [133], mechanical strain [139], and dopants/intercalants [140, 141, 142] along with its strong interatomic bonds making defect creation difficult at even elevated temperatures [143] give graphene ideal properties for practical integration into devices.

While considerable effort has been made to fabricate freestanding graphene, its fragility and difficulty in producing large defect-free sheets have made popular the investigations of high quality growth on various metallic and semiconducting substrates. The sheets can subsequently be transferred to insulating or polymer surfaces [144, 145] for use in devices. One persistent issue in integrating graphene into electronics applications has been the intrinsic zero bandgap of the pristine surface. With a tunable band gap being ideal for device applications, one method of achieving this is through chemical doping or through fine tuning interactions with the neighboring substrate. An increasingly common approach for modifying this interaction is through intercalation of either atomic or chemical species. As such, studies directly probing the electronic band structure of graphene in response to its neighboring interface are highly desirable and have been investigated through Raman spectroscopy, STM, ARPES, and electrical methods.

We use ARPES to study these interactions on two unique substrates, Ni(111) and SiC (0001), via two approaches. First, we directly observe electron dynamics to see timescales of fundamental interactions of excited electrons with lattice and other electrons. By comparing differences in these timescales for nearly-ideal graphene/ SiC with bi-layer graphene/ Ni(111), the underlying mechanisms can be explored. Next, in order to explore the controllable modification of the interaction of graphene with the substrate, we study the adsorption and intercalation of Sodium on the initially strongly-coupled Ni(111)/ graphene surface.

5.1 Theoretical description

Graphene is composed of a honeycomb array of carbon atoms, where each carbon atom has four valence electrons. Three of these electrons sp^2 in-plane hybridize, forming σ bonds with the neighboring carbon atoms as shown schematically in Fig 5.1a. These strong covalent bonds are what

is responsible for graphene's exceptional structural stiffness [146]. The remaining out-of-plane p_z electron forms π bonds with neighboring atoms to create delocalized "rings" of π electron orbitals.

The electronic structure of graphene can be reasonably well understood through even a simplified tight-binding model. Its unit cell is composed of two sublattices, labeled "A" and "B" in Fig 5.1b, where the equivalency of these two sublattices greatly affects it's resultant band structure. In reciprocal space, this corresponds to a hexagonal Brillioun zone, shown in gray in Fig 5.1c, with high symmetry points of $\overline{\Gamma}, \overline{M}, \overline{K}, and \overline{K}'$ points highlighted. Most of the interest in graphene's electronic properties centers around studying the $\overline{K}$ and $\overline{K}'$ points, due to its bands crossing the Fermi level with linear dispersion in these regions, as discussed below.

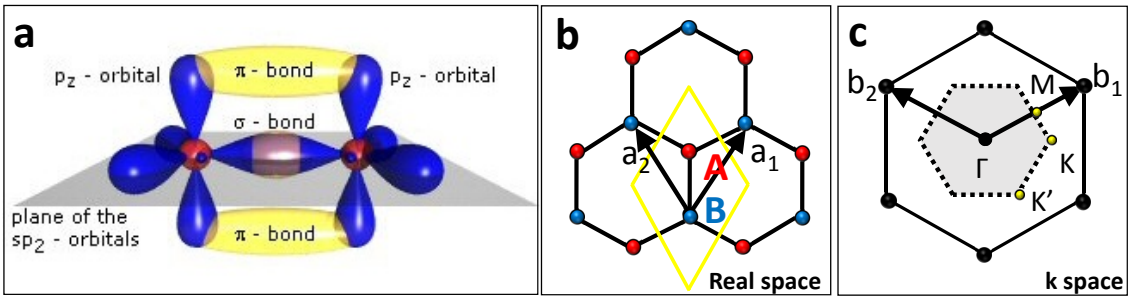

Figure 5.1: (a) representative orbital structure for C-C bonding, from [147] (b) real space lattice with A and B sublattices modeled via lattice vectors labeled as a_1 and a_2. Unit cell is outlined in yellow. (c) reciprocal space lattice with Brillioun Zone shown in gray.

The energy band structure taking into account the possibility for different symmetries on sublattices A and B can be found through solving the energy Eigenvalue equation

$$\hat{H}(k)c(k) = E(k)\hat{S}(k)c(k) \tag{5.1}$$

where E(k) and c(k) denote the eigenvalues and eigen-wavefunctions, respectively. For the π band that we are primarily interested in for our studies, $\hat{H}(k)$ can be represented, taking into account only nearest neighbor interactions, as:

$$\hat{H}(k) = \begin{pmatrix} \Delta/2 & -\gamma_0 f(k) \\ -\gamma_0 f^*(k) & -\Delta/2 \end{pmatrix} \tag{5.2}$$

where

$$f(k) = e^{ik_y a/\sqrt{3}} + 2cos(k_x a/2)e^{-ik_y a/2\sqrt{3}} \tag{5.3}$$

with Δ describing the asymmetry between the A and B sublattices (opening a band gap $|\Delta|$) and γ_0 is the nearest neighbor hopping interaction that can be described by the Fermi velocity according to $v = (\sqrt{3}/2)a\gamma_0/\hbar$, with a being the lattice constant [148, 149]. The overlap integral $\hat{S}(k)$ accounts for any nonorthogonality of π orbitals on neighboring sites and is given by:

$$\hat{S}(k) = \begin{pmatrix} 1 & s_0 f(k) \\ s_0 f^*(k) & 1 \end{pmatrix} \tag{5.4}$$

where s_0 describes the nonorthogonality of the orbitals. The secular equation $det(\hat{H} - E\hat{S}) = 0$ can then be solved to determine the energy eigenvalues, and the band structure E(k):

$$det \begin{pmatrix} \Delta/2 - E & -(\gamma_0 + Es_0)f(k) \\ -(\gamma_0 + Es_0)f^*(k) & -\Delta/2 - E \end{pmatrix} = 0$$

$$\frac{-\Delta^2}{4} + E^2 - |f(k)|^2[E^2 s_0^2 + 2Es_0\gamma_0 + \gamma_0^2] = 0$$

$$E(k) = \frac{\pm 2|f(k)|^2 s_0\gamma_0 - \left[\Delta^2(1 - |f(k)|^2 s_0^2) + 4|f(k)|^2\gamma_0^2)\right]^{1/2}}{2(1 + |f(k)|^2 s_0^2)} \tag{5.5}$$

Where the plus and minus sign correspond to the π^* and π states, respectively. While in a slightly complicated form, we can study details of Eq. 5.5 for both ideal and "non-ideal" graphene. For the ideal graphene case, the A and B sublattices are symmetric and $\Delta = 0$ with $s_0 << 1$. This results in an energy dispersion of $E(k) = \pm\gamma_0|f(k)|$ for the π and π^* state, as plotted as a function of k_x and k_y in Fig 5.2a. The Fermi level is seen to intersect the bands at singular points at the $\overline{K}$ and $\overline{K}'$ points, as shown with the red plane, leaving an unfilled antibonding π^* state. In the vicinity of these $\overline{K}$ points, the energy dispersion can be approximated as $E(q) = \pm\hbar v|q|$ where q is the small momentum vector measured relative to each $\overline{K}$ point. This gives a linear dispersion around the $\overline{K}$ points (lineout shown in Fig 5.2b) that is analogous to the relativistic dispersion $E = \pm\sqrt{(m^2c^4 + c^2p^2)}$ with vanishing effective mass and the Fermi velocity ($\sim 1 * 10^6$ m/s) replacing c. Charge carriers within graphene (both electrons and holes) therefore behave like

relativistic Dirac electrons, causing much of graphene's extraordinary behavior. In line with this, the $\overline{K}$ points where this linear dispersion occur have been dubbed "Dirac points" and are almost exclusively the focus of the ARPES characterizations in this work and others.

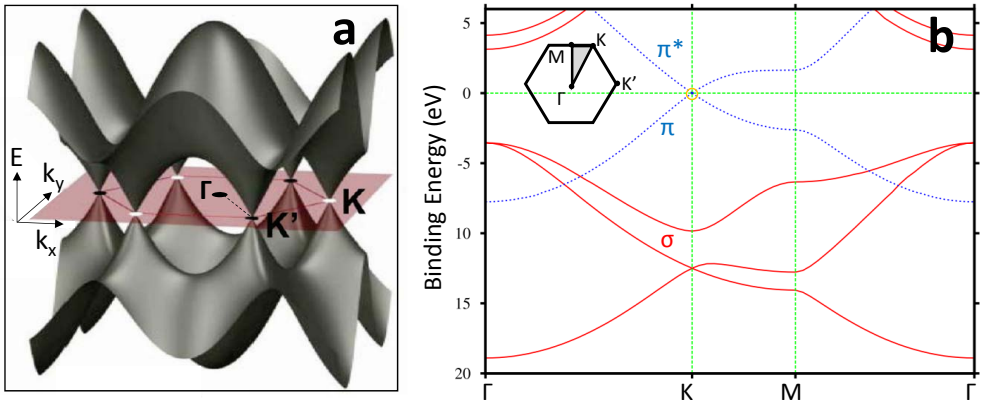

Figure 5.2: (a) 3D band structure of graphene with Energy shown in the vertical direction. Red plane denotes the Fermi level for ideal, undoped graphene. Adapted with permission from [150]. (b) Band structure lineouts for graphene along $\Gamma MK\Gamma$ path shown in inset. Three σ bands (red) arise due to the in-plane sp^2 orbital hybridization and π state arises from the out-of-plane p_z hybridization. The Dirac point is highlighted in orange, with the unoccupied π^* state above E_F. Adapted with permission from [151].

By breaking the A/B sublattice symmetry, a band gap ($|\Delta|$) at the Dirac point is opened and the full expression for $E(k)$ in Eq 5.5 can be used to model the energy dispersion. For most practical applications, this band gap opening is desirable in order to tune the electrical characteristics of the device. This has been accomplished by external field biasing in bilayer graphene systems [152], different edge terminations in graphene nanoribbons [153], or, as we will probe further, controllable coupling of the A/B sublattices to the underlying substrate [154].

5.2 Graphene on different substrates

As seen in Section 5.1 through closely analyzing the π band dispersion relation, graphene's electronic properties are inherently sensitive to the symmetry of it's sublattices. Any break in this symmetry results in a band gap that is dependent on the degree of coupling to the underlying substrate according to Eq 5.5. While a band gap is necessary for practical use in graphene-incorporating

devices like transistors, this coupling not only needs to be well understood, but highly controllable for a well behaved device. Several growth methods for graphene are currently being investigated, with each substrate choice having a varying degree of coupling with its graphene overlayers and resulting in a wide range of electronic behavior. In graphene production, there is a definite tradeoff in the degree of this substrate interaction and ease of sample growth. The most common of these methods are presented here.

Mechanical and Chemical exfoliation: One method for the formation of graphene sheets has been physical or chemical exfoliation of bulk graphite. Physical exfoliation, or the so called "scotch tape" technique, usually results in a range of film thicknesses, requiring extra testing to weed out single layer flakes from multilayer ones [155]. Chemical exfoliation, through solution phase, has shown promise for large area wafers [156] but are traditionally defect riddled due to the necessary chemical surface treatments. Only recent work has begun to demonstrate low-defect large area sheets [157] that might make this method more promising for future work.

SiC Substrates: One of the most prominent methods of graphene growth is an epitaxial method whereby a SiC substrate is annealed at high temperatures ($>$ 1150C). This results in the sublimation of the surface silicon and leaves carbon atoms in a well ordered multilayer graphitic structure on the surface. This procedure yields a slightly different graphene structure when done on either the C-face or Si-faces of the SiC but with very little electronic coupling to the substrate itself [135]. Large area, relatively defect-free growth [158, 159] as well as the ability for subsequent patterning using standard lithographic techniques [160] make this method attractive in achieving graphene (and graphene ribbons) with precisely tuned electrical characteristics [161]. Due to the insulating nature of the SiC substrates, subsequent transfer of the graphene to another substrate, often introducing defects and tears, is also not necessary. However, due to the necessary UHV and high temperature growth requirements, this may impose practical limitations on integrating graphene into current production methods.

Metal Substrates: Alternatively, epitaxial graphene growth through catalytic cracking of hydrocarbons onto transition metal (TM) surfaces has been seen to readily yield large area ($>$ 3

inch wafer), low defect sheets [145, 144]. The most common of these substrates investigated have been Ni(111)[162], Ir(111) [163], Pt(111) [164], Cu [165], and Ru(0001) [139]. However, this growth scheme has two dominant issues that have been the subject of intensive investigation. First, the metallic nature of the substrate will most likely necessitate transferring the sheets to an insulating substrate after large-area growth for use in devices [166, 145, 144, 167]. This is complicated by the second issue, where hybridization between the d-states of the metal and the π state of the graphene strongly alters the graphene's electronic structure and makes physical separation of the graphene layer from the substrate difficult. The weakening of this interaction via either physical or chemical modification of the graphene/ TM substrate interface has therefore been of great interest and will the subject of our investigations in Section 5.6.

5.3 Dynamical Investigations

In addition to investigating the static band structure of graphene on various substrates, understanding graphene's nonequilibrium carrier dynamics is essential for understanding its potential transport properties. Nonequilibrium carrier dynamics are governed by carrier-carrier scattering and *interband* (between valence/conduction band) /*intraband* (within same band) carrier-phonon scattering with acoustic and optical phonons. These have typically been investigated through ultrafast optical methods to capture the short timescale carrier-carrier dynamics that occur within the first 100 fs [168, 169]. In general, the return to equilibrium state electron/hole distributions is commonly broken into 3 steps after the initial optical excitation that creates a large population of non-equilibrium carriers [170, 171].

(1) within the first 50 fs, the initial nonthermal carrier population thermalizes, due to dominant electron-electron scattering, to a distribution well characterized by a hot Fermi-Dirac distribution

(2) intraband carrier-phonon scattering becomes the dominant relaxation mechanism at intermediate times of 0.4-1.7 ps

(3) electron-hole recombination dominant from 1- 15 ps until distribution is again in equilibrium

It should be noted that the mechanisms assigned to the timescales above are found to be the dominant mechanisms and their contribution is likely nonzero at other times (eg. electron/hole recombination contributing to the intermediate decay time in (2)). Previous investigations with short temporal resolution are then able to disentangle the timescales of these dominant relaxation mechanisms, but are divided in their modeling of the populations with either a single or two [172] Fermi-Dirac distributions that individually model electrons and holes. Recent time-resolved terahertz measurements have even been able to tune the photoresponse of the excited carriers from metal to semiconductor-like through electrostatic gating and actively controlling the Fermi level [173], demonstrating the sensitive nature of the carriers to the electronic distribution. Due to the inherently indirect probing of these optical measurements, ARPES allows for direct measurement of electron/hole relaxation and has only recently been used to investigate the dynamics of p-type [174, 175] and n-type [176] graphene.

5.4 Chapter Organization

In the remaining experimental sections, we investigate two unique graphene behavioral regimes: a near-ideal/ weakly coupled (SiC substrate) and a strongly coupled (Ni(111) substrate) graphene system. Section 5.5 characterizes and probes the electron/ hole dynamics of the C-face SiC(0001)/Graphene system. Section 5.6 then provides a detailed investigation of the Ni(111)/Graphene system, directly modifying the strong substrate/graphene coupling via intercalation of alkali atoms to recover a near ideal electronic structure.

5.5 SiC/ Graphene

Graphene forms epitaxially on 4H- or 6H- silicon carbide substrates through Si desorption at elevated temperatures. It is able to be grown on both the silicon terminated (0001) or carbon terminated $(000\bar{1})$ faces, producing notably different behavior in the resultant graphene growth. While

the growth on the Si-face is self terminating after 1-2 layers, the C-face has been seen to grow thick layers from 5-100 layers depending on growth conditions [158], with larger domain sizes measured for the $(000\bar{1})$ vs (0001) termination of 200nm vs 3-100nm, respectively [177]. With Si-termination, the resultant graphene sheet is well decoupled electronically from the underlying SiC substrate. In the C-face substrate however, the first layer in the multisheet stacks is a nonconductive "buffer layer" covalently bonded to the substrate and greatly modifies the resultant band structure [178]. Subsequent graphene layers are then electronically decoupled [135, 179] due to the stacked layers being rotated 30° or ±2.2° with respect to each other. This maintains graphene's 2D electronic structure until ∼ 10 layers, where a more graphite-like behavior is seen [180]. The Si-face graphene maintains a 30° rotational stacking that only weakly interacts with the underlying substrate via Van der Waals forces [181]. Work has been done similar to our alkali intercalation studies in Section 5.6 to try to modify the buffer layer/substrate coupling in $(000\bar{1})$ samples through oxygen [182] or hydrogen [183] intercalation. However, in our following dynamical studies on SiC/ graphene, only pristine surfaces were probed without modification to the degree of substrate coupling.

5.5.1 Sample Preparation

Si-terminated and C-terminated graphene were prepared *ex-situ* on 4H-SiC(0001) substrates according to [177]. Following an acetone/ethanol surface clean, a high temperature (> 1500 C) forming gas (95% Ar/ 5% H_2) anneal hydrogen etched the surface to produce a well-ordered, scratch-free surface. Prolonged high temperature heating (> 1500 C) in a vacuum environment then produced either 1-2 graphene layers for Si-terminated and 5-6 graphene layers for C-terminated through Si evaporation.

Samples were flashed to 1000 C via e-beam heating upon insertion into UHV to remove residual surface adsorbed contaminants like oxygen, water, and hydrocarbons. Noticeable broadening of the Dirac cone features was seen after roughly 10 hours of measurements due to readsorption of contaminants. These were removed through subsequent flashes to 1000 C, recovering the original energy width of the spectral features. Si-face and C-face samples were initially characterized in

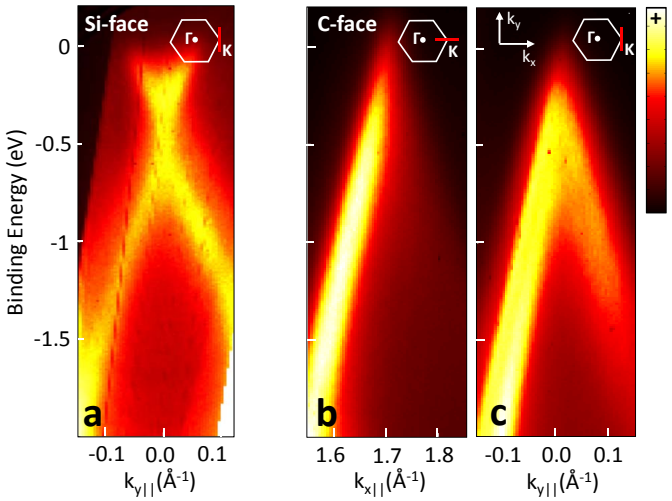

Figure 5.3: Dirac cone at K-point for Si-face (a) and C-face (b-c) graphene collected using He I and He II radiation, respectively.

UHV with ARPES spectra using He II radiation, as shown in Fig 5.3. Si-face grown graphene is typically n-doped due to a Schottky potential barrier being formed between the graphene layer and underlying SiC substrate. This induces an electron charge transfer from SiC to the graphene sheet giving an overall n-type doping [184], as seen in Fig 5.3a. In contrast, the C-face graphene multiple layer composition and rotational faults make its topmost layers well decoupled from the underlying SiC substrate and nearly undoped with the Fermi level being at the Dirac point, as seen in Fig 5.3b-c [185].

A notable characteristic of the photoemission spectra shown in Fig 5.3 is the difference in intensity of the two branches of the Dirac cone dependent on the sampled cut through k-space. This is due to selection effects, where amplitude interference effects from the two atoms in each graphene unit cell result in a dominant intensity for only one branch for measurements along Γ-K. This effect has been well described by simple "two source interference" effects [148] and Fermi's Golden rule final state calculations [186, 187, 188] and has been verified in other ARPES studies on both SiC [189, 178] and metal [190, 191] substrates. A more equal intensity of the two branches is seen when measuring along the k_y direction as defined in Fig 5.3 and shown for Si (a) and C-face (c) spectra.

As shown in Section 5.5.2, measurements with s-polarized light along the Γ-K direction are able to recover some of the intensity of the "dark arm" due to polarization-dependent photoemission matrix elements [188].

Finally, LEED characterization of both samples showed sharp spots, similar to those in Ref [177], indicative of a well ordered surface. C-face samples showed rotational blurring of the primary LEED spots characteristic of the rotational stacking of the 5-7 graphene layers.

5.5.2 Time resolved Measurements

Since we were interested in probing the near ideal graphene surface, the C-terminated graphene was chosen due to its Fermi level being closer to the Dirac point (undoped). Carrier dynamics were then probed along Γ-K with 45 eV high harmonics in the pump-probe geometry described previously with a 1×10^{10} W/cm^2 1.5 eV pump pulse for initial carrier excitation. This pump power corresponds to an initial photoexcited carrier concentration of 9.3×10^{11}/pulse assuming an absorption coefficient of $\sim 2.3\%$ [192] Spectra were taken using a +3V bias. After the spatial/temporal overlap procedure outlined in Section 3.6, spatial overlap of the pump and probe beams was optimized by maximizing the intensity of the LAPE signal seen at time zero. This was done with $50\%s$, $50\%p$ -polarized probe light to have both arms of the π band visible up to the Dirac point. When dressed with p-polarized light, this gave a larger intensity sideband signal that was easier to optimize than if the procedure was done using just one arm of the π band.

Using spectra at large negative delay times as a reference (delay = -500fs), a difference spectra could be calculated to highlight increases (red) and decreases (blue) in spectral intensity as a function of delay, as seen in Fig 5.4. Fig 5.4a-b show the difference spectrum using s/p-polarization (and p-polarized pump) at t=0 fs and +45 fs, respectively. The intense LAPE sideband signal can be seen as the +1.5 eV shifted red band, with the corresponding decreased spectral intensity (blue) in the π band primary photoemission peak. This intensity increase due to LAPE overwhelms any increase that would be seen from the hot electron dynamics expected at small delay times. By t=45 fs, the LAPE sideband intensity subsides completely, leaving visible the remaining hot electrons in

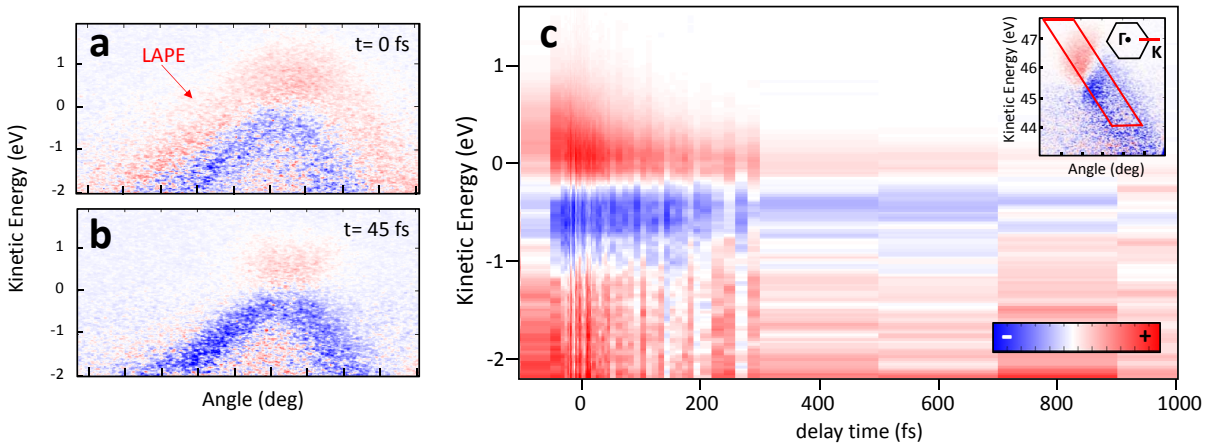

Figure 5.4: (a) Difference map of angle resolved spectra at time-zero using 1/2 s 1/2p polarized light and p-polarized pump, with red (blue) denoting increased (decreased) signal relative to negative times. The LAPE signal is denoted as the red band 1.5eV above the original dirac cone (b) after LAPE, at t=45 fs (c) time resolved EDC along red momentum-integrated rectangle denoted in inset using p-polarized harmonics and a s-polarized pump.

the previously unoccupied π^* band (shown in red).

After initial delay scans were performed using s/p polarized harmonics, the polarization was rotated fully to p-polarization to show only one arm of the π band. This gave a comparatively higher intensity photoemission signal that gave better statistics for later data analysis. The pump was set to s-polarization to eliminate any LAPE sidebands at small delay times, allowing us to isolate any spectral intensity variations that were purely due to carrier dynamics. EDCs were then extracted along the linear dispersion of the π/π^* band according to the bounding box shown inset in Fig 5.4c and plotted as a function of delay time, revealing electron (red) and hole (blue) dynamics.

Alternatively, the electron/ hole distributions were integrated over the bounding boxes shown inset in Fig 5.5a (original, non-difference spectra) to isolate the intensity change for excited electrons (red) and remaining holes (black) as a function of delay. Plotted as a function of normalized intensity, we are able to more quantitatively visualize the total population of carriers in the conduction (π^*) and valence (π) bands as they are created and relax. This shows an exponentially

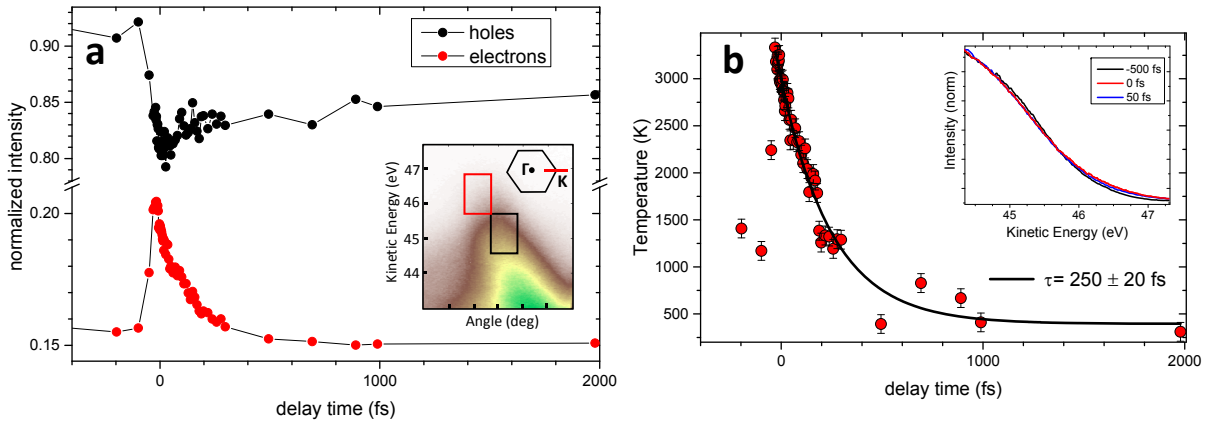

Figure 5.5: (a) Normalized intensity for electron (red) and hole (black) dynamics as extracted from rectangular regions in inset. (b) extracted electronic temperature vs delay time assuming a Fermi-dirac distribution fit around the Fermi energy. Selected delay times showing the broadening at times around t=0 is shown inset. A single exponential fit, shown in black, gives a decay time of $\tau = 250fs$.

decaying population as a function of delay time. EDCs can be extracted along the same line as Fig 5.4c to more carefully analyze the Fermi edge as a function of delay time, shown inset in Fig 5.5b for 0 and 50 fs. Compared to negative delay times, $t = 0$ shows a notable broadening of the edge, with a gradual return at later times. This distribution can be fitted for each delay time according to a Fermi-Dirac distribution:

$$f(E, \mu, T_{elec}) = \frac{1}{exp((E - \mu/k_b T_{elec}) + 1)} \tag{5.6}$$

where μ is the chemical potential, E is the kinetic energy (corrected for sample bias), k_b is the Boltzmann constant, and T_{elec} is the electronic temperature. Deconvolving the distribution to account for broadening due to the high harmonics spectral width, this yielded the T_{elec} as a function of delay time shown in Fig 5.5b, giving a peak electronic temperature of 3400 K and single exponential decay time of 250 ± 20 fs. This is similar to initial decay times seen for p-doped samples [193]. Due to the pump excitation of 1.55 eV, one would expect direct interband transitions from π to π^* that give a strongly non-thermal distribution modeled with *separate* electron and hole populations (ie 2 distinct Fermi-Dirac Distributions) [174]. However, changes to the Fermi distribution were too

minimal for fitting with two Fermi-Dirac distributions to be accurate. As such, the temperatures reported in Fig 5.5b are only for a single distribution. Due to the broad Fermi distribution and small change upon excitation, a significant difference in fitting a single versus double exponential was also not observed, indicating possible need for narrower energy bandwidth harmonics (to give a less intrinsically broad Fermi edge) and more delay times collected in the slower decay regions (0.5-2 ps) to give a better exponential fit. Two decay times would be in line with the expected behavior where, after initial thermalization of the excited electron distribution, the distribution relaxes through primarily electron-phonon (optical) scattering [171] followed by slower timescale electron-phonon (acoustic) scattering [194].

However, its is interesting to note that even with our single exponential observed decay, the timescales determined by this and other investigations [193, 174, 175, 176, 168] are similar to those determined previously for graphite [195], showing that the coupling between each sheet in graphite does not greatly effect the relaxation dynamics of the carriers in each individual graphene-like layer.

5.6 Ni(111)/Graphene

Of the range of transition metal substrates of interest for graphene growth, Ni(111) shows promise due to its small lattice mismatch with free-standing graphene (1.3 %) [196]. This, paired with its chemical vapor deposition (CVD) growth method, results in large area, large grain graphene sheets with minimized defects that might otherwise arise due to lattice dislocations and strain with the underlying substrate. However, strong coupling between the graphene and Ni(111) substrate is seen due to two main factors. First, the small interlayer spacing between the carbon layer and Nickel layer make the overlapping p_z orbitals from the carbon layer with the underlying Nickel $3d$ orbitals strongly hybridize, as shown schematically in Fig 5.6b. Second, the graphene overlayer is strongly asymmetric in its A/B sublattices due to its arrangement over the Ni(111) face-centered cubic (fcc) lattice. One sublattice is situated directly over the 1st Nickel layer (top site) while the other sublattice is located over Nickel atoms in the 3rd atomic layer (hollow site) (seen in 5.6a). Combined with the small interlayer spacing, this creates one sublattice with strongly hybridized

orbitals and one nearly unperturbed (Fig 5.6c with differences between the p_z orbitals highlighted in red and purple), leading to a large asymmetry and therefore large bandgap in graphene's electronic structure.

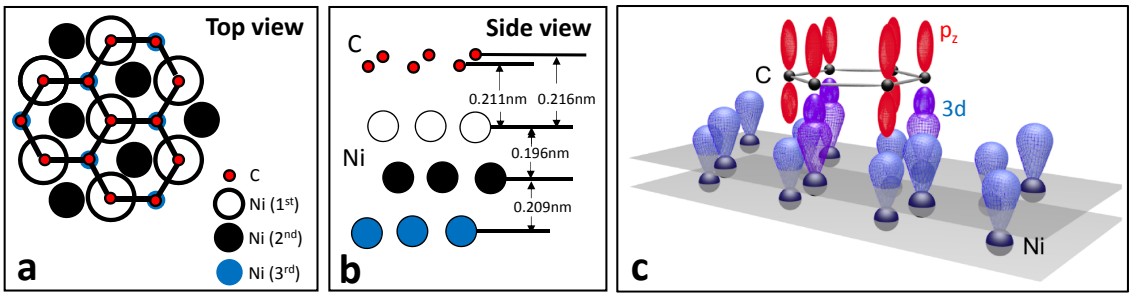

Figure 5.6: Top (a) and side (b) view of Graphene/ Ni(111) lattice showing difference in carbon atoms situated on top 1st layer Ni atoms (top sites) and on top 3rd layer Ni atoms (hollow sites), adapted with permission from [196]. (c) Representation of strongly coupled graphene p_z/Ni 3d orbital coupling for top sites (purple), with unperturbed graphene orbitals for hollow sites (red).

This strong coupling between graphene and the Ni(111) substrate induces dramatic modifications of the electronic states near the Fermi level [197]. The π state is seen to be strongly hybridized with the Ni(111) d states and split into an array of bands [197, 191, 190, 198, 199]. Some of these states intersect at the K-point and form structures below the Fermi level that are akin to the Dirac cone. However, these have been experimentally not well understood and have proved difficult to interrogate [198, 200, 201]. Methods to restore the pristine character of Gr/Ni(111) by introducing adsorbates has therefore attracted interest [141, 191, 190, 198, 199, 149, 202], as will be discussed further in Section 5.6.2.

Band structure measurements of Gr/Ni(111) along $\overline{\Gamma - K}$ [199, 200, 149] and perpendicular to Γ-K [141, 200, 201] of the Brillouin zone have verified this strong modification of the π state near the $\overline{K}$-point, as we measure in Fig 5.7 a-b. Probed along the $\overline{\Gamma - K}$ direction, graphene's π and σ states can be seen along with the Ni $3d$ bands with the same asymmetry of the π state intensity seen at the $\overline{K}$ -point due to the selection effects previously discussed in Sec 5.5.1. The exact position of the $\overline{K}$-point is established from the minimum the σ_3 state. Similarly determined,

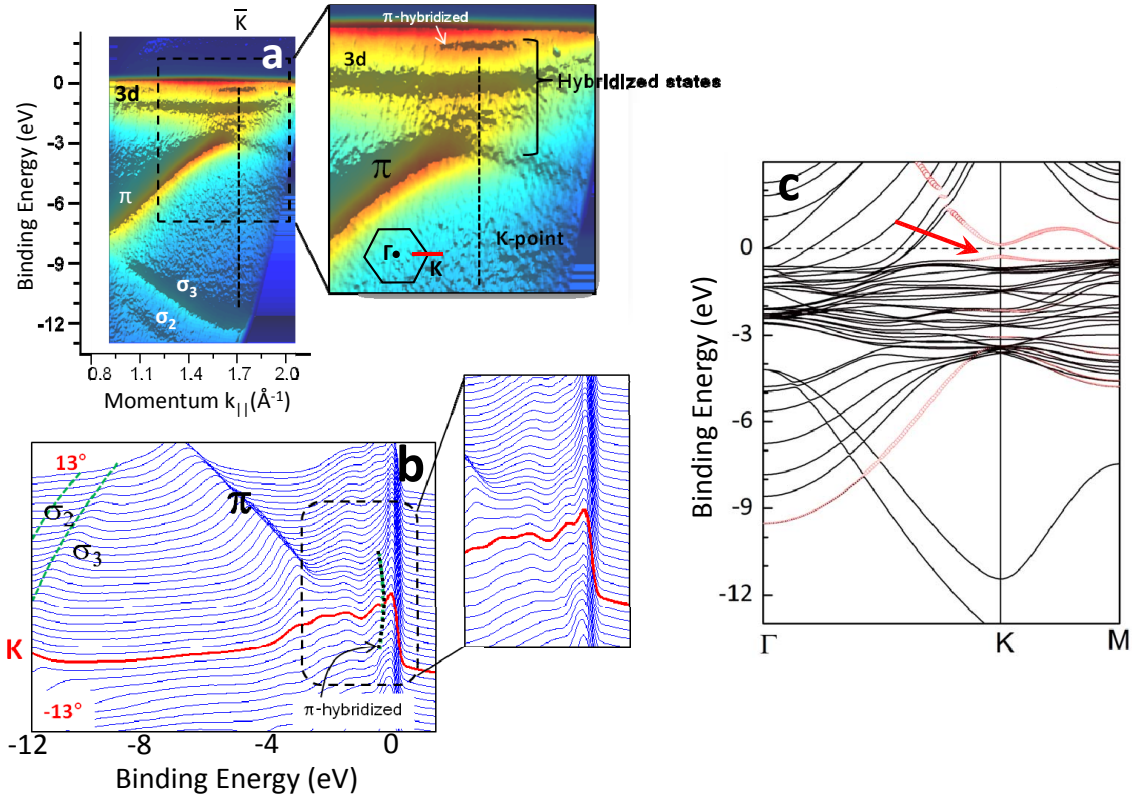

Figure 5.7: (a) Experimental collected ARPES spectrum of Gr/Ni(111) near the K point, taken along Γ-K as shown in the expanded panel. The hybridization of the π state near the K-point is shown in the expanded panel, with the vertical dashed line indicating the K-point (established from the minimum of graphene's σ_3 state). The manifold of states arising from Ni 3d and graphene π state hybridization is indicated with the bracket. (b) corresponding EDC lineouts of (a) as a function of momenta (vertical) with graphene states noted. The EDC lineout at the K-point is indicated in red. The weak feature near the Fermi level is a hybridized state in panel (c) shown in red. (c) DFT calculated majority states near the K-point, with graphene $2p_z$ states highlighted in red.

the exact position of the $\overline{\Gamma}$ point can be determined from the minimum of the π band. In the expanded panel around the $\overline{K}$-point, the π state maximum is seen to be roughly 2.8 eV below the Fermi edge then for graphene on SiC(000$\bar{1}$), pointing to hybridization between the Ni d band and graphene π state upon these states intersecting [197, 149]. This collection of hybridized states near the Fermi level is indicated with the bracket. In support of this, the dispersion of the π state is seen to be notably lower in the momentum range from 1.5 Å^{-1} to 1.7 Å^{-1}. This is due to π state coupling to the Ni states, which is strong in the corresponding momentum range down to -3 eV. Fig

5.7b shows the corresponding EDCs for the raw ARPES spectra in (a) to highlight the maximum in the π band seen at -2.8 eV. Also indicated is a subtle π hybridized band (in dashed black) directly below the Fermi level, and noted in the expanded panel of Fig 5.7a.

To gain further insights into the Gr π/ Ni 3d state coupling, DFT calculations were performed assuming the stacking configuration in Fig 5.6a. Shown in Fig 5.7c, the d band and the π state are notably mixed and split into a dense manifold of states for energies down to -3 eV. States relevant to the $2p_z$ state of graphene are shown in red. It should be noted that these calculations omit spectral weights or matrix elements effects seen in ARPES, making it possible to show all relevant states along $\overline{\Gamma - K}$. Our experimental spectrum in Fig 5.7a-b, however, is dominated by the strongest spectral features. The intensity of the majority of these hybridized states is low measured along $\overline{\Gamma - K}$ due to matrix element effects, which are induced by hybridization [203, 204, 200]. These states have been previously characterized using higher energy photons and/or other cuts through the Brillouin zone [200, 201] and are not important for the intercalation studies presented in Section 5.6.2.

Lastly, due a lower density of Ni(111) states at the K point around the Fermi level, the extent of the π state hybridization with the Ni d bands is notably lower. As such, the remnants of the π state near the Fermi level can be identified, as denoted with the red arrow. This corresponds well with the subtle π hybridized band identified in Fig 5.7a-b, showing excellent agreement of calculated spectra with experiment.

5.6.1 Sample Preparation

The Ni(111) substrates were initially prepared by sputtering 500 nm of nickel onto α-Al_2O_3(0001) substrates, as described in reference [205]. Substrates were then transferred into the UHV chamber and cleaned by cycles of annealing at a temperature of 1100 K, followed by mild sputtering at an elevated temperature of 1100 K and at a beam-energy of 1 keV. LEED measurements exhibited a clear (111) nickel structure, as shown in Fig. 5.8a. Magnetic force microscopy (MFM) characterizations, shown in Fig. 5.8b, demonstrated clear “worm-like” magnetic domains out of plane with

the surface with ∼500 nm size, with opposite out-of-plane magnetization indicated with black and yellow. Due to the small domain size relative to the EUV focal size (400 μm), the spatially-averaged residual magnetic contribution is seen to not greatly influence the resolution of the photoemission measurements.

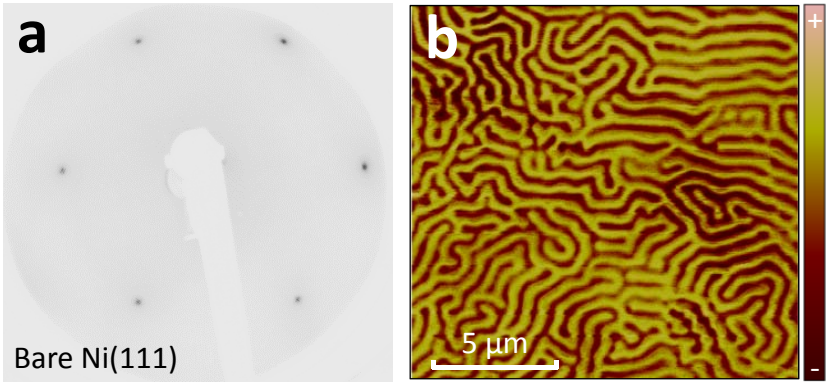

Figure 5.8: (a) LEED of bare Ni(111) sample showing well ordered (111) surface structure (b) MFM image of bare Ni(111) substrate used for graphene growth. The visible out of plane magnetization domains are shown with out of plane up (+) and down (-) domains seen with bright and dark regions, respectively.

The surface on Ni(111) was subsequently graphitized through a chemical vapor deposition (CVD) method of catalytic decomposition of ethylene gas (C_2H_4) onto the Ni(111) surface heated to 900 K, as described in Ref [202]. The deposited carbon layer was then dissolved into the Ni(111) film using a series of repeated flashes to 1100 K. Due to the solubility of carbon in nickel at 1100 K being roughly 3 times higher than at 900 K, slow cooling of the substrate leads to precipitating of the dissolved carbon to the surface. This surface re-segregation was achieved through cooling to room temperature at rates of ca. 8-10 K/min. Using this graphene formation method, faster cooling rates than this have shown a high density of defects and small domain sizes [206]. This procedure yielded high quality, single-layer graphene with estimated domains approximately 100 μm in size [139]. The resultant quality of the nickel and graphene surfaces was verified using a combination of LEED, TPD, and ARPES diagnostics.

Notable differences in growth were seen depending on the C_2H_4 exposure, maximum elevated

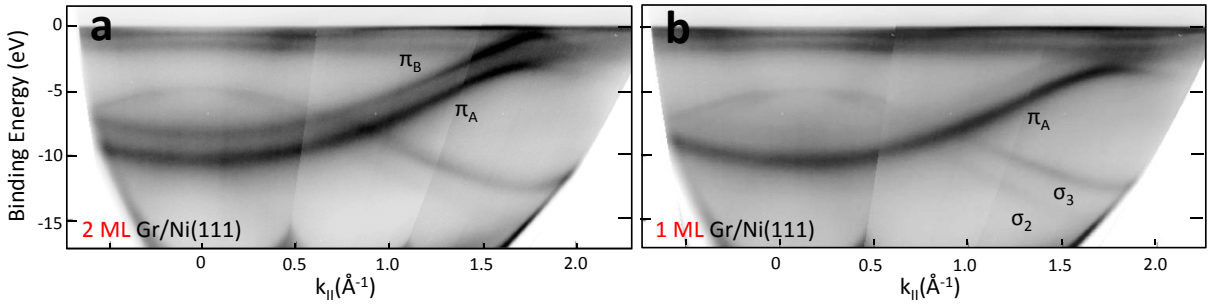

Figure 5.9: ARPES Spectra for bilayer (a) and single layer (b) graphene/Ni(111). Two distinct π bands are seen in the 2ML case: one strongly hybridized (π_A) and one nearly ideal (π_B). A very slight signature of the π_B band can be seen in the single layer case, indicating that small patches of 2ML exist over the photoemitted area, on top of the predominantly 1ML graphene surface.

temperature during hydrocarbon cracking, and the cooling rate of the surface after Carbon dissolution. Previous studies have characterized the multilayer growth of graphene on metal surfaces as strongly dependent on cooling rate after initial dissolving of carbon into the bulk [166, 207]. After carbon deposition, the carbon concentration within the metallic bulk exponentially decays from the surface. As one would expect due to the re-segregation being a nonequilibrium process, fast cooling rates (20 K/ sec) yield poor crystalline carbon structures due to the bulk dissolved carbon losing its mobility before being able to diffuse to the surface layer. Too slow of cooling ($<$ 0.1 K/ sec) gives the carbon enough time to diffuse further into the bulk, leaving a small number of C atoms available to diffuse to the surface to produce little to no graphene coverage. Within the large "medium" range of cooling temperatures that we were operating within, the cooling rate (and total concentration of dissolved C atoms) determined the number of layers segregated on the surface. In particular, bilayer graphene spectra were commonly observed, as identified by the presence of a second π band (labeled "π_B") extending nearly up to the Fermi energy, as shown in Fig 5.9a. This second π band was seen to be near ideal and well decoupled from hybridization with the Ni(111) substrate due to little interaction with its underlying graphene layer, similar to the decoupled multilayer graphene seen in C-terminated SiC(0001)/graphene system (Sec 5.5.1). Previous studies have obtained precise control of bilayer formation through controlled temperature cooling

rates [208] and a self-limiting bilayer growth after initially rotated graphene layer with respect to the underlaying substrate [209].

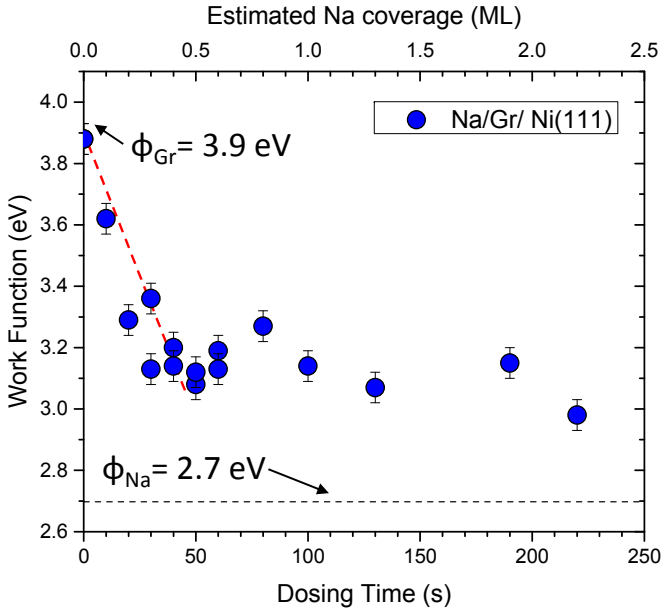

Figure 5.10: Work function of Na/Graphene surface as measured via photoemission as a function of dosing time. Estimated surface coverage of Na is given assuming trends seen in previous studies of alkali/ graphitic systems. The bulk sodium work function [210] and bare Graphene/Ni(111) work function [211, 202] are denoted according to previously established values.

For alkali intercalation studies, graphene samples were doped with Na deposited from the *in-situ* alkali deposition source at a pressure of 10^{-9} Torr at room temperature. Alkali surface coverage was then measured through photoemission work function measurements (with the sample perpendicular to the analyzer for accurate measurements [212]) and calibrated to sample exposure time, as shown in Fig 5.10. The overall trend of a rapid initial work function change at coverages < 0.5 ML and subsequent "saturation" at higher coverages agrees reasonably well with trends seen for K/ graphite and alkali/ Mono-layer graphite systems [213, 202]. These previous calibrations were used to establish a ML coverage estimate for our Na/Graphene/Ni(111) system, as labeled on the top axis. Initial work function measurements of the bare Graphene/ Ni(111) surface were also seen to be in excellent agreement with previously measured values [211, 202]. All intercalation

studies presented here were performed within the "saturation" regime of ~ 0.8 ML Na coverage. It should be noted that no clear LEED superstructure of Na on Graphene was observed for the 0.8ML dosing either in intercalated or adsorbed studies. This is consistent with previous studies of Cs intercalation on graphene which only saw superstructures, and therefore well organized crystalline arrangement, for > 0.9ML or low temperatures [214].

A one hour, low temperature anneal (between 300-400K) was then done to rearrange Na atoms into a uniform sub-monolayer (in case of non-uniform deposition from the filament source). No significant desorption of Na or intercalation was observed during this time, as determined from the unchanging surface work function and oxidation studies (presented below). Intercalation studies were then performed via ramping the temperature above 400K, using ARPES and the He II photon source to observe resultant changes in the electronic structure.

5.6.2 Intercalation of Alkali Atoms

Intercalation of noble metals into Graphene has been shown to break down hybridization at the graphene-metal interface, making it possible to transfer graphene from Ni(111) onto different substrates for utilization in devices [207]. Physical intercalation of atoms like Au [140], Ag, Cu, and Fe [137] results in the reduction of coupling to underlying substrate due to increasing the spacing between the carbon and substrate lattices, resulting in decreased orbital hybridization. Similarly, the "chemical" intercalation of alkalis [202] is seen to result in a similar decoupling due to preoccupying the metal substrate orbitals and yielding nearly unperturbed carbon p_z orbitals.

The mechanism of decoupling Gr/Ni(111) by intercalation of noble metals is well understood but, there is little understanding of decoupling by alkali metals [197, 191, 215, 216, 217, 218, 219, 220, 221, 167]. Although intercalated alkali atoms should detach graphene in a similar matter to noble metals, while also transferring charge and therefore n-doping, studies to date show significant inconsistency in experimental results. On one hand, intercalation of Na (K and Cs) was shown to reduce the energy gap between the non-hybridized states at the $\overline{K}$-point (the π-to-π^* energy gap) to 1.3 eV [202, 149]. On the other hand, a recent study using angle-resolved photoemission

spectroscopy (ARPES) and density functional theory (DFT) showed that the energy gap is reduced to 0 eV after intercalation [201]. The origin of the large energy gap found in past experiments and the role of alkali metal adsorption in decoupling are still not clear, with the issue not being previously addressed. In total, mechanisms of alkali metals intercalation of graphene have been studied extensively using DFT, ARPES, and scanning tunneling microscopy [214, 222, 223, 224, 225, 226].

In the study presented here, we use ARPES to probe states near the K-point during the course of atomic Na adsorption onto and intercalation into Gr/Ni(111). Changes in the dispersion of states near the $\overline{K}$-point and the Fermi velocity are sensitive probes of the interactions between graphene and the substrate [227]. We use changes in the energy and dispersion of the π state at high momenta to examine the role of Na in decoupling graphene's strong interaction with the substrate. Two distinct mechanisms of decoupling can be identified, which have not been uniquely observed previously. The difference in these two mechanisms arises from the position of the adsorbate with respect to graphene. Specifically, we find that Na on top of graphene induces decoupling of the substrate, which results in lowering the π-to-π^* energy gap to $\sim$1.3 eV and changes the π state dispersion at high momenta. Although Na is still surface adsorbed, which we confirm experimentally through ARPES and oxidation studies (Sec 5.6.2.1), this decoupling was previously attributed to intercalation of Na (K and Cs) into Gr/Ni(111) [149, 202]. We also show that adsorption followed by intercalation induces a stronger decoupling that restores the nearly pristine character of the Dirac cone, resulting in a significant closing of the π-to-π^* energy gap. These experimental findings are confirmed by DFT band structure calculations and Bader charge analysis, as discussed in Sec 5.6.2.3.

5.6.2.1 Oxygen Exposure of Adsorbed/ Intercalated Surface

In order to confirm that the Na atoms had been intercalated, we exposed the Na/Gr/Ni(111) (before intercalation) and Gr/Na/Gr(111) (after intercalation) samples to oxygen at room temperature. Due to Na oxidizing readily in the presence of oxygen even at low concentrations [228], oxi-

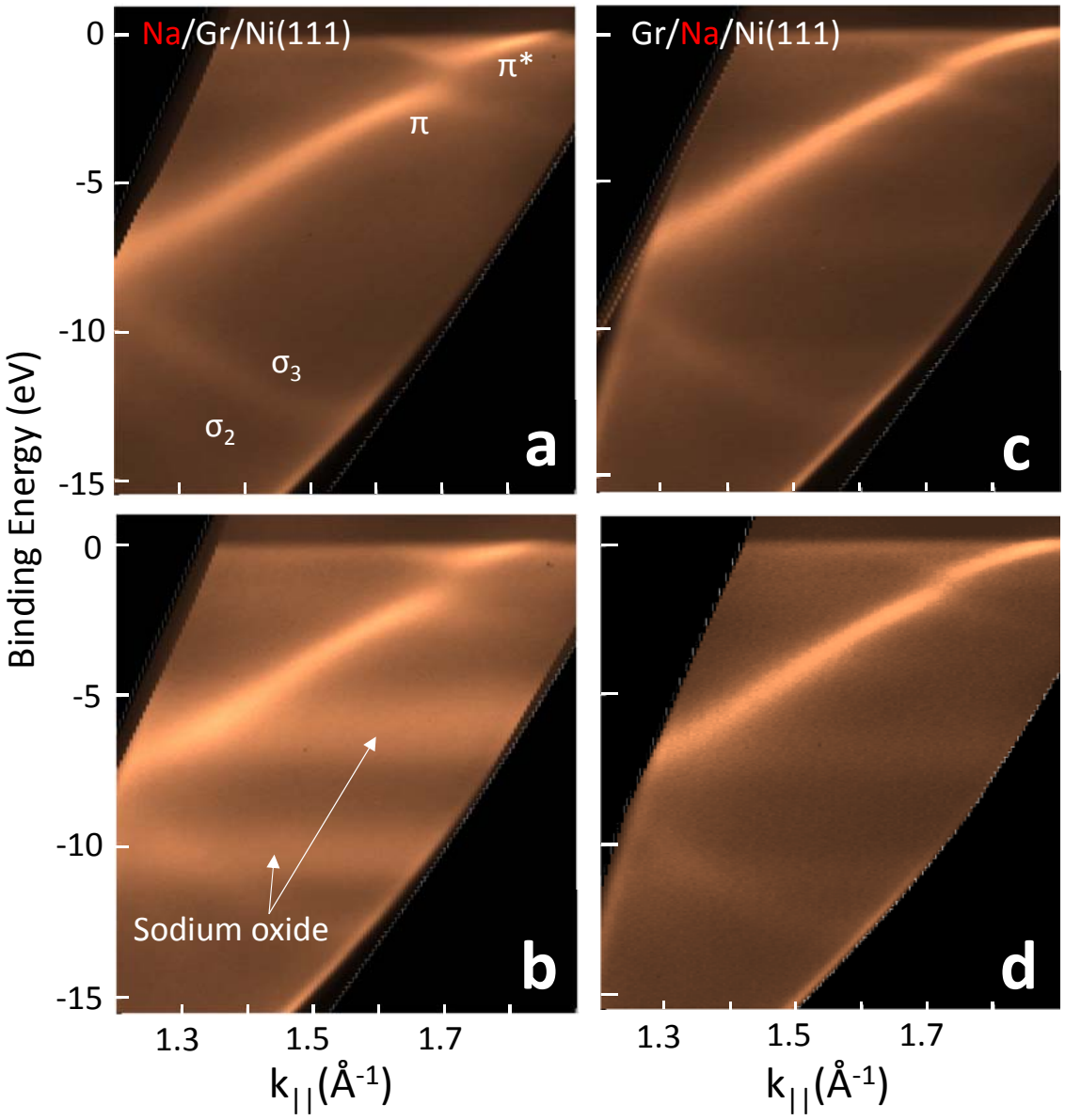

Figure 5.11: (a) Electronic structure of Gr/Ni(111) near the K-point after adsorption and uniform rearrangement 0.8 ML of adsorbate on top, note large band gap of ∼1.3 eV. (b) Same sample as in (a) after exposure to oxygen at 10^{-8} Torr for 40 min with visible sodium oxide states (c) Gr/Ni(111) after adsorption and intercalation of 0.8 ML of Na, with reduced band gap. (d) Same sample as in (c) after exposure to oxygen at 10^{-8} Torr for 40 min, with no significant sodium oxide lines visible (small amount seen due to residual surface adsorbed Na).

dation should occur if the alkali atoms are not "protected" under the layer of graphene. Graphene has been seen to protect intercalated Fe atoms from oxidation, due to oxygen being unable to

penetrate into graphene at room temperature [137, 229].

Samples remained exposed to a flow of oxygen leaked in to maintain a constant chamber pressure of 10^{-8} Torr for ca. 40 minutes. ARPES spectra were recorded during this time using He II radiation. Figure 5.11a shows spectra recorded after adsorbing (and not intercalating) 0.8 ML of Na on top of Gr/Ni(111). The analyzer pass energy was chosen to allow simultaneous detection of high and low kinetic energy electrons, from the Fermi level down to the σ_2 and σ_3 states. The π^* state near the Fermi level and the π-to-π^* energy gap of 1.3 eV indicates that the adsorbate remains on top, as discussed further in Section 5.6.2.2, due to the weak decoupling of the C p_z orbitals with the Ni(111) substrate.

Shown in Fig. 5.11b, two strong spectral features emerge after oxygen exposure, near -6.5 eV and -10.5 eV. These features are due to sodium oxide valence states [228], indicating that the Na adsorbate, residing on top of the graphene layer, is oxidized upon O_2 exposure. After intercalation (as shown in Fig. 5.11c), no sodium oxide states are observed. This indicates that the adsorbate is protected under the graphene layer and is not able to oxidize. A very weak line at ca. -6.5 eV is visible in Fig. 5.11d that indicates trace amounts of sodium oxides formed from the very small fraction of remaining surface adsorbed Na atoms. With this oxidation study serving to validate the existence of two separate configurations of the Na/Gr/Ni(111) system (with the Na either being intercalated underneath Gr/Ni(111) of adsorbed on the surface), the transition from surface adsorbed Na to intercalated Na and its corresponding effects on the graphene band structure could be probed in detail.

5.6.2.2 Intercalation through Thermal Annealing

After initially dosing the clean Gr/Ni(111) surface (Fig 5.12a) with 0.8 ML Na, the π^* state was seen to be populated and shifted to below the Fermi level, as seen in Fig 5.12b. The π state maximum also moves closer to the Fermi level (indicated with the yellow arrow) from its initialy maximum of -2.8 eV and the slope is increased around the K-point, with a lowering of the π-to-π^* energy gap to $\sim$1.3 eV. Since n-doping should neither shift a populated state towards the Fermi

level nor change the state dispersion, these changes of the π state after Na adsorption cannot be explained as simply due to n-doping. Instead, we conclude that this lower energy gap is due to a lower coupling between graphene and the substrate after adsorption rather than only n-doping of the original π/π^* bands.

After initial adsorption, changes to the band structure could be seen upon Na intercalation via thermal annealing. The band gap was seen to reduce significantly after complete intercalation, as seen in Fig 5.12c. Validation that this state corresponds to complete Na intercalation was done through the oxidation studies presented in Sec. 5.6.2.1. The spectral intensity of the hybridized states clearly evident in Fig 5.12a is also strongly diminished after adsorption as seen in Fig. 5.12b, supporting the idea that the extent of Gr π/Ni 3d hybridization is reduced after adsorption. Panels (b1) and (b2) show spectra during this transition, with the progressively decreasing band gap attributed to an increasing number of Na atoms being intercalated underneath the graphene layer with a decreasing fraction still remaining on the surface.

5.6.2.3 DFT calculations and Bader Charge Analysis

In order to gain more insight into the observed graphene decoupling, DFT and Bader charge analysis studies were performed in collaboration with Manos Mavrikakis' group at University of Wisconsin. The specific computational details of this analysis can be found in Appendix A.5. Compared to the freestanding graphene case (Fig 5.13a), the dispersion of the Gr/Ni(111) π band near the $\overline{K}$-point is not linear (Fig 5.13b and Fig 5.7c shown for larger energy range), in agreement with the experimental ARPES spectra. The π^* state is also seen to be shifted above the Fermi level, as highlighted in red. Note that the energy window shown in Fig 5.13 was performed around the Fermi level down to 4 eV BE to more closely study the evolution of the π/π^* states upon Na adsorption and intercalation.

Figures 5.13c and 5.13d show calculated electronic structures of Gr/Ni(111) with Na on top and intercalated, respectively. The hybridized π^* state above the Fermi level and the remnants of the π state below the Fermi level are shifted down in energy after Na adsorption (Fig 5.13c). Due

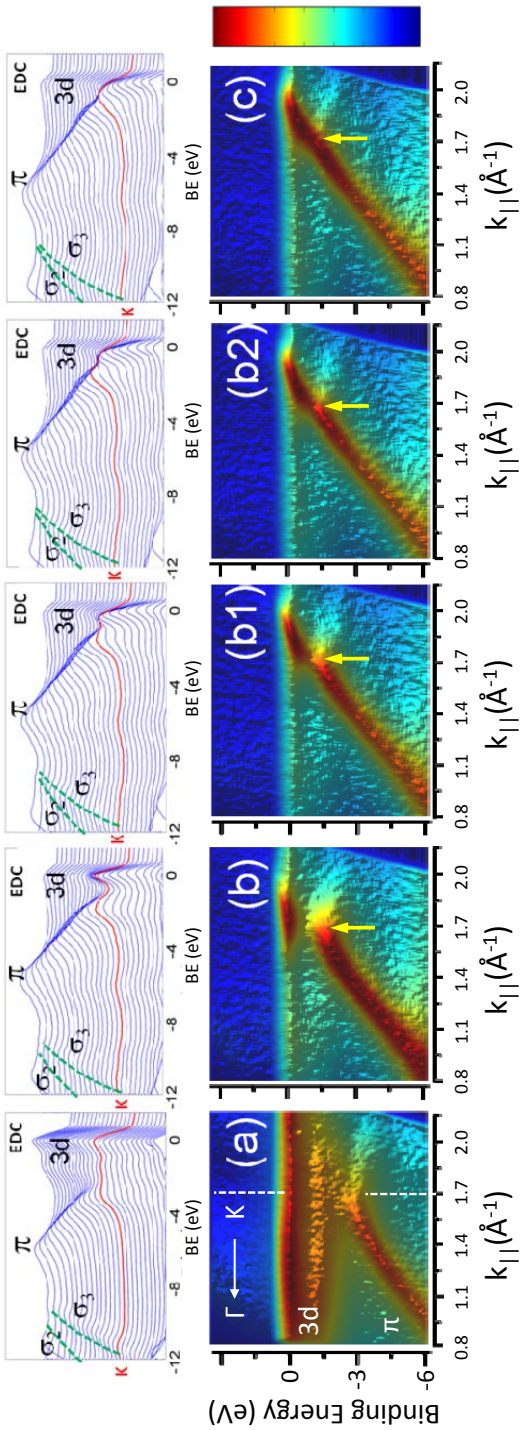

Figure 5.12: (a) Band structure of Gr/Ni(111), with the $\overline{K}$-point indicated with the vertical arrow. The insets above show the energy distribution curves (EDCs) near the $\overline{K}$-point ($\overline{K}$-point EDC is indicated in red) as a function of detection angle. (b) After adsorption of 0.8 ML Na on top Gr/Ni(111). The minimum of the π^* state is visible near the Fermi level. Yellow vertical arrows indicate the rough maximum of the π state, established from its turning point. (b1-b2) during intercalation of Na atoms, shown with an increasing fraction of intercalated to surface adsorbed Na (c) After annealing and full intercalation of Na to underneath graphene. Note nearly closed gap.

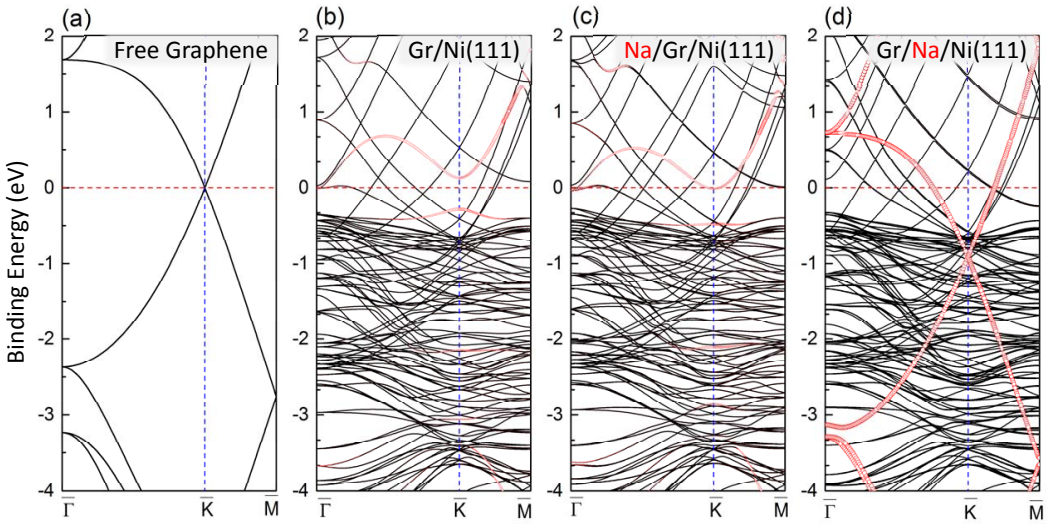

Figure 5.13: Band structures for (a) freestanding graphene, (b) Gr/Ni(111), (c) Na/Gr/Ni(111), and (d) Gr/Na/Ni(111), as calculated using a (2x2) supercell and 0.75 ML Na coverage. The contributions of graphene's $2p_z$ states are highlighted in red in panels (b)-(d).

to the Fermi level shifting upwards after adsorption due to the n-doping of the graphene, all other states in Fig 5.13c are seen to shift down in comparison with Fig 5.13b. The hybridized states below the Fermi level remain fixed after adsorption, which we link to screening effects associated with charge density rearrangements, leaving all dramatic effects to the band structure felt by the most valence of electronic states. After intercalation (Fig 5.13d), the Dirac cone is seen to be entirely restored, with the original n-doping of the graphene still present.

Bader charge analysis, showing the charge density difference initially and before/after adsorption (with the isosurface representation shown in Fig. 5.14), was performed to provide a more physical interpretation of the DFT and ARPES spectra presented above. Plots are shown for isosurfaces of $\pm 0.02e/\text{Å}^3$, with charge accumulation shown in red and depletion in blue. As discussed previously and shown schematically in Fig 5.6c, in Gr/Ni(111) the $2p_z$ orbital of graphene and Ni(111) $3d$ orbitals overlap at the substrate top-sites giving rise to a strong chemical bond. This leads to the charge density redistribution and strong accumulation region between the Carbon and top-most Ni layer, as shown in Fig 5.14a. Bader charge analysis shows these orbitals are

hybridized in the energetically most stable arrangement, leading to a net charge transfer of 0.10 e to graphene, with e being the elementary charge. This charge rearrangement in the initial system involves predominantly the $2p_z$ atomic orbitals as in-plane sp^2 orbitals are seen to not significantly hybridize.

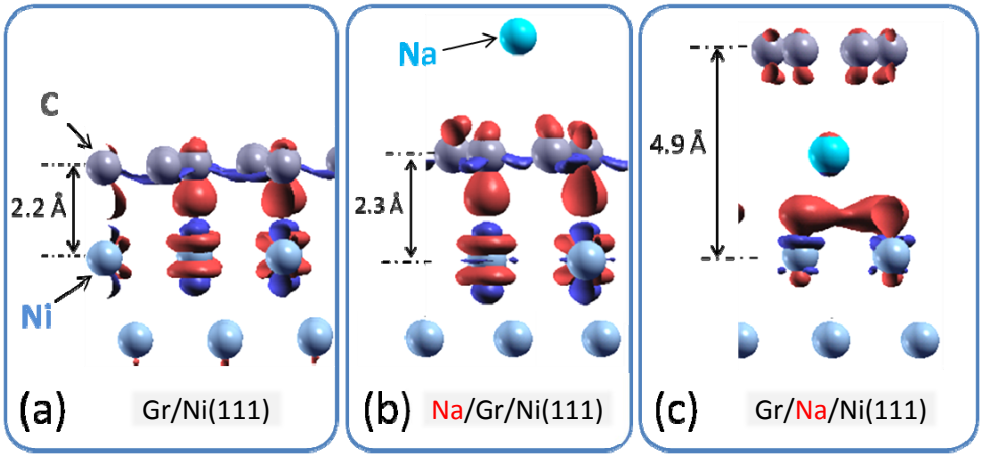

Figure 5.14: Charge density difference plots, for isosurfaces of ± 0.02 e/$\AA^3$ for (a) Gr/Ni(111), (b) Na/Gr/Ni(111), and (c) Gr/Na/Ni(111). Charge density accumulation is shown in red and depletion in blue. The adsorption energy of Na on Gr/Ni is -1.00 eV at a Na coverage of 1 ML, referenced to the total energies of atomic Na and Gr/Ni(111).

After adsorption, this charge distribution and its associated energetics shift dramatically due to the electrons supplied to graphene by Na (n-doping). The extent of hybridization between the C and Ni atomic orbitals is then lower after adsorption since graphene energetically favors receiving the charge from Na rather than sharing it with Ni(111). Bader charge analysis shows that Na adsorption supplies a net charge of 0.36 e per atom to graphene and no charge to the substrate. This causes an interfacial dipole that lifts graphene slightly off the substrate ($\sim 0.1\AA$ as shown in the isosurface plot in Fig 5.14b). Graphene is then seen to receive only 0.05 e per atom from the Ni substrate after adsorption, compared to its initial 0.10 e per atom. This indicates that the overlap of the Gr p_z/Ni $3d$ atomic orbitals is weaker. The consequence of this is that the structure of Gr/Ni(111) is slightly relaxed and the layer of graphene is lifted up to 2.30 Å above the substrate. Although more detailed energetics are more complex to model, it is clear that strong hybridization

is energetically less favorable when graphene is n-doped. Lower electronegativity (and therefore a higher charge transfer per atom) of adsorbates like K and Cs would yield even stronger decoupling, consistent with previous measurements on Gr/Ni(111) [202].

Analyzing the corresponding band structure in Fig. 5.13d and the isosurfaces presented in Fig. 5.14, we see the graphene is lifted up to 4.9 Å above the substrate, effectively cutting off any interaction with the substrate as no bonding can be supported over such a distance. The hybridization is blocked by an atomic spacer of Na and thus there is no energy gap at the $\overline{K}$-point. The remnant gap opening ($\leqq$ 100 meV) or the minor band back-bending seen in Fig. 5.12(c) is a result of superposition of regions with complete intercalated Na and regions where Na still remains on top. This is expected here due to the coverage of Na (0.8 ML) and possibly some bottlenecks in the intercalation paths.

5.6.3 Discussion and Conclusions

Our ARPES measurements in Sec 5.6.2.2 supported by the DFT calculation and Bader charge analysis in Sec 5.6.2.3 point to two unique configurations for the Na- Gr/Ni(111) system: surface adsorbed and intercalated Na. Previous studies, which observed lowering of the π-to-π^* energy gap to 1.3 eV after adsorption of Na (K, Cs) onto Gr/Ni(111) overlooked changes in the dispersion of π near the $\overline{K}$-point [149, 202]. The lowering of the energy gap was attributed to intercalation of Na (K, Cs) into graphene, although no proof of intercalation was shown. Other studies, under identical conditions, showed the intercalated ARPES spectrum with no gap at all [201]. By observing the transition of Na from surface adsorbed to intercalated with the electronic band structure constantly probed via ARPES, we are able to resolve these inconsistencies.

First, we observe a surface adsorbed Na configuration after deposition. We exclude intercalation as the origin of the band structure changes in Fig 5.12b through the oxidation studies presented in Sec 5.6.2.1, where O_2 exposure of the surface gave rise to photoemission lines from sodium oxides [228]. We also exclude that this state is due to Na intercalation at isolated areas causing patches of decoupled and still-coupled graphene since such decoupling has been shown to produce a super-

position of two π states, one from intercalated and one from non-intercalated areas [201]. Static Angle-resolved or angle-integrated X-Ray photoemission spectroscopy (XPS) using high energy photons to look at photoemission lines from deeply bound core levels has traditionally been used as a surface-sensitive gauge for coverage of surface adsorbates and overlayers. However, XPS measurements cannot confirm intercalation of Na into graphene since changes in the intensity of XPS lines from a monolayer of Na (K, Cs) adsorbed on graphene are often due to formation of thick islands of adsorbates on top rather than intercalation, making XPS intensity differences in the observed core level states difficult to interpret [223, 229, 230, 137]. We emphasize that this decoupling via surface adsorption involves notably different mechanisms than decoupling through intercalation of noble metals into Gr/Ni(111) [141, 190, 198, 201, 215, 216, 223, 229, 230, 231, 232, 233]. In the noble metal case, bulky atoms break down hybridization at the graphene-substrate interface, resulting in detaching graphene from the substrate and closing the energy gap between non-hybridized states at the K-point. When the adsorbate remains on the surface, it changes the energetics and induces relaxation of the bonding at the graphene-substrate interface. However, it does not "detach" graphene from the substrate by entirely eliminating the orbital hybridization.

Upon intercalation, we find that the energy gap is reduced to ≤ 100 meV and the Dirac cone is nearly restored. The Fermi velocity, which we can use as a gauge of the coupling to the substrate [227], is increased after intercalation towards the value of freestanding graphene ($\sim 1.6 \times 10^6 m/s$). Our ARPES experiments and DFT calculations show that intercalation of Na is nearly the same in its decoupling effectiveness as intercalation of noble metals, although strong n-doping is concurrent with this decoupling for the case with alkalis.

Although recent experiments have suggested that Na may intercalate spontaneously due to a low energy barrier [201], we do not observe spontaneous intercalation at room temperature. Instead, we find that intercalation is not possible unless the graphene layer contains defects or grain boundaries and unless the mobility of Na is increased by temperature. Our DFT calculations further support this observation. Although surface adsorbed Na is not the optimally stable configuration from the energetics standpoint, with the intercalated configuration being preferable, intercalation

is kinetically-limited without grain boundaries and defects. Performing similar intercalation studies as in Sec 5.6.2.2 on multiple Gr/Ni(111) samples grown under different conditions, we were able to achieve relatively good control over defect concentration in graphene by introducing oxide impurities into the Ni(111) substrate. Initiating graphene growth at lower temperatures was seen to produce impurities of amorphous carbon [196]. Under these conditions, when graphene showed relatively weak ARPES spectral features and a high background of secondary electrons (indicating poorer crystal quality resulting in electron scattering), intercalation was possible at lower temperatures. Intercalation into a higher quality graphene like that found in Sec 5.6.2.2 required elevated temperatures, with intercalation into the highest quality graphene needing temperatures close to the Na desorption threshold. These studies indicate the Na intercalation is highly morphology dependent.

In summary, we show two distinct configurations of surface adsorption and intercalation for Na deposited onto Gr/Ni(111). The presence of Na atoms on top of Gr/Ni(111) partially decouples graphene from the underlying substrate, as evident from a decrease of the π-to-π^* energy gap to 1.3 eV, while intercalation recovers the near-pristine graphene, dramatically reducing this energy gap. The ability to control the extent of this graphene-to-substrate coupling using a charge transfer from adsorbates, rather than intercalation, opens new possibilities in using optical excitations to control the electronic state of graphene. This technique might also allow for switching the graphene-to-substrate coupling in the spirit of previous work with alkali adsorbates on noble metal surfaces [234, 235, 236]. Potentially, a similar scheme can be applied to other graphene systems making it useful in novel devices.

Chapter 6

Band bending Studies on InGaAs/high-k/metal Gate Stacks

The revolutionary progress in the complementary metal-oxide-semiconductor (CMOS) integrated circuit (IC) industry over the last 40 years can largely be attributed to the industry's ability to satisfy three primary demands: high switching speed, low static power consumption, and a range of power, output and voltages in the device. [237, 238] The push for increased chip performance at a low cost has meant an increasingly larger density of devices on a printed IC wafer, with added benefits to performance as device size is scaled down [239]. This continued miniaturization of devices has kept a consistent pace of quadrupling the number of components on a chip every 3 years. From 1970 to 2010, the number of transistors per mm^2 on a high-production processor increased from 200 to over 1 million, the progress of which is shown in Fig 6.1 (right) [240]. The workhorse of this Ultra-Large Scale Integration (ULSI) IC industry has been the metal-oxide-semiconductor field effect transistor (MOSFET), serving as the basic "switch" component for more intricate circuits (a general illustration of which is shown Fig 6.1 (left)). The on/off capability of the device, meaning the number of mobile charge carriers in the conducting channel, is tuned through capacitive coupling (hence the "field effect") comprised of a metal gate, insulating oxide, and semiconducting bulk (enlarged inset) and is controlled by the voltage applied to the metal gate of the device. For a more general discussion of MOSFETs, the reader is referred to Ref. [241].

Thus far, the ability to scale these devices has been facilitated by the inherent beauty of the Si/SiO_2 system. Using doped Silicon as the semiconducting substrate, a native large-scale, defect-free SiO_2 layer is readily grown with a resistivity $> 10^{16}$ Ωcm [242]. This near perfect

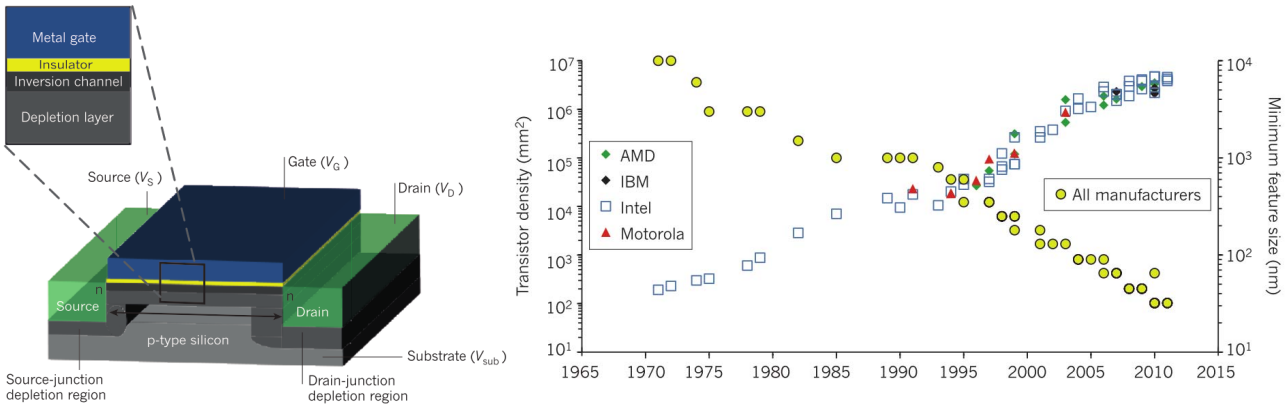

Figure 6.1: (left) Conventional layout of n-channel MOSFET. The "gate stack" comprised of a metal gate, insulator, inversion layer (with voltage bias applied to gate, V_G), and p-type semiconductor is shown enlarged. (right) Evolution of the minimum feature size on a ULSI IC processor over time. Adapted with permission from [240]

growth, and relatively defect-free subsequent SiO_2 growth, is crucial in giving a ideal interface whose defects would otherwise serve as scattering centers for charge carriers, inhibiting device performance. However, as device scaling has required the scaling down of both lateral and vertical dimensions [243] to produce comparable overall capacitance, the oxide thickness within this MOS "gate stack", has become so thin as to induce quantum mechanical issues in device performance. With gate oxide thickness approaching 1-2 nm (or only 3 - 4 *atomic layers* thick), electron tunneling through the oxide becomes considerable [244, 245] elemental diffusion from the neighboring layers becomes a problem [245, 246]. This leads to device degradation and large power consumption even when the device is in the off state. Threatening to lead to an "end of scaling" in MOS devices, this problem has been addressed with replacement of SiO_2 with high dielectric constant (high-κ) materials.

Modeling the gate stack as a parallel plate capacitor, the capacitance can be expressed as: $C = \kappa\epsilon_0 A/t$, where κ is the dielectric constant, A is the lateral area of the capacitor, ϵ_0 is vacuum permittivity, and t is the thickness of the oxide. A higher κ therefore is equivalent to a reduction in oxide thickness. Candidates such as Al_2O_3, ZrO_2, and HfO_2 (with κ of 10, 22, and 30, respectively compared to 3.9 for SiO_2 [245]) have emerged as possible replacements for this oxide

layer. Performance-inhibiting integration challenges with high-κ oxides, such as charge trapping at the high-κ/ semiconductor interface due to poor interface quality and fixed charge sites within the oxide [247, 30] have been successfully addressed through judicious material choice and processing techniques, and have now been integrated into commercial products.

Of increasing interest has been the replacement of the doped-Silicon semiconducting "base" with a higher electron mobility material, leading to higher injection current into the channel and faster device switching. III-V materials (formed from group III & V in the periodic table) have already been widely implemented in devices like bipolar transistors and photodetectors. These materials offer an improved electron mobility ten times that of silicon. It should be noted that its hole mobility is relatively low compared to other materials like Germanium, which have been greatly explored for use in pFET devices. However, incorporation of these materials, like $In_{0.53}Ga_{0.47}As$, has presented additional challenges when paired with high-κ oxides, with a defect-free III-V/high-κ interface being difficult to achieve due to oxide reformation during deposition [248] and a lower thermal processing budget needed to minimize elemental diffusion from the III-V material [249]. Trapped charge within the oxide, be it at the interface (border traps) or within the bulk (bulk traps), can greatly influence the overall performance and reliability of the resultant devices due to (1) it changing the electronic bands of the semiconductor (2) it acting as scattering centers for charge carriers and (3) the addition of electronic states within the band gap of the semiconductor that can serve as energetic traps for carriers.

Multiple techniques including the addition of interfacial layers between the III-V and high-κ [250, 251], activated plasma cleaning of the III-V surface [252, 253, 254], and forming gas annealing [255] have been employed to minimize these charge defects, generally being characterized by electrical measurements (C-V, I-V) of a resultant MOS capacitor (MOScap). While this characterization method (discussed in Section 6.1.2) is sensitive in detecting the overall density of interface charge traps (D_{it}) within the stack, it fails to capture how and when these defects form. Due to the high-temperature processing required to pattern these samples, it is inherently unable to probe the evolution of charge defects at subsequent stages of processing that would otherwise give insight

into its driving mechanisms. Additionally, this method becomes problematic in studying systems with large defect density, as may be the case with III-V systems.

In the following study, we investigate this overall charge state through directly probing the band bending at the InGaAs/high-κ interface. By employing a pump-probe photoelectron spectroscopy technique similar to those discussed in previous studies, we first probe changes in band bending at subsequent layer depositions to build the full InGaAs/high-κ/TiN stack. To simulate the effect of thermal processing, annealing studies were performed on InGaAs/high-κ and InGaAs/high-κ/TiN wafers to probe the change in the net charge state as one approaches the high temperatures required of device production. In this manner, insight into the creation and changes in the overall number of charged defects within the stack can be probed. The effect of a forming gas anneal was then studied on the TiN gated stacks to fully reproduce processing conditions. Band bending extracted from PES measurements were then directly compared to the V_{fb} from conventional C-V electrical measurements on an identical set of wafers subject to full MOScap patterning.

6.1 Technical Background

Unlike the bulk systems presented previously in this work, semiconductor multilayer system present several unique attributes in their electronic structure that are crucial in understanding the following studies. In an ideal MOS stack, energy bands of the semiconductor are bent down (p-type) or up (n-type) in response to the net dipole created due to (1) charge transfer from the metal into the semiconductor via Schottky transfer of electrons from dissimilar vacuum work functions ($\Phi_{metal} \neq \Phi_{semi}$) and (2) the presence of trapped charges within and at the interface of the oxide.

Shown in Fig 6.2 for a p-type semiconductor, these conduction (E_C) and valence (E_V) bands can be flattened using an applied external voltage to modify the E_F of the metal and modifying the overall dipole (blue arrow) within the stack. As depicted, these bands can also be further bent from depletion into inversion (red) with a bias of opposite sign. When the intrinsic level (E_I) crosses E_F, this opens a channel for minority carriers within the material (thus being able to conduct the majority carrier between the source and drain in a MOSFET). Through determining

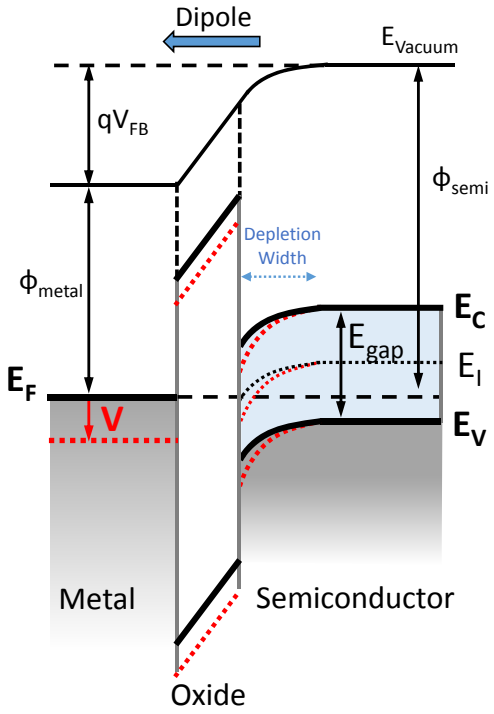

Figure 6.2: Band Diagram for p-type MOS capacitor at zero (black bands) and with applied bias V (red bands). E_C and E_V denote the energetic positions within the semiconductor of the conduction band and valence band, respectively, with E_I denoting the intrinsic level. Adapted with permission from [256]

the amount of voltage needed to flatten the electronic bands, the initial amount of band bending can be determined. In C-V electrical characterizations, this is accomplished through directly applying a bias to the metal and ramping the applied voltage. In the pump-probe photoemission technique, this is accomplished by canceling the initial dipole with freed charges. In the following sections, the experimental techniques of C-V/I-V characterization and band-flattening using pump-probe EUV photoemission will be outlined in more detail.

6.1.1 Band Flattening Technique

The net charge state of the sample was studied via directly probing the amount of band bending at the III-V interface. Using a pump/probe photoemission spectroscopy scheme outlined in Fig 6.3(a), with further details found in Ref [257, 258], the bands at the semiconductor/oxide

interface can be flattened completely. A representative photoemission spectrum under bent band conditions (black) within the semiconductor is shown in Fig 6.3(b), plotting photoemission yield as a function of binding energy in relation to the Fermi energy (E_F).

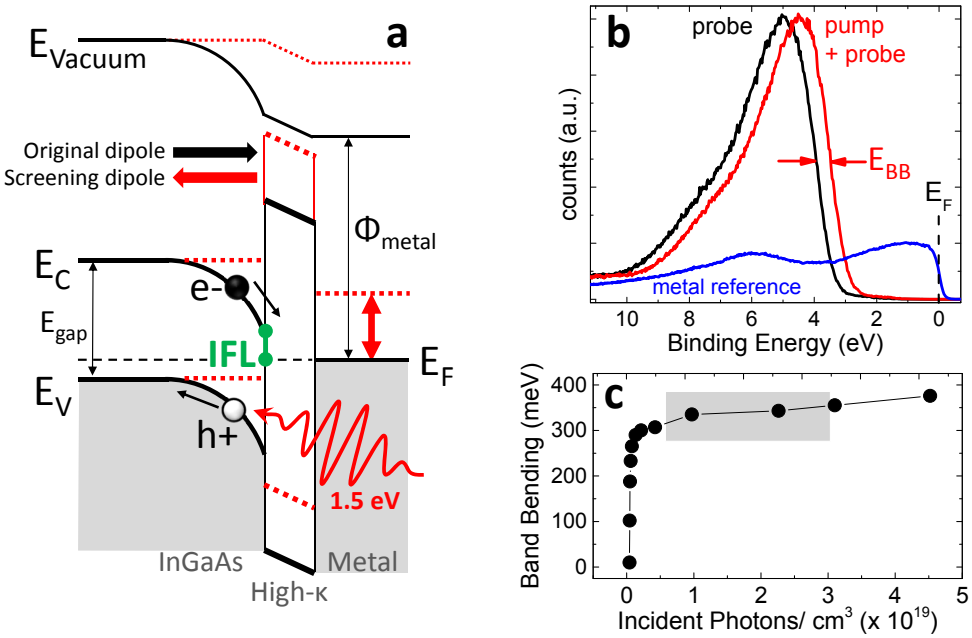

Figure 6.3: (a) Band diagram for $In_{0.53}Ga_{0.47}As$/ High-κ/ Metal Gate stack with band bending at the III-V/high-κ interface (black) and after band flattening due to screening of IR-generated electron-hole pairs (red). The Interfacial Fermi level (IFL) is shown in green denoting the Fermi level relative to the conduction band edge. (b) a typical photoemission spectrum showing the shift (denoted by red arrows, with energy E_{BB}) in the spectrum after band flattening. (c) shift in photoemission spectrum as a function of IR pump fluence

Due to good electrical contact of the sample with the surrounding system, the E_F of the sample was ensured to remain fixed to that of the system, as calibrated with an in-situ deposited Molybdenum film (blue). After excitation of the III-V substrate with an IR (1.5 eV) pulse, an electron-hole plasma is produced that rapidly rearranges to screen the original dipole field. The resultant flattening of the semiconductor bands, shown in red in Fig 6.3(a), results in a corresponding shift of the photoemission spectrum by the amount of band bending (Fig 6.3(b) red and red arrows). Confirmation that the bands were fully flattened was done through measuring this shift as a function of IR pump intensity (Fig 6.3(c)). Band bending measurements presented here were

performed in the fully flattened region (gray) where this shift is constant as a function of pump fluence.

6.1.2 C-V/I-V Characterizations

Capacitance-voltage measurements can provide a wide array of information about MOS capacitor stacks including oxide thickness, trapped charge, threshold voltage, density of interface traps, and flatband voltage (as we care about in our studies) [259]. In varying the applied voltage, the resultant capacitance of the system can be measured. In this configuration, a parallel plate capacitor is effectively formed with the metal gate, oxide, and the majority carriers within the semiconductor, as illustrated in Fig 6.4. Applying a DC bias using an AC signal, a range of frequencies are can be tested that are sensitive to difference capacitances within the system. Three regions of behavior are seen that have a frequency-dependent response: Accumulation, depletion, and inversion, with a flatband voltage (V_{FB}) demarcating accumulation into depletion and threshold voltage (V_{TH}) demarcating depletion into inversion.

In an ideal MOS structure, the system can be thought of as two capacitors in series, an oxide capacitance and a depletion layer capacitance within the semiconductor. In accumulation, there is no depletion layer and the effective capacitance is equal to the capacitance of the oxide ($C_{eff} = C_{ox}$). In depletion, the effective capacitance is the addition of the oxide capacitance and depletion layer capacitance in series ($C_{eff} = \frac{1}{1/C_{ox}+l_d/\epsilon_s}$ where l_d is the depletion layer width at the specific applied voltage and ϵ_s is the dielectric constant of the semiconductor). In inversion, two regimes exist due to the response of the system at low and high frequencies. At low frequencies, the effective capacitance is that of the oxide ($C_{eff} = C_{ox}$) due to charge being added/removed from the inversion layer. At high frequencies, the capacitance is similar to that in depletion, but with the maximum value of the depletion width.

In non-ideal structures, mobile charge, fixed charge defects, and the addition of surface energy states modify this C-V characterization. Due to the dependence of flatband voltage on position of charge from electrode, the changing position of *mobile* charge with time and voltage leads to

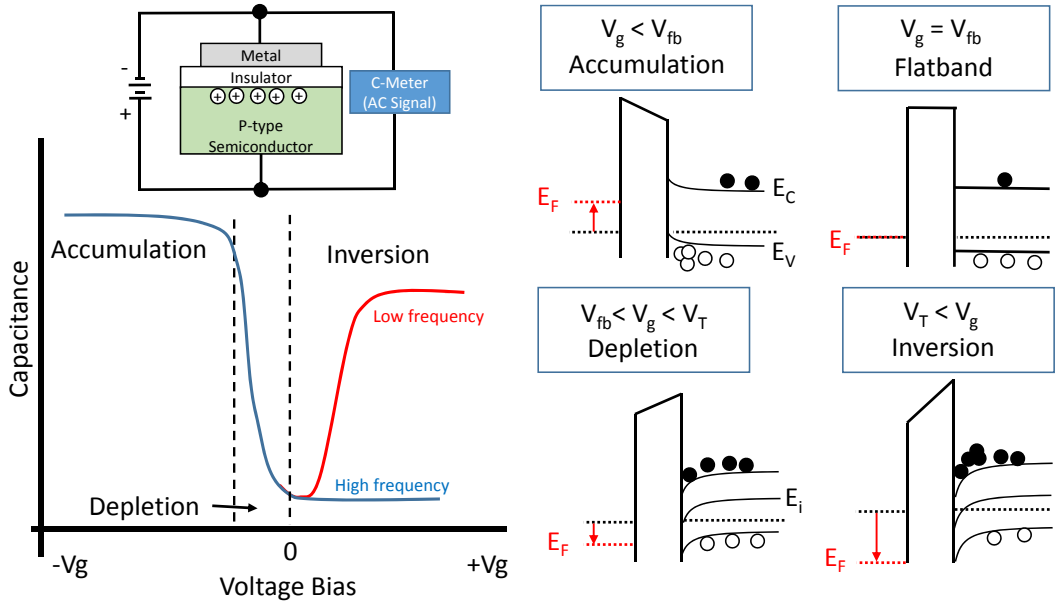

Figure 6.4: C-V measurement technique (with measurement circuit shown top) and corresponding band diagrams (right) under accumulation, flatband, depletion, and inversion. White and black points represent holes and electrons, respectively. Left panel adapted from [259].

capacitance shifts dependent on the sign of the charge and hysteresis changes. *Fixed* charge in the oxide shifts the measured curve along the voltage axis. This shift reduces linearly as the position of the charge relative to the gate is reduced (starting at metal-oxide interface). Fixed charge can be due to incorporation during deposition or formation during processing. The response of these charges and interface states is also frequency dependent. At high frequencies, the interface traps are not able to respond fast enough to the AC signal to be filled, making their contribution to the overall capacitance approach zero. The interface states only respond to the slowly changing DC bias and act as a fixed charge within the stack, stretching out the C-V curve along the horizontal axis [260]. At low frequencies, these charges are able to respond and give a "false inversion"-like behavior. For a more in depth discussion of trapped charge within III-V gate stacks, the reader is referred to Ref [261, 262, 263].

Common techniques to quantify the density of the interface states [249, 263] using values obtained from C-Vs have been highly debated in III-V systems due to the common, usually dramatic

frequency dispersion [264]. Frequency dispersion in accumulation has been attributed to border traps within the oxide [265]. These have been successfully modeled with trapped charges distributed through the bulk of the oxide [264] and via simultaneously taking into account the contribution of border and interface traps [261]. Ideally, the total amount of fixed charge in the system can be determined through comparing the calculated and measured V_{FB}.

6.2 Experimental Configuration

Experiments were conducted on an apparatus at the IBM Watson Research Center (Yorktown Heights, NY) using a similar experimental approach as the one outlined in Chapter 3 with several notable changes. The general layout is shown in Fig 6.5. The output of a 1 kHz Ti:Sapphire regenerative amplifier producing 35 fs pulses at 800 nm was focused into a Argon gas jet for high harmonic production. Individual harmonics were spectral selected by tuning the grazing incidence angle of a toroidal grating, focusing the pulses colinearly with the IR pump pulse onto the sample. For the studies presented here, band-bending measurements were carried out using the 17th harmonic (26.4 eV), with the 25th harmonic (38 eV) used to monitor changes In $4d$ and Ga $3d$ core level states that could indicate chemical shifts pointing to changes in In and Ga bonding.

Photoelectrons were then collected over an emission angle of $\pm 20^{\circ}$ using an electrostatic parabolic mirror and collimated into the μ-metal shielded, drift tube time-of-flight (TOF) detector with 64 anodes. Integrating over the entire collection angle is equivalent to averaging over the $k_{||}$ component of the band structure according to:

$$\Delta k_{||} = 0.512\sqrt{E_{kin}} cos(\theta)\Delta\theta \tag{6.1}$$

with $k_{||}$ in $\mathring{A}^{-1}$ and E_{kin} in eV. For the InGaAs studies using the 17th harmonic (26.3 eV) up to the 25th (38.7), this gives a $\Delta k_{||}$ range averaging over $\sim$0.9 and 1.1 $\mathring{A}^{-1}$, respectively. With the sample and chamber in good electrical contact, equilibrating the their Fermi levels, E_F was routinely verified (to account for triggering drift in the electronics) using a 15 nm thick *in-situ* deposited Molybdenum film.

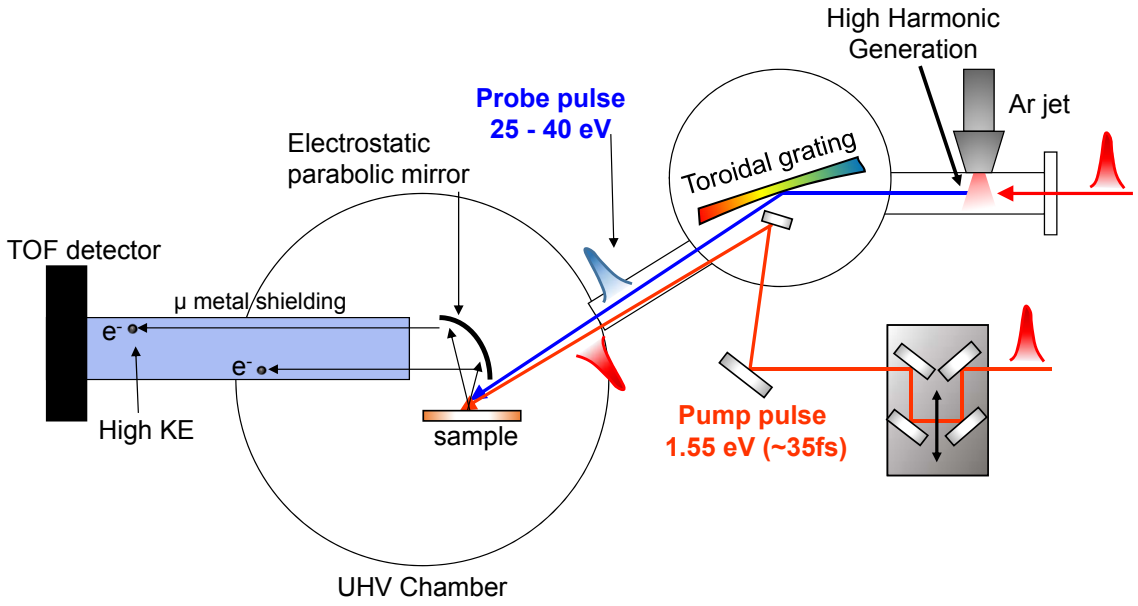

Figure 6.5: Experimental setup for band flattening studies. Notable differences from previous studies include the use of a gas jet for HHG and an angle-integrated time-of-flight detector. Adapted with permission from [266]

$In_{0.53}Ga_{0.47}As$ samples of $1\mu m$ thickness were prepared by MOCVD on InP(001) substrates with a nominal doping of $6 * 10^{16}/cm^2$ for both n-type (Si doped) and p-type (Zn doped). For the deposition-stage studies, new samples were simply removed after the high-κ growth process and after the metal gate deposition. A $(NH_4)_2S$-last *ex-situ* treatment was used to remove native oxides on the InGaAs surface and passivate the surface with sulfur. This was followed by air transfer to an atomic layer deposition (ALD) tool within a few minutes, and ALD growth of the high-k layer at 300 C. High-k thicknesses of 2 nm and 4 nm were grown of either Al_2O_3 or HfO_2 to have a direct comparison of thickness dependence and elemental oxide composition on the charge defect behavior. Thicknesses were verified with Rutherford backscattering spectrometry to be within 0.1 nm of the nominal value. With no additional surface preparation, 5 nm of TiN was then grown via Physical Vapor Deposition (PVD) at room temperature on top of the high-κ layer. All samples studied, including wafers undergoing patterning for MOScap samples, were batch-processed at each step to minimize potential variations due to any potential process drift

in the deposition tools. For deposition-stage studies, samples were characterized by pump-probe photoemission after the high-k growth process and after the metal gate deposition, respectively. Samples for C-V electrical characterization were then patterned into MOS capacitors, incorporating a high temperature ($>$ 400 C) forming gas (95% N_2 5% H_2) anneal shown to reduce D_{it} in previous electrical studies[255, 267].

6.3 Surface Cleaning Investigations on InGaAs using Activated Hydrogen

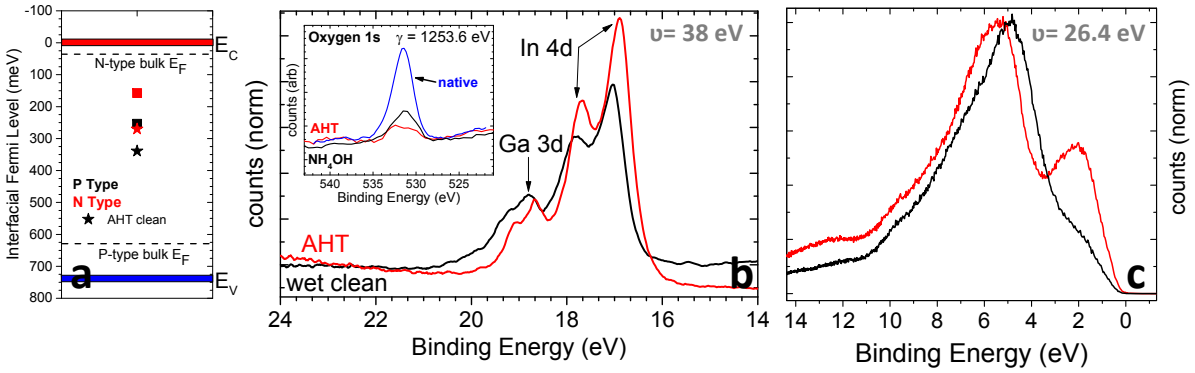

Figure 6.6: Core level peaks for In 4d and Ga 3d measured with PES comparing wet cleaned vs activated hydrogen cleaned surfaces. (inset) XPS spectra of the Oxygen 1s core level comparing native oxide (blue), wet cleaned (black) and activated hydrogen treatment (red)

Initial measurements on the NH_4OH/ $(NH_4)_2S$ treated InGaAs surface showed an IFL close to the conduction band edge for both n and p-type substrate (squares, Fig 6.6a), suggesting a positive (p-type)/ negative (n-type) surface charge possibly due to the presence of a residual surface oxide. To probe this further, activated hydrogen treatments (AHT) were performed *in situ* using H_2 gas cracked over a glowing Tungsten filament ($2 * 10^{-5}$ Torr, 30 min, 120 W) to determine whether this surface charge could be minimized. These treatments have been shown to efficiently remove oxidized In, Ga, and As species from the surface [268, 269]. Through X-Ray Photoemission spectroscopy (XPS) using a Mg K-α photon source (1253.6 eV), the intensity of the Oxygen 1s core level served as a gauge of residual oxide left on the InGaAs surface. Compared to the original native oxide (blue in Fig 6.6(b), inset), the NH_4OH treatment still left a residual surface oxide (black) compared to its

near total removal after a 30 min AHT clean (red). Looking also at the In 4d and Ga 3d levels using 38 eV photons, the wet clean treatment (black, Fig 6.6 c) shows peaks shifted to higher binding energy and broadened compared to the AHT cleaned (red). Both features are a clear indication of oxidized In and Ga species that are removed after treatment. After AHT cleaning, both the n and p-type IFLs were seen to move toward mid-gap, denoted with stars in Fig 6.6(a). This is consistent with a negative charge build up on the surface due to dangling bonds or residual contamination. Due to this inherent sensitivity of the bare InGaAs to surface contamination and treatment, scaling of band bending with high-κ thickness were instead used to deduce the nature of bulk and interface charges after high-k deposition.

6.4 Results and Discussion

6.4.1 Stack Deposition Studies

The effect of each deposited layer on band bending was probed through studying the InGaAs surface after high-κ ($In_{0.53}Ga_{0.47}As$ /high-κ) and subsequent TiN ($In_{0.53}Ga_{0.47}As$ /high-κ/TiN) deposition. Knowing the measured band bending, band gap, and valence band offset from the Fermi level in the bulk of the III-V, the position of the Fermi level at the III-V/high-κ interface could be determined. This Interfacial Fermi Level (IFL), shown in green in Fig 6.3(a), was calculated referenced to the conduction band according to: $E_{IFL} = (E_C - E_F) + E_{BB}$ for n-type and $E_{IFL} = E_{gap} - (E_F - E_V) - E_{BB}$ for p-type, where $(E_C - E_F) = 31$meV and $(E_F - E_V) = 113$ meV for the nominal substrate doping and E_{BB} is the total band bending as determined from PES measurements.

With the addition of the high-κ layer, both the Al_2O_3 and HfO_2 n-type samples show similar IFLs at 260 meV, as shown in Fig 6.7. The p-type samples demonstrate a larger variation, with the InGaAs/ HfO_2 being closer to the conduction band edge (220 meV) than Al_2O_3 (370 meV). InGaAs/high-κ samples of 4 nm thickness showed marked charging at the surface due to the photoemission process, giving uncorrectable shifts in the spectrum. As such, those results are

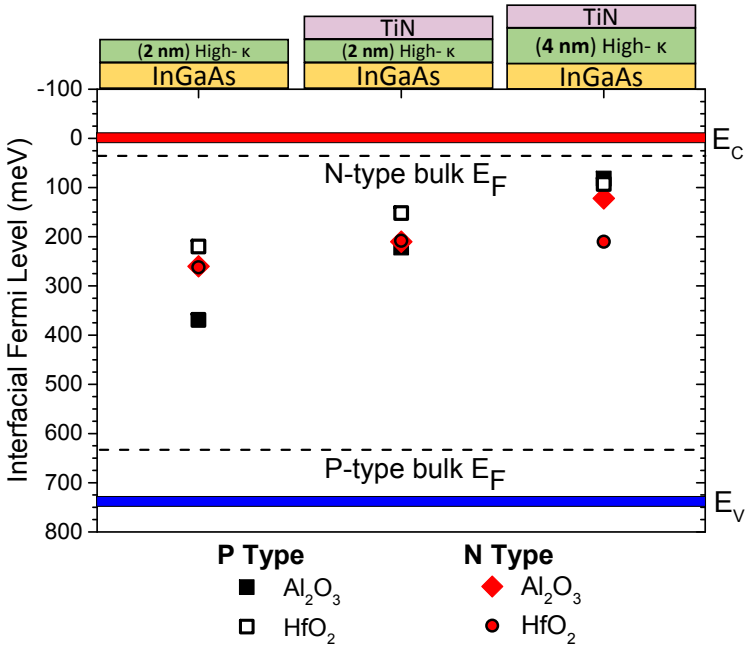

Figure 6.7: Measured interfacial Fermi level for n & p-type InGaAs/high-k and InGaAs/high-k/TiN of 2nm and 4nm high-κ thickness, shown for both Al_2O_3 and HfO_2. Interfacial Fermi level is shown referenced to the conduction band (red band), with the nominal band gap of 760 meV for InGaAs indicated.

not presented here. With the addition of the TiN layer, a systematic shift in IFLs for all samples was observed toward the conduction band edge. This can be understood in terms of the expected Schottky transfer of electrons from the lower work function TiN metal (Φ_p=4.5 eV) to the higher work function InGaAs upon deposition. The smaller change in the n-type samples (55 meV) compared to the p-type samples (70 meV for HfO_2 and 140 meV for Al_2O_3) is consistent with the smaller work function difference and, hence, less charge transfer upon deposition.

In comparing metal-gated stacks of different high-κ thicknesses, the sign of the trapped charge within the high-κ layer could be determined. With high-κ layer thicknesses of 2 nm versus 4 nm, both stacks with Al_2O_3 as well as the p-type HfO_2 shift further toward the conduction band. Some of this shift is anticipated with the thickening of the oxide, simply assuming a uniformly distributed bulk charge density. Accounting only for the change in thickness effect on the overall band bending, this would comprise a 12 meV and 8 meV shift toward E_C for p-type and n-type

Al_2O_3 stacks, respectively. Instead, a shift of 140 meV (p-type) and 85 meV (n-type) is seen. Similarly for HfO_2 stacks, due to its high dielectric constant, a < 5 meV shift is expected for the increased thickness. This is compared to the 60 meV shift measured for p-type, with a negligible shift actually measured in the n-type stack. Since the samples were deposited with identical TiN, the origin of this excess change to band bending must reside within the oxide. The increase in band bending for the p-type and corresponding decrease in the n-type stacks indicate a positive trapped charge. This is in agreement with electrical characterizations in previous work studying III-V/high-κ/metal gate stacks that found positive trapped charge within HfO_2 stacks [31] and positive bulk/ negative interfacial charge in Al_2O_3 stacks [270, 260].

6.4.2 Thermal Treatment of stacks

Knowing the positive nature of the trapped charge within the oxide, its stability and evolution could be probed as a function of thermal annealing to simulate processing conditions. Annealing was done using direct current heating for 5 seconds at each subsequent temperature, with PES measurements performed at room temperature. Several key aspects were seen in the behavior of the IFL with annealing temperature, shown in Fig 6.8. First, the non metal-gated Al_2O_3 samples (Fig 6.8a) demonstrated clear trends in both p and n-type stacks with the IFL showing a near linear dependence with increasing temperature. [1]

Two dominant regions of behavior are seen for the InGaAs/ high-κ/TiN stacks, denoted in white and gray background, with a more dramatic trend seen in Al_2O_3 stacks. In the low temperature region below 300-350C, IFLs for both 2 nm and 4 nm stacks move toward mid gap with increasing temperature. Due to the initial presence of positive charge within the oxide, this indicates a decrease in the magnitude of this charge. At higher temperatures above 350C, the IFL moved back toward the conduction band, indicating an increase in the magnitude of the positive charge within the oxide. The less dominant trend seen in HfO_2 stacks (Fig 6.8d) supports previous

[1] Due to the insulating nature of the high-κ layer, the as-received room temperature measurement (20 C) was sensitive to charges associated with adsorbed surface contamination like water and hydrocarbons. XPS verified a 200 C anneal was sufficient in removing the majority of carbon contamination from the surface, yielding accurate band bending measurements in the $>$ 200C region.

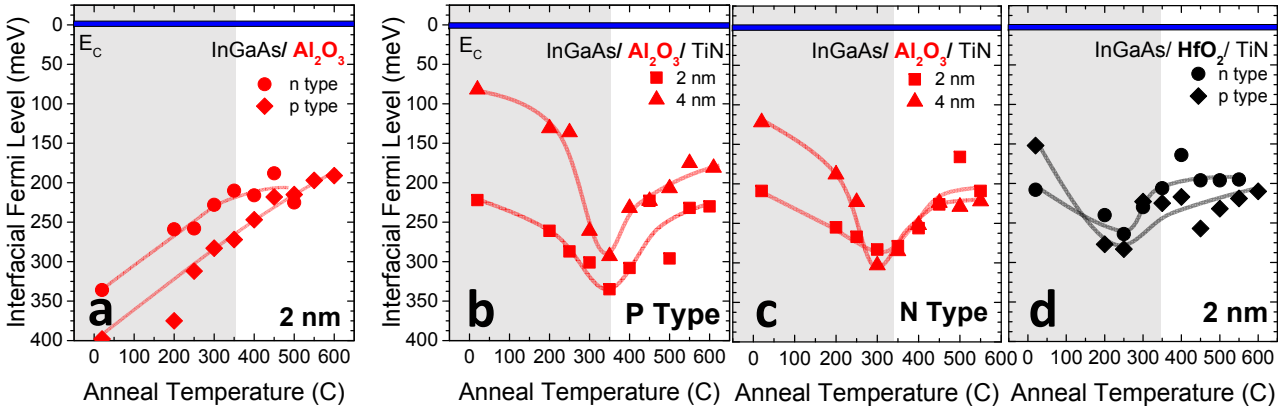

Figure 6.8: annealing temperature vs interfacial Fermi level plots for (a) non-metal gated InGaAs/ Al_2O_3, (b) p-type InGaAs/ Al_2O_3/TiN, (c) p-type/ Al_2O_3/TiN, and (d) InGaAs/HfO_2/TiN samples. Lines in plots a-d denote general trends in data. Marker size is indicative of experimental error.

studies that have found that HfO_2 grown directly onto III-V yields a non-pristine interface due to the regrowth of In, Ga, and As oxides during deposition, whereas Al_2O_3 growth has a "self-cleaning behavior of removing surface oxides on the InGaAs during deposition [248, 271]. The addition of interfacial layers have been suggested to produce lower defect HfO_2 stacks [251]. It is then to be expected that directly deposited HfO_2 on III-V materials would exhibit a more complex behavior with thermal annealing due to the varying breakdown and evolution of these different elemental oxides at the interface.

Certain observations can be made in comparing the annealing behavior of the non-metal gated InGaAs/ Al_2O_3 with the InGaAs/ Al_2O_3/TiN stacks. First, the high temperature ($>$ 350 C) behavior is common to both metal gated and non-metal gated stacks. Second, for the lower temperature ($<$ 350 C) region, the move toward mid-gap seen in the metal gated samples is unique. This suggests that the low temperature behavior in the metal-gated samples is due to the interaction of the deposited TiN layer with the high-κ oxide while the high temperature behavior is due to changes within either the high-κ layer or at the high-κ/III-V interface. The high-κ associated change at higher temperatures is anticipated since high-κ deposition occurs $\sim$350 C. This would mean that most high-κ defect changes within the lower temperature range would have already

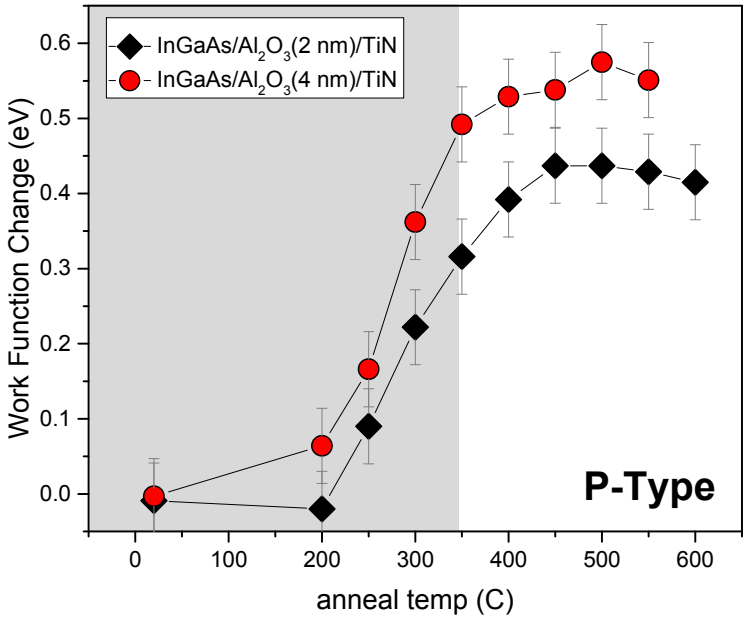

Figure 6.9: Change in vacuum work function (metal) during thermal annealing of TiN in $InGaAs/Al_2O_3/TiN$ stacks for 2nm and 4nm Al_2O_3 thicknesses.

taken place during deposition. Previous studies of HfO_2 on Si attributed a similar IFL behavior as due to positive oxygen vacancy generation within the bulk of the HfO_2 [31].

Associating the low temperature behavior with changes within or at the interface of the TiN, as concluded from Figure 6.8, is further supported with studying the change in work function of TiN as a function of thermal annealing, as determined in Figure 6.9. The vacuum work function was seen to increase dramatically in the lower temperature region (gray) and roughly stabilize at higher temperatures. In the case shown for p-type, this increase at lower temperatures would result in a decrease in the initial charge transfer from the TiN to the InGaAs to give a decrease in the overall band bending, walking the IFL away from the conduction band edge. This behavior is consistent with the IFL measurements presented in Fig 6.8. The increased change in work function for the thicker oxide also suggests a link to changes within the high-κ. A mechanism for this behavior would be the possible compositional change at the TiN/high-κ interface, with the oxidation of the TiN leading to an increased vacuum work function. TiN has also been shown to diffuse oxygen

[272, 273] and subsequently passivate oxygen vacancies within HfO_2 [274], which would also yield a decrease in overall positive charge with increasing temperature.

6.4.3 C-V/ I-V Characterizations

Measuring C-V and I-V characteristics on MOScap samples from clone wafers allowed for direct comparison of PES band bending measurements (V_{fb} for C-V traces) in the metal gated samples. C-V measurements were performed with a Agilent E4980A CV meter and a HP4145B parameter analyzer operating within the lower frequency range from 100 Hz- 100 kHz to probe the response of defects within the stack. The results for the n & p type stacks with 4 nm of Al_2O_3 or HfO_2 are shown in Figure 6.10. For the InGaAs/HfO_2/TiN samples, the p type demonstrated a large defect response with notably large hysteresis and a large frequency dispersion from 100 Hz to 100 kHz. This is consistent with previous studies on n-type samples [267] and with the photoemission measurements presented in Fig 3d, where the less pronounced behavior with annealing temperature points to a non-ideal high-κ/ InGaAs interface due to oxides. N-type HfO_2 stacks were seen to have less hysteresis and dispersion. We note, however, that large current leakage in n-type samples for both Al_2O_3 and HfO_2 prevented accurate capacitance measurement for frequencies lower than 10 kHz. InGaAs/Al_2O_3/TiN stacks demonstrated markedly less dispersion, consistent with previous studies [275], allowing for extraction of V_{fb} to compare with high temperature PES measurements.

Proper V_{fb} extraction method for III-V is debated [276], however, extracting corresponding voltage at the theoretically expected values for capacitance density (at our nominal doping) gives a reasonably good estimate of V_{fb}. The highest frequency C-V curves (100kHz) for n and p type Al_2O_3 were used in order to minimize the contribution to capacitance due to charge defects. Extracted V_{fb} for the calculated capacitance density values of 480pF/cm^2 for n-type and 580pF/cm^2 for p-type were seen to be 60 $\pm$ 50 and -540 $\pm$ meV, respectively. A large difference of 140 meV is seen in the p-type samples between the extracted V_{fb} and the PES band bending value of -400 $\pm$ 20 meV. This discrepancy was postulated as due to extra, thermally-significant processing steps performed on the MOScap samples that were not performed on the non-patterned PES samples,

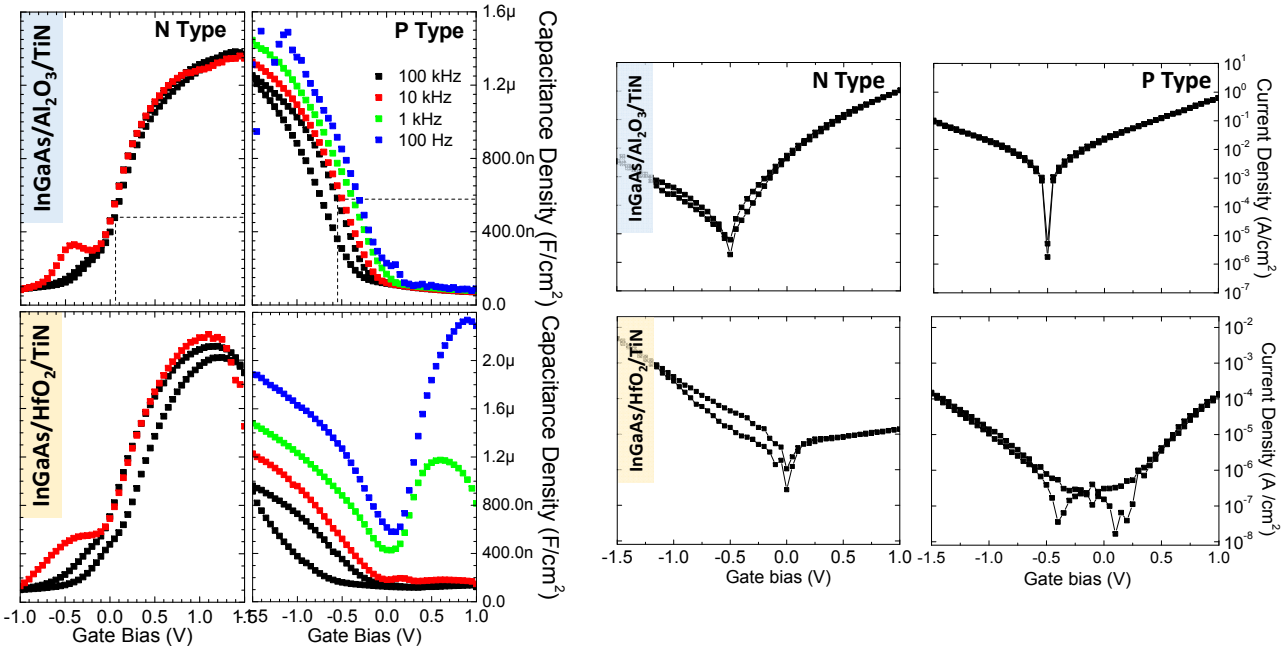

Figure 6.10: (left) C-V characterization for p-type and n-type InGaAs/4 nm high-κ/5nm TiN stacks with Al_2O_3 and HfO_2 measured at room temperature. Extracted V_{fb} values for Al_2O_3 samples are denoted with dashed lines. (right) corresponding I-V characterizations.

namely a high temperature ($>$ 400C) forming gas anneal. To test this, a forming gas anneal under identical conditions was performed on the p-type sample and the band bending remeasured with photoemission. With the p-type sample, the measured post-forming gas anneal value of 480 $\pm$ 20 meV was closer to the MOScap V_{fb} than pre-forming gas anneal, demonstrating agreement between the extracted V_{fb} in electrical characterization and PES measurements as long as all processing steps were replicated. The remaining discrepancy of 60 meV between PES and C-V measurements accounts for a defect density of only $3 * 10^{11}/cm^2$. Due to this increase in V_{fb} and positive charge known to be residing within the oxide, two possible scenarios can be occurring upon forming gas annealing. First, there could be an addition of positive charge to the stack due to creation of additional oxygen vacancies during the prolonged elevated temperature exposure of the oxide. Otherwise, hydrogen would need to passivate a negative charge residing within the stack. Recent theory [247] and electrical characterizations [270] of InGaAs/ Al_2O_3/TiN stacks have indicated a

possible positive charge within an Al-rich bulk portion of the oxide and a negative charge along an O-rich interface. Upon forming gas anneal then, hydrogen passivates dangling bonds and decreases negative charge along the interface. While either scenario is possible, additional studies on hydrogen passivation of defects [255] point to the latter as the most probable mechanism.

6.5 Conclusions

Our studies have identified three unique stages effecting a net *positive* charge within InGaAs/high-κ/TiN gate stacks, incorporating Al_2O_3 and HfO_2, after deposition and thermal treatment:

(1) Charge transfer upon metal deposition between the TiN and InGaAs due to dissimilar work functions.

(2) A low temperature region (< 350 C) decreasing net positive charge associated with changes at the TiN/high-κ interface.

(3) A high temperature region (> 350 C) increasing net positive charge associated with changes within the high-κ itself.

Furthermore, photoemission band bending measurements used to discern these behaviors show good agreement with conventional C-V measurements on identical wafers after similar processing.

Chapter 7

Future Outlook and Conclusions

Several of the experiments in this presented work can benefit from two milestones that have recently (within < 2 years) been realized in high harmonic generation: (1) high energy-resolution harmonics driven with 2ω light [14] and (2) the successful demonstration of circular harmonics [277]. The following sections outline the extension of presented experiments possible utilizing these techniques, followed by general conclusions of the work presented in this thesis.

7.1 Circular harmonic Generation

In the traditional description of laser–driven high harmonic generation, a circularly polarized driving field fails to produce harmonics due to the initially ionized electron never being able to trace a path to recollide with its parent ion. However, as theoretical descriptions [278, 50] and a recent experimental implementation [277] have shown, this restriction can be overcome by wave-mixing of two disparate driving frequencies. Driven with copropogating 400 nm and 800 nm light of opposite helicity, the resultant electric field component traces out a Lissajous curve, or trefoil shape, that produces three linear bursts of harmonics that rotate over one optical cycle (shown in Fig 7.1, left). Yielding a pulse train that contains alternating left circular polarization (LCP) and right-circular polarization (RCP) (shown in Fig 7.1 right), these effectively circular harmonics have been used in magnetic circular dichroism (MCD) measurements on Co [277] to demonstrate their potential for future material applications.

With the benefit of generating circularly polarized harmonics comes tremendous potential

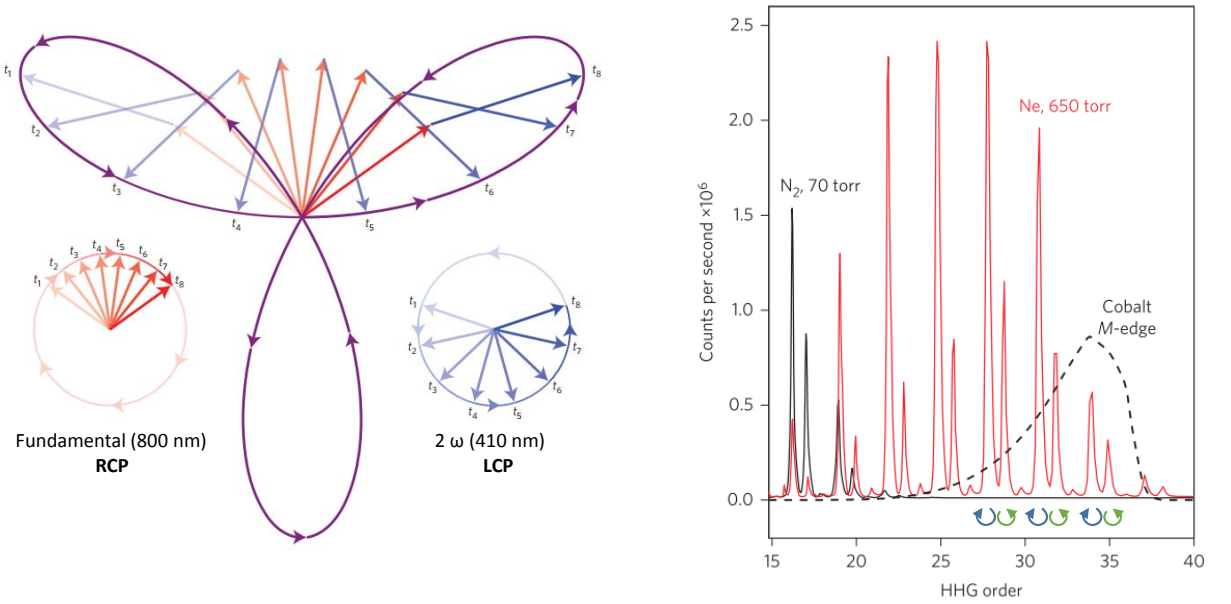

Figure 7.1: (left) Resultant net electric field with the addition of 800 nm and 410 nm opposite helicity driving light, explicitly shown at 8 different instances in time. Adapted with permission from [279]. (right) Circularly polarized harmonics generated with N_2 and Ne (with the Co M-edge shown for reference). Alternating harmonic polarizations of LCP and RCP are indicated in blue and green. Adapted with permission from [277].

in photoemission spectroscopy: time-resolved *spin-resolved* studies. In general, photoelectrons emitted with circularly polarized light have been seen to be nearly 100% spin polarized, owing to the spin polarization transfer from the photons to the electrons via spin-orbit interaction (see Ref [280] and references therein). With the desire to study spin-split ("spin polarized") electronic bands in magnetic and even non-magnetic materials [1] , two main approaches to date have been used to study spin-dependent photoelectron dynamics, either through circular polarized harmonics generated via a helical undulator [282] or using a spin-resolved photoelectron detector [283]. Spin-resolved ARPES studies on beamline generated circular harmonics have been used to selectively excite photoelectrons for quantum phase measurements in graphene (phase difference between the 2 sublattices) [284] and topological insulators (Berry's phase) [285]. Spin-resolved photoelectron detectors, selectively sorting up and down spins after photoemission of both, have been success-

[1] With splitting due to spin-orbit interaction via the Fano effect [281]

fully used to map spin-polarized band structures in materials [286, 287]. However, these systems are usually characterized by a lower throughput efficiency (and hence lower number of collected photoelectron events), making time-resolved material studies difficult. Spin-resolved studies have also mapped the transient valence band structure of Gd(0001) during a ultrafast demagnetization process [288], but the large exchange splitting of the bands made explicit spin-resolved detection not necessary.

7.1.1 RABITT studies on Cu(111)

In the RABITT measurements presented in Chapter 4, the interfering sidebands of the comb of generated harmonics allowed both the intrinsic chirp of the harmonics and quantum phase of the valence Cu(111) states to be measured. Following its original prescription to be used in characterizing the harmonic comb, a similar experiment can be conducted on Cu(111) to characterize the chirp and generation of the comb of circular harmonics. Investigations are already underway and have revealed relative phase delays between harmonics of opposite helicity.

In addition to characterization of the harmonics themselves, the presented studies revealing information on the electronic states of Cu(111) can be extended to other material systems. Of particular interest is the extension of the metallic valence band studies in Chapter 4 to include dielectric systems. With, for example, Xe adsorbed onto Cu(111), any screening effects contributing to the metallic Cu(111) dynamics can be minimized due to the near-unity dielectric constant. Preliminary work done on Xe overlayers on Mg(111) in the context of free-electron classical transport through the overlayer using attosecond streaking [100]. The electron interferometry technique employed here would allow for a more detailed study comparing the conduction band dynamics of the underlying Cu(111) surface with the Xe bands, provided the Xe adlayer was sufficiently thin to be able to simultaneously resolve bands from both materials.

7.1.2 Graphene

In the measurements presented on Graphene in Chapter 5, photoemission with linear polarized harmonics only allowed for the study of electron dynamics in Graphene/SiC(0001) and studies on the modification of graphene's electronic structure with the addition of alkali adsorbates. In using our linearly polarized harmonics, modeling the specific form of the transition matrix elements that would otherwise allow us to directly extract the phase, is made difficult by experimental intensity fluctuations and accounting for all final state effects [289]. By spin-selectively photoemitting electrons via circular harmonics, these issues can be minimized. Static spin-resolved ARPES measurements on Graphene using circularly polarized harmonics have been used to directly extract the Berry's phase of both mono and bilayer Graphene [284, 290], with good agreement to theory. Electron dynamics using linear harmonics have also been mapped in Graphene/SiC(0001) and Graphene/Ni(111), showing little deviation from similar measurements on graphitic systems.

To date however, these two studies have not been combined, where the tracking the spin-resolved electron dynamics of graphene have not been directly probed with ARPES. These types of studies would be able to inform on spin-dependent scattering processing such as Elliott-Yafet and Dyakonov-Perel mechanisms. Elliot-Yafet scattering refers to a "spin flip" mechanism mediated by scattering with impurities, defects, or phonons while Dyakonov-Perel scattering results in electrons feeling an effective magnetic field, that changes in direction upon each momentum-changing scattering event, resulting in random spin precession [291, 292]. These mechanisms act on different momentum scattering times [293], allowing one to determine the relative contributions to graphene's overall electron dynamics if probed on a sufficiently fast timescale. Indirect measurements [291, 294] have attempted to determine which spin scattering mechanism is dominant, with results suggesting a prominent Elliott-Yafet contribution. These dynamics would be directly accessible using circularly polarized harmonics in graphene photoemission studies. Furthermore, these studies could be extended to adsorbate modified graphene systems, like H-terminated "graphane", where the controlled addition of impurities and modification of graphene's electronic structure would influence

the dominant spin-scattering timescales [295].

7.1.3 Topological Insulators

In the same vein as the graphene system, topological insulators, whose band structures exhibit a similar Dirac cone feature to that of graphene, have attracted considerable interest for ARPES studies recently [296, 297, 298]. Previous time-resolved studies of have used circular polarized *pump* excitations to study exotic phenomena such as driven spin-polarized photocurrents [299], induced band gap opening [296], and temporally mapping the spin "texture" of the dirac cone [297]. Unlike graphene, the surface helical Dirac fermions (as measured over the Fermi surface) in topological insulators interact with phonons as well as electrons from the bulk reservoir [300, 298]. Attempts at disentangling these interactions by resolving these electron dynamics has been done via spin resolved reflectivity measurements [301] or a circularly polarized excitation [298]. With the addition of a circularly polarized *probe*, the spin topography of this band structure could be mapped more precisely over time.

7.1.4 Surface-Adsorbate Systems

Additionally, studies have even seen spin-dependent charge transport for surface-adsorbate systems like Ar adsorbed onto Fe(110), Co(0001), and Ni(111) [302]. These studies found a faster charge transfer for minority electrons in the Fe and Co systems, with little difference in the Ni system. With the transfer time difference attributed to the relative abundance of empty electronic states in the material, similar studies can be performed to directly probe the spin state of the system over the course of the ultrafast (2-3 fs) charge transfer. Similar dynamical studies on spin-resolved relaxation can be used to study the substrate-induced polarization of adatoms [303] and spin-polarized auger electron processes [282]

7.2 Time-resolved High energy-resolution Studies

With the implementation of narrow energy-bandwidth (< 150 meV), high photon energy (21 [14] - 60 eV [73]) harmonics, previous limitations for choosing experimental systems with widely-separated band structure features are greatly lifted. With these narrow harmonics measured to have a pulse length of 20 fs, this also gives enough temporal resolution to capture all but the fastest of electron dynamics.

7.2.1 Directly resolving interface states in InGaAs

Of particular interest, is directly resolving the dynamics of defect interface states in InGaAs. In the studies presented in Chapter 6, the number of charged defects in a MOS stack are quantified as they evolve with addition of deposited layers and annealing temperature. One remaining piece of this puzzle is the nature of the electronic interface states themselves: What is the density of trap states in the InGaAs band gap? It there a dominant interface state? What is the timescale in which these defect states fill and empty with carriers? A dominant interface state could contribute to "pinning" the Fermi level in InGaAs [304, 305], a concern in being able to tune the electronic bands with an applied bias and calling into question its viability for use in MOSFET devices. Direct evidence for these interface states have been seen in Inverse photoemission studies on GaAs [306] and electron microscopy [307], but the exact occupation and density of states is seen to vary greatly with surface preparation and interface quality [308]. Probing the distribution and dynamics of these narrow bandwidth states upon carrier relaxation can therefore help in mapping the dominant scattering mechanisms and timescales that are important for understanding electronic device performance.

Similar to the studies proposed in Section 7.1.2, GaAs has also been seen to exhibit a photo-induced spin Hall effect, where spin-oriented optically excited surface electrons diffuse into the bulk via spin-dependent scattering [309, 299]. The relaxation dynamics of these electrons has been measured through time-resolved Faraday rotation [310] to be exceptionally long (10-100 ns) due to

lack of spin-orbit coupling in its conduction band. The dominant mechanism in this spin scattering band has been suggested to be temperature dependent as well, with Dyakonov-Perel transitioning to Elliott-Yafet at low temperatures [311]. As such, a temperature dependent, spin-resolved study of carrier dynamics in GaAs and III-V family materials will be useful in determining the relative contributions of these processes to carrier relaxation.

7.3 Conclusion

This thesis employed high-harmonic driven ARPES to measure electronic properties of materials from metallic surfaces to post-silicon technologies like Graphene and III-V structures. The experimental implementations utilized range from the conventional pump-probe scheme for time-resolved carrier dynamics studies, to attosecond spectroscopy and photovoltage band flattening techniques to measure fundamental electronic state phases and device-inhibiting charge defects. These results serve as a springboard for further study utilizing the recently developed techniques of narrow energy-bandwidth and circularly polarized high harmonics.

Bibliography

[1] H. Petek and S. Ogawa, "FEMTOSECOND TIME-RESOLVED PHOTOEMISSION STUDIES OF ELECTRON DYNAMICS IN METALS," Progress in Surface Science, vol. 56, no. 4, pp. 239–310, 1997.

[2] J. C. Miller and R. F. Haglund Laser Ablation and Desorption, no. Academic Press, Boston, 1997.

[3] E. Beaurepaire, J.-C. Merle, a. Daunois, and J.-Y. Bigot, "Ultrafast Spin Dynamics in Ferromagnetic Nickel," Physical Review Letters, vol. 76, pp. 4250–4253, May 1996.

[4] R. Cavanagh, D. King, J. Stephenson, and T. Heinz, "Dynamics of Nonthermal Reactions : Femtosecond Surface Chemistry," J. Phys. Chem, vol. 97, pp. 786–798, 1993.

[5] N. Aschroft and N. Mermin Solid State Physics, no. Holt, Rinehart, Winston, Hong Kong, 1987.

[6] T. Haarlammert and H. Zacharias, "Application of high harmonic radiation in surface science," Current Opinion in Solid State and Materials Science, vol. 13, pp. 13–27, Feb. 2009.

[7] R. Tobin, "VIBRATIONAL LINEWIDTHS OF ADSORBED MOLECULES: EXPERIMENTAL CONSIDERATIONS AND RESULTS," Surface Science, vol. 183, pp. 226–250, 1987.

[8] M. Bonn, S. Funk, C. Hess, D. Denzler, C. Stampfl, M. Scheffler, M. Wolf, and G. Ertl, "Phonon- Versus Electron-Mediated Desorption and Oxidation of CO on," Science, vol. 285, no. August, pp. 1042–1045, 1999.

[9] K. Zhao, Q. Zhang, M. Chini, Y. Wu, X. Wang, and Z. Chang, "Tailoring a 67 attosecond pulse through advantageous phase-mismatch," Optics L, vol. 37, no. 18, pp. 3891–3893, 2012.

[10] M. Chini, B. Zhao, H. Wang, Y. Cheng, S. X. Hu, and Z. Chang, "Subcycle ac Stark Shift of Helium Excited States Probed with Isolated Attosecond Pulses," Physical Review Letters, vol. 109, p. 073601, Aug. 2012.

[11] C. Spielmann, N. H. Burnett, S. Sartania, R. Koppitsch, C. Kan, M. Lenzner, P. Wobrauschek, and F. Krausz, "Generation of Coherent X-rays in the Water Window Using 5-Femtosecond Laser Pulses," Science, vol. 278, no. October, 1997.

[12] T. Popmintchev, M.-c. Chen, D. Popmintchev, P. Arpin, S. Brown, S. Ali, G. Andriukaitis, T. Bal, O. D. Mücke, A. Pugzlys, A. Baltu, B. Shim, S. E. Schrauth, A. Gaeta, C. Hernández-garcía, L. Plaja, A. Becker, A. Jaron-becker, M. M. Murnane, and H. C. Kapteyn, "Bright Coherent Ultrahigh Harmonics in the keV X-ray Regime from Mid-Infrared Femtosecond Lasers," Science, vol. 336, pp. 1287–1291, 2012.

[13] S. Mathias, L. Miaja-Avila, M. M. Murnane, H. Kapteyn, M. Aeschlimann, and M. Bauer, "Angle-resolved photoemission spectroscopy with a femtosecond high harmonic light source using a two-dimensional imaging electron analyzer.," The Review of scientific instruments, vol. 78, p. 083105, Aug. 2007.

[14] S. Eich, a. Stange, a.V. Carr, J. Urbancic, T. Popmintchev, M. Wiesenmayer, K. Jansen, a. Ruffing, S. Jakobs, T. Rohwer, S. Hellmann, C. Chen, P. Matyba, L. Kipp, K. Rossnagel, M. Bauer, M. Murnane, H. Kapteyn, S. Mathias, and M. Aeschlimann, "Time- and angle-resolved photoemission spectroscopy with optimized high-harmonic pulses using frequency-doubled Ti:Sapphire lasers," Journal of Electron Spectroscopy and Related Phenomena, vol. 195, pp. 231–236, Aug. 2014.

[15] R. Haight, J. a. Silberman, and M. I. Lilie, "Novel system for picosecond photoemission spectroscopy," Review of Scientific Instruments, vol. 59, no. 9, p. 1941, 1988.

[16] M. Bauer, C. Lei, K. Read, R. Tobey, J. Gland, M. Murnane, and H. Kapteyn, "Direct Observation of Surface Chemistry Using Ultrafast Soft-X-Ray Pulses," Physical Review Letters, vol. 87, p. 025501, June 2001.

[17] T. Rohwer, S. Hellmann, M. Wiesenmayer, C. Sohrt, A. Stange, B. Slomski, A. Carr, Y. Liu, L. M. Avila, M. Kalläne, S. Mathias, L. Kipp, K. Rossnagel, and M. Bauer, "Collapse of long-range charge order tracked by time-resolved photoemission at high momenta," Nature, vol. 471, pp. 490–493, Mar. 2011.

[18] A. Melzer, D. Kampa, J. Wang, and T. Fauster, "Time-resolved photoemission at the Si(100)-Ga surface using a femtosecond higher-harmonic laser source," Physical Review B, vol. 80, p. 205424, Nov. 2009.

[19] R. Jiang, D. Mou, Y. Wu, L. Huang, C. D. McMillen, J. Kolis, H. G. Giesber, J. J. Egan, and A. Kaminski, "Tunable vacuum ultraviolet laser based spectrometer for angle resolved photoemission spectroscopy.," The Review of scientific instruments, vol. 85, p. 033902, Mar. 2014.

[20] L. Perfetti, P. a. Loukakos, M. Lisowski, U. Bovensiepen, H. Eisaki, and M. Wolf, "Ultrafast Electron Relaxation in Superconducting Bi_{2}Sr_{2}CaCu_{2}O_{8+δ} by Time-Resolved Photoelectron Spectroscopy," Physical Review Letters, vol. 99, p. 197001, Nov. 2007.

[21] W. Ackermann, G. Asova, V. Ayvazyan, a. Azima, N. Baboi, J. Bähr, V. Balandin, B. Beutner, a. Brandt, a. Bolzmann, R. Brinkmann, O. I. Brovko, M. Castellano, P. Castro, L. Catani, E. Chiadroni, S. Choroba, a. Cianchi, J. T. Costello, D. Cubaynes, J. Dardis, W. Decking, H. Delsim-Hashemi, a. Delserieys, G. Di Pirro, M. Dohlus, S. Düsterer, a. Eckhardt, H. T. Edwards, B. Faatz, J. Feldhaus, K. Flöttmann, J. Frisch, L. Fröhlich, T. Garvey, U. Gensch, C. Gerth, M. Görler, N. Golubeva, H.-J. Grabosch, M. Grecki, O. Grimm, K. Hacker, U. Hahn, J. H. Han, K. Honkavaara, T. Hott, M. Hüning, Y. Ivanisenko, E. Jaeschke,

W. Jalmuzna, T. Jezynski, R. Kammering, V. Katalev, K. Kavanagh, E. T. Kennedy, S. Khodyachykh, K. Klose, V. Kocharyan, M. Körfer, M. Kollewe, W. Koprek, S. Korepanov, D. Kostin, M. Krassilnikov, G. Kube, M. Kuhlmann, C. L. S. Lewis, L. Lilje, T. Limberg, D. Lipka, F. Löhl, H. Luna, M. Luong, M. Martins, M. Meyer, P. Michelato, V. Miltchev, W. D. Möller, L. Monaco, W. F. O. Müller, O. Napieralski, O. Napoly, P. Nicolosi, D. Nölle, T. Nuñez, a. Oppelt, C. Pagani, R. Paparella, N. Pchalek, J. Pedregosa-Gutierrez, B. Petersen, B. Petrosyan, G. Petrosyan, L. Petrosyan, J. Pflüger, E. Plönjes, L. Poletto, K. Pozniak, E. Prat, D. Proch, P. Pucyk, P. Radcliffe, H. Redlin, K. Rehlich, M. Richter, M. Roehrs, J. Roensch, R. Romaniuk, M. Ross, J. Rossbach, V. Rybnikov, M. Sachwitz, E. L. Saldin, W. Sandner, H. Schlarb, B. Schmidt, M. Schmitz, P. Schmüser, J. R. Schneider, E. a. Schneidmiller, S. Schnepp, S. Schreiber, M. Seidel, D. Sertore, a. V. Shabunov, C. Simon, S. Simrock, E. Sombrowski, a. a. Sorokin, P. Spanknebel, R. Spesyvtsev, L. Staykov, B. Steffen, F. Stephan, F. Stulle, H. Thom, K. Tiedtke, M. Tischer, S. Toleikis, R. Treusch, D. Trines, I. Tsakov, E. Vogel, T. Weiland, H. Weise, M. Wellhöfer, M. Wendt, I. Will, a. Winter, K. Wittenburg, W. Wurth, P. Yeates, M. V. Yurkov, I. Zagorodnov, and K. Zapfe, "Operation of a free-electron laser from the extreme ultraviolet to the water window," Nature Photonics, vol. 1, pp. 336–342, June 2007.

[22] S. Hellmann, M. Beye, C. Sohrt, T. Rohwer, F. Sorgenfrei, H. Redlin, M. Kalläne, M. Marczynski-Bühlow, F. Hennies, M. Bauer, a. Föhlisch, L. Kipp, W. Wurth, and K. Rossnagel, "Ultrafast Melting of a Charge-Density Wave in the Mott Insulator 1T-TaS_{2}," Physical Review Letters, vol. 105, p. 187401, Oct. 2010.

[23] M. Dell'Angela, T. Anniyev, M. Beye, R. Coffee, J. Gladh, T. Katayama, S. Kaya, O. Krupin, J. Larue, D. Nordlund, H. Ogasawara, L. G. M. Pettersson, W. F. Schlotter, J. A. Sellberg, F. Sorgenfrei, J. J. Turner, M. Wolf, W. Wurth, and A. Nilsson, "Real-Time Observation of Surface Bond Breaking with an X-ray Laser," Science, vol. 959, no. March, pp. 1302–1306, 2013.

[24] M. Drescher, M. Hentschel, R. Kienberger, M. Uiberacker, V. Yakovlev, a. Scrinzi, T. Westerwalbesloh, U. Kleineberg, U. Heinzmann, and F. Krausz, "Time-resolved atomic inner-shell spectroscopy.," Nature, vol. 419, pp. 803–7, Oct. 2002.

[25] B. Goldstein and D. Szostak, "SURFACE PHOTOVOLTAGE, BAND-BENDING AND SURFACE STATES ON aSi:H*," Surface Science, vol. 99, pp. 235–258, 1980.

[26] L. Kronik and Y. Shapira, "Surface photovoltage phenomena : theory , experiment , and applications," Surface Science Reports, vol. 37, pp. 1–206, 1999.

[27] C. Marchiori, M. El Kazzi, L. Czornomaz, D. Pierucci, M. Silly, F. Sirotti, S. Abel, E. Uccelli, M. Sousa, and J. Fompeyrine, "Nanoscale physics and defect state chemistry at amorphous-Si/In 0.53 Ga 0.47 As interfaces," Journal of Physics D: Applied Physics, vol. 47, p. 055101, Feb. 2014.

[28] J. Demuth, W. Thompson, N. DiBardo, and R. Imbihl, "Photoemission-Based Photovoltage Probe of Semiconductor Surface and Interface Electronic Structure," Physical Review Letters, vol. 56, no. 13, pp. 1408–1411, 1986.

[29] W. Widdra, D. Bröcker, T. Gieß el, I. Hertel, W. Krüger, a. Liero, F. Noack, V. Petrov, D. Pop, P. Schmidt, R. Weber, I. Will, and B. Winter, "Time-resolved core level photoemis-

sion: surface photovoltage dynamics of the SiO2/Si(100) interface," Surface Science, vol. 543, pp. 87–94, Oct. 2003.

[30] H. Arimura, R. Haight, S. L. Brown, A. Kellock, A. Callegari, M. Copel, H. Watanabe, V. Narayanan, and T. Ando, "Temperature-dependent La- and Al-induced dipole behavior monitored by femtosecond pump/probe photoelectron spectroscopy," Applied Physics Letters, vol. 96, no. 13, p. 132902, 2010.

[31] D. Lim, R. Haight, M. Copel, and E. Cartier, "Oxygen defects and Fermi level location in metal-hafnium oxide-silicon structures," Applied Physics Letters, vol. 87, no. 7, p. 072902, 2005.

[32] H. P. Bonzel and C. H. Kleint, "On the history of photoemission," Progress in Surface Science, vol. 49, no. 2, pp. 107–153, 1995.

[33] M. Helander, M. Greiner, Z. Wang, and Z. Lu, "Pitfalls in measuring work function using photoelectron spectroscopy," Applied Surface Science, vol. 256, pp. 2602–2605, Feb. 2010.

[34] J. Sitte, "Relation between reference levels, work functions, and contact potential difference in photoelectron spectroscopy," Chemical Physics Letters, vol. 42, no. 1, pp. 131–132, 1976.

[35] A. Damascelli, Z. Hussain, and Z.-X. Shen, "Angle-resolved photoemission studies of the cuprate superconductors," Reviews of Modern Physics, vol. 75, no. April, 2003.

[36] S. Hufner Photoemission Spectroscopy: Principles and Applications, no. 3rd Ed, Springer, 2010.

[37] P. Feibelman and D. Eastman, "Photoemission spectroscopy Correspondence between quantum theory and experimental phenomenology," Physical Review B, vol. 10, no. 12, 1974.

[38] A. Mcpherson, G. Gibson, H. Jara, U. Johann, T. S. Luk, I. A. Mcintyre, K. Boyer, and C. K. Rhodes, "Studies of multiphoton production of vacuum-ultraviolet radiation in the rare gases," Journal of Optical Society of America B, vol. 4, no. 4, pp. 595–601, 1987.

[39] Durfee, A. Rundquist, S. Backus, Z. Chang, C. Herne, H. Kapteyn, and M. Murnane, "Guided wave phase matching of ultrashort pulse light," Journal of Nonlinear Optical Physics and Materials, vol. 8, no. 2, pp. 211–234, 1999.

[40] T. Pfeifer, C. Spielmann, and G. Gerber, "Femtosecond x-ray science," Reports on Progress in Physics, vol. 69, pp. 443–505, Feb. 2006.

[41] J. J. Rocca, "Table-top soft x-ray lasers," Review of Scientific Instruments, vol. 70, no. 10, p. 3799, 1999.

[42] M. Lewenstein, P. Balcou, M. Y. Ivanov, A. L. Huillier, and P. Corkum, "Theory of high-harmonic generation by low-frequency laser fields," Physical Review A, vol. 49, no. 3, 1994.

[43] P. Corkum, "Plasma Perspective on Strong-Field Multiphoton Ionization," Physical review letters, vol. 71, no. 13, pp. 1994–1997, 1993.

[44] S. K. J. Kulander K C and K. J. L, "Dynamics of short-pulse excitation, ionization and harmonic conversion," Proc. Work-shop on Super-Intense Laser Atom Physics (SILAP) III, 1993.

[45] T. Donnelly, T. Ditmire, K. Neuman, M. Perry, and R. Falcone, "High-Order Harmonic Generation in Atom Clusters," Physical Review Letters, vol. 76, pp. 2472–2475, Apr. 1996.

[46] J. Itatani, J. Levesque, D. Zeidler, H. Niikura, H. Pepin, J. C. Kieffer, P. B. Corkum, and D. M. Villeneuve, "Tomographic imaging of molecular orbitals," Nature, vol. 432, no. December, 2004.

[47] D. von der Linde, T. Engers, G. Jenke, and P. Agostini, "Generation of high-order harmonics from solid surfaces by intense femtosecond laser pulses," Physical Review A, Rapid Communications, vol. 52, no. 1, pp. 25–27, 1995.

[48] T. Popmintchev, M.-C. Chen, P. Arpin, M. M. Murnane, and H. C. Kapteyn, "The attosecond nonlinear optics of bright coherent X-ray generation," Nature Photonics, vol. 4, pp. 822–832, Dec. 2010.

[49] M. V. Ammosov and V. P. Krainov, "Tunnel ionization of complex atoms and of atomic ions in an alternating electromagnetic field," Sov. Phys. JETP, vol. 64, no. 6, 1986.

[50] A. Fleischer, O. Kfir, T. Diskin, P. Sidorenko, and O. Cohen, "Spin angular momentum and tunable polarization in high-harmonic generation," Nature Photonics, vol. 8, pp. 543–549, June 2014.

[51] Z. Chang, A. Rundquist, H. Wang, M. Murnane, and H. Kapteyn, "Generation of Coherent Soft X Rays at 2.7 nm Using High Harmonics," Physical Review Letters, vol. 79, pp. 2967–2970, Oct. 1997.

[52] H. C. Kapteyn, M. M. Murnane, and I. P. Christov, "Extreme Nonlinear Optics :," Physics Today, vol. 58, no. 3, 2005.

[53] A. Rundquist, C. G. D. Iii, Z. Chang, C. Herne, S. Backus, M. M. Murnane, and H. C. Kapteyn, "Phase-Matched Generation of Coherent Soft X-rays," Science, vol. 280, p. 1412, 1998.

[54] M. Seah and W. Dench, "Quantitative Electron Spectroscopy of Surfaces," Surf. Interface Analysis, vol. 2, no. 1, 1979.

[55] L. Miaja-Avila, J. Yin, S. Backus, G. Saathoff, M. Aeschlimann, M. Murnane, and H. Kapteyn, "Ultrafast studies of electronic processes at surfaces using the laser-assisted photoelectric effect with long-wavelength dressing light," Physical Review A, vol. 79, p. 030901, Mar. 2009.

[56] M. Aeschlimann, C. a. Schmuttenmaer, H. E. Elsayed-Ali, R. J. D. Miller, J. Cao, Y. Gao, and D. a. Mantell, "Observation of surface enhanced multiphoton photoemission from metal surfaces in the short pulse limit," The Journal of Chemical Physics, vol. 102, no. 21, p. 8606, 1995.

[57] U. Morgner, F. X. Kärtner, S. H. Cho, Y. Chen, H. a. Haus, J. G. Fujimoto, E. P. Ippen, V. Scheuer, G. Angelow, and T. Tschudi, "Sub-two-cycle pulses from a Kerr-lens mode-locked Ti:sapphire laser," Optics Letters, vol. 24, p. 411, Mar. 1999.

[58] S. Backus, C. G. Durfee, M. M. Murnane, and H. C. Kapteyn, "High power ultrafast lasers," Review of Scientific Instruments, vol. 69, no. 3, p. 1207, 1998.

[59] D. C. Brown, J. M. Singley, K. Kowalewski, J. Guelzow, and V. Vitali, "High sustained average power cw and ultrafast Yb:YAG near-diffraction-limited cryogenic solid-state laser.," Optics express, vol. 18, pp. 24770–92, Nov. 2010.

[60] a. Pietzsch, a. Föhlisch, M. Beye, M. Deppe, F. Hennies, M. Nagasono, E. Suljoti, W. Wurth, C. Gahl, K. Döbrich, and a. Melnikov, "Towards time resolved core level photoelectron spectroscopy with femtosecond x-ray free-electron lasers," New Journal of Physics, vol. 10, p. 033004, Mar. 2008.

[61] S. Passlack, S. Mathias, O. Andreyev, D. Mittnacht, M. Aeschlimann, and M. Bauer, "Space charge effects in photoemission with a low repetition, high intensity femtosecond laser source," Journal of Applied Physics, vol. 100, no. 2, p. 024912, 2006.

[62] B. J. Siwick, J. R. Dwyer, R. E. Jordan, and R. J. D. Miller, "Ultrafast electron optics: Propagation dynamics of femtosecond electron packets," Journal of Applied Physics, vol. 92, no. 3, p. 1643, 2002.

[63] S. Hellmann, T. Ott, L. Kipp, and K. Rossnagel, "Vacuum space-charge effects in nano-ARPES," Physical Review B, vol. 85, p. 075109, Feb. 2012.

[64] X. Zhou, B. Wannberg, W. Yang, V. Brouet, Z. Sun, J. Douglas, D. Dessau, Z. Hussain, and Z.-X. Shen, "Space charge effect and mirror charge effect in photoemission spectroscopy," Journal of Electron Spectroscopy and Related Phenomena, vol. 142, pp. 27–38, Jan. 2005.

[65] M. D. Seaberg, Nanoscale EUV Microscopy on a Tabletop. PhD thesis, University of Colorado Boulder, 2014.

[66] F. Shimizu, "FREQUENCY BROADENING IN LIQUIDS BY A SHORT LIGHT PULSE," Physical Review Letters, vol. 19, no. 19, 1967.

[67] N. Wagner, E. Gibson, T. Popmintchev, I. Christov, M. Murnane, and H. Kapteyn, "Self-Compression of Ultrashort Pulses through Ionization-Induced Spatiotemporal Reshaping," Physical Review Letters, vol. 93, p. 173902, Oct. 2004.

[68] W. Wood, C. Siders, and M. Downer, "Measurement of Femtosecond Ionization Dynamics of Atmospheric Density Gases by Spectral Blueshifting," Physical Review Letters, vol. 67, no. 25, pp. 3–6, 1991.

[69] J. Knapp, F. Himpsel, and D. Eastman, "Experimental energy band dispersions and lifetimes for valence and conduction bands of copper using angle-resolved photoemission," Physical Review B, vol. 19, no. 10, 1979.

[70] S. Louie, P. Thiry, R. Pinchaux, Y. Petroff, D. Chandesris, and J. Lecante, "Periodic Oscillations of the Frequency-Dependent Photoelectric Cross Sections of Surface States: Theory and Experiment," Physical Review Letters, vol. 44, no. 8, pp. 549–553, 1980.

[71] S. Mathias, C. La-o vorakiat, P. Grychtol, P. Granitzka, E. Turgut, J. M. Shaw, M. Aeschlimann, M. M. Murnane, and H. C. Kapteyn, "Probing the timescale of the exchange interaction in a ferromagnetic alloy," PNAS, vol. 109, no. 13, pp. 4792–4797, 2012.

[72] L. X. Yang, G. Rohde, T. Rohwer, A. Stange, K. Hanff, C. Sohrt, L. Rettig, R. Cortes, F. Chen, D. L. Feng, T. Wolf, B. Kamble, I. Eremin, T. Popmintchev, M. M. Murnane, H. C. Kapteyn, L. Kipp, J. Fink, M. Bauer, U. Bovensiepen, and K. Rossnagel, "Ultrafast Modulation of the Chemical Potential in BaFe2As," Physical Review Letters, vol. 112, p. 207001, May 2014.

[73] K. Ishizaka, T. Kiss, T. Yamamoto, Y. Ishida, T. Saitoh, M. Matsunami, R. Eguchi, T. Ohtsuki, a. Kosuge, T. Kanai, M. Nohara, H. Takagi, S. Watanabe, and S. Shin, "Femtosecond core-level photoemision spectroscopy on 1T-TaS_{2} using a 60-eV laser source," Physical Review B, vol. 83, p. 081104, Feb. 2011.

[74] G. M. Blumenstock, M. L. Gintert, and R. Meski-Kuha, "Extreme ultraviolet optical properties of ion-beam-deposited boron carbide thin films," Proc. SPIE 2515, X-Ray and Extreme Ultraviolet Optics, no. 558, pp. 558–564, 1995.

[75] E. M. G. B. L. Henke and J. C. Davis, "X-Ray Interactions: Photoabsorption, Scattering, Transmission, and Reflection at E = 5030,000 eV, Z = 192," At. Data Nucl. Data Tables, vol. 54, no. 181, 1993.

[76] M. Nisoli, S. D. Silvestri, O. Svelto, and R. Szip, "Compression of high-energy laser pulses below 5 fs," Optics Letters, vol. 22, no. 8, pp. 522–524, 1997.

[77] A. Börzsönyi, Z. Heiner, a. P. Kovács, M. P. Kalashnikov, and K. Osvay, "Measurement of pressure dependent nonlinear refractive index of inert gases.," Optics express, vol. 18, pp. 25847–54, Dec. 2010.

[78] L.-l. Göttingen, "Hollow-fiber pulse compressor for KrF lasers," Applied Physics B, vol. 82, pp. 567–570, 2006.

[79] P. Béjot, J. Kasparian, S. Henin, V. Loriot, T. Vieillard, E. Hertz, O. Faucher, B. Lavorel, and J.-P. Wolf, "Higher-Order Kerr Terms Allow Ionization-Free Filamentation in Gases," Physical Review Letters, vol. 104, p. 103903, Mar. 2010.

[80] A. Suda, M. Hatayama, K. Nagasaka, and K. Midorikawa, "Generation of sub-10-fs, 5-mJ-optical pulses using a hollow fiber with a pressure gradient," Applied Physics Letters, vol. 86, no. 11, p. 111116, 2005.

[81] J. a. R. Samson and H. Liebl, "Duoplasmatron as a Vacuum Ultraviolet Light Source," Review of Scientific Instruments, vol. 33, no. 12, p. 1340, 1962.

[82] C.-f. Lei, "Using ultrafast extreme-ultraviolet pulses for time-resolved dynamics of molecules chemisorbed on metal surfaces," PhD Thesis, 2003.

[83] S. Mahl, "Phoibos Hemispherical Analyzer Series: Phoibos 100 documentation," Specs Gmbh, 2013.

[84] C.-M. Cheng, "Angle–resolved photoemission spectroscopy resolved photoemission spectroscopy (ARPES) for 2D layered structure : graphene and topological insulators," NTHU Semianr, 2013.

[85] P. D. C. King, R. C. Hatch, M. Bianchi, R. Ovsyannikov, C. Lupulescu, G. Landolt, B. Slomski, J. H. Dil, D. Guan, J. L. Mi, E. D. L. Rienks, J. Fink, a. Lindblad, S. Svensson, S. Bao, G. Balakrishnan, B. B. Iversen, J. Osterwalder, W. Eberhardt, F. Baumberger, and P. Hofmann, "Large Tunable Rashba Spin Splitting of a Two-Dimensional Electron Gas in Bi_{2}Se_{3}," Physical Review Letters, vol. 107, p. 096802, Aug. 2011.

[86] a. Föhlisch, P. Feulner, F. Hennies, a. Fink, D. Menzel, D. Sanchez-Portal, P. M. Echenique, and W. Wurth, "Direct observation of electron dynamics in the attosecond domain.," Nature, vol. 436, pp. 373–6, July 2005.

[87] F. Calegari, D. Ayuso, a. Trabattoni, L. Belshaw, S. De Camillis, S. Anumula, F. Frassetto, L. Poletto, a. Palacios, P. Decleva, J. B. Greenwood, F. Martín, and M. Nisoli, "Ultrafast electron dynamics in phenylalanine initiated by attosecond pulses.," Science (New York, N.Y.), vol. 346, pp. 336–9, Oct. 2014.

[88] H. Wang, M. Chini, S. Chen, C.-H. Zhang, F. He, Y. Cheng, Y. Wu, U. Thumm, and Z. Chang, "Attosecond Time-Resolved Autoionization of Argon," Physical Review Letters, vol. 105, p. 143002, Oct. 2010.

[89] a. L. Cavalieri, N. Müller, T. Uphues, V. S. Yakovlev, a. Baltuska, B. Horvath, B. Schmidt, L. Blümel, R. Holzwarth, S. Hendel, M. Drescher, U. Kleineberg, P. M. Echenique, R. Kienberger, F. Krausz, and U. Heinzmann, "Attosecond spectroscopy in condensed matter.," Nature, vol. 449, pp. 1029–32, Oct. 2007.

[90] S. Neppl, R. Ernstorfer, E. M. Bothschafter, a. L. Cavalieri, D. Menzel, J. V. Barth, F. Krausz, R. Kienberger, and P. Feulner, "Attosecond Time-Resolved Photoemission from Core and Valence States of Magnesium," Physical Review Letters, vol. 109, p. 087401, Aug. 2012.

[91] S. Neppl, R. Ernstorfer, a. L. Cavalieri, C. Lemell, G. Wachter, E. Magerl, E. M. Bothschafter, M. Jobst, M. Hofstetter, U. Kleineberg, J. V. Barth, D. Menzel, J. Burgdörfer, P. Feulner, F. Krausz, and R. Kienberger, "Direct observation of electron propagation and dielectric screening on the atomic length scale," Nature, vol. 517, pp. 342–346, Jan. 2015.

[92] M. Schultze, M. Fiess, N. Karpowicz, J. Gagnon, M. Korbman, M. Hofstetter, S. Neppl, a. L. Cavalieri, Y. Komninos, T. Mercouris, C. a. Nicolaides, R. Pazourek, S. Nagele, J. Feist, J. Burgdörfer, a. M. Azzeer, R. Ernstorfer, R. Kienberger, U. Kleineberg, E. Goulielmakis, F. Krausz, and V. S. Yakovlev, "Delay in photoemission.," Science (New York, N.Y.), vol. 328, pp. 1658–62, June 2010.

[93] M. Swoboda, T. Fordell, K. Klünder, J. M. Dahlström, M. Miranda, C. Buth, K. J. Schafer, J. Mauritsson, a. LHuillier, and M. Gisselbrecht, "Phase Measurement of Resonant Two-Photon Ionization in Helium," Physical Review Letters, vol. 104, p. 103003, Mar. 2010.

[94] C. Palatchi, J. M. Dahlström, a. S. Kheifets, I. a. Ivanov, D. M. Canaday, P. Agostini, and L. F. DiMauro, "Atomic delay in helium, neon, argon and krypton," Journal of Physics B: Atomic, Molecular and Optical Physics, vol. 47, p. 245003, Dec. 2014.

[95] K. Klünder, J. M. Dahlström, M. Gisselbrecht, T. Fordell, M. Swoboda, D. Guénot, P. Johnsson, J. Caillat, J. Mauritsson, a. Maquet, R. Taïeb, and a. LHuillier, "Probing Single-Photon Ionization on the Attosecond Time Scale," Physical Review Letters, vol. 106, p. 143002, Apr. 2011.

[96] S. Haessler, B. Fabre, J. Higuet, J. Caillat, T. Ruchon, P. Breger, B. Carré, E. Constant, a. Maquet, E. Mével, P. Salières, R. Taïeb, and Y. Mairesse, "Phase-resolved attosecond near-threshold photoionization of molecular nitrogen," Physical Review A, vol. 80, p. 011404, July 2009.

[97] U. Heinzmann, "Attosecond Physics," vol. 177, pp. 231–253, 2013.

[98] P. M. Paul, E. S. Toma, P. Breger, G. Mullot, F. Auge, P. Balcou, H. G. Muller, and P. Agostini, "Observation of a train of attosecond pulses from high harmonic generation.," Science (New York, N.Y.), vol. 292, pp. 1689–92, June 2001.

[99] R. López-Martens, K. Varjú, P. Johnsson, J. Mauritsson, Y. Mairesse, P. Salières, M. Gaarde, K. Schafer, A. Persson, S. Svanberg, C.-G. Wahlström, and A. LHuillier, "Amplitude and Phase Control of Attosecond Light Pulses," Physical Review Letters, vol. 94, p. 033001, Jan. 2005.

[100] S. Neppl, Attosecond Tme-Resolved Photoemission from Surfaces and Interfaces. PhD thesis, Technische Universitat Munchen, 2012.

[101] A. Baltuska, T. Udem, M. Uiberacker, M. Hentschel, E. Goulielmakis, C. Gohle, R. Holzwarth, V. Yakovlev, A. Scrinzi, T. Hansch, and F. Krausz, "Attosecond control of electronic processes by intense light fields," Nature, vol. 421, no. February, 2003.

[102] M. J. Abel, T. Pfeifer, P. M. Nagel, W. Boutu, M. J. Bell, C. P. Steiner, D. M. Neumark, and S. R. Leone, "Isolated attosecond pulses from ionization gating of high-harmonic emission," Chemical Physics, vol. 366, no. 1-3, pp. 9–14, 2009.

[103] P. B. Corkum, N. H. Burnett, and M. Y. Ivanov, "Subfemtosecond pulses.," Optics letters, vol. 19, no. 22, p. 1870, 1994.

[104] V. S. Yakovlev, J. Gagnon, N. Karpowicz, and F. Krausz, "Attosecond streaking enables the measurement of quantum phase," Physical Review Letters, vol. 105, no. August, pp. 3–6, 2010.

[105] G. Saathoff, L. Miaja-Avila, M. Aeschlimann, M. Murnane, and H. Kapteyn, "Laser-assisted photoemission from surfaces," Physical Review A, vol. 77, p. 022903, Feb. 2008.

[106] L. Miaja-Avila, G. Saathoff, S. Mathias, J. Yin, C. La-o vorakiat, M. Bauer, M. Aeschlimann, M. Murnane, and H. Kapteyn, "Direct Measurement of Core-Level Relaxation Dynamics on a Surface-Adsorbate System," Physical Review Letters, vol. 101, p. 046101, July 2008.

[107] C.-H. Zhang and U. Thumm, "Laser-assisted photoemission from adsorbate-covered metal surfaces: Time-resolved core-hole relaxation dynamics from sideband profiles," Physical Review A, vol. 80, p. 032902, Sept. 2009.

[108] H. Muller, "Reconstruction of attosecond harmonic beating by interference of two-photon transitions," Applied Physics B, vol. 74, pp. s17–s21, Apr. 2002.

[109] K. Varjú, P. Johnsson, T. Remetter, E. Gustafsson, E. Constant, E. Cormier, E. Mével, and A. L. Huillier, "Experimental Studies of Attosecond Pulse Trains," Laser Physics, vol. 15, no. 6, pp. 888–898, 2005.

[110] D. Guénot, K. Klünder, C. L. Arnold, D. Kroon, J. M. Dahlström, M. Miranda, T. Fordell, M. Gisselbrecht, P. Johnsson, J. Mauritsson, E. Lindroth, a. Maquet, R. Taïeb, a. LHuillier, and a. S. Kheifets, "Photoemission-time-delay measurements and calculations close to the 3s-ionization-cross-section minimum in Ar," Physical Review A, vol. 85, p. 053424, May 2012.

[111] J. M. Dahlström, a. LHuillier, a. Maquet, H. Search, C. Journals, A. Contact, M. Iopscience, and I. P. Address, "Introduction to attosecond delays in photoionization," Journal of Physics B: Atomic, Molecular and Optical Physics, vol. 45, p. 183001, 2012.

[112] J. Dahlström, T. Fordell, E. Mansten, T. Ruchon, M. Swoboda, K. Klünder, M. Gisselbrecht, a. LHuillier, and J. Mauritsson, "Atomic and macroscopic measurements of attosecond pulse trains," Physical Review A, vol. 80, p. 033836, Sept. 2009.

[113] D. Jones, S. Diddams, J. Ranka, a. Stentz, R. Windeler, J. Hall, and S. Cundiff, "Carrier-envelope phase control of femtosecond mode-locked lasers and direct optical frequency synthesis," Science (New York, N.Y.), vol. 288, no. April, pp. 635–40, 2000.

[114] E. S. Toma and H. Muller, "Calculation of matrix elements for mixed extreme-ultravioletinfrared two-photon above-threshold ionization of argon," Journal of Physics B: Atomic, Molecular and Optical Physics, vol. 35, pp. 3435–3442, 2002.

[115] V. Veniard, R. Taieb, and A. Maquet, "Phase dependence of (N+1) color (N¿1) ir-uv photoionization of atoms with higher harmonics," Physical Review A, vol. 54, no. 1, pp. 721–728, 1996.

[116] a. S. Kheifets and I. a. Ivanov, "Delay in atomic photoionization," Physical Review Letters, vol. 105, no. December, pp. 1–4, 2010.

[117] a. S. Kheifets, "Time delay in valence-shell photoionization of noble-gas atoms," Physical Review A - Atomic, Molecular, and Optical Physics, vol. 87, no. April, pp. 1–9, 2013.

[118] a. K. Kazansky and N. M. Kabachnik, "Sideband structure in angle-resolved electron spectra from laser-assisted Auger decay generated by ultra-short pulses," Journal of Physics B: Atomic, Molecular and Optical Physics, vol. 42, p. 121002, June 2009.

[119] J. Baggesen and L. Madsen, "Theory for time-resolved measurements of laser-induced electron emission from metal surfaces," Physical Review A, vol. 78, p. 032903, Sept. 2008.

[120] C.-H. Zhang and U. Thumm, "Attosecond Photoelectron Spectroscopy of Metal Surfaces," Physical Review Letters, vol. 102, p. 123601, Mar. 2009.

[121] C.-H. Zhang and U. Thumm, "Effect of wave-function localization on the time delay in photoemission from surfaces," Physical Review A, vol. 84, p. 065403, Dec. 2011.

[122] C. Lemell, B. Solleder, K. Tkési, and J. Burgdörfer, "Simulation of attosecond streaking of electrons emitted from a tungsten surface," Physical Review A, vol. 79, p. 062901, June 2009.

[123] C.-H. Zhang and U. Thumm, "Probing dielectric-response effects with attosecond time-resolved streaked photoelectron spectroscopy of metal surfaces," Physical Review A, vol. 84, p. 063403, Dec. 2011.

[124] L. Miaja-Avila, C. Lei, M. Aeschlimann, J. Gland, M. Murnane, H. Kapteyn, and G. Saathoff, "Laser-Assisted Photoelectric Effect from Surfaces," Physical Review Letters, vol. 97, p. 113604, Sept. 2006.

[125] R. Courths, H. Wern, and S. Hufner, "THE TAMM SURFACE STATE ON Cu(111) AND Ag(111)," Solid State Communications, vol. 61, no. 4, pp. 257–260, 1987.

[126] A. Winkelmann, C. Tusche, a. Akin Ünal, M. Ellguth, J. Henk, and J. Kirschner, "Analysis of the electronic structure of copper via two-dimensional photoelectron momentum distribution patterns," New Journal of Physics, vol. 14, p. 043009, Apr. 2012.

[127] N. Smith, R. Benbow, and Z. Hurych, "Photoemission spectra and band structures of d-band metals. VIII. Normal emission from Cu(111)," Physical Review B, vol. 21, no. 10, 1980.

[128] X. Li, Z. Zhang, and V. Henrich, "Inelastic Electron Background Function for Ultraviolet Photoelectron-Spectra," Journal of Electron Spectroscopy and Related Phenomena, vol. 63, pp. 253–265, 1993.

[129] J. Dahlström, D. Guénot, K. Klünder, M. Gisselbrecht, J. Mauritsson, a. LHuillier, a. Maquet, and R. Taïeb, "Theory of attosecond delays in laser-assisted photoionization," Chemical Physics, vol. 414, pp. 53–64, Mar. 2013.

[130] E. P. Må nsson, D. Guénot, C. L. Arnold, D. Kroon, S. Kasper, J. M. Dahlström, E. Lindroth, A. S. Kheifets, A. LHuillier, S. L. Sorensen, and M. Gisselbrecht, "Double ionization probed on the attosecond timescale," Nature Physics, vol. 10, pp. 207–211, Jan. 2014.

[131] L. Schulz, "The Optical Constants of Silver, Gold, Copper, and Aluminum. I. The Absorption Coefficient k," Journal of Optical Society of America, vol. 44, no. 5, 1954.

[132] A. Zangwill Physics at Surfaces, no. New York:Cambridge: University Press, p454, 1988.

[133] K. S. Novoselov, a. K. Geim, S. V. Morozov, D. Jiang, Y. Zhang, S. V. Dubonos, I. V. Grigorieva, and a. a. Firsov, "Electric field effect in atomically thin carbon films.," Science (New York, N.Y.), vol. 306, pp. 666–9, Oct. 2004.

[134] K. S. Novoselov, a. K. Geim, S. V. Morozov, D. Jiang, M. I. Katsnelson, I. V. Grigorieva, S. V. Dubonos, and a. a. Firsov, "Two-dimensional gas of massless Dirac fermions in graphene.," Nature, vol. 438, pp. 197–200, Nov. 2005.

[135] C. Berger, Z. Song, T. Li, X. Li, A. Y. Ogbazghi, R. Feng, Z. Dai, A. N. Marchenkov, E. H. Conrad, P. N. First, and W. A. D. Heer, "Ultrathin Epitaxial Graphite : 2D Electron Gas Properties and a Route toward," J. Phys. Chem. B, vol. 108, pp. 19912–19916, 2004.

[136] M. Batzill, "The surface science of graphene: Metal interfaces, CVD synthesis, nanoribbons, chemical modifications, and defects," Surface Science Reports, vol. 67, pp. 83–115, Mar. 2012.

[137] Y. S. Dedkov, M. Fonin, and C. Laubschat, "A possible source of spin-polarized electrons: The inert graphene/Ni(111) system," Applied Physics Letters, vol. 92, no. 5, p. 052506, 2008.

[138] K. Bolotin, K. Sikes, Z. Jiang, M. Klima, G. Fudenberg, J. Hone, P. Kim, and H. Stormer, "Ultrahigh electron mobility in suspended graphene," Solid State Communications, vol. 146, pp. 351–355, June 2008.

[139] P. W. Sutter, J.-I. Flege, and E. a. Sutter, "Epitaxial graphene on ruthenium.," Nature materials, vol. 7, pp. 406–11, May 2008.

[140] C. Enderlein, Y. S. Kim, a. Bostwick, E. Rotenberg, and K. Horn, "The formation of an energy gap in graphene on ruthenium by controlling the interface," New Journal of Physics, vol. 12, p. 033014, Mar. 2010.

[141] M. Papagno, S. Rusponi, P. M. Sheverdyaeva, S. Vlaic, M. Etzkorn, D. Pacilé, P. Moras, C. Carbone, and H. Brune, "Large band gap opening between graphene Dirac cones induced by Na adsorption onto an Ir superlattice.," ACS nano, vol. 6, pp. 199–204, Jan. 2012.

[142] T. Jayasekera, B. D. Kong, K. W. Kim, and M. Buongiorno Nardelli, "Band Engineering and Magnetic Doping of Epitaxial Graphene on SiC (0001)," Physical Review Letters, vol. 104, p. 146801, Apr. 2010.

[143] N. D. Mermin, "Crystalline Order in Two Dimensions," Physical Review, vol. 176, no. 1, 1968.

[144] K. S. Kim, Y. Zhao, H. Jang, S. Y. Lee, J. M. Kim, K. S. Kim, J.-H. Ahn, P. Kim, J.-Y. Choi, and B. H. Hong, "Large-scale pattern growth of graphene films for stretchable transparent electrodes.," Nature, vol. 457, pp. 706–10, Feb. 2009.

[145] Y. Lee, S. Bae, H. Jang, S. Jang, S.-E. Zhu, S. H. Sim, Y. I. Song, B. H. Hong, and J.-H. Ahn, "Wafer-scale synthesis and transfer of graphene films.," Nano letters, vol. 10, pp. 490–3, Feb. 2010.

[146] T. J. Booth, P. Blake, R. R. Nair, D. Jiang, E. W. Hill, U. Bangert, A. Bleloch, M. Gass, K. S. Novoselov, M. I. Katsnelson, and a. K. Geim, "Macroscopic graphene membranes and their extraordinary stiffness.," Nano letters, vol. 8, pp. 2442–6, Aug. 2008.

[147] http://www.elume.com/projects/organic semiconductors 2013.

[148] M. Mucha-Kruczyski, O. Tsyplyatyev, A. Grishin, E. McCann, V. Falko, A. Bostwick, and E. Rotenberg, "Characterization of graphene through anisotropy of constant-energy maps in angle-resolved photoemission," Physical Review B, vol. 77, p. 195403, May 2008.

[149] A. Grüneis and D. Vyalikh, "Tunable hybridization between electronic states of graphene and a metal surface," Physical Review B, vol. 77, p. 193401, May 2008.

[150] P. Avouris, "Graphene: Electronic and Photonic Properties and Devices.," Nano letters, pp. 4285–4294, Sept. 2010.

[151] D. Boukhvalov, M. Katsnelson, and a. Lichtenstein, "Hydrogen on graphene: Electronic structure, total energy, structural distortions and magnetism from first-principles calculations," Physical Review B, vol. 77, p. 035427, Jan. 2008.

[152] T. Ohta, A. Bostwick, T. Seyller, K. Horn, and E. Rotenberg, "Controlling the electronic structure of bilayer graphene.," Science (New York, N.Y.), vol. 313, pp. 951–4, Aug. 2006.

[153] K. Nakada, M. Fujita, G. Dresselhaus, and M. Dresselhaus, "Edge state in graphene ribbons: Nanometer size effect and edge shape dependence," Physical Review B, vol. 54, pp. 17954–17961, Dec. 1996.

[154] G. Giovannetti, P. Khomyakov, G. Brocks, V. Karpan, J. van den Brink, and P. Kelly, "Doping Graphene with Metal Contacts," Physical Review Letters, vol. 101, p. 026803, July 2008.

[155] a. K. Geim, "Graphene: status and prospects.," Science (New York, N.Y.), vol. 324, pp. 1530–4, June 2009.

[156] S. Gilje, S. Han, M. Wang, K. L. Wang, and R. B. Kaner, "A chemical route to graphene for device applications.," Nano letters, vol. 7, pp. 3394–8, Nov. 2007.

[157] K. R. Paton, E. Varrla, C. Backes, R. J. Smith, U. Khan, A. O'Neill, C. Boland, M. Lotya, O. M. Istrate, P. King, T. Higgins, S. Barwich, P. May, P. Puczkarski, I. Ahmed, M. Moebius, H. Pettersson, E. Long, J. a. Coelho, S. E. O'Brien, E. K. McGuire, B. M. Sanchez, G. S. Duesberg, N. McEvoy, T. J. Pennycook, C. Downing, A. Crossley, V. Nicolosi, and J. N. Coleman, "Scalable production of large quantities of defect-free few-layer graphene by shear exfoliation in liquids.," Nature materials, vol. 13, pp. 624–30, June 2014.

[158] W. a. de Heer, C. Berger, X. Wu, P. N. First, E. H. Conrad, X. Li, T. Li, M. Sprinkle, J. Hass, M. L. Sadowski, M. Potemski, and G. Martinez, "Epitaxial graphene," Solid State Communications, vol. 143, pp. 92–100, July 2007.

[159] K. V. Emtsev, A. Bostwick, K. Horn, J. Jobst, G. L. Kellogg, L. Ley, J. L. McChesney, T. Ohta, S. a. Reshanov, J. Röhrl, E. Rotenberg, A. K. Schmid, D. Waldmann, H. B. Weber, and T. Seyller, "Towards wafer-size graphene layers by atmospheric pressure graphitization of silicon carbide.," Nature materials, vol. 8, pp. 203–7, Mar. 2009.

[160] C. Berger, Z. Song, X. Li, X. Wu, N. Brown, C. Naud, D. Mayou, T. Li, J. Hass, A. N. Marchenkov, E. H. Conrad, P. N. First, and W. a. de Heer, "Electronic confinement and coherence in patterned epitaxial graphene.," Science (New York, N.Y.), vol. 312, pp. 1191–6, May 2006.

[161] Y.-W. Son, M. L. Cohen, and S. G. Louie, "Energy Gaps in Graphene Nanoribbons," Physical Review Letters, vol. 97, p. 216803, Nov. 2006.

[162] M. Eizenberg and J. Blakely, "CARBON MONOLAYER PHASE CONDENSATION ON Ni(111)," Surface Science, vol. 82, pp. 228–236, 1979.

[163] A. NDiaye, S. Bleikamp, P. Feibelman, and T. Michely, "Two-Dimensional Ir Cluster Lattice on a Graphene Moiré on Ir(111)," Physical Review Letters, vol. 97, p. 215501, Nov. 2006.

[164] T. A. Land, T. Michely, R. J. Behm, and J. C. Hemminger, "STM investigation of single layer graphite structures produced on Pt (111) by hydrocarbon decomposition," Surface Science, vol. 264, pp. 261–270, 1992.

[165] L. Gao, J. R. Guest, and N. P. Guisinger, "Epitaxial graphene on Cu(111).," Nano letters, vol. 10, pp. 3512–6, Sept. 2010.

[166] Q. Yu, J. Lian, S. Siriponglert, H. Li, Y. P. Chen, and S.-S. Pei, "Graphene segregated on Ni surfaces and transferred to insulators," Applied Physics Letters, vol. 93, no. 11, p. 113103, 2008.

[167] W. Regan, N. Alem, B. Aleman, B. Geng, C. Girit, L. Maserati, F. Wang, M. Crommie, and a. Zettl, "A direct transfer of layer-area graphene," Applied Physics Letters, vol. 96, no. 11, p. 113102, 2010.

[168] M. Breusing, S. Kuehn, T. Winzer, E. Malić, F. Milde, N. Severin, J. P. Rabe, C. Ropers, a. Knorr, and T. Elsaesser, "Ultrafast nonequilibrium carrier dynamics in a single graphene layer," Physical Review B, vol. 83, p. 153410, Apr. 2011.

[169] D. Brida, a. Tomadin, C. Manzoni, Y. J. Kim, a. Lombardo, S. Milana, R. R. Nair, K. S. Novoselov, a. C. Ferrari, G. Cerullo, and M. Polini, "Ultrafast collinear scattering and carrier multiplication in graphene.," Nature communications, vol. 4, p. 1987, Jan. 2013.

[170] J. M. Dawlaty, S. Shivaraman, M. Chandrashekhar, F. Rana, and M. G. Spencer, "Measurement of ultrafast carrier dynamics in epitaxial graphene," Applied Physics Letters, vol. 92, no. 4, p. 042116, 2008.

[171] P. a. George, J. Strait, J. Dawlaty, S. Shivaraman, M. Chandrashekhar, F. Rana, and M. G. Spencer, "Ultrafast optical-pump terahertz-probe spectroscopy of the carrier relaxation and recombination dynamics in epitaxial graphene.," Nano letters, vol. 8, pp. 4248–51, Dec. 2008.

[172] T. Li, L. Luo, M. Hupalo, J. Zhang, M. C. Tringides, J. Schmalian, and J. Wang, "Femtosecond Population Inversion and Stimulated Emission of Dense Dirac Fermions in Graphene," Physical Review Letters, vol. 108, p. 167401, Apr. 2012.

[173] S.-F. Shi, T.-T. Tang, B. Zeng, L. Ju, Q. Zhou, a. Zettl, and F. Wang, "Controlling graphene ultrafast hot carrier response from metal-like to semiconductor-like by electrostatic gating.," Nano letters, vol. 14, pp. 1578–82, Mar. 2014.

[174] I. Gierz, J. C. Petersen, M. Mitrano, C. Cacho, I. C. E. Turcu, E. Springate, A. Stöhr, A. Köhler, U. Starke, and A. Cavalleri, "Snapshots of non-equilibrium Dirac carrier distributions in graphene.," Nature materials, vol. 12, pp. 1119–24, Dec. 2013.

[175] J. C. Johannsen, S. r. Ulstrup, F. Cilento, A. Crepaldi, M. Zacchigna, C. Cacho, I. C. E. Turcu, E. Springate, F. Fromm, C. Raidel, T. Seyller, F. Parmigiani, M. Grioni, and P. Hofmann, "Direct View of Hot Carrier Dynamics in Graphene," Physical Review Letters, vol. 111, p. 027403, July 2013.

[176] T. Someya, H. Fukidome, Y. Ishida, R. Yoshida, T. Iimori, R. Yukawa, K. Akikubo, S. Yamamoto, S. Yamamoto, T. Yamamoto, T. Kanai, K. Funakubo, M. Suemitsu, J. Itatani, F. Komori, S. Shin, and I. Matsuda, "Observing hot carrier distribution in an n-type epitaxial graphene on a SiC substrate," Applied Physics Letters, vol. 104, p. 161103, Apr. 2014.

[177] J. Hass, R. Feng, T. Li, X. Li, Z. Zong, W. a. de Heer, P. N. First, E. H. Conrad, C. a. Jeffrey, and C. Berger, "Highly ordered graphene for two dimensional electronics," Applied Physics Letters, vol. 89, no. 14, p. 143106, 2006.

[178] K. V. Emtsev, F. Speck, T. Seyller, and L. Ley, "Interaction, growth, and ordering of epitaxial graphene on SiC{0001} surfaces: A comparative photoelectron spectroscopy study," Physical Review B, vol. 77, p. 155303, Apr. 2008.

[179] J. Hass, F. Varchon, J. Millán-Otoya, M. Sprinkle, N. Sharma, W. de Heer, C. Berger, P. First, L. Magaud, and E. Conrad, "Why Multilayer Graphene on 4H-SiC(0001) Behaves Like a Single Sheet of Graphene," Physical Review Letters, vol. 100, p. 125504, Mar. 2008.

[180] Y. Zhang, Y.-W. Tan, H. L. Stormer, and P. Kim, "Experimental observation of the quantum Hall effect and Berry's phase in graphene.," Nature, vol. 438, pp. 201–4, Nov. 2005.

[181] I. Forbeaux, J.-M. Themlin, a. Charrier, F. Thibaudau, and J.-M. Debever, "Solid-state graphitization mechanisms of silicon carbide 6HSiC polar faces," Applied Surface Science, vol. 162-163, pp. 406–412, Aug. 2000.

[182] S. Oida, F. R. McFeely, J. B. Hannon, R. M. Tromp, M. Copel, Z. Chen, Y. Sun, D. B. Farmer, and J. Yurkas, "Decoupling graphene from SiC(0001) via oxidation," Physical Review B, vol. 82, p. 041411, July 2010.

[183] C. Riedl, C. Coletti, T. Iwasaki, a. a. Zakharov, and U. Starke, "Quasi-Free-Standing Epitaxial Graphene on SiC Obtained by Hydrogen Intercalation," Physical Review Letters, vol. 103, p. 246804, Dec. 2009.

[184] T. Seyller, K. V. Emtsev, F. Speck, K.-Y. Gao, and L. Ley, "Schottky barrier between 6H-SiC and graphite: Implications for metal/SiC contact formation," Applied Physics Letters, vol. 88, no. 24, p. 242103, 2006.

[185] D. a. Siegel, C. G. Hwang, a. V. Fedorov, and a. Lanzara, "Quasifreestanding multilayer graphene films on the carbon face of SiC," Physical Review B, vol. 81, p. 241417, June 2010.

[186] E. Shirley, L. Terminello, A. Santoni, and F. Himpsel, "Brillouin-zone-selection effects in graphite photoelectron angular distributions," Physics Review B, vol. 51, no. 19, 1995.

[187] H. Daimon, S. Imada, H. Nishimoto, and S. Suga, "Sturcture Factor in Photoemission from Valence Band," Journal of Electron Spectroscopy and Related Phenomena, vol. 76, pp. 487–492, 1995.

[188] I. Gierz, J. Henk, H. Höchst, C. R. Ast, and K. Kern, "Illuminating the dark corridor in graphene: Polarization dependence of angle-resolved photoemission spectroscopy on graphene," Physical Review B, vol. 83, p. 121408, Mar. 2011.

[189] A. Bostwick, T. Ohta, T. Seyller, K. Horn, and E. Rotenberg, "Quasiparticle dynamics in graphene," Nature Physics, vol. 3, pp. 36–40, Dec. 2006.

[190] a. Varykhalov, J. Sánchez-Barriga, a. Shikin, C. Biswas, E. Vescovo, a. Rybkin, D. Marchenko, and O. Rader, "Electronic and Magnetic Properties of Quasifreestanding Graphene on Ni," Physical Review Letters, vol. 101, p. 157601, Oct. 2008.

[191] A. L. Walter, S. Nie, A. Bostwick, K. S. Kim, L. Moreschini, Y. J. Chang, D. Innocenti, K. Horn, K. F. McCarty, and E. Rotenberg, "Electronic structure of graphene on single-crystal copper substrates," Physical Review B, vol. 84, p. 195443, Nov. 2011.

[192] L. Falkovsky and S. Pershoguba, "Optical far-infrared properties of a graphene monolayer and multilayer," Physical Review B, vol. 76, p. 153410, Oct. 2007.

[193] J. C. Johannsen, S. r. Ulstrup, A. Crepaldi, F. Cilento, M. Zacchigna, J. A. Miwa, C. Cacho, R. T. Chapman, E. Springate, F. Fromm, C. Raidel, T. Seyller, P. D. C. King, F. Parmigiani, M. Grioni, and P. Hofmann, "Tunable Carrier Multiplication and Cooling in Graphene," Nano letters, 2014.

[194] H. Wang, J. H. Strait, P. a. George, S. Shivaraman, V. B. Shields, M. Chandrashekhar, J. Hwang, F. Rana, M. G. Spencer, C. S. Ruiz-Vargas, and J. Park, "Ultrafast relaxation dynamics of hot optical phonons in graphene," Applied Physics Letters, vol. 96, no. 8, p. 081917, 2010.

[195] M. Breusing, C. Ropers, and T. Elsaesser, "Ultrafast Carrier Dynamics in Graphite," Physical Review Letters, vol. 102, p. 086809, Feb. 2009.

[196] Y. Gamo, a. Nagashima, M. Wakabayashi, M. Terai, and C. Oshima, "Atomic structure of monolayer graphite formed on Ni(111)," Surface Science, vol. 374, pp. 61–64, Mar. 1997.

[197] E. Voloshina and Y. Dedkov, "Graphene on metallic surfaces: problems and perspectives.," Physical chemistry chemical physics : PCCP, vol. 14, pp. 13502–14, Oct. 2012.

[198] a. Varykhalov, M. R. Scholz, T. K. Kim, and O. Rader, "Effect of noble-metal contacts on doping and band gap of graphene," Physical Review B, vol. 82, p. 121101, Sept. 2010.

[199] D. Haberer, D. V. Vyalikh, S. Taioli, B. Dora, M. Farjam, J. Fink, D. Marchenko, T. Pichler, K. Ziegler, S. Simonucci, M. S. Dresselhaus, M. Knupfer, B. Büchner, and a. Grüneis, "Tunable band gap in hydrogenated quasi-free-standing graphene.," Nano letters, vol. 10, pp. 3360–6, Sept. 2010.

[200] a. Varykhalov, D. Marchenko, J. Sánchez-Barriga, M. R. Scholz, B. Verberck, B. Trauzettel, T. O. Wehling, C. Carbone, and O. Rader, "Intact Dirac Cones at Broken Sublattice Symmetry: Photoemission Study of Graphene on Ni and Co," Physical Review X, vol. 2, p. 041017, Dec. 2012.

[201] Y. S. Park, J. H. Park, H. N. Hwang, T. S. Laishram, K. S. Kim, M. H. Kang, and C. C. Hwang, "Quasi-Free-Standing Graphene Monolayer on a Ni Crystal through Spontaneous Na Intercalation," Physical Review X, vol. 4, p. 031016, July 2014.

[202] A. Nagashima, N. Tejima, and C. Oshima, "Electronic states of the pristine and alkali-metal-intercalated monolayer graphite/Ni (111) systems," Physical Review B, vol. 50, no. 23, 1994.

[203] M. Mulazzi, M. Hochstrasser, M. Corso, I. Vobornik, J. Fujii, J. Osterwalder, J. Henk, and G. Rossi, "Matrix element effects in angle-resolved valence band photoemission with polarized light from the Ni(111) surface," Physical Review B, vol. 74, p. 035118, July 2006.

[204] T. Haarlammert, L. Bignardi, C. Winter, G. Fecher, P. Rudolf, and H. Zacharias, "Final-state effects in photoemission experiments from graphene on Ni(111)," The European Physical Journal B, vol. 86, p. 225, May 2013.

[205] D. L. Miller, M. W. Keller, J. M. Shaw, A. N. Chiaramonti, and R. R. Keller, "Epitaxial (111) films of Cu, Ni, and CuxNiy on αAl2O3 (0001) for graphene growth by chemical vapor deposition," Journal of Applied Physics, vol. 112, no. 6, p. 064317, 2012.

[206] K. F. McCarty, P. J. Feibelman, E. Loginova, and N. C. Bartelt, "Kinetics and thermodynamics of carbon segregation and graphene growth on Ru(0001)," Carbon, vol. 47, pp. 1806–1813, June 2009.

[207] A. Reina, X. Jia, J. Ho, D. Nezich, H. Son, V. Bulovic, M. S. Dresselhaus, and J. Kong, "Large area, few-layer graphene films on arbitrary substrates by chemical vapor deposition.," Nano letters, vol. 9, pp. 30–5, Jan. 2009.

[208] A. Umair and H. Raza, "Controlled synthesis of bilayer graphene on nickel," Nano Express, vol. 7, no. 437, 2012.

[209] A. Dahal, R. Addou, P. Sutter, and M. Batzill, "Graphene monolayer rotation on Ni(111) facilitates bilayer graphene growth," Applied Physics Letters, vol. 100, no. 24, p. 241602, 2012.

[210] R. Gerlach and T. Rhodin, "Binding and Charge Transfer associated with alkali metal adsorption on single crystal nickel surfaces," Surface Science, vol. 19, pp. 403–426, 1970.

[211] C. Oshima and A. Nagashima, "Ultra-thin epitaxial films of graphite and hexagonal boron nitride on solid surfaces," Journal of Physics: Condensed Matter, vol. 9, pp. 1–20, Jan. 1997.

[212] M. Helander, M. Greiner, Z. Wang, and Z. Lu, "Pitfalls in measuring work function using photoelectron spectroscopy," Feb. 2010.

[213] B. Hellsing, D. V. Chakarov, L. Osterlund, V. P. Zhdanov, and B. Kasemo, "Photoinduced desorption of potassium atoms from a two dimensional overlayer on graphite," The Journal of Chemical Physics, vol. 106, no. 3, p. 982, 1997.

[214] M. Petrović, I. Šrut Rakić, S. Runte, C. Busse, J. T. Sadowski, P. Lazić, I. Pletikosić, Z.-H. Pan, M. Milun, P. Pervan, N. Atodiresei, R. Brako, D. Šokčević, T. Valla, T. Michely, and M. Kralj, "The mechanism of caesium intercalation of graphene.," Nature communications, vol. 4, p. 2772, Nov. 2013.

[215] M. Amft, S. Lebègue, O. Eriksson, and N. V. Skorodumova, "Adsorption of Cu, Ag, and Au atoms on graphene including van der Waals interactions.," Journal of physics. Condensed matter : an Institute of Physics journal, vol. 23, p. 395001, Oct. 2011.

[216] Y. Ren, S. Chen, W. Cai, Y. Zhu, C. Zhu, and R. S. Ruoff, "Controlling the electrical transport properties of graphene by in situ metal deposition," Applied Physics Letters, vol. 97, no. 5, p. 053107, 2010.

[217] A. Dahal and M. Batzill, "Graphene-nickel interfaces: a review.," Nanoscale, vol. 6, pp. 2548–62, Mar. 2014.

[218] L. Zhang, N. Vinogradov, A. Preobrajenski, S. Butorin, J. Zhu, and J. Guo, "Probing substrate-induced perturbations on the band structure of graphene on Ni(111) by soft X-ray emission spectroscopy," Chemical Physics Letters, vol. 580, pp. 43–47, Aug. 2013.

[219] S. M. Kozlov, F. Vin, and A. Go, "Bonding Mechanisms of Graphene on Metal Surfaces," Journal of Physical Chemistry C, vol. 13, no. 116, 2012.

[220] M. Weser, E. N. Voloshina, K. Horn, and Y. S. Dedkov, "Electronic structure and magnetic properties of the graphene/Fe/Ni111 intercalation-like system.," Physical chemistry chemical physics : PCCP, vol. 13, pp. 7534–9, Apr. 2011.

[221] J. Rusz, a. B. Preobrajenski, M. L. Ng, N. a. Vinogradov, N. Må rtensson, O. Wessely, B. Sanyal, and O. Eriksson, "Dynamical effects in x-ray absorption spectra of graphene and monolayered h-BN on Ni(111)," Physical Review B, vol. 81, p. 073402, Feb. 2010.

[222] D. V. Chakarov, L. Osterlund, B. Hellsing, V. P. Zhdanov, and B. Kasemo, "Photostimulated desorption of metal adatoms : potassium on graphite," Surface Science, vol. 3, no. 311, 1994.

[223] S. Watcharinyanon, L. I. Johansson, C. Xia, and C. Virojanadara, "Changes in structural and electronic properties of graphene grown on 6H-SiC(0001) induced by Na deposition," Journal of Applied Physics, vol. 111, no. 8, p. 083711, 2012.

[224] D. W. Boukhvalov and C. Virojanadara, "Penetration of alkali atoms throughout a graphene membrane: theoretical modeling.," Nanoscale, vol. 4, pp. 1749–53, Mar. 2012.

[225] Y. Li, G. Zhou, J. Li, J. Wu, B.-L. Gu, and W. Duan, "Lithium Intercalation Induced Decoupling of Epitaxial Graphene on SiC(0001): Electronic Property and Dynamic Process," The Journal of Physical Chemistry C, vol. 115, pp. 23992–23997, Dec. 2011.

[226] S.-M. Choi and S.-H. Jhi, "Electronic property of Na-doped epitaxial graphenes on SiC," Applied Physics Letters, vol. 94, no. 15, p. 153108, 2009.

[227] C. Hwang, D. a. Siegel, S.-K. Mo, W. Regan, A. Ismach, Y. Zhang, A. Zettl, and A. Lanzara, "Fermi velocity engineering in graphene by substrate modification," Scientific Reports, vol. 2, pp. 2–5, Aug. 2012.

[228] M. Shek, X. Pan, M. Strongin, and M. Ruckman, "Interaction of oxygen with sodium at 80 and 20 K," Physical Review B, vol. 34, no. 6, 1986.

[229] Y. S. Dedkov, M. Fonin, U. Rudiger, and C. Laubschat, "Graphene-protected iron layer on Ni(111)," Applied Physics Letters, vol. 93, no. 2, p. 022509, 2008.

[230] A. Sandin, T. Jayasekera, J. E. Rowe, K. W. Kim, M. Buongiorno Nardelli, and D. B. Dougherty, "Multiple coexisting intercalation structures of sodium in epitaxial graphene-SiC interfaces," Physical Review B, vol. 85, p. 125410, Mar. 2012.

[231] D. V. Chakarov, L. Osterlund, B. Hellsing, and B. Kasemo, "Photon induced desorption and intercalation of potassium atoms deposited on graphite (0001)," Applied Surface Science, vol. 106, pp. 186–192, 1996.

[232] J. L. McChesney, A. Bostwick, T. Ohta, T. Seyller, K. Horn, J. González, and E. Rotenberg, "Extended van Hove Singularity and Superconducting Instability in Doped Graphene," Physical Review Letters, vol. 104, p. 136803, Apr. 2010.

[233] C. Xia, S. Watcharinyanon, a.a. Zakharov, L. Johansson, R. Yakimova, and C. Virojanadara, "Detailed studies of Na intercalation on furnace-grown graphene on 6H-SiC(0001)," Surface Science, vol. 613, pp. 88–94, July 2013.

[234] a. Sandell, O. Hjortstam, a. Nilsson, P. Brühwiler, O. Eriksson, P. Bennich, P. Rudolf, J. Wills, B. Johansson, and N. Må rtensson, "Bonding of an Isolated K atom to a Surface: Experiment and Theory," Physical Review Letters, vol. 78, pp. 4994–4997, June 1997.

[235] K. Watanabe, N. Takagi, and Y. Matsumoto, "Direct Time-Domain Observation of Ultrafast Dephasing in Adsorbate-Substrate Vibration under the Influence of a Hot Electron Bath: Cs Adatoms on Pt(111)," Physical Review Letters, vol. 92, p. 057401, Feb. 2004.

[236] C. Jeon, H.-C. Shin, I. Song, M. Kim, J.-H. Park, J. Nam, D.-H. Oh, S. Woo, C.-C. Hwang, C.-Y. Park, and J. R. Ahn, "Opening and reversible control of a wide energy gap in uniform monolayer graphene.," Scientific reports, vol. 3, p. 2725, Jan. 2013.

[237] T. Hori Gate Dielectrics and MOS ULSIs, no. Springer, New York, 1997.

[238] G. D. Wilk, R. M. Wallace, and J. M. Anthony, "High-κ gate dielectrics: Current status and materials properties considerations," Journal of Applied Physics, vol. 89, no. 10, p. 5243, 2001.

[239] T. Toyabe, H. Kadera, and H. Kodera, "Generalized Scaling Theory and Its Application," IEEE Transactions on Electron Devices, vol. 41, no. 4, pp. 1283–1290, 1984.

[240] I. Ferain, C. a. Colinge, and J.-P. Colinge, "Multigate transistors as the future of classical metal-oxide-semiconductor field-effect transistors," Nature, vol. 479, pp. 310–6, Nov. 2011.

[241] S. M. Sze Physics of Semiconductor Devices, no. Wiley, New York, 2007.

[242] M. Schulz, "The end of the road for silicon ?," Nature, vol. 399, no. June, 1999.

[243] R. Dennard, F. Gaensslen, H. Yu, V. Rideout, E. Bassous, and A. LeBlanc, "Design of Ion-Implanted Small MOSFET S Dimensions with Very Small Physical Dimensions," IEEE Journal of Solid-state Circuits, vol. 9, no. 5, 1974.

[244] D. A. Buchanan, "Scaling the gate dielectric : Materials , integration , and reliability," IBM Journal of Research and Development, vol. 43, no. 3, pp. 245–264, 1999.

[245] M. L. Green, E. P. Gusev, R. Degraeve, and E. L. Garfunkel, "Ultrathin (¡4 nm) SiO[sub 2] and SiON gate dielectric layers for silicon microelectronics: Understanding the processing, structure, and physical and electrical limits," Applied Physics Reviews, vol. 90, no. 5, p. 2057, 2001.

[246] E. P. Gusev, V. Narayanan, and M. M. Frank, "Advanced high-κ dielectric stacks with polySi and metal gates: Recent progress and current challenges," IBM Journal of Research and Development, vol. 50, pp. 387–410, July 2006.

[247] J. R. Weber, a. Janotti, and C. G. Van de Walle, "Native defects in Al[sub 2]O[sub 3] and their impact on III-V/Al[sub 2]O[sub 3] metal-oxide-semiconductor-based devices," Journal of Applied Physics, vol. 109, no. 3, p. 033715, 2011.

[248] M. M. Frank, G. D. Wilk, D. Starodub, T. Gustafsson, E. Garfunkel, Y. J. Chabal, J. Grazul, and D. a. Muller, "HfO[sub 2] and Al[sub 2]O[sub 3] gate dielectrics on GaAs grown by atomic layer deposition," Applied Physics Letters, vol. 86, no. 15, p. 152904, 2005.

[249] P. D. Ye, "Main determinants for IIIV metal-oxide-semiconductor field-effect transistors (invited)," Journal of Vacuum Science & Technology A: Vacuum, Surfaces, and Films, vol. 26, no. 4, p. 697, 2008.

[250] S. Koveshnikov, W. Tsai, I. Ok, J. C. Lee, V. Torkanov, M. Yakimov, and S. Oktyabrsky, "Metal-oxide-semiconductor capacitors on GaAs with high-k gate oxide and amorphous silicon interface passivation layer," Applied Physics Letters, vol. 88, no. 2, p. 022106, 2006.

[251] M. El Kazzi, L. Czornomaz, C. Rossel, C. Gerl, D. Caimi, H. Siegwart, J. Fompeyrine, and C. Marchiori, "Thermally stable, sub-nanometer equivalent oxide thickness gate stack for gate-first In0.53Ga0.47As metal-oxide-semiconductor field-effect-transistors," Applied Physics Letters, vol. 100, no. 6, p. 063505, 2012.

[252] A. D. Carter, W. J. Mitchell, B. J. Thibeault, J. J. M. Law, and M. J. W. Rodwell, "Al$_{2}$O$_{3}$ Growth on (100) In$_{0.53}$Ga$_{0.47}$As Initiated by Cyclic Trimethylaluminum and Hydrogen Plasma Exposures," Applied Physics Express, vol. 4, p. 091102, Aug. 2011.

[253] W. Melitz, J. Shen, T. Kent, A. C. Kummel, and R. Droopad, "InGaAs surface preparation for atomic layer deposition by hydrogen cleaning and improvement with high temperature anneal," Journal of Applied Physics, vol. 110, no. 1, p. 013713, 2011.

[254] V. Chobpattana, T. E. Mates, W. J. Mitchell, J. Y. Zhang, and S. Stemmer, "Influence of plasma-based in-situ surface cleaning procedures on HfO2/In0.53Ga0.47As gate stack properties," Journal of Applied Physics, vol. 114, no. 15, p. 154108, 2013.

[255] V. Djara, S. Member, K. Cherkaoui, M. Schmidt, S. Monaghan, E. O. Connor, I. M. Povey, D. O. Connell, M. E. Pemble, and P. K. Hurley, "Impact of Forming Gas Anneling on the performance of surface channel InGaAs MOSFETs With an ALD Al 2 O 3 Gate Dielectric," vol. 59, no. 4, pp. 1084–1090, 2012.

[256] C. Y. Ytterdal, T and T. Fjeldly Device Modeling for Analog and RF CMOS Circuit Design, no. Wiley, New York, 2003.

[257] D. Lim and R. Haight, "In situ photovoltage measurements using femtosecond pump-probe photoelectron spectroscopy and its application to metalHfO[sub 2]Si structures," Journal of Vacuum Science & Technology A: Vacuum, Surfaces, and Films, vol. 23, no. 6, p. 1698, 2005.

[258] D. Bröcker, T. Gieß el, and W. Widdra, "Charge carrier dynamics at the SiO2/Si(100) surface: a time-resolved photoemission study with combined laser and synchrotron radiation," Chemical Physics, vol. 299, pp. 247–251, Apr. 2004.

[259] L. Stauffer Fundamentals of Semiconductor C-V Measurements, no. Keithley Instruments Distributions, 2009.

[260] R. D. Long, B. Shin, S. Monaghan, K. Cherkaoui, J. Cagnon, S. Stemmer, P. C. McIntyre, and P. K. Hurley, "Charged Defect Quantification in PtAl2O3In0.53Ga0.47AsInP MOS Capacitors," Journal of The Electrochemical Society, vol. 158, no. 5, p. G103, 2011.

[261] G. Brammertz, A. Alian, D. H.-c. Lin, M. Meuris, M. Caymax, and W. Wang, "A Combined Interface and Border Trap Model for High-Mobility Substrate Metal Oxide Semiconductor

Devices Applied to In 0 . 53 Ga 0 . 47 As and InP Capacitors," IEEE Transactions on Electron Devices, vol. 58, no. 11, pp. 3890–3897, 2011.

[262] P. K. Hurley, E. O. Connor, V. Djara, S. Member, S. Monaghan, S. Member, I. M. Povey, R. D. Long, B. Sheehan, J. Lin, P. C. Mcintyre, B. Brennan, R. M. Wallace, M. E. Pemble, and K. Cherkaoui, "The Characterization and Passivation of Fixed Oxide Charges and Interface States in the Al 2 O 3 / InGaAs MOS System," IEEE Transactions on Device and Materials Reliability, vol. 13, no. 4, pp. 429–443, 2013.

[263] R. Engel-Herbert, Y. Hwang, and S. Stemmer, "Comparison of methods to quantify interface trap densities at dielectric/III-V semiconductor interfaces," Journal of Applied Physics, vol. 108, no. 12, p. 124101, 2010.

[264] Y. Yuan, L. Wang, B. Yu, B. Shin, J. Ahn, P. C. Mcintyre, P. M. Asbeck, M. J. W. Rodwell, and Y. Taur, "A Distributed Model for Border Traps in Al2O3 - InGaAs MOS Devices," IEEE Transactions on Electron Devices, vol. 32, no. 4, pp. 485–487, 2011.

[265] E. J. Kim, L. Wang, P. M. Asbeck, K. C. Saraswat, and P. C. McIntyre, "Border traps in Al[sub 2]O[sub 3]/In[sub 0.53]Ga[sub 0.47]As (100) gate stacks and their passivation by hydrogen anneals," Applied Physics Letters, vol. 96, no. 1, p. 012906, 2010.

[266] D. Lim and R. Haight, "Temperature dependent defect formation and charging in hafnium oxides and silicates," Journal of Vacuum Science & Technology B: Microelectronics and Nanometer Structures, vol. 23, no. 1, p. 201, 2005.

[267] Y. C. Chang, M. L. Huang, K. Y. Lee, Y. J. Lee, T. D. Lin, M. Hong, J. Kwo, T. S. Lay, C. C. Liao, and K. Y. Cheng, "Atomic-layer-deposited HfO[sub 2] on In[sub 0.53]Ga[sub 0.47]As: Passivation and energy-band parameters," Applied Physics Letters, vol. 92, no. 7, p. 072901, 2008.

[268] B. Brennan and G. Hughes, "Identification and thermal stability of the native oxides on InGaAs using synchrotron radiation based photoemission," Journal of Applied Physics, vol. 108, no. 5, p. 053516, 2010.

[269] F. S. Aguirre-Tostado, M. Milojevic, C. L. Hinkle, E. M. Vogel, R. M. Wallace, S. McDonnell, and G. J. Hughes, "Indium stability on InGaAs during atomic H surface cleaning," Applied Physics Letters, vol. 92, no. 17, p. 171906, 2008.

[270] B. Shin, J. R. Weber, R. D. Long, P. K. Hurley, C. G. Van de Walle, and P. C. McIntyre, "Origin and passivation of fixed charge in atomic layer deposited aluminum oxide gate insulators on chemically treated InGaAs substrates," Applied Physics Letters, vol. 96, no. 15, p. 152908, 2010.

[271] C. L. Hinkle, a. M. Sonnet, E. M. Vogel, S. McDonnell, G. J. Hughes, M. Milojevic, B. Lee, F. S. Aguirre-Tostado, K. J. Choi, H. C. Kim, J. Kim, and R. M. Wallace, "GaAs interfacial self-cleaning by atomic layer deposition," Applied Physics Letters, vol. 92, no. 7, p. 071901, 2008.

[272] S. Kim, S. L. Brown, S. M. Rossnagel, J. Bruley, M. Copel, M. J. P. Hopstaken, V. Narayanan, and M. M. Frank, "Oxygen migration in TiO[sub 2]-based higher-k gate stacks," Journal of Applied Physics, vol. 107, no. 5, p. 054102, 2010.

[273] M. M. Frank, S. Kim, S. L. Brown, J. Bruley, M. Copel, M. Hopstaken, M. Chudzik, and V. Narayanan, "Scaling the MOSFET gate dielectric: From high-k to higher-k? (Invited Paper)," Microelectronic Engineering, vol. 86, pp. 1603–1608, July 2009.

[274] E. Cartier, M. Hopstaken, and M. Copel, "Oxygen passivation of vacancy defects in metal-nitride gated HfO[sub 2]/SiO[sub 2]/Si devices," Applied Physics Letters, vol. 95, no. 4, p. 042901, 2009.

[275] M. L. Huang, Y. C. Chang, C. H. Chang, Y. J. Lee, P. Chang, J. Kwo, T. B. Wu, and M. Hong, "Surface passivation of III-V compound semiconductors using atomic-layer-deposition-grown Al[sub 2]O[sub 3]," Applied Physics Letters, vol. 87, no. 25, p. 252104, 2005.

[276] K. Piskorski and H. M. Przewlocki, "The methods to determine flat-band voltage V FB in semiconductor of a MOS structure," MIPRO Proceedings, no. May 24-28, pp. 37–42, 2010.

[277] O. Kfir, P. Grychtol, E. Turgut, R. Knut, D. Zusin, D. Popmintchev, T. Popmintchev, H. Nembach, J. M. Shaw, A. Fleischer, H. Kapteyn, M. Murnane, and O. Cohen, "Generation of bright phase-matched circularly-polarized extreme ultraviolet high harmonics," Nature Photonics, pp. 1–7, Dec. 2014.

[278] C. Long, W. Becker, and J. McIver, "Model calculations of polarization-dependent two-color high-harmonic generation," Physical Review A, vol. 52, no. 3, pp. 2262–2278, 1995.

[279] M. Ivanov and E. Pisanty, "High-harmonic generation: Taking control of polarization," Nature Photonics, vol. 8, pp. 501–503, June 2014.

[280] U. Heinzmann and J. H. Dil, "Spin-orbit-induced photoelectron spin polarization in angle-resolved photoemission from both atomic and condensed matter targets.," Journal of physics. Condensed matter : an Institute of Physics journal, vol. 24, p. 173001, May 2012.

[281] J. Kessler Polarized Electrons, no. Berlin, Springer, 2nd Ed, 1985.

[282] G. Snell, M. Drescher, N. Müller, U. Heinzmann, U. Hergenhahn, J. Viefhaus, F. Heiser, U. Becker, and N. Brookes, "Spin Polarized Auger Electrons: The Xe M4,5N4,5N4,5 Case," Physical Review Letters, vol. 76, pp. 3923–3926, May 1996.

[283] P. D. Johnson, "Spin-polarized photoemission," Reports on Progress in Physics, vol. 60, pp. 1217–1304, Nov. 1997.

[284] I. Gierz, M. Lindroos, H. Höchst, C. R. Ast, and K. Kern, "Graphene sublattice symmetry and isospin determined by circular dichroism in angle-resolved photoemission spectroscopy.," Nano letters, vol. 12, pp. 3900–4, Aug. 2012.

[285] S.-Y. Xu, M. Neupane, C. Liu, D. Zhang, A. Richardella, L. Andrew Wray, N. Alidoust, M. Leandersson, T. Balasubramanian, J. Sánchez-Barriga, O. Rader, G. Landolt, B. Slomski, J. Hugo Dil, J. Osterwalder, T.-R. Chang, H.-T. Jeng, H. Lin, A. Bansil, N. Samarth, and M. Zahid Hasan, "Hedgehog spin texture and Berrys phase tuning in a magnetic topological insulator," Nature Physics, vol. 8, pp. 616–622, June 2012.

[286] a. Scholl, L. Baumgarten, R. Jacquemin, and W. Eberhardt, "Ultrafast Spin Dynamics of Ferromagnetic Thin Films Observed by fs Spin-Resolved Two-Photon Photoemission," Physical Review Letters, vol. 79, pp. 5146–5149, Dec. 1997.

[287] K. Maiti, M. Malagoli, a. Dallmeyer, and C. Carbone, "Finite Temperature Magnetism in Gd: Evidence against a Stoner Behavior," Physical Review Letters, vol. 88, p. 167205, Apr. 2002.

[288] R. Carley, K. Döbrich, B. Frietsch, C. Gahl, M. Teichmann, O. Schwarzkopf, P. Wernet, and M. Weinelt, "Femtosecond Laser Excitation Drives Ferromagnetic Gadolinium out of Magnetic Equilibrium," Physical Review Letters, vol. 109, p. 057401, July 2012.

[289] G. Schonhense, "Circular Dichroism and Spin Polarization in Photoemission from Adsorbates and Non-Magnetic Solids," Physica Scripta, vol. T31, pp. 254–275, 1990.

[290] Y. Liu, G. Bian, T. Miller, and T.-C. Chiang, "Visualizing Electronic Chirality and Berry Phases in Graphene Systems Using Photoemission with Circularly Polarized Light," Physical Review Letters, vol. 107, p. 166803, Oct. 2011.

[291] N. Tombros, S. Tanabe, a. Veligura, C. Jozsa, M. Popinciuc, H. Jonkman, and B. van Wees, "Anisotropic Spin Relaxation in Graphene," Physical Review Letters, vol. 101, p. 046601, July 2008.

[292] D. Huertas-Hernando, F. Guinea, and A. Brataas, "Spin-Orbit-Mediated Spin Relaxation in Graphene," Physical Review Letters, vol. 103, p. 146801, Sept. 2009.

[293] J. Fabian, A. Matos-Abiague, C. Ertler, P. Stano, and I. Zutic, "SEMICONDUCTOR SPINTRONICS," arXiv:0711.1461, 2007.

[294] N. Tombros, C. Jozsa, M. Popinciuc, H. T. Jonkman, and B. J. van Wees, "Electronic spin transport and spin precession in single graphene layers at room temperature.," Nature, vol. 448, pp. 571–4, Aug. 2007.

[295] a. Castro Neto and F. Guinea, "Impurity-Induced Spin-Orbit Coupling in Graphene," Physical Review Letters, vol. 103, p. 026804, July 2009.

[296] Y. H. Wang, H. Steinberg, Jarillo-Herrero, and N. Gedik, "Observation of Floquet-Bloch States on the Surface of a Topological Insulator," Science, vol. 108, no. 2011, 2013.

[297] Y. Wang and N. Gedik, "Circular dichroism in angle-resolved photoemission spectroscopy of topological insulators," physica status solidi (RRL) - Rapid Research Letters, vol. 7, pp. 64–71, Feb. 2013.

[298] Y. H. Wang, D. Hsieh, E. J. Sie, H. Steinberg, D. R. Gardner, Y. S. Lee, P. Jarillo-Herrero, and N. Gedik, "Measurement of Intrinsic Dirac Fermion Cooling on the Surface of the Topological Insulator Bi_{2}Se_{3} Using Time-Resolved and Angle-Resolved Photoemission Spectroscopy," Physical Review Letters, vol. 109, p. 127401, Sept. 2012.

[299] J. W. McIver, D. Hsieh, H. Steinberg, P. Jarillo-Herrero, and N. Gedik, "Control over topological insulator photocurrents with light polarization.," Nature nanotechnology, vol. 7, pp. 96–100, Feb. 2012.

[300] M. Z. Hasan and C. L. Kane, "Colloquium: Topological insulators," Reviews of Modern Physics, vol. 82, pp. 3045–3067, Nov. 2010.

[301] D. Hsieh, F. Mahmood, J. W. McIver, D. R. Gardner, Y. S. Lee, and N. Gedik, "Selective Probing of Photoinduced Charge and Spin Dynamics in the Bulk and Surface of a Topological Insulator," Physical Review Letters, vol. 107, p. 077401, Aug. 2011.

[302] F. Blobner, R. Han, A. Kim, W. Wurth, and P. Feulner, "Spin-Dependent Electron Transfer Dynamics Probed by Resonant Photoemission Spectroscopy," Physical Review Letters, vol. 112, p. 086801, Feb. 2014.

[303] A. Clarke, N. Brookes, P. Johnson, M. Weinert, B. Sinkovic, and N. Smith, "Spin-polarized photoemission studies of the adsorption of 0 and S on Fe(001)," Physical Review B, vol. 41, no. 14, 1990.

[304] C. L. Hinkle, M. Milojevic, B. Brennan, a. M. Sonnet, F. S. Aguirre-Tostado, G. J. Hughes, E. M. Vogel, and R. M. Wallace, "Detection of Ga suboxides and their impact on III-V passivation and Fermi-level pinning," Applied Physics Letters, vol. 94, no. 16, p. 162101, 2009.

[305] H. Hasegawa and M. Akazawa, "Surface passivation technology for IIIV semiconductor nanoelectronics," Applied Surface Science, vol. 255, pp. 628–632, Nov. 2008.

[306] D. Straub, M. Skibowski, and F. Himpsel, "Conduction-band dispersion, critical points, and unoccupied surface states on CxaAs(110): A high-resolution angle-resolved inverse photoemission study," Physical Review B, vol. 32, no. 8, 1985.

[307] L. D. Bell and W. Kaiser, "Observation of Interface Band Structure by Ballistic-Electron-Emission Microscopy," Physical Review Letters, vol. 61, no. 20, pp. 2368–2371, 1988.

[308] J. Lloyd-Hughes, S. K. E. Merchant, L. Fu, H. H. Tan, C. Jagadish, E. Castro-Camus, and M. B. Johnston, "Influence of surface passivation on ultrafast carrier dynamics and terahertz radiation generation in GaAs," Applied Physics Letters, vol. 89, no. 23, p. 232102, 2006.

[309] A. Bakun, B. Zakharchenya, A. Rogachev, M. Tkachuk, and V. Fleisher, "Observation of a surface photocurrent caused by optical prientation of electrons in a semiconductor," Pis'ma Zh. Eksp. Teor. Fiz, vol. 40, no. 11, pp. 464–466, 1984.

[310] J. M. Kikkawa and D. D. Awschalom, "Resonant Spin Amplification in n -Type GaAs," Physical Review Le, vol. 80, no. 19, pp. 4313–4316, 1998.

[311] P. Song and K. Kim, "Spin relaxation of conduction electrons in bulk III-V semiconductors," Physical Review B, vol. 66, p. 035207, July 2002.

[312] G. Kresse and J. Furthmueller, "Efficient iterative schemes for ab initio total-energy calculations using a plane-wave basis set ," Physical Review B, vol. 54, no. 16, 1996.

[313] P. Blochl, "Projector augmented-wave method," Physical Review B, vol. 50, no. 24, 1994.

[314] G. Kresse and D. Joubert, "From ultrasoft pseudopotentials to the projector augmented-wave method," Physical Review B, vol. 59, no. 3, pp. 11–19, 1999.

[315] J. Klimeš, D. R. Bowler, and A. Michaelides, "Chemical accuracy for the van der Waals density functional.," Journal of physics. Condensed matter, vol. 22, p. 022201, Jan. 2010.

[316] J. Klimeš, D. R. Bowler, and A. Michaelides, "Van der Waals density functionals applied to solids," Physical Review B, vol. 83, p. 195131, May 2011.

[317] M. Dion, H. Rydberg, E. Schröder, D. C. Langreth, and B. I. Lundqvist, "Van der Waals Density Functional for General Geometries," Physical Review Letters, vol. 92, p. 246401, June 2004.

[318] H. J. Monkhorst and J. D. Pack, "SPECIAL POINTS FOR BRILLOUIN-ZONE INTEGRATIONS," Physical Review B, vol. 13, no. 12, pp. 5188–5192, 1976.

Appendix A

Supplemental Material

A.1 Multilayer Mirror Characterization and Coatings

In calculating the theoretical reflectivity when designing the multilayers, several properties of the mirrors needed to be specified, including:

- *Interdiffusion thickness*: The thickness of the intermixed layer between the two multilayer materials. This is material dependent and can vary from ∼0.4 nm for Mo/Si to ∼1.5 nm for Mg/SiC coatings.

- γ: The ratio of the bottom layer thickness to the period (ie. a difference in the relative thickness between the one multilayer material and the other). This was set between 0.3-0.9 depending on the coating and had the effect of slightly shifting the wavelength of the peak in reflectivity.

- *Number of Periods*: Total number of deposited layers, where the deposition of both multilayer materials is defined as one period. Typical number of periods is 40 for the mirrors used here, producing the narrow reflectivity bandwidth seen in Fig A.1. More broadband reflectivities (with higher peak reflectivity) were also designed using as few as 20 periods.

- *Incident Angle* θ: Incident angle of the EUV beam onto the mirror surface. Angles as little as 3 degrees produce as noticeable shift in the central peak reflectivity wavelength. Mirrors were initially designed for a working angle of 3 degrees incidence due to the "Z" layout of the beam in the mirror chamber.

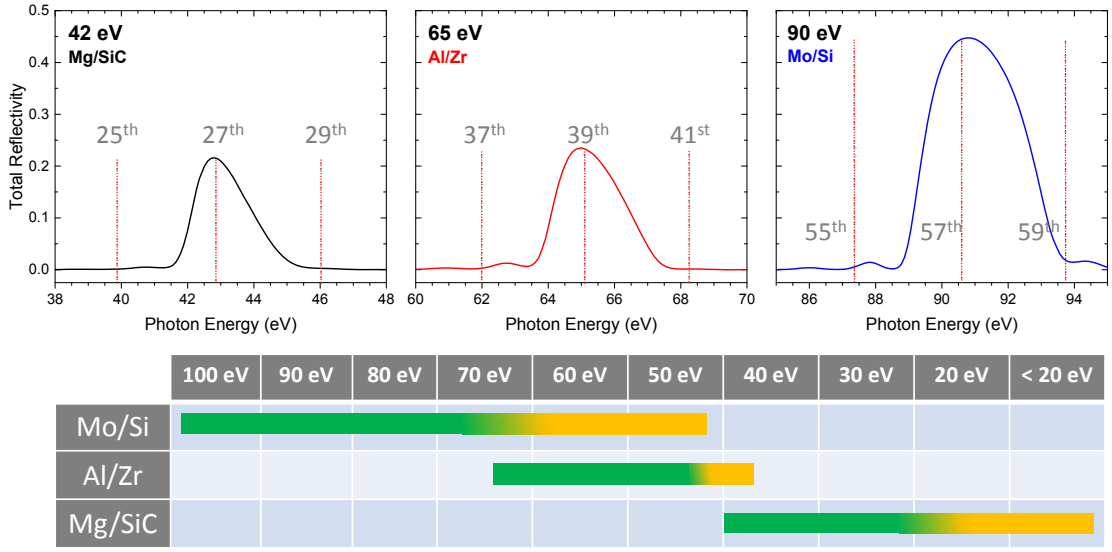

Figure A.1: Multilayer mirror reflectivity for most commonly used wavelength and corresponding multilayer material shown with optimal photon energy range

A.2 1ω Optical interference unique from RABITT effect

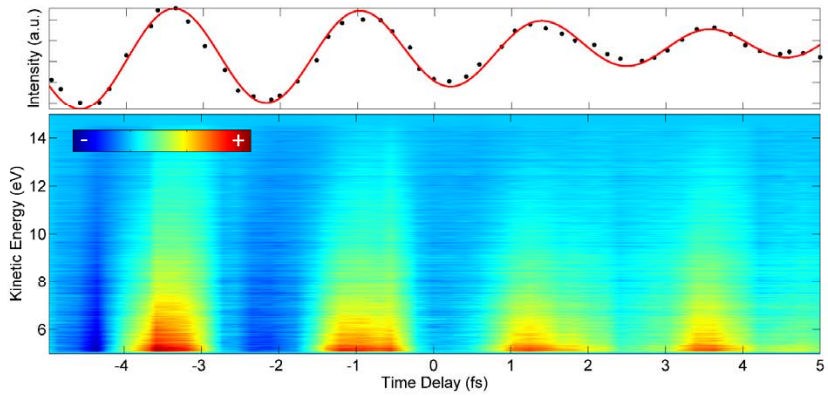

Figure A.2: Multiphoton ionization integrated over ±6 degrees emission angle as a function of delay. Top temporal lineout is integrated over a kinetic energy region from 6-12 eV to show oscillations with 1 period.

The observed 1ω oscillation shown in Fig. A.2 (period = 2.6 fs) is the optical interference of the incident pump and probe pulses above the surface. This measurement shows that the 2ω frequency interferences discussed previously are not simply an optical interference effect.The

stability of the laser and HHG optical paths was measured using above-threshold ionization induced in Cu(111) by synchronized IR pump and probe fields.

A.3 Surface Emission from Cu(111) in RABITT studies

For laser-assisted photoemission in the presence of a moderate intensity laser field ($2.8 * 10^{11} W/cm^2$, 8μJ/pulse), the sidebands intensity disappears at the minimum interference. In this case, the PES is identical to that with no temporally overlapped IR/HHG pulses. This is shown in Fig. Fig. 4.7(b). However, when a higher laser intensity is used, the sidebands do not disappear at this minimum point. An IR field of $4 * 10^{11} W/cm^2$ (12μ J/pulse) is sufficient to produce a residual incoherent background, shown in Fig S5(a). Note that laser-assisted photoemission is strong in all cases before background subtraction. While an intensity difference was still high between the minimum and maximum of the sideband oscillation amplitude, the minimum is not zero.

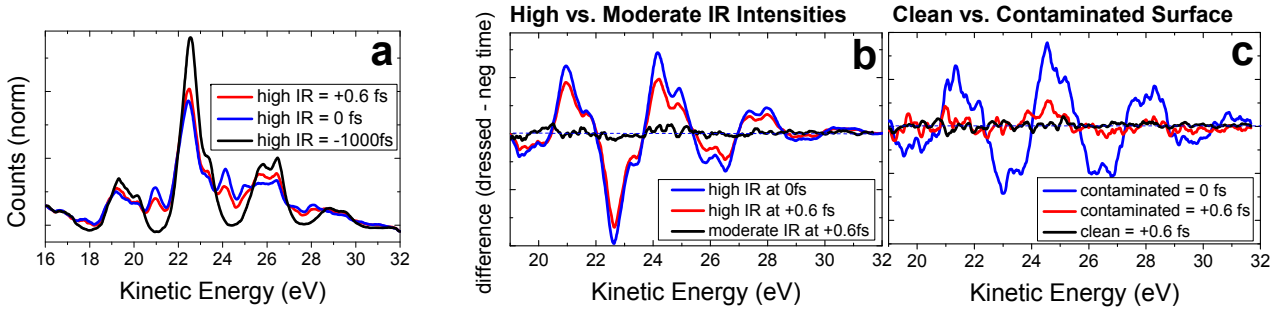

Figure A.3: (a) Sidebands generated by an intense IR field shown with raw integrated intensity spectrum. (b) The corresponding difference spectra. Note that sidebands do not vanish at minimum, comparing spectrum with a weaker IR field (black) vs. red (strong). (c) Comparison of surface contaminated and clean sample: sideband at the minimum intensity is not zero (compare red vs. black traces, for contaminated vs. clean).

This incoherent background becomes strong two hours after the surface was cleaned - even for low and moderate intensities of the IR field. Since this effect can be eliminated by re-cleaning the surface, we attribute it to a gradual contamination on the surface. This is a clear indication that the coherent interference oscillations we observe occur at the surface, since they disappear before any other PES or LAPE spectral intensity changes. If the coherent sideband interferences

originated from the bulk, they should be less sensitive to surface contamination, provided other bulk features were not affected by contamination. Furthermore, the reduction in contrast (addition of an incoherent background) at higher IR laser intensity can be explained as due to a high number of electrons emitted from the surface at high laser fluence, leading to incoherent electron-electron scattering events that destroy the quantum coherence.

Further support of the surface emission of the photoemitted states is seen through analyzing the initial energy of the observed sp and d band features. Plotting each harmonic's photoemitted spectra on a scale relative to the Fermi energy, the peaks of the sp and d spectral features are seen to be constant over the harmonic comb. This implies no dispersion in the $k_{\perp}$ direction of the bands and only a $k_{||}$ component of the momenta.

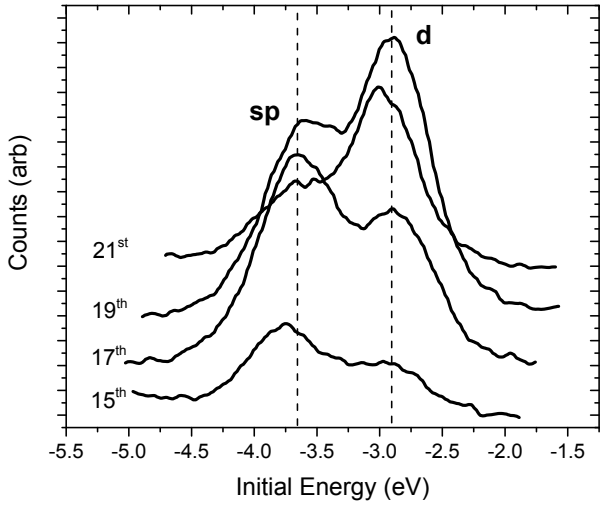

Figure A.4: $k_{\perp}$ dispersion for sp and d states over the harmonic comb

A.4 Fourier Analysis Method- RABITT studies on Cu(111)

Figure A.5(a) shows the photoemission spectrum of Cu(111) measured along the $\overline{\Gamma M}$ direction of the surface Brillouin zone, using a He Iα source. The spectrum shows the momentum regions used in extracting time-resolved information on the surface state and non-surface (sp and d bands) spectral features.

We defined two integration regions to obtain time-resolved information for each unique state. Due to the finite extent of the surface state, Region (1) is the momentum range where the bulk bands exist, not overlapping with the surface state (i.e. from ± 0.15 $\mathring{A}^{-1}$ to 0.3 $\mathring{A}^{-1}$). Region (2) is where the surface state momentum overlaps and is dominant over the bulk sp band (ie. from $\pm 0.15 \mathring{A}^{-1}$). Integrated intensities of the surface state, sp & d bands, and sidebands over these regions (1) and (2) can then be uniquely extracted. The representative lineout shown in Fig A.5(b) is obtained by integrating over the momentum axis of Region (1) in Fig. A.5(a).

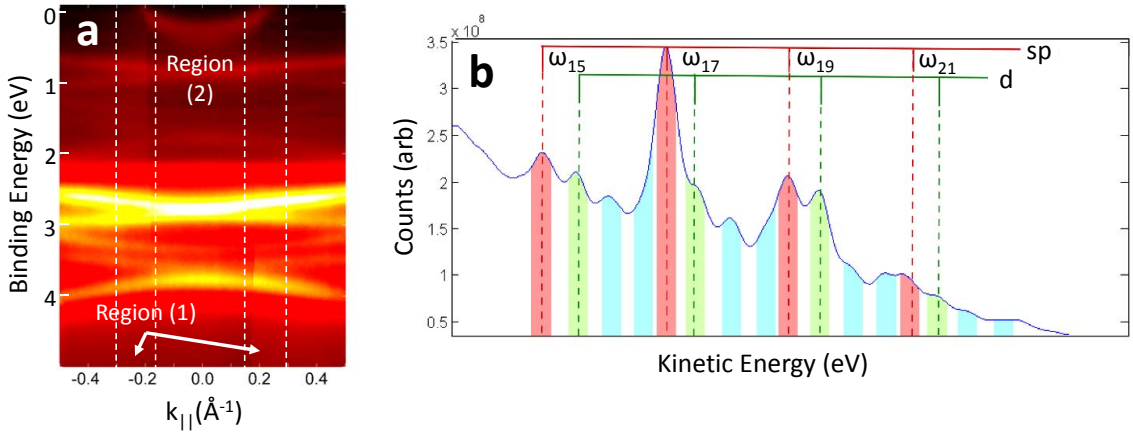

Figure A.5: (a) Photoemission spectrum of Cu(111) along the $\overline{\Gamma M}$ direction of the surface Brillion zone. The non-surface state integration (Region 1) and the surface state integration region (Region 2) are shown with dashed vertical lines. (b) Representative integrated intensity region for the sp (red), d (green), and sideband (blue) peaks for each harmonic. Integration regions widths were defined with respect to the centers of peaks as ± 0.1 eV

Intensities corresponding to each state were extracted from each momentum-integrated spectrum in multiple temporal scans from -3 fs to +3 fs, collected over short ($\sim$ 5 sec) integration times per time-delay step. We then applied Fourier analysis to N $>$ 100 scans to obtain the relative phase of the sideband oscillation. Shorter acquisition times for each scan ($\sim$ 3 min) made it possible to obtain more spectra for analysis, while still preserving good signal-to-noise. The autopower:

$$S_{xx}(f) = \sum_{n=1}^{N} |\widetilde{x}_n^* \widetilde{x}_n| \tag{A.1}$$

where $\widetilde{x}n$ is the Fourier transform of the $(\omega_{17} + \omega))$ sidebands n^{th} temporal scan, was calculated

for each scan to gauge the relative signal-to-noise ratio. Only scans with a dominant power in one frequency mode were used in analysis.

The average cross-spectral density power was calculated to compare the bulk sidebands (from either sp or d band) with the surface state sideband for each harmonic. The average cross-spectral density power was calculated for each harmonic according to:

$$S_{xy}(f) = \sum_{n=1}^{N} |\widetilde{x}_n^* \widetilde{y}_n| \tag{A.2}$$

where $\widetilde{x}n$ is the Fourier transform of the bulk band n^{th} temporal scan, $\widetilde{y}_n$ is the Fourier transform of the surface state n^{th} temporal scan, summing over all N scans. The peaks of S_{xy} demonstrate the oscillation frequencies common in both the surface state and bulk band temporal scans. This showed a dominant peak corresponding to a period of 1.32 $\pm$ 0.03 fs for all observed harmonics.

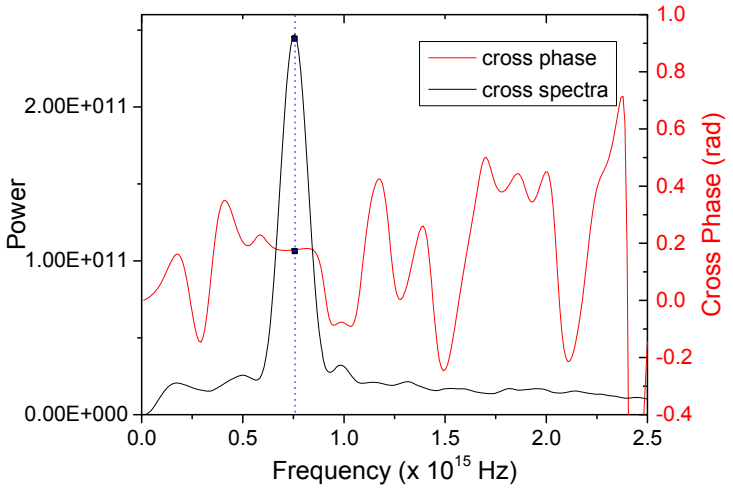

Figure A.6: Average cross-spectral density power for the sp band and surface state at kinetic energy of 21.3 eV (black trace) Using the maximum mode from the cross-spectral power, the average cross phase at that mode can be extracted (red trace).

The average cross-phase of the dominant S_{xy} peak gives the relative phase of the bulk band sidebands with respect to the surface state sideband. This is shown for the sp band sideband relative to the surface state sideband at 21.3 eV, shown in red in Fig. A.6.

The coherence function relating the bulk sidebands to the surface state sideband, for each

harmonic, was also calculated, according to:

$$\gamma_{xy} = \frac{|\sum_{n=1}^{N} \widetilde{x}_n^* \widetilde{y}_n|}{\sqrt{\sum_{n=1}^{N} |\widetilde{x}_n|^2 \sum_{n=1}^{N} |\widetilde{y}_n|^2}} \tag{A.3}$$

This demonstrated how well-defined the phase relationship between the bulk sideband and surface state sideband was as a function of frequency. At the peak frequency (2 ω), previously extracted from the cross-spectral power, the coherence was consistently seen to be greater than 0.9 for all harmonics and for both the sp and d band sidebands, indicating strongly correlated behavior [black trace in Fig. A.7].

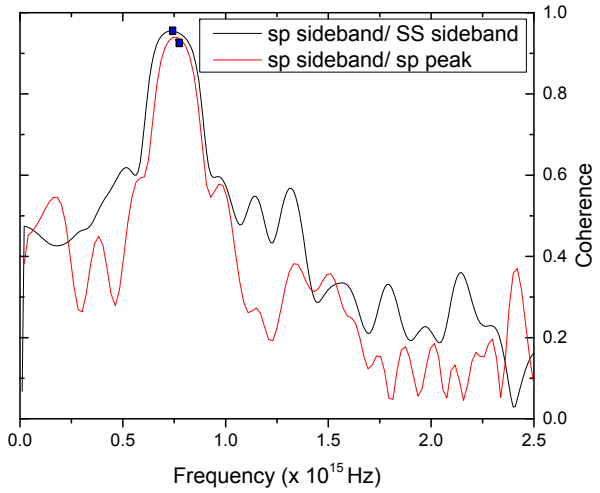

Figure A.7: The coherence function for the sideband feature at 21.3 eV (in red). The sp band sideband oscillation and surface state sideband oscillation were seen to be highly coherent. High coherence was also seen between the oscillation of this sideband peak and its corresponding direct photoemission peak (black).

The one-photon peak and its sideband also were seen to be strongly coherent at the peak of the frequency mode extracted from the average cross-spectra ($7.5 * 10^{14}$ Hz or 1.32 fs), red trace in Fig. A.7. Pairing this information with the extracted cross-phase value, we see that: (1) the sideband and its primary peak have a well-defined phase relationship at the same (2 ω) frequency, and (2) the sideband feature oscillates out of phase from its corresponding one-photon photoelectron peak.

For each harmonic, the coherence value was used in calculating the final error on the extracted cross-phase between the bulk and surface state sidebands. This was calculated from:

$$\epsilon_\gamma = \sqrt{\frac{(1-\gamma_{xy}(f_{max})}{\gamma_{xy}(f_{max})*}2N^{1/2}} \tag{A.4}$$

where f_{max} is the frequency of the maximum in the cross-spectral power, as indicated by the blue markers in figure A.6, and N is the total number of scans. This gives the error values quoted in Fig. 4.8.

A.5 Details of DFT and Bader Charge Analysis for Na intercalation on Gr/Ni(111)

All calculations for the results presented in Section 5.6.2.3 were performed using the VASP code [312] based on spin-polarized density functional theory (DFT). The projector augmented wave potentials were used for electron-ion interactions [313, 314]. Van der Waals dispersion forces were accounted for through the optB88-vdW functional by using the vdW-DF approach [315, 316, 317]. The 2p electrons of Na were explicitly treated as valence electrons by using the semi-core potential and the electron wave function was expanded using plane waves with an energy cutoff of 400 eV. The Ni(111) surface was modeled by a six layer slab separated from its periodic image in z-direction by a vacuum of at least 13 $\AA$. The graphene was adsorbed on the Ni(111) surface by applying the commensurate condition. A (1x1) primitive cell in the top-fcc configuration (one carbon atop of Ni and the other carbon above the fcc hollow site, as shown in Fig 5.6a) was used to model the graphene/Ni(111) system.

To model the Na adsorption on top of graphene/Ni(111) or after intercalation, a single Na atom was adsorbed on top of graphene or was intercalated between graphene and Ni(111) in (3x3) and (2x2) surface unit cells, corresponding to a Na coverage of 1 ML and 0.75 ML, respectively. The Brillouin zones of (1x1), (3x3), and (2x2) were sampled using (17x17x1), (11x11x1), and (9x9x1) Monkhorst-Pack k-point mesh [318], respectively. The three bottom-most Ni(111) layers were fixed during relaxation. All structures were fully relaxed until the Hellmann-Feynman forces acting on

the atoms were smaller than 0.01 eV/$\AA$. The dipole correction was included and the electrostatic potential was adjusted accordingly [318]. To investigate the effect of Na adsorption and intercalation on the graphene states, the band structures of the Na/Gr/Ni(111) and Gr/Na/Ni(111) systems (as shown in Fig 5.13) were calculated in a larger (2x2) supercell. This made it possible to compare the experimental ARPES data with the calculated band structures without unfolding the band structures of the supercell.